

FIRST PRINCIPLES INVESTIGATIONS OF
ELECTROLYTE MATERIALS IN ALL-SOLID-STATE BATTERIES

BY

YAN LI

A Dissertation Submitted to the Graduate Faculty of
WAKE FOREST UNIVERSITY GRADUATE SCHOOL OF ARTS AND SCIENCES

in Partial Fulfillment of the Requirements

for the Degree of

DOCTOR OF PHILOSOPHY

Physics

December 2021

Winston-Salem, North Carolina

Approved By:

Natalie Holzwarth, Ph.D., Advisor

Abdessadek Lachgar, Ph.D., Chair

Oana Jurchescu, Ph.D.

William C. Kerr, Ph.D.

Timo Thonhauser, Ph.D.

ACKNOWLEDGEMENTS

First and foremost, I am deeply grateful to my esteemed advisor Prof. Natalie Holzwarth for her professional guidance and enthusiastic encouragement at every stage of my Ph.D. study and research. Prof. Holzwarth is my role model for being a brilliant physicist with an impressive open-minded and rigorous attitude toward science. When I was a beginner, she was remarkably patient to teach me those basics and steering me to be productive from the start. Every interaction with her is insightful, pleasant, and relaxed. Not only setting an example of an excellent academic mentor, Prof. Holzwarth also understands my possible worries outside the research and is always ready to help if I need it. No matter when, where, and what, the enjoyable journal spending with Prof. Holzwarth is a treasured memory and an unforgettable experience for me.

Besides, I would like to express my sincere gratitude to my committee members Prof. Abdessadek Lachgar, Prof. Oana Jurchescu, Prof. William C. Kerr, and Prof. Timo Thonhauser for their time to evaluate my qualifications and for giving intelligent comments and suggestions.

I am also using this opportunity to express my immense acknowledgment to the rest of the wonderful faculty, staff, and students at the department of physics for creating a fun, supportive, and harmonious environment. In particular, I appreciate the members of condensed matter physics for those helpful discussions and constant motivation.

Furthermore, my profound thanks extends to Dr. Zackary Hood, an alum of the chemistry department who now works at Argonne National Laboratory, for the great collaboration on two projects. It has been very fortunate for us to be able to gain the experimental perspective by consulting with him. I also wish to thank the HPC Team Adam Carlson, Cody Stevens, and Sean Anderson for their valuable technical support in running our calculations on the Wake Forest University DEAC cluster.

Financial support from NSF Grants with Nos. DMR-1507942 and DMR-1940324 is gratefully acknowledged as well.

Last but not least, I must express my most heartfelt gratitude to my amazing family for their love, unwavering support and belief in me over the years. I am so appreciative to have the warm, thoughtful, and caring family that I do.

Table of Contents

List of Figures	x
List of Tables	xi
List of Abbreviations	xii
Abstract	xiii
Part 1 Background	1
Chapter 1 Introduction	2
1.1 Fundamental understanding of Li ion batteries	2
1.2 Electrolyte of Li ion battery	5
1.3 Categories of solid state electrolytes	8
1.4 Objective and structure of this work	11
Chapter 2 Starting theoretical framework and numerical methods	14
2.1 Many-body Schrödinger equation	14
2.2 Born-Oppenheimer approximation	16
2.3 Hartree-Fock method	19
2.4 Density functional theory	24
2.4.1 Hohenberg-Kohn theorem	24

2.4.2	Kohn-Sham equations	27
2.5	Pseudopotentials basics	31
Chapter 3 Phonons in crystals		36
3.1	Dynamics of three-dimensional crystals	36
3.2	Density functional perturbation theory	40
3.3	LO-TO splitting	44
Chapter 4 Theory of ionic transport in solids		48
4.1	Common diffusion mechanisms	48
4.2	The Nernst-Einstein equation and the Haven ratio	51
4.3	Modeling method of ionic transport	54
4.3.1	Nudged elastic band method	54
4.3.2	Ab initio molecular dynamics	57
Part 2 Summary of Research Work		62
Chapter 5 First principles simulations of $\text{Li}_4\text{P}_2\text{S}_6$, and $\text{Na}_4\text{P}_2\text{S}_6$, and $\text{Li}_2\text{Na}_2\text{P}_2\text{S}_6$		63
5.1	Overview	63
5.2	Published work	64
Chapter 6 Continuity of phonon dispersion curves of anisotropic ionic materials		65
6.1	Overview	65
6.2	Published work	66
Chapter 7 First principles simulations of Li_3BO_3, Li_3BN_2 and doped materials		67
7.1	Overview	67

7.2	Published work	69
Chapter 8 First principles simulations of Li boracites $\text{Li}_4\text{B}_7\text{O}_{12}\text{Cl}$		
	and $\text{Li}_5\text{B}_7\text{O}_{12.5}\text{Cl}$	70
8.1	Overview	70
8.2	Manuscripts in preparation	72
Chapter 9 First principles simulations of idealized $\text{Li}_{7.5}\text{B}_{10}\text{S}_{18}\text{X}_{1.5}$ (X		
	= Cl, Br, I)	73
9.1	Introduction	73
9.2	Computational methods	75
9.3	Crystal structures	75
9.4	Stability analysis	81
9.5	Molecular dynamics simulations for Li ions	81
Chapter 10 Conclusions		89
Appendices		91
Chapter A Computational and experimental (re)investigation of the		
	structural and electrolyte properties of $\text{Li}_4\text{P}_2\text{S}_6$, and $\text{Na}_4\text{P}_2\text{S}_6$,	
	and $\text{Li}_2\text{Na}_2\text{P}_2\text{S}_6$	92
Chapter B Continuity of phonon dispersion curves in layered ionic		
	materials	111
Chapter C Computational study of Li_3BO_3 and Li_3BN_2 I: Electrolyte		
	properties of pure and doped crystals	122

Chapter D Computational study of Li_3BO_3 and Li_3BN_2 II: Stability analysis of pure phases and of model interfaces with Li anodes	135
Chapter E First principles simulations of Li boracites $\text{Li}_4\text{B}_7\text{O}_{12}\text{Cl}$ and $\text{Li}_5\text{B}_7\text{O}_{12.5}\text{Cl}$	151
Part 3 References	169
Part 4 Curriculum Vitae	185

List of Figures

1.1	Schematic of basic components and operation principle of a Li ion battery cell with LiCoO_2 as positive electrode and graphite as negative electrode. Reprinted (adapted) with permission from Illa <i>et al.</i> ¹ Copyright 2018 Springer.	4
1.2	Histogram of the number of solid electrolyte publications from the year 2011 to the year 2020. Results were obtained by searching for titles with “solid electrolyte” in Web of Science core collection database.	7
1.3	Ionic conductivity for the representative electrolyte materials. Reprinted with permission from Kamaya <i>et al.</i> ² Copyright 2011 Nature Publishing Group.	10
4.1	Schematic illustration of (a) vacancy, (b) interstitial, and (c) interstitialcy mechanism of diffusion. The solid blue sphere, empty sphere, and arrow represent current atomic position, to be occupied position, and hopping direction, respectively.	49
9.1	Polyhedral diagrams of conventional cells of $\text{Li}_{7.5}\text{B}_{10}\text{S}_{18}\text{Cl}_{1.5}$, comparing (a) experimental structure deduced from diffraction data with (b) the optimized structure of this work. The Li, B, S, and Cl ions are represented by blue, black, yellow, and green balls, respectively.	77

9.2	Summary of results for the three different halides $\text{Li}_{7.5}\text{B}_{10}\text{S}_{18}\text{X}_{1.5}$ with $\text{X} = \text{Cl}$ (a and d), Br (b and e), I (c and f), comparing computationally optimized structures on the top row with the structures deduced by Kaup <i>et al.</i> ³ on the bottom row. The color conventions are the same as in Fig. 9.1 except that the B-O framework is indicated with thin stick.	78
9.3	Plots of the pair distribution functions for $\text{Li}_{7.5}\text{B}_{10}\text{S}_{18}\text{X}_{1.5}$ with $\text{X} = \text{Cl}$ (red), Br (blue), I (green), comparing results deduced from (a) the experimental neutron diffraction by Kaup <i>et al.</i> ³ with results (b) calculated from MD simulations at $\langle T \rangle \approx 400$ K, averaged over 30 ps of simulation time.	80
9.4	Isosurface plots of $P^u(\mathbf{r}) = 0.04\text{\AA}^{-3}$ for Li (a, b, and c) and X (d, e, and f) ions in $\text{Li}_{7.5}\text{B}_{10}\text{S}_{18}\text{X}_{1.5}$ with $\text{X} = \text{Cl}$, Br , I , visualized along the c -axis. The results are determined from molecular dynamics simulations at $\langle T \rangle = 768, 775, \text{ and } 779$ K, respectively. The $\text{B}_{10}\text{S}_{18}$ units are represented by the thin sticks.	83
9.5	MSD plot for Li ions of $\text{Li}_{7.5}\text{B}_{10}\text{S}_{18}\text{Cl}_{1.5}$ at various simulation temperatures as indicated by the text near each curve.	84
9.6	Plots of Li ion conductivity from MD simulations in comparison with experimental conductivity measurements.	85
9.7	Frequency distribution of number of hopping events of Li ions in time interval of 0.5 ps for $\text{Li}_{7.5}\text{B}_{10}\text{S}_{18}\text{X}_{1.5}$ with $\text{X} = \text{Cl}$ (green), Br (brown), and I (violet). The values of vertical axes are obtained from MD simulations of 50 ps duration using primitive cell models at $\langle T \rangle = 768, 775, \text{ and } 779$ K, respectively.	86

9.8 Histograms of the number of visitors of each host site type with label indicated on the horizontal axes for $\text{Li}_{7.5}\text{B}_{10}\text{S}_{18}\text{X}_{1.5}$ with $\text{X} = \text{Cl}$ (green), Br (brown), and I (violet). The values of vertical axes are obtained from MD simulations of 50 ps duration using primitive cell models at $\langle T \rangle = 768, 775,$ and 779 K, respectively. 87

List of Tables

9.1	Summary of lattice parameters and inequivalent fractional positions of Li and X ions for the most stable ordered phases of $\text{Li}_{7.5}\text{B}_{10}\text{S}_{18}\text{X}_{1.5}$ with $\text{X} = \text{Cl}, \text{Br}, \text{I}$. The experiment data were taken from Kaup <i>et al.</i> ³	79
9.2	Computed energy differences ($\Delta U_{SL} = U_{SL}^P - U_{SL}^R$) between reactants (R) and products (P) for reactions indicated by the first column. All energies are given in eV units.	82
9.3	Vacancy energies E_v (in eV/formula unit) for unique vacancy sites in $\text{Li}_{7.5}\text{B}_{10}\text{S}_{18}\text{X}_{1.5}$ ($\text{X} = \text{Cl}, \text{Br}, \text{and I}$). The zero of energy was taken to be the lowest vacancy energy.	88

List of Abbreviations

DFT	Density Functional Theory
DFPT	Density Functional Perturbation Theory
PAW	Projector Augmented Wave
LDA	Local Density Approximation
GGA	Generalized Gradient Approximation
NEB	Nudged Elastic Band
MD	Molecular Dynamics
AIMD	Ab Initio Molecular Dynamics
LO	Longitudinal Optical
TO	Transverse Optical

Abstract

Research into solid electrolytes has recently attracted significant interest along with the emerging demands of developing all-solid-state batteries with major benefits of superior safety, high energy density, and long operation life. The general purpose of this dissertation work is to apply first principles calculations and other computational techniques to reliably explain and predict the detailed structural and ionic transport properties of known and designed solid electrolyte materials. On this basis, five research projects are incorporated into the present work. In the first project, we have focused on $\text{Na}_4\text{P}_2\text{S}_6$ and $\text{Li}_4\text{P}_2\text{S}_6$ for which the structures optimized within the framework of density functional theory with PBEsol and harmonic phonon approximations agree with the experimental findings. Compared to the poor ionic conductor $\text{Li}_4\text{P}_2\text{S}_6$, $\text{Na}_4\text{P}_2\text{S}_6$ appears to be a competitive electrolyte for Na ion batteries. Of particular interest is that the Na ion conductivity can be enhanced by alloying $\text{Na}_4\text{P}_2\text{S}_6$ with Li to form new favorable electrolyte $\text{Li}_2\text{Na}_2\text{P}_2\text{S}_6$. In an effort to understand the discontinuities in the phonon dispersion curves of anisotropic ionic materials, the second part of this work investigates in detail the coupling of long wavelength electromagnetic waves with the vibrational modes of ionic crystals from some fresh perspectives. We then modeled the stability and ionic conduction mechanisms of pure and doped Li_3BO_3 and Li_3BN_2 crystals. By performing extended quasi-harmonic phonon analysis, the X-ray diffraction data of the corrected α form of Li_3BN_2 presents improved agreement with the experimental measurements. Given that the Li ion migration

in the high ionic conducting phases of both materials proceeds most likely via vacancy mechanisms, we computationally substituted F for O in Li_3BO_3 and B for C in $\beta\text{-Li}_3\text{BN}_2$ to introduce excess Li vacancies, finding increased ionic conductivity relative to the pure compounds. Continuing computational efforts are devoted to exploring the structural stability and diffusion mechanisms of lithium haloboracites $\text{Li}_4\text{B}_7\text{O}_{12}\text{Cl}$ and $\text{Li}_5\text{B}_7\text{O}_{12.5}\text{Cl}$. Although the two materials, both characterized by rigid B-O frameworks, have remarkable similarities in atomic arrangements, our simulations show that they exhibit distinct performances as electrolytes. Further attempt finds the Li ion conductivity can be promoted by substituting S for O in $\text{Li}_4\text{B}_7\text{O}_{12}\text{Cl}$ to form $\text{Li}_4\text{B}_7\text{S}_{12}\text{Cl}$. Our current efforts focus on the crystalline members of the $\text{Li}_{7.5}\text{B}_{10}\text{S}_{18}\text{X}_{1.5}$ ($\text{X} = \text{Cl}, \text{Br}, \text{I}$) family, which are identified to be superionic conductors with measured room-temperature ionic conductivity on the order of 10^{-3} S/cm. The preliminary simulations are consistent with the experimental report, indicating that these materials are very promising solid electrolytes for possible use in solid-state Li ion batteries.

Part 1

Background

Chapter 1

Introduction

1.1 Fundamental understanding of Li ion batteries

A lithium (Li) ion battery is a leading type of rechargeable battery that stores and releases energy by Li ions moving between the two terminals of the electrochemical cell. Due to their superior advantages, lightweight, high energy density, stable performance, long battery life, *etc.*, Li ion batteries are widely used in various applications, from portable electronic devices such as mobile phones and laptop computers to large-capacity power sources needed for electric vehicles. In terms of lessening world dependence on traditional fossil fuels, Li ion batteries play an important role in energy storage technologies used with renewable solar and wind resources, to make a fossil-fuel-free society possible. As the most essential energy transport and storage medium at present, Li-ion batteries have benefited the intelligent life of human beings and are benefiting the world in unpredictable ways with the continuous improvement of battery performance.

The story of exploring Li ion batteries goes back to the energy issues caused by the oil crisis in the 1970s. In this context, Stanley Whittingham, who was working at Exxon with the aspiration of developing fossil-fuel-free energy technologies, proposed

the pioneering concept of Li ion batteries.⁴ He developed TiS_2 as an intercalation material accommodating Li ions as the positive electrode material and pure metallic Li as the negative electrode material, to bring out the world's first prototype Li ion battery that can be charged and discharged with a voltage of 2 volts. In 1981, John Banister Goodenough found that the layered positive electrode material LiCoO_2 is more suitable for storing Li ions than TiS_2 because of its high energy density.⁵ This innovation has enhanced the voltage of Li ion batteries to 4 volts, pushing forward a significant step for the development of more robust and practical modern batteries. Inspired by the discovery of Goodenough, Akira Yoshino⁶ patented the first near-commercial Li ion battery. Instead of using the high reactivity of metallic Li as the anode, he employed a safer carbon-based material called petroleum coke, which also allows the insertion of Li ions. In 1991, the Li ion battery invented by Akira Yoshino was successfully commercialized by Sony Corporation, marking the large-scale commercialization of Li ion batteries. With more than three decades of improvements in science and technology, Li ion batteries have made considerable progress in terms of performance, cost, and safety and have revolutionized all aspects of our daily life and industrial production. On October 9, 2019, the 2019 Nobel Prize in Chemistry was awarded jointly to the three scientists mentioned above to acknowledge their outstanding contributions in promoting the development of Li ion batteries, which further affirmed the tremendous value of Li ion batteries in our era.

An individual electrochemical unit of a Li ion battery consists of three major functional components: the positive electrode (cathode during discharge), the negative electrode (anode during discharge), and the electrolyte. While the positive and negative electrodes are made up from different chemically active materials determining the energy density of the battery, the electrolyte provides a medium for Li ions transfer between the electrodes. As a rechargeable battery, the conversion of chemical energy into electrical energy and vice-versa in the cell of a Li ion battery is carried out

by the transport of Li ions between two electrodes through the electrolyte. For this reason, the Li ion battery is also commonly referred to as the “rocking-chair battery” or “swing battery”. Customarily, the processes of Li ions moving in and out of the structures of two electrode materials are called intercalation(insertion) and deintercalation(extraction), respectively. Taking LiCoO_2 as the positive electrode material and graphite as the negative electrode as an example,

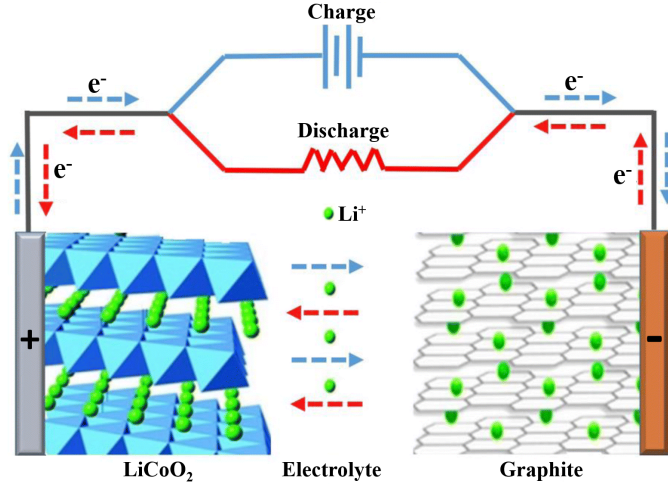
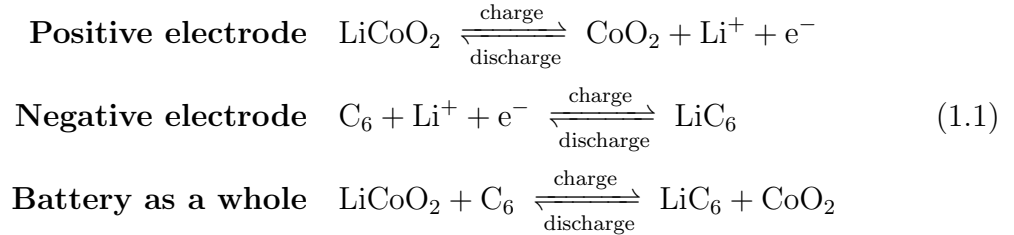


Figure 1.1: Schematic of basic components and operation principle of a Li ion battery cell with LiCoO_2 as positive electrode and graphite as negative electrode. Reprinted (adapted) with permission from Illa *et al.*¹ Copyright 2018 Springer.

The corresponding chemistry (oxidation/reduction reactions) accompanied by Li ion transport takes place according to the following equations⁷



The movement of Li ions within the battery cell is driven by the potential difference between the two electrode terminals upon charge and discharge. Specifically, when the battery is charging up, the Li ions are deintercalated from the high-potential positive electrode material, move internally through the electrolyte toward the neg-

ative electrode, and sequentially insert into the pore spaces of the layered graphite material. At the same time, the compensating electrons flow through the external circuit generating the current. They combine with the graphite at the negative electrode, forming neutral LiC_6 . When the battery is discharging, the character of each electrode is switched, as the Li ions are extracted from the negative electrode, move back to the positive electrode through the electrolyte, and revert to the original component LiCoO_2 together with the electrons flowing back through the external circuit. During this process, the stored chemical energy is converted into electrical energy to power the applied load. It can be seen that the charging-discharging cycle of a Li ion battery is ideally reversible, including small structural variations of each fundamental constituent during the process. Although for years of intense research, advanced electrodes and electrolyte materials for Li ion batteries are continuously being discovered, their overall structure and working principle have remained basically unchanged.

1.2 Electrolyte of Li ion battery

Li ion battery electrolytes can be grouped into liquid electrolytes, solid electrolytes, and solid-liquid hybrid electrolytes that have been extensively studied recently. Acting as a crucial medium for ionic conduction, the electrolytes for Li ion batteries should satisfy the following stringent set of requirements:⁸⁻¹¹ (1) Excellent ionic conductivity with adequate diffusion of Li ions. Generally, the ionic conductivity of commercial electrolytes ranges from 3×10^{-3} to 2×10^{-2} S/cm; (2) Electronically insulating to avoid self-discharge of the battery cell; (3) Strong thermal stability at a wide operating temperature range (-40 - 60 °C); (4) No substantial degradation due to the electrochemical reaction over a broad potential window; (5) Certain mechanical strength and elasticity for accommodating volume changes of the electrode materials and to preserve the physical stability during operation; (6) Compatible interface

with electrode materials to minimize Li ion transport resistance; (7) Environmentally friendly, safe, non-toxic and non-polluting.

The Li ion batteries typically use organic liquid electrolytes containing a conducting Li salt, commonly LiPF_6 , dissolved together with various additives in an organic solvent system such as cyclic carbonate (PC, EC), and chain carbonate (DEC, DMC, EMC).^{8,12} While the conventional liquid electrolytes have significant merits of high ionic conductivity, their drawbacks in terms of safety, such as leakage, corrosion, and flammability are obvious and inevitable. In the case of experiencing external shocks and collisions or operating in harsh conditions, there are risks of short circuits, overheating, overcharge, and so on. These may lead to accidents involving severe combustion or explosion accidents with thermal runaway inside the battery. In addition, to maximize the energy density of the existing battery system, it is preferential to employ the pure Li metal as the anode material^{13,14} for its desirable attributes of lowest electrochemical potential (-3.04 V versus the standard hydrogen electrode), lightweight (0.53 g/cm^{-3}), and ultrahigh theoretical specific capacity (3860 mAh/g). However, there are some technical issues that must be addressed. For example in the case of overcharged or charging too fast, some migrated Li ions may not be able to catch up with the pace to access the void space of the negative electrode, forming metallic Li by occasionally trapping electrons in the vicinity of the electrode-electrolyte interface. The deposited “dead lithium” grows into dendritic crystals, commonly known as dendrites,^{15,16} which will greatly reduce the battery capacity and the reversibility of energy conversion. Furthermore, they may pierce the separator and results in safety hazards.

Driven by the rapid development of electric vehicles and large-scale energy storage, the construction of Li ion batteries with high energy densities has attracted more and more interest from academia and industry. What comes along is that the higher the energy density of the battery, the more critical it is to ensure operational safety. In

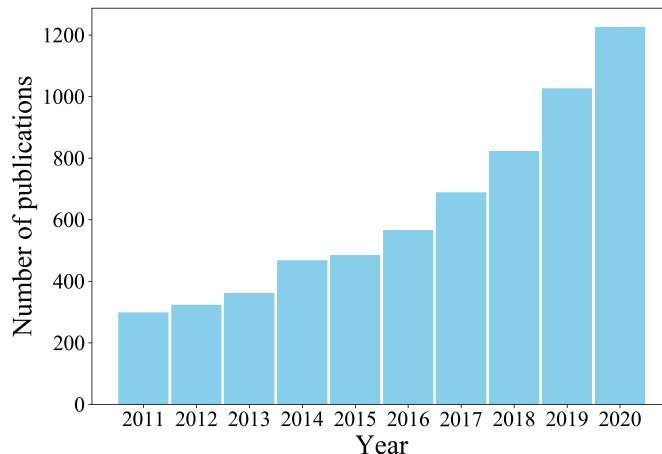


Figure 1.2: Histogram of the number of solid electrolyte publications from the year 2011 to the year 2020. Results were obtained by searching for titles with “solid electrolyte” in Web of Science core collection database.

this context, solid electrolytes that replace organic liquid electrolytes and separators are expected to provide a viable solution to overcome the safety issues. Besides, by assembling solid electrolytes with the high-potential positive electrodes and Li metal negative electrodes, the resulting all-solid-state batteries are projected to bypass the two critical bottlenecks, namely, narrow electrochemical window and low energy density, of conventional Li ion batteries. Due to those distinctive features, there has been a growing worldwide upsurge in research on solid electrolyte materials in recent years, as quantified in Fig. 1.2. Specifically, the significant advantages of solid electrolytes are:^{9,17,18} (1) Robust safety and high thermal stability for eliminating potential safety hazards such as flammability, corrosion, volatilization, and leakage of liquid electrolytes; (2) Large electronic band gaps leading to minimal conductivity due to electrons; (3) Key component to forming all-solid-state batteries with competitive energy density. Since there is no liquid content and the separator, together with the metallic Li directly used as the negative electrode, the energy density of all-solid-state batteries is remarkably enhanced, up to 400 Wh/kg of specific energy; (4) Excellent structural rigidity and mechanical strength which can effectively inhibit the growth of the Li dendrites and greatly improve the battery’s cycle performance and service

life; (5) Superior chemical stability and physical stability; (6) Wide electrochemical window of 5 V versus Li/Li⁺ or more.

However, there are still shortcomings for most solid electrolytes, such as high cost, complicated production processes, low room-temperature ionic conductivity, poor stability of the electrode-electrolyte interface, and large-scale grain boundaries, *etc.*,¹⁹ that dramatically hinder the practicality of solid electrolytes for commercial use. Encouragingly, those challenges are met actively through joint intellectual efforts from both theory and experiment. For example, researchers have been striving to develop machine learning tools and other advanced computational techniques to gain insights into structure–property relationships and to accelerate the discovery of new materials with highly optimized properties.^{20,21}

1.3 Categories of solid state electrolytes

The solid electrolyte materials with the most marketable prospects are generally classified into two main categories:^{22,23} solid polymer electrolytes and inorganic solid electrolytes, while the latter being further subdivided into oxide and sulfide solid electrolytes.

The solid polymer electrolytes, formed by diverse solvent-free alkali metal salts dissolved into an organic polymer matrix, have been regarded as a promising solid electrolyte candidate for Li metal battery following the detection of ionic transport since 1970s.²⁴ Primarily attributed to their great solvation power and compelling capacity of ion transport,²⁵ the polymer matrix composites include classic polyethylene oxide (PEO), and its derivatives polypropylene oxide (PPO), polyacrylonitrile (PAN), and polyvinylidene fluoride (PVDF), *etc.* are commonly adopted as solid hosts to conduct ions through a segmental motion of the polymer chains.^{9,26} The polymer-based solid electrolytes are recognized for having high safety, good flexibil-

ity, excellent interface compatibility, and processability.²⁷ However, the generally low room-temperature ionic conductivity, as well as narrow electrochemical window, remain to be improved in order to meet the needs of commercial applications.

The inorganic solid electrolytes cover a vast family of materials which are featured most intuitively by structural distinctions. Among them, the earlier successfully developed LiPON (lithium phosphorus oxynitride) by Bates *et al.*²⁸⁻³⁰ at the Oak Ridge National Laboratory in 1990s represents a typical class of inorganic oxide solid electrolytes. The exploration of LiPON type electrolytes in terms of synthesis, properties, and electronic structure has been attracting substantial interest because of the merits of high chemical stability, reasonable ionic conductivity, and good compatibility with both metallic Li anode and a high voltage cathode.³¹⁻³⁴ To date, LiPON is still the best option to fabricate the all-solid-state thin film batteries and has been commercialized for years.²³ Motivated by the discovery of LiPON, there are a number of attractive structural families of oxide-based electrolytes being extensively studied, including Li conducting garnets such as $\text{Li}_5\text{La}_3\text{M}_2\text{O}_{12}$ ($\text{M} = \text{Nb}, \text{Ta}$) and $\text{Li}_3\text{Ln}_3\text{Te}_2\text{O}_{12}$ ($\text{Ln} = \text{Y}, \text{Pr}, \text{Nd}, \text{Sm-Lu}$),³⁵ LISICON-like (Li superionic conductor) of various variants of $\text{Li}_{2+2x}\text{Zn}_{1-x}\text{GeO}_4$ ($-0.36 \leq x \leq 0.87$),³⁶ NASICON-like (sodium superionic conductor) derived from the example structure with chemical formula $\text{Na}_{1+x}\text{Zr}_2\text{Si}_x\text{P}_{3-x}\text{O}_{12}$ ($0 \leq x \leq 3$),³⁷ and perovskite such as $\text{Li}_{3x}\text{La}_{2/3-x}\text{TiO}_3$ ($0.01 \leq x \leq 0.15$) formed by Li ions being placed on the A-type site of the prototype structure ABO_3 ($\text{A} = \text{La}, \text{Sr}, \text{or Ca}; \text{B} = \text{Al or Ti}$).³⁸

The inorganic sulfide solid electrolytes mainly contain crystalline thio-LISICON-type LGPS with orthorhombic $\beta\text{-Li}_3\text{PS}_4$ structure and amorphous sulfide $\text{Li}_2\text{S-M}_x\text{S}_y\text{-P}_2\text{S}_5$ ($\text{M} = \text{Al}, \text{Si}, \text{etc.}$)²³ As opposed to the O ion, the S ion has a larger atomic radius, lower electronegativity, and higher polarizability. Those features, in principle, hold the promise of relatively fast ion transport in the interconnected network of expanded conduction channels. For example, as illustrated in Fig. 1.3 for different

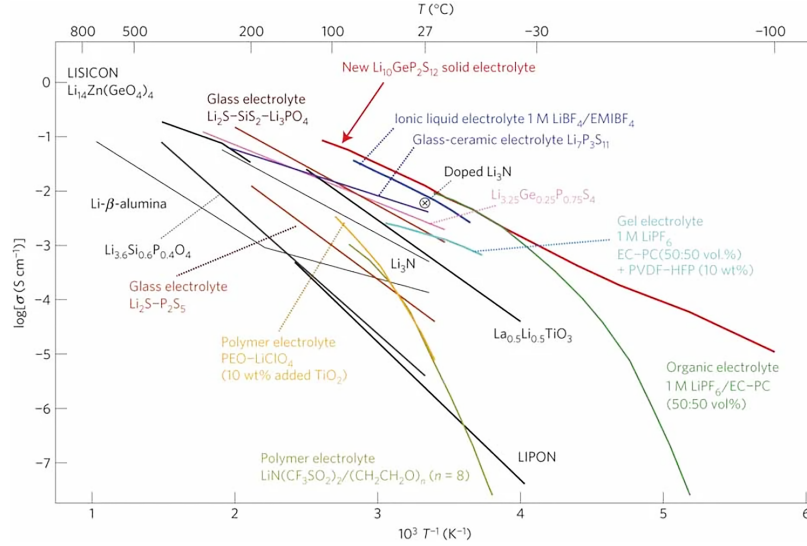


Figure 1.3: Ionic conductivity for the representative electrolyte materials. Reprinted with permission from Kamaya *et al.*² Copyright 2011 Nature Publishing Group.

types of Li ion conductors, the widely studied $\text{Li}_{10}\text{GeP}_2\text{S}_{12}$ was found to exhibit excellent ionic conductivity of 10^{-2} S/cm at room temperature,² which is comparable to that of liquid electrolytes currently the most used in the market. However, the air or moisture sensitivity and suboptimal electrode/electrolyte interface are remaining the major challenges for sulfide-based electrolytes.^{39,40}

Similar to Li ion conducting electrolytes, the investigation on the counterpart Na ion electrolytes for solid state Na ion batteries is also an essential part of electrochemical energy storage technologies. In 2019, Hayashi *et al.*⁴¹ reported a Na ion sulfide solid electrolyte with the composition of $\text{Na}_{2.88}\text{Sb}_{0.88}\text{W}_{0.12}\text{S}_4$. The measured room temperature ionic conductivity for this novel material is up to 3.2×10^{-2} S/cm, exceeding that of the best Li ion thiophosphate conductor $\text{Li}_{9.54}\text{Si}_{1.74}\text{P}_{1.44}\text{S}_{11.7}\text{Cl}_{0.3}$ ($\sigma_{25\text{ }^\circ\text{C}} = 2.5 \times 10^{-2}$ S/cm) which has the $\text{Li}_{10}\text{GeP}_2\text{S}_{12}$ -type crystal structure.⁴² More recently, another example of superior Na ion conductor $\text{Na}_{3-x}\text{Y}_{1-x}\text{Zr}_x\text{Cl}_6$ (NYZC), with ionic conductivity of 6.6×10^{-5} S/cm at room temperature, was characterized to be chemically stable and mechanically compatible when incorporated into high-voltage oxide cathodes.⁴³ Those findings, together with the lower cost and higher

abundance of sodium resources, make Na ion conductors the immense potential candidate for developing long lifespan, high performance, and cost-effective solid state Na ion batteries.

1.4 Objective and structure of this work

In terms of computational materials science, reliable simulation modeling is of great value for assessing the critical physical processes of the actual materials. The general purpose of the present work is to apply computer simulations developed based on first principles approaches to understand the fundamental and technological properties of bulk inorganic solid electrolyte materials designed to be used with pure Li or Na anodes.

In our research projects, we have been focusing on crystalline materials and the detailed diffusion process of working ions in viable ionic conductors. Following the methods within the framework of density functional theory (DFT)^{44,45} and density functional perturbation theory (DFPT)⁴⁶⁻⁵⁰ of past computational studies, it is straightforward to investigate many of the known crystal structures to find the static lattice energies and the corresponding Helmholtz free energies of vibration in the harmonic phonon approximation. This would allow us to examine the relative stabilities of crystals that have been determined to have multiple structures. In the aspect of analyzing the electrolyte properties, the calculation results using nudged elastic band (NEB)⁵¹⁻⁵³ methodology and ab initio molecular dynamics (AIMD) techniques can provide insight into the Li or Na ion migration mechanisms that are responsible for ionic conductivity. As a key to the success of the battery system, the behavior of the idealized interface between electrolyte and electrode such as pure metallic Li or Na anode is also conveniently accessible through modeling study. Overall, the goal of our computational effort from first principles is, in the first place, to provide a systematic

and quantitative comparison with experimental measurements on an already existing electrolyte material and to help interpret the related experimental phenomenon qualitatively and quantitatively. Additionally, reliable and accurate predictions using computational tools could offer experimentalists great guidance to synthesize new plausible materials starting from theoretically proposed compounds and structures.

The present chapter (Chapter 1) has presented the basics of batteries and the significance of studying solid electrolyte materials. The other chapters of this dissertation are structured as follows. Chapter 2 is devoted to giving an overview of the theoretical and computational approximations that constitute the elemental basis of effective DFT modeling. Based upon the theory discussed in the previous chapter, Chapter 3 generalizes the concepts for understanding and calculating the vibrational properties of crystalline solids. Chapter 4 briefly introduces diffusion and ionic conductivity in ionic solids, and two well-developed numerical approaches, namely nudged elastic band for estimating transition states and molecular dynamics simulations for statistically evaluating ionic transport process. Summaries of first-author publications are presented in Chapters 5-9. To be specific, in Chapter 5 we studied the structural and electrolyte properties of known electrolytes $\text{Li}_4\text{P}_2\text{S}_6$ and $\text{Na}_4\text{P}_2\text{S}_6$, and the predicted mixed-ion material with the composition $\text{Li}_2\text{Na}_2\text{P}_2\text{S}_6$ through a collaborative effort with Prof. Natalie Holzwarth and Dr. Zachary Hood. Motivated by the observed discontinuous phonon dispersion curves of anisotropic ionic materials, Chapter 6, with the work done in collaboration with Prof. Natalie Holzwarth and Prof. William C. Kerr, discusses in detail the coupling of long-wavelength electromagnetic waves with lattice vibrations from some new perspectives. Chapter 7 includes two closely related papers on similar materials Li_3BO_3 and Li_3BN_2 , one focuses on electrolyte properties of pure and doped crystals, the other contributes the stability analysis of pure phases and of model interfaces with Li anodes. Those two companion works covered in Chapter 7 were done collaboratively with Prof. Natalie

Holzwarth and Dr. Zachary Hood. Chapter 8 presents the current computational results on Li ion conducting boracites $\text{Li}_4\text{B}_7\text{O}_{12}\text{Cl}$ with fractional occupied Li sites and $\text{Li}_5\text{B}_7\text{O}_{12.5}\text{Cl}$ with all fully occupied sites. This project addresses the question of what factors led to the dramatic differences in electrolyte properties between two materials similar in crystal structures. Chapter 9 is an ongoing study of recently reported Li thioborate halides with formula $\text{Li}_{7.5}\text{B}_{10}\text{S}_{18}\text{X}_{1.5}$ ($\text{X} = \text{Cl}, \text{Br}, \text{and I}$) which exhibit excellent ionically conducting properties with measured room-temperature ionic conductivity on the order of 10^{-3} S/cm. A summary and some conclusions of this dissertation are presented in Chapter 10.

Presently there are various software packages developed for electronic structure calculations and materials modeling. In our work, we mainly use ABINIT⁵⁴ and QUANTUM ESPRESSO⁵⁵ with implemented projector augmented wave (PAW) pseudopotentials. Both packages are based on quantum equations of DFT and consist of a set of computer codes that provide powerful capacities in analyzing various properties of materials. The ATOMPAW,⁵⁶ for which the source code and the related documents available at the website <http://users.wfu.edu/natalie/papers/pwpaw/man.html>, generates atomic datasets for use in first principles simulations using the PAW formalism. Computations were performed on the Wake Forest University Distributed Environment for Academic Computing (DEAC) cluster, a centrally managed resource with support provided in part by the university and in part by contributions from grants.

Chapter 2

Starting theoretical framework and numerical methods

“The fundamental laws necessary for the mathematical treatment of a large part of physics and the whole of chemistry are thus completely known, and the difficulty lies only in the fact that application of these laws leads to equations that are too complex to be solved.”

– Paul Dirac, 1929

2.1 Many-body Schrödinger equation

The understanding of the equilibrium behaviour of quantum particles requires to solve quantum mechanic Schrödinger equation⁵⁷ to obtain eigenstates and the corresponding eigenvalues in the ground state. For example, the time-independent version of the Schrödinger equation for a stationary electronic state containing N electrons with coordinates $\mathbf{r}_1, \mathbf{r}_2, \dots, \mathbf{r}_N$ and M nuclei with coordinates $\mathbf{R}_1, \mathbf{R}_2, \dots, \mathbf{R}_M$ has the form

$$\hat{H}_{\text{tot}}\Psi(\mathbf{r}_1, \mathbf{r}_2, \dots, \mathbf{r}_N; \mathbf{R}_1, \mathbf{R}_2, \dots, \mathbf{R}_M) = E_{\text{tot}}\Psi(\mathbf{r}_1, \mathbf{r}_2, \dots, \mathbf{r}_N; \mathbf{R}_1, \mathbf{R}_2, \dots, \mathbf{R}_M), \quad (2.1)$$

here Ψ is the many-body wavefunction which depends on positions of all electrons and all nuclei, E_{tot} represents the energy eigenvalue described by Ψ . The full Hamiltonian \hat{H}_{tot} is given by

$$\begin{aligned}\hat{H}_{\text{tot}} &= \hat{T}_e(\mathbf{r}) + \hat{T}_N(\mathbf{R}) + \hat{V}_{eN}(\mathbf{r}, \mathbf{R}) + \hat{V}_{ee}(\mathbf{r}) + \hat{V}_{NN}(\mathbf{R}) \\ &= -\frac{\hbar^2}{2m} \sum_i \nabla_i^2 - \sum_I \frac{\hbar^2}{2M_I} \nabla_I^2 - \sum_{i,I} \frac{Z_I e^2}{|\mathbf{r}_i - \mathbf{R}_I|} + \frac{e^2}{2} \sum_{i \neq j} \frac{1}{|\mathbf{r}_i - \mathbf{r}_j|} + \frac{e^2}{2} \sum_{I \neq J} \frac{Z_I Z_J}{|\mathbf{R}_I - \mathbf{R}_J|},\end{aligned}\quad (2.2)$$

where m denotes the mass of electrons, M_I represents the mass of the I th nucleus having atomic number Z_I , the indices $i(j)$, $I(J)$ run from 1 to N and 1 to M , respectively. The five terms included in the above expression, in order, are kinetic energy of N electrons, kinetic energy of M nuclei, Coulomb attraction between electrons and nuclei, Coulomb repulsion between electron pairs, Coulomb repulsion between nuclei pairs. We now demand that the total wavefunction be normalized

$$\langle \Psi | \Psi \rangle = \int |\Psi(\mathbf{r}_1, \mathbf{r}_2, \dots, \mathbf{r}_N; \mathbf{R}_1, \mathbf{R}_2, \dots, \mathbf{R}_M)|^2 d\mathbf{r}_1, d\mathbf{r}_2, \dots, d\mathbf{r}_N d\mathbf{R}_1, d\mathbf{R}_2, \dots, d\mathbf{R}_M = 1. \quad (2.3)$$

In practice, we put effort only into the electron density $\rho(\mathbf{r})$, namely the probability of finding any electron at \mathbf{r} . Conceptually, the quantity is equivalent to the sum of the probability $P(\mathbf{r}_i = \mathbf{r})$ of finding electron number i at position \mathbf{r} . Since in quantum mechanics electrons are identical fermions, the electron density can then be written as

$$\begin{aligned}\rho(\mathbf{r}) &= \sum_i P(\mathbf{r}_i = \mathbf{r}) = NP(\mathbf{r}_1 = \mathbf{r}) \\ &= N \int |\Psi(\mathbf{r}, \mathbf{r}_2, \dots, \mathbf{r}_N; \mathbf{R}_1, \mathbf{R}_2, \dots, \mathbf{R}_M)|^2 d\mathbf{r}_2, \dots, d\mathbf{r}_N d\mathbf{R}_1, d\mathbf{R}_2, \dots, d\mathbf{R}_M,\end{aligned}\quad (2.4)$$

here the integral was computed over all possible nuclear coordinates. Integrating $\rho(\mathbf{r})$ throughout the whole material yields the total number of electrons N of the system

$$\int \rho(\mathbf{r}) d\mathbf{r} = N. \quad (2.5)$$

The many-body Schrödinger equations given by Eq. (2.1) is easy to be written

down, but in practice, solving it for a large number of interacting electrons and nuclei is too complicated. In fact, solving this equation directly is essentially an impossible task for most many-body systems. Through efforts over many years, numerous physical models and theories have been proposed to simplify this problem and developed the so-called “first principles approach” which refers to studying the materials properties through a series of well-established physical approximations and simplifications starting from the complete form of the many-body Schrödinger equation.

2.2 Born-Oppenheimer approximation

In the study of solids and molecules, it is reasonable to assume that the nuclei are hold immobile in known places, or as a consequence of heavier masses, only move a pretty short distance with trivial velocities in comparison with electrons. Therefore for each configuration during the evaluation of the system, the electrons respond instantaneously to the motion of the nuclei, namely, the electrons can always remain the lowest-energy eigenstates associated with the nuclear coordinates. Under this idea which goes under the name of the Born-Oppenheimer approximation,^{58,59} it is possible to separate the electronic and the nuclear coordinates in the many-body wave function

$$\Psi(\mathbf{r}_1, \mathbf{r}_2, \dots, \mathbf{r}_N; \mathbf{R}_1, \mathbf{R}_2, \dots, \mathbf{R}_M) = \Psi_{\mathbf{R}}(\{\mathbf{r}\})\chi(\{\mathbf{R}\}), \quad (2.6)$$

where $\Psi_{\mathbf{R}}(\{\mathbf{r}\}) = \Psi_{\mathbf{R}}(\mathbf{r}_1, \mathbf{r}_2, \dots, \mathbf{r}_N)$ represents the normalized electron-only wavefunction depending parametrically on the fixed nuclear configuration, and $\chi(\{\mathbf{R}\}) = \chi(\mathbf{R}_1, \mathbf{R}_2, \dots, \mathbf{R}_M)$ represents the nuclear-only wavefunction. Before proceeding further, we need to aware that in a rigorous treatment the total wavefunction Ψ should be written as a linear combination in the product form $\Psi = \sum_l \Psi_{\mathbf{R}}^l(\{\mathbf{r}\})\chi^l(\{\mathbf{R}\})$ starting from the lowest electronic eigenstate $l = 0$. For the purpose of illustrating the idea of Born-Oppenheimer approximation, we assume that only the lowest-energy term is being used in the linear combination. Combining Eqs. (2.1), (2.2), and (2.6),

the full Schrödinger equation reads

$$\left[\hat{T}_e(\mathbf{r}) + \hat{T}_N(\mathbf{R}) + \hat{V}_{eN}(\mathbf{r}, \mathbf{R}) + \hat{V}_{ee}(\mathbf{r}) + \hat{V}_{NN}(\mathbf{R}) \right] \Psi_{\mathbf{R}}(\{\mathbf{r}\})\chi(\{\mathbf{R}\}) = E_{\text{tot}} \Psi_{\mathbf{R}}(\{\mathbf{r}\})\chi(\{\mathbf{R}\}). \quad (2.7)$$

The fact that $M_I \gg m$ implies that in contrast to a wide-ranging movements of electrons, the motions of nuclei are quite localized, presenting a steep wavefunction in a very narrow region around their original coordinates. We can therefore approximate

$$\hat{T}_N \Psi_{\mathbf{R}}(\{\mathbf{r}\})\chi(\{\mathbf{R}\}) = - \sum_I \frac{\hbar^2}{2M_I} \nabla_I^2 [\Psi_{\mathbf{R}}(\{\mathbf{r}\})\chi(\{\mathbf{R}\})] \approx - \sum_I \frac{\hbar^2}{2M_I} \Psi_{\mathbf{R}}(\{\mathbf{r}\}) \nabla_I^2 \chi(\{\mathbf{R}\}). \quad (2.8)$$

This approximation allows us to deal with electrons for a set of clamped nuclei and separate out the Schrödinger equation for electrons from Eq. (2.7)

$$\hat{H}_{\mathbf{R}} \Psi_{\mathbf{R}}(\{\mathbf{r}\}) = E_{\mathbf{R}} \Psi_{\mathbf{R}}(\{\mathbf{r}\}), \quad (2.9)$$

here $E_{\mathbf{R}} = E(\mathbf{R}_1, \mathbf{R}_2, \dots, \mathbf{R}_M)$ is the total energy of the electrons as a function of nuclear coordinates. The corresponding electronic Hamiltonian is given by

$$\begin{aligned} \hat{H}_{\mathbf{R}} &= \hat{T}_e(\mathbf{r}) + \hat{V}_{eN}(\mathbf{r}, \mathbf{R}) + \hat{V}_{ee}(\mathbf{r}) \\ &= - \frac{\hbar^2}{2m} \sum_i \nabla_i^2 - \sum_{i,I} \frac{Z_I e^2}{|\mathbf{r}_i - \mathbf{R}_I|} + \frac{e^2}{2} \sum_{i \neq j} \frac{1}{|\mathbf{r}_i - \mathbf{r}_j|}. \end{aligned} \quad (2.10)$$

Substituting Eqs. (2.9) and (2.10) back into Eq. (2.7) yields

$$E_{\mathbf{R}} \Psi_{\mathbf{R}} \chi + \left[- \sum_I \frac{\hbar^2}{2M_I} \nabla_I^2 + \frac{e^2}{2} \sum_{I \neq J} \frac{Z_I Z_J}{|\mathbf{R}_I - \mathbf{R}_J|} \right] \Psi_{\mathbf{R}} \chi = E_{\text{tot}} \Psi_{\mathbf{R}} \chi. \quad (2.11)$$

Multiplying both sides of Eq. (2.11) by $\Psi_{\mathbf{R}}^*$ from the left and integrating over the whole electronic space, we find the Schrödinger equation for nuclei alone turns out to be

$$\hat{H}_N \chi(\{\mathbf{R}\}) = \left[- \sum_I \frac{\hbar^2}{2M_I} \nabla_I^2 + U(\mathbf{R}_1, \mathbf{R}_2, \dots, \mathbf{R}_M) \right] \chi(\{\mathbf{R}\}) = E_{\text{tot}} \chi(\{\mathbf{R}\}), \quad (2.12)$$

where the total potential energy of the nuclei is defined as

$$U(\mathbf{R}_1, \mathbf{R}_2, \dots, \mathbf{R}_M) = \frac{e^2}{2} \sum_{I \neq J} \frac{Z_I Z_J}{|\mathbf{R}_I - \mathbf{R}_J|} + E(\mathbf{R}_1, \mathbf{R}_2, \dots, \mathbf{R}_M). \quad (2.13)$$

From here, we can intuitively see that the total electronic energy $E(\mathbf{R}_1, \mathbf{R}_2, \dots, \mathbf{R}_M)$ enters into the nuclear Schrödinger equation and acts as an effective potential. In other words, when we write the Schrödinger equations for the electronic system and the nuclear system separately, it should be understood that the label of the nuclear coordinate \mathbf{R} appears only as a parameter in the electronic Schrödinger function. Once we solve for the electron-only wavefunction and obtain the total electronic energy $E(\mathbf{R}_1, \mathbf{R}_2, \dots, \mathbf{R}_M)$, we can use this available quantity as one term of the potential energies in the nuclear Schrödinger equation, and then access the nuclear wavefunction as well as the total energy of the system by solving the Schrödinger equation in Eq. (2.12).

In terms of equilibrium structures of materials, the dynamics of the nuclei can be described very well using classical approach, thus the force action on the I th nucleus is simply given by

$$\mathbf{F}_I = -\frac{\partial U(\{\mathbf{R}\})}{\partial \mathbf{R}_I} = -\frac{\partial E(\{\mathbf{R}\})}{\partial \mathbf{R}_I} - \frac{\partial V_{\text{NN}}(\{\mathbf{R}\})}{\partial \mathbf{R}_I}. \quad (2.14)$$

Applying the Hellmann-Feynman theorem,^{60,61} the differential of $E(\{\mathbf{R}\})$ with respect to the nuclear position is simplified to

$$-\frac{\partial E(\{\mathbf{R}\})}{\partial \mathbf{R}_I} = -\left\langle \Psi_{\mathbf{R}} \left| \frac{\partial \hat{H}_{\mathbf{R}}}{\partial \mathbf{R}_I} \right| \Psi_{\mathbf{R}} \right\rangle. \quad (2.15)$$

Thus Eq. (2.14) can be written as

$$\mathbf{F}_I = Z_I e^2 \left[\int \rho(\mathbf{r}) \frac{\mathbf{r} - \mathbf{R}_I}{|\mathbf{r} - \mathbf{R}_I|^3} d\mathbf{r} - \sum_{J \neq I} Z_J \frac{\mathbf{R}_J - \mathbf{R}_I}{|\mathbf{R}_J - \mathbf{R}_I|^3} \right]. \quad (2.16)$$

2.3 Hartree-Fock method

Within the framework of Born-Oppenheimer approximation, the many-particle system was simplified into a many-electron system. Now we concentrate on the quantum behavior of electrons by recalling Eq. (2.10)

$$\hat{H} = -\frac{\hbar^2}{2m} \sum_i \nabla_i^2 - \sum_{i,I} \frac{Z_I e^2}{|\mathbf{r}_i - \mathbf{R}_I|} + \frac{e^2}{2} \sum_{i \neq j} \frac{1}{|\mathbf{r}_i - \mathbf{r}_j|}. \quad (2.17)$$

Notice that when analyzing a system of electrons moving in a given field of fixed nuclei, $\hat{H} \equiv \hat{H}_{\mathbf{R}}$ in Eq. (2.10). The subscript “ \mathbf{R} ” standing for the dependence on nuclear coordinates has been taken out to simplify the notation. This equation can be simplified further by introducing a convenient notion $V_{\text{ext}}(\mathbf{r})$, given by

$$V_{\text{ext}}(\mathbf{r}) = - \sum_I \frac{Z_I e^2}{|\mathbf{r} - \mathbf{R}_I|}, \quad (2.18)$$

which represents the Coulomb potential generated by all nuclei at an electron position. At this point it is obviously that the nuclear coordinates, $\{\mathbf{R}_I\}$, have disappeared completely so we can rewrite Eq. (2.17) as

$$\hat{H} = \sum_i \left[-\frac{\hbar^2}{2m} \nabla_i^2 + V_{\text{ext}}(\mathbf{r}_i) \right] + \frac{e^2}{2} \sum_{i \neq j} \frac{1}{|\mathbf{r}_i - \mathbf{r}_j|}. \quad (2.19)$$

The Coulomb interaction between large numbers of electrons makes attempting the exact solution for the electronic Schrödinger equation nearly impossible. One of the approximations that can immediately come to mind is to leave out the electron-electron interaction term, in such a way that the electrons would be independent of each other, generating a set of non-interacting single-particle equations. Mathemati-

cally, that is to say

$$\hat{H}\Psi = E\Psi \quad \rightarrow \quad \sum_i \hat{H}_0(\mathbf{r}_i)\Psi = E\Psi, \quad (2.20)$$

where the single-particle Hamiltonian \hat{H}_0 takes the explicit form

$$\hat{H}_0(\mathbf{r}) = -\frac{\hbar^2}{2m}\nabla^2 + V_{\text{ext}}(\mathbf{r}). \quad (2.21)$$

For each eigenstate $\psi_i(\mathbf{r})$, we have

$$\hat{H}_0(\mathbf{r})\psi_i(\mathbf{r}) = \varepsilon_i\psi_i(\mathbf{r}), \quad (2.22)$$

where ε_i denotes the eigenvalue of the i th eigenstate which can be solved exactly. Based on this approximation, the total wavefunction of the electronic Schrödinger equation can be written as a product of the solutions to the single-particle equations

$$\Psi(\mathbf{r}_1, \mathbf{r}_2, \dots, \mathbf{r}_N) = \prod_i \psi_i(\mathbf{r}). \quad (2.23)$$

And the total electronic energy E is simply obtained by adding up the energies of all occupied single-electron energies ε_i

$$E = \langle \Psi | \hat{H} | \Psi \rangle = \sum_i \langle \psi_i(\mathbf{r}) | \hat{H}_0 | \psi_i(\mathbf{r}) \rangle = \sum_i \varepsilon_i. \quad (2.24)$$

The idea discussed above goes under the name of independent electrons approximation, which shows quite clearly that we can achieve a great simplification of the many-electron problem by describing the total wavefunction Ψ of $3N$ variables using N three-dimensional single-particle wavefunctions. But all this came at a cost of diminishing the exact physical process due to ignoring a significant contribution of interacting electrons to the Hamiltonian.

Bear in mind that because of the quantum nature of electrons as fermions, the many-electron wavefunction must be adjusted to satisfy Pauli's exclusion principle,⁶² that is, no two fermions can occupy the same quantum state, this requirement can be satisfied by writing the total wavefunction in the form of a Slater determinant of single electron configurations⁶³

$$\Psi(\mathbf{r}_1, \mathbf{r}_2, \dots, \mathbf{r}_N) = \frac{1}{\sqrt{N!}} \begin{vmatrix} \psi_1(\mathbf{r}_1) & \psi_1(\mathbf{r}_2) & \cdots & \psi_1(\mathbf{r}_N) \\ \psi_2(\mathbf{r}_1) & \psi_2(\mathbf{r}_2) & \cdots & \psi_2(\mathbf{r}_N) \\ \vdots & \vdots & \ddots & \vdots \\ \psi_N(\mathbf{r}_1) & \psi_N(\mathbf{r}_2) & \cdots & \psi_N(\mathbf{r}_N) \end{vmatrix} \quad (2.25)$$

At this point, we can think about pursuing a more accurate solution for the electronic Schrödinger equation by taking the Coulomb repulsion between electron pairs into account while maintaining single-particle descriptions

$$\left[\sum_i \hat{H}_0(\mathbf{r}_i) + \frac{e^2}{2} \sum_{i \neq j} \frac{1}{|\mathbf{r}_i - \mathbf{r}_j|} \right] \Psi = E\Psi, \quad (2.26)$$

where $\hat{H}_0(\mathbf{r})$ is given by Eq. (2.21). Assuming that the many-electron wavefunction, Ψ , takes the form of Slater determinant as the same as Eq. (2.25), this leads to the question that how to determine the best single-particle wavefunctions ψ_i used in the matrix. To seek an answer, we can apply the variational method which is based on the idea that the wavefunction with the minimum energy is the lowest energy state. Suppose Ψ is the ground state wavefunction of the system having lowest energy E_{\min} , we must have

$$E_{\min} = \langle \Psi | \hat{H} | \Psi \rangle. \quad (2.27)$$

Since the wavefunction Ψ formed with elements $\psi_i(\mathbf{r})$ through Slater determinant of Eq. (2.25), the total energy E would be a functional of $\psi_i(\mathbf{r})$. The variational method,

then, involves choosing these orbitals $\psi_i(\mathbf{r})$ so as to minimize the total energy E

$$\frac{\delta E}{\delta \psi_i} = 0. \quad (2.28)$$

Also, the single-particle wavefunctions are required to be orthonormal

$$\langle \psi_i | \psi_j \rangle = \delta_{ij}. \quad (2.29)$$

The further procedure of the minimization along with the constraints in Eq. (2.29) can be proceeded by using the method of Lagrange multipliers,⁶⁴ that is, replacing E with a new functional L

$$L[\{\psi_i(\mathbf{r})\}; \lambda_{ij}] = E[\{\psi_i(\mathbf{r})\}] - \sum_{ij} \lambda_{ij} [\langle \psi_i | \psi_j \rangle - \delta_{ij}], \quad (2.30)$$

where the unknown constants λ_{ij} are called Lagrange multipliers. By construction, the orthogonality constraints can be automatically incorporated in functional L . As a consequence, the constrained minimization problem is transferred into searching for the independent Lagrange multipliers which produce the equivalent functional derivative

$$\frac{\delta E}{\delta \psi_i} = 0 \quad \rightarrow \quad \frac{\delta L}{\delta \psi_i} = 0 \quad (2.31)$$

as well as maintain the precise orthonormality constraints

$$\langle \psi_i | \psi_j \rangle = \delta_{ij} \quad \rightarrow \quad \frac{\delta L}{\delta \lambda_{ij}} = 0. \quad (2.32)$$

In the end, we can arrive at N simultaneous integro-differential equations, the so-called Hartree-Fock equations⁶⁵

$$\left[-\frac{\hbar^2}{2m} \nabla^2 + V_{\text{ext}}(\mathbf{r}) + V_{\text{H}}(\mathbf{r}) \right] \psi_i(\mathbf{r}) + \int V_{\text{X}}(\mathbf{r}, \mathbf{r}') \psi_i(\mathbf{r}') d\mathbf{r}' = \sum_j \lambda_{ij} \psi_j(\mathbf{r}) \quad (2.33)$$

with

$$V_{\text{H}}(\mathbf{r}) = e^2 \int \frac{\rho(\mathbf{r}')}{|\mathbf{r} - \mathbf{r}'|} d\mathbf{r}', \quad V_{\text{X}}(\mathbf{r}, \mathbf{r}') = -e^2 \sum_j \frac{\psi_j^*(\mathbf{r}')\psi_j(\mathbf{r})}{|\mathbf{r} - \mathbf{r}'|} \quad (2.34)$$

denoting the Hartree potential and the Fock exchange potential, respectively. It is intuitive to see that V_{H} is an average repulsive interaction between a certain electron with all other electrons. Alternatively, this term can be thought of as resulting from the distribution of electronic charge $\rho(\mathbf{r})$ through Poisson's equation in electrostatics⁶⁶

$$\nabla^2 V_{\text{H}}(\mathbf{r}) = -4\pi e^2 \rho(\mathbf{r}), \quad (2.35)$$

where the charge density is given by

$$\rho(\mathbf{r}) = \sum_i |\psi_i(\mathbf{r})|^2. \quad (2.36)$$

This idea was originally proposed by Hartree⁶⁷ in 1928, and thus the letter H is used as an label. Another term V_{X} enters because of the exchange interaction accompanying with the switch of variables \mathbf{r} and \mathbf{r}' , which is essentially arising from the antisymmetry requirement for the many-electron wavefunction. The potential terms V_{H} and V_{X} for calculating orbital ψ_i depend on the orbitals of all other Hartree-Fock equations, which means that we must solve the Hartree-Fock equations iteratively; namely, we guess some reasonable orbitals to start the calculation and then construct the subsequent guesses based on the previous guesses until the energies converge. For this reason, the approach developed to solve such coupled equations is called the self-consistent field (SCF) method, which is widely used to describe many-body problems. The merit of the Hartree-Fock approximation is that it converts the many-electron interaction problem into a single-particle problem with electrons immersed in an effective potential. However, this method carries a drawback: it does not include the correlation effects between electrons and thus lacks quantitative accuracy.

2.4 Density functional theory

Through discussion in Section 2.3, we can develop a sense that the key idea of solving the electronic Schrödinger equation is to translate the many-electron problem into a set of single-particle equations with approximating effective potentials. The density functional theory (DFT) developed by Kohn, Hohenberg, and Sham^{68,69} provides a further approximation for the Born-Oppenheimer electronic Schrödinger equation, which, on the one hand, maintains a single-particle description for a system of non-interacting electrons, and on the other hand, reduces the computational complexity by representing some correlation effects in a particular way with no compromised accuracy as far as possible.

2.4.1 Hohenberg-Kohn theorem

The density functional theory can be traced back to the Thomas-Fermi model developed by Thomas and Fermi^{70,71} in the 1920s. They represented the kinetic energy of an atom as a functional of electron density, plus the classical expression of the nucleus-electron and electron-electron interactions (both of which can be expressed by electron density) to calculate the energy of an atom. The Thomas-Fermi model took an important first step towards the density functional approach, but the accuracy of the Thomas-Fermi equation is limited because the atomic exchange energy pointed out by Hohenberg-Kohn theorem that will be discussed in this section is not considered.

Before we move on, let us go back to the expression of the total energy of the many-electron system described by the full many-body wavefunction Ψ and write it down again for convenience

$$E = \langle \Psi | \hat{H} | \Psi \rangle = \int \Psi^*(\mathbf{r}_1, \dots, \mathbf{r}_N) \hat{H} \Psi(\mathbf{r}_1, \dots, \mathbf{r}_N) d\mathbf{r}_1 \cdots d\mathbf{r}_N, \quad (2.37)$$

where the electronic Hamiltonian is given by

$$\hat{H} = \sum_i V_{\text{ext}}(\mathbf{r}_i) + \hat{T}_e + \hat{V}_{\text{ee}}, \quad (2.38)$$

here \hat{T}_e and \hat{V}_{ee} represent the kinetic energy operator and the Coulomb repulsion operator between electrons, respectively

$$\hat{T}_e = -\frac{\hbar^2}{2m} \sum_i \nabla_i^2; \quad \hat{V}_{\text{ee}} = \frac{e^2}{2} \sum_{i \neq j} \frac{1}{|\mathbf{r}_i - \mathbf{r}_j|}. \quad (2.39)$$

The above two operators are the same for any state of the system, and therefore \hat{H} is practically determined by the number of electrons N , and the external potential $V_{\text{ext}}(\mathbf{r})$. With the help of Eq. (2.4), the external potential energy can be written in terms of electron density $\rho(\mathbf{r})$

$$\langle \Psi | \sum_i V_{\text{ext}}(\mathbf{r}_i) | \Psi \rangle = \int \rho(\mathbf{r}) V_{\text{ext}}(\mathbf{r}) d\mathbf{r}. \quad (2.40)$$

Then Eq. (2.37) becomes

$$E = \int \rho(\mathbf{r}) V_{\text{ext}}(\mathbf{r}) d\mathbf{r} + \langle \Psi | \hat{T}_e + \hat{V}_{\text{ee}} | \Psi \rangle. \quad (2.41)$$

Back in 1964, Hohenberg and Kohn⁶⁸ proposed two ingeniously simple theorems which lay the theoretical foundation for DFT:

Theorem I: The external potential $V_{\text{ext}}(\mathbf{r})$ of any interacting particle system is a unique functional of the electron density $\rho(\mathbf{r})$ in the ground state.

Theorem II: The ground state energy of the system can be obtained using the variational principle; the trial density that minimizes the total energy is the ground state electron density.

Theorem I illustrates that the ground state density $\rho(\mathbf{r})$ uniquely determines the

external potential $V_{\text{ext}}(\mathbf{r})$. This theorem can be easily proved by reductio ad absurdum. Assume that for the same electron density $\rho(\mathbf{r})$, there exists two different sets of Hamiltonians, external potentials, non-degenerate ground state wavefunctions, and the associated energies $(\hat{H}_1, V_{\text{ext},1}, \Psi_1, E_1)$ and $(\hat{H}_2, V_{\text{ext},2}, \Psi_2, E_2)$. According to variation principle, we must have

$$E_1 < \langle \Psi_2 | \hat{H}_1 | \Psi_2 \rangle = \langle \Psi_2 | \hat{H}_2 + (\hat{H}_1 - \hat{H}_2) | \Psi_2 \rangle = E_2 + \int \rho(\mathbf{r}) [V_{\text{ext},1}(\mathbf{r}) - V_{\text{ext},2}(\mathbf{r})] d\mathbf{r}. \quad (2.42)$$

Switching the labels 1 and 2 still stands

$$E_2 < \langle \Psi_1 | \hat{H}_2 | \Psi_1 \rangle = \langle \Psi_1 | \hat{H}_1 + (\hat{H}_2 - \hat{H}_1) | \Psi_1 \rangle = E_1 + \int \rho(\mathbf{r}) [V_{\text{ext},2}(\mathbf{r}) - V_{\text{ext},1}(\mathbf{r})] d\mathbf{r}. \quad (2.43)$$

Adding up Eqs. (2.42) and (2.43) we find

$$E_1 + E_2 < E_1 + E_2, \quad (2.44)$$

which is clearly a contradiction, and thus the first theorem demonstrates one-to-one mapping between the external potentials and the charge densities of the ground states in many-electron systems.

It is also straightforward to verify the second Hohenberg-Kohn theorem. We have seen that the external potential $V_{\text{ext}}(\mathbf{r})$ is uniquely determined by the electron density $\rho(\mathbf{r})$, the change in the external potential $V_{\text{ext}}(\mathbf{r})$ in turn leads to the change in the ground state wavefunction Ψ . Since the ground state energy E is already a functional of Ψ , one may infer from the chain, $\rho(\mathbf{r}) \rightarrow V_{\text{ext}}(\mathbf{r}) \rightarrow \Psi \rightarrow E$, that the total energy can be represented as a functional of the density $\rho(\mathbf{r})$: $E = F[\rho(\mathbf{r})]$. The next step is to show that the ground state energy, *i.e.* the minimum value of this functional, is obtained when $\rho(\mathbf{r}) = \rho_0(\mathbf{r})$ where $\rho_0(\mathbf{r})$ is the ground state density. When the

system is in the ground state, the lowest possible energy will be

$$E = F[\rho_0(\mathbf{r})]. \quad (2.45)$$

Applying the variational principle, we can come across a comparison for a higher energy associated with a different density

$$E_1 = F[\rho_1(\mathbf{r})] > E = F[\rho_0(\mathbf{r})]. \quad (2.46)$$

So far, the second theorem becomes transparent as it simply states that the minimum of functional $F[\rho(\mathbf{r})]$ with respect to the density $\rho(\mathbf{r})$ gives rise to the energy of the ground state, and naturally the density at which the functional derivative vanishes is then the ground state density. Compared to evaluating the entire many-electron wavefunction $\Psi(\mathbf{r}_1, \mathbf{r}_2, \dots, \mathbf{r}_N)$ which involves $3N$ variables in the Hartree-Fock approximation, all observables of the system now solely depend on the ground state electron density $\rho(\mathbf{r})$ having three coordinates only, making it possible to greatly simplify the calculations and analyze larger-scale systems.

2.4.2 Kohn-Sham equations

The powerful Hohenberg-Kohn theorem tells us the many-electron wavefunction and the total energy in the ground state are uniquely determined by electron density through a functional representation. As a consequence we can rewrite Eq. (2.41) as

$$F[\rho] = \int \rho(\mathbf{r})V_{\text{ext}}(\mathbf{r})d\mathbf{r} + \langle \Psi[\rho(\mathbf{r})] | \hat{T}_e + \hat{V}_{\text{ee}} | \Psi[\rho(\mathbf{r})] \rangle. \quad (2.47)$$

Then the question is, what is the form of such functional in practice? Thanks to Kohn and Sham⁶⁹ as they formulated a simple method with retained nature of Hohenberg-Kohn theorem for performing DFT calculations. The idea, as indicated by the fol-

lowing equation, was to separate the unknown energy functional Eq. (2.47) of the full interacting system into known contributions evaluating from independent electron approximations and an unknown contribution, the exchange and correlation energy, to count the difference

$$F[\rho] = \int \rho(\mathbf{r})V_{\text{ext}}(\mathbf{r})d\mathbf{r} + T_e[\rho(\mathbf{r})] + E_H[\rho(\mathbf{r})] + E_{\text{xc}}[\rho(\mathbf{r})]. \quad (2.48)$$

The kinetic energy functional is approximated using the kinetic energy of the non-interacting system of electrons having density $\rho(\mathbf{r})$

$$\rho(\mathbf{r}) = 2 \sum_n^{N/2} |\psi_n(\mathbf{r})|^2 \quad (2.49)$$

and

$$T[\rho] = -2 \frac{\hbar^2}{2m} \sum_n^{N/2} \int \psi_n^*(\mathbf{r}) \nabla^2 \psi_n(\mathbf{r}) d\mathbf{r}, \quad (2.50)$$

where $\psi_n(\mathbf{r})$ represent the so-called Kohn-Sham orbitals with index n , which represents the spatial part of the single particle states, running from 1 to the highest occupied state. The factor of 2 in Eqs. (2.49) and (2.50) is to take into account the fact that when the system is nonmagnetic each orbital state accommodates two electrons of opposite spin. For simplicity, we assume N is even. In the case that N is odd, the spin multiplicity needs to be modified. The term $E_{\mathbf{H}}[\rho(\mathbf{r})]$ is the Hartree energy of the electrons, as demonstrated in Section 2.3, stemming from the concept of classical electrostatics

$$E_{\mathbf{H}}[\rho] = \frac{e^2}{2} \int \int \frac{\rho(\mathbf{r})\rho(\mathbf{r}')}{|\mathbf{r} - \mathbf{r}'|} d\mathbf{r}d\mathbf{r}'. \quad (2.51)$$

While the tricky term $E_{\text{xc}}[\rho(\mathbf{r})]$ is the exchange-correlation energy, which contains everything that is unaccounted for. By assembling together the explicit expression

we have so far for each piece, Eq. (2.48) will look like

$$\begin{aligned}
E = F[\rho] &= \int \rho(\mathbf{r})V_{\text{ext}}(\mathbf{r})d\mathbf{r} - 2\frac{\hbar^2}{2m} \sum_n^{N/2} \int \psi_n^*(\mathbf{r})\nabla^2\psi_n(\mathbf{r})d\mathbf{r} \\
&+ \frac{e^2}{2} \iint \frac{\rho(\mathbf{r})\rho(\mathbf{r}')}{|\mathbf{r} - \mathbf{r}'|}d\mathbf{r}d\mathbf{r}' + E_{\text{xc}}[\rho(\mathbf{r})].
\end{aligned}
\tag{2.52}$$

Here $\{\psi_i\}$ form an orthonormal bases which satisfy

$$\int \psi_n^*(\mathbf{r})\psi_m(\mathbf{r})d\mathbf{r} = \delta_{nm}.
\tag{2.53}$$

Applying the Hoenberg-Kohn variational principle to determine the electron density

$$\left. \frac{\delta F[\rho]}{\delta \rho} \right|_{\rho_0} = 0.
\tag{2.54}$$

We now arrive at the following so called Kohn-Sham equations

$$\left[-\frac{\hbar^2}{2m}\nabla^2 + V_{\text{ext}}(\mathbf{r}) + V_{\text{H}}(\mathbf{r}) + V_{\text{xc}}(\mathbf{r}) \right] \psi_n(\mathbf{r}) = \varepsilon_n\psi_n(\mathbf{r}),
\tag{2.55}$$

where the exchange and correlation potential, $V_{\text{xc}}(\mathbf{r})$, is given by

$$V_{\text{xc}}(\mathbf{r}) = \left. \frac{\delta E_{\text{xc}}[\rho]}{\delta \rho} \right|_{\rho(\mathbf{r})}.
\tag{2.56}$$

Equations (2.55) and (2.56), together with the external potential

$$V_{\text{ext}}(\mathbf{r}) = -\sum_I \frac{Z_I e^2}{|\mathbf{r} - \mathbf{R}_I|},
\tag{2.57}$$

the Hartree potential

$$\nabla^2 V_{\text{H}}(\mathbf{r}) = -4\pi e^2 \rho(\mathbf{r})
\tag{2.58}$$

and the expression for the electron density Eq. (2.49) form the backbone of self-consistent calculations for Kohn-Sham equations. For a particular system, the external potential, Eq. (2.57), can be determined from the given nuclear coordinates. The SCF loop then proceeds by initializing a charge density $\rho(\mathbf{r})$ which can be evaluated from the sum of the densities of isolated atoms arranged within the simulation cell. Thereupon the Hartree potential Eq. (2.58), the exchange-correlation potential Eq. (2.56), and thus the total effective potential $V_{\text{eff}} = V_{\text{ext}} + V_{\text{H}} + V_{\text{xc}}$ are sought in turn. By solving the Kohn-Sham equation given by Eq. (2.55), a better estimate of the electron density $\rho(\mathbf{r})$ is constructed from the complete Kohn-Sham orbitals ψ_n through Eq. (2.49). By repeating this step to approach the desired accuracy, the total ground state energy of the system is determined at the point when achieving self-consistency. That is, the input density matches the output density within a preset tolerance.

The Hohenberg-Kohn theorem and the Kohn-Sham equation have been hailed as the two cornerstones of DFT. The Kohn-Sham equation clarifies everything other than the exchange-correlation functional, which is the central quantity categorizing the complex interaction items. From then on, plenty of work begins around the crucial task of constructing the approximate form of exchange-correlation functionals which directly determines the calculation accuracy of DFT. Presently, the local density approximation (LDA)^{72,73} and the generalized gradient approximation (GGA)⁷⁴⁻⁷⁷ are the most common approximation methods to describe the exchange-correlation effects. LDA approximation takes the homogeneous electron gas as a local approximation to a real material, that is, the exchange-correlation energy E_{xc} is a localized functional of electron density $\rho(\mathbf{r})$ of the homogeneous electron gas. Assuming that the electron density in the system is approximately spatially uniform, then E_{xc} can be expressed as

$$E_{\text{xc}}^{\text{LDA}}[\rho] = \int \varepsilon_{\text{xc}}^{\text{LDA}}[\rho(\mathbf{r})]\rho(\mathbf{r})\text{d}\mathbf{r}, \quad (2.59)$$

here ε_{xc} represents the exchange-correlation energy density and can be approximated

to $\varepsilon_{xc}^{\text{LDA}}(\mathbf{r}_0, \rho(\mathbf{r})) = \varepsilon_{xc}^{\text{hom}}(\rho(\mathbf{r}_0))$, where “hom” stands for “homogeneous”. According to Eq. (2.56), we have

$$V_{xc}^{\text{LDA}} = \varepsilon_{xc}^{\text{LDA}}(\rho) + \rho(\mathbf{r}) \frac{\delta \varepsilon_{xc}(\rho(\mathbf{r}))}{\delta \rho(\mathbf{r})}. \quad (2.60)$$

The GGA approximations also take into account the gradient of the electron density, $\nabla \rho(\mathbf{r})$

$$E_{xc}^{\text{GGA}}[\rho] = \int \varepsilon_{xc}^{\text{GGA}}[\rho(\mathbf{r}), \nabla \rho(\mathbf{r})] \rho(\mathbf{r}) d\mathbf{r}. \quad (2.61)$$

The commonly used GGA functionals include PBE,⁷⁷ PW91,⁷⁶ Becke88,⁷⁵ PBEsol⁷⁸ *etc.* For analyzing a system in which the changing density is sharply varying across the region, the GGA might be more applicable than LDA. Among them, the PBEsol form is being the preference for our materials because of good agreement between simulations and experiments for phonon analysis.⁷⁹ All these mentioned exchange-correlation functionals and other various types are available in Libxc library⁸⁰ and can be implemented in density functional theory programs.

2.5 Pseudopotentials basics

In previous sections, we have seen that the complicated many-body problem of interacting electrons and nuclei has been mapped within the framework of the Born-Oppenheimer approximation and DFT onto a problem of single-particles moving in a set of fixed nuclei with an effective potential. In order to solve the resulting single-particle Kohn-Sham equations for systems such as crystalline solids, numerically it is common to expand the orbitals of the Kohn-Sham equations into a set of basis functions. For periodic materials, the wavefunction $\psi(\mathbf{r})$ can be indexed by two quantum numbers: the band index n and the wave vector \mathbf{k} in the Brillouin zone, and thus the single particle state $\psi(\mathbf{r})$ is generally being denoted as $\psi_{n\mathbf{k}}(\mathbf{r})$ in practical

calculations. According to the Bloch theorem, we have

$$\psi_{n\mathbf{k}}(\mathbf{r} + \mathbf{T}) = e^{i\mathbf{k}\cdot\mathbf{T}}\psi_{n,\mathbf{k}}(\mathbf{r}), \quad (2.62)$$

where \mathbf{T} is any translational vector leaving the Hamiltonian invariant. The wavefunction can be further described in terms of a periodic function $u_{n,\mathbf{k}}(\mathbf{r})$

$$\psi_{n\mathbf{k}}(\mathbf{r}) = u_{n,\mathbf{k}}(\mathbf{r})e^{i\mathbf{k}\cdot\mathbf{r}}. \quad (2.63)$$

It is now convenient to express all the measurable periodic properties of the system in terms of a discrete summation of plane waves

$$u_{n\mathbf{k}}(\mathbf{r}) = \frac{1}{\sqrt{\Omega}} \sum_{\mathbf{G}} \tilde{u}_{n\mathbf{k}}(\mathbf{G})e^{i\mathbf{G}\cdot\mathbf{r}} \quad (2.64)$$

$$\psi_{n\mathbf{k}}(\mathbf{r}) = \frac{1}{\sqrt{\Omega}} \sum_{\mathbf{G}} \tilde{u}_{n\mathbf{k}}(\mathbf{G})e^{i(\mathbf{G}+\mathbf{k})\cdot\mathbf{r}} \quad (2.65)$$

$$\rho(\mathbf{r}) = \sum_{\mathbf{G}} \tilde{\rho}(\mathbf{G})e^{i\mathbf{G}\cdot\mathbf{r}} \quad (2.66)$$

$$V_{\text{eff}}(\mathbf{r}) = \sum_{\mathbf{G}} \tilde{V}(\mathbf{G})e^{i\mathbf{G}\cdot\mathbf{r}}, \quad (2.67)$$

here Ω is usually the volume of the unit cell. The reciprocal lattice vectors \mathbf{G} are defined as

$$\mathbf{G} = m_1\mathbf{b}_1 + m_2\mathbf{b}_2 + m_3\mathbf{b}_3 \quad (2.68)$$

with \mathbf{b}_1 , \mathbf{b}_2 , and \mathbf{b}_3 the reciprocal primitive vectors, and m_1 , m_2 , and m_3 the integers. In practice, by using the natural basis in the form of Fourier transform implied by Eqs. (2.64-2.67) with sufficiently small $\tilde{V}(\mathbf{G})$ for large \mathbf{G} , only those plane waves which satisfy

$$\frac{\hbar^2}{2m}|\mathbf{G} + \mathbf{k}|^2 \leq E_{\text{cutoff}} \quad (2.69)$$

provide accurate descriptions for the periodic functions. At this point, the intractable task of solving Kohn-Sham equations is greatly simplified since the calculation has been transferred to be carried out at a set of discrete \mathbf{k} -points in the first Brillouin zone for n bands which is of the order of the number of electrons in the simulation cell.

However, the size of the planewave basis set required for a given system is actually different throughout the calculation space. This is because, in condensed matter systems, the orbitals tend to oscillate strongly near nucleus and thus demand more Fourier components presented to achieve convergence, while the orbitals in most of the space beyond those regions are much more smoothly varying, and therefore fewer basis sets are needed. For the purpose of computational efficiency, it is reasonable to divide electrons into core and valence contributions, $\rho(\mathbf{r}) = \rho_c(\mathbf{r}) + \rho_v(\mathbf{r})$, and use the pseudopotentials instead of exact potentials in the plane wave representation. Specifically, the so-called pseudopotential is an effective potential that is constructed to account for the effect of the core electrons inside a sphere defined by a cut-off radius r_c . Typically, the pseudopotential generation procedure starts with the solutions for isolated atoms using the Kohn-Sham approach

$$H(\mathbf{r})|\phi_i(\mathbf{r})\rangle = \left[-\frac{\hbar}{2m}\nabla^2 + V_{\text{eff}}(r) \right] |\phi_i(\mathbf{r})\rangle = \varepsilon_i |\phi_i(\mathbf{r})\rangle, \quad (2.70)$$

where the effective potential takes the form

$$V_{\text{eff}}(r) \equiv -\frac{Ze^2}{r} + e^2 \int \frac{\rho_c(r') + \rho_v(r')}{|\mathbf{r} - \mathbf{r}'|} d\mathbf{r}' + V_{\text{xc}}[\rho_c(r) + \rho_v(r)]. \quad (2.71)$$

Notice that for a single atom, the wavefunctions can be written as a product of a radial function and a spherical harmonic due to the spherical symmetry

$$|\phi_i(\mathbf{r})\rangle = |\phi_{nlm}(\mathbf{r})\rangle = r^{-1}\varphi_{nl}(r)Y_{lm}. \quad (2.72)$$

The pseudopotential is designed in the way that the pseudo (PS) wavefunction, $|\tilde{\psi}\rangle$, and the all-electron (AE) wavefunction, $|\psi\rangle$, are identical outside the augmentation region $r \geq r_c$ so that all correct behaviors of electrons are restored. Strategically the pseudopotentials can be generated in atomic calculations and then used to compute properties of solids or molecules, taking into account the expansion for valence electrons only. The total energy of the system is then obtained by adding up the contributions from the core states of each atomic species and the pseudo-part energy evaluated outside the augmentation spheres.

As a brief introduction to pseudopotentials, it is a preference for us to discuss the basic idea of Projector Augmented Waves (PAW), the method that has been using in our research work. Most of the notations follow closely the work of Bloechl.⁸¹ For the valence electrons, a transformation from pseudo wavefunction $|\tilde{\psi}\rangle$ to all-electron wavefunction $|\psi\rangle$ is defined as

$$|\psi\rangle = |\tilde{\psi}\rangle + \sum_i \left(|\phi_i\rangle - |\tilde{\phi}_i\rangle \right) \langle \tilde{p}_i | \tilde{\psi} \rangle, \quad (2.73)$$

where ϕ_i , $\tilde{\phi}_i$, and \tilde{p}_i represent the all-electron basis functions, pseudopotential basis functions, and projector functions, respectively. The summation over i refers to the summation over all angular momentum quantum numbers (l, m) and the atomic type indexed by a . The character of an arbitrary pseudo-wavefunction $|\tilde{\psi}\rangle$ at one site can be calculated by multiplication with the projector function at that site

$$c_i = \langle \tilde{p}_i | \tilde{\psi} \rangle. \quad (2.74)$$

Inside each sphere the wavefunctions can be determined as

$$|\tilde{\psi}\rangle^{\text{sphere}} \approx \sum_i |\tilde{\phi}_i\rangle c_i \quad (2.75)$$

and

$$|\psi\rangle^{\text{sphere}} \approx \sum_i |\phi_i\rangle c_i. \quad (2.76)$$

The projector functions and the PS wavefunction must obey

$$\sum_i |\tilde{\phi}_i\rangle \langle \tilde{p}_i| \approx 1 \quad \text{with} \quad r \leq r_c \quad (2.77)$$

to satisfy

$$\sum_i \tilde{\phi}_i \langle \tilde{p} | \tilde{\psi} \rangle = |\tilde{\psi}\rangle \quad (2.78)$$

or equivalently we must have

$$\langle \tilde{p}_i | \tilde{\phi}_j \rangle = \delta_{ij}. \quad (2.79)$$

PAW wavefunctions are designed to maintain the orthogonality of the plane waves to the core states in a pseudized atomic environment. This approach is typically implemented in the frozen core approximation⁸² in which the core electrons of a system are assumed to be frozen at their ground state atomic values and the valence electrons are evaluated variationally. It also requires the precalculated dataset storing $\{\varphi_i(\mathbf{r}), \tilde{\varphi}_i(\mathbf{r}), \tilde{p}_i(\mathbf{r})\}$ for a specified atomic species.

Chapter 3

Phonons in crystals

The Born-Oppenheimer adiabatic approximation discussed in Section 2.2 also provides a conceptual framework to describe the lattice vibration. In the study of nuclear motion with small displacements from the equilibrium positions, the total ground-state energy of the electronic-nuclear system as a function of a set of nuclear positions forms what is so called the potential energy surface or Born-Oppenheimer surface, which can be expanded in a Taylor series around the equilibrium configuration. Generally, the vibrational modes and frequencies are calculated by diagonalization of the matrix composed by the coefficients, *i.e.* the interatomic force constants, associated with each term of the expansion.

3.1 Dynamics of three-dimensional crystals

Before attempting to understand the lattice dynamics of three-dimensional crystals, it is convenient to do some housekeeping with the symbols and notations. Consider a perfect crystalline solid composed by N_c unit cells, the equilibrium position of the I th atom is given by

$$\mathbf{R}_I = \mathbf{R}_l + \tau_s, \quad (3.1)$$

where \mathbf{R}_l denotes the location of the l th unit cell, namely, the translation vectors in the Bravais lattice, which can be expressed as a sum of the three primitive translation vectors $\mathbf{a}_1, \mathbf{a}_2$, and \mathbf{a}_3 with integer coefficients l_1, l_2 , and l_3 , τ_s represents the position of atom s in the unit cell. Accordingly, each atom is labeled by two indices (l, s) .

In the case of introducing small deviation $\mathbf{u}_s(l)$ from the equilibrium position of atom s in the l th unit cell, the corresponding atomic position becomes

$$\mathbf{R}_I = \mathbf{R}_l + \tau_s + \mathbf{u}_s(l). \quad (3.2)$$

Within the harmonic approximation, the energy of the electronic-nuclear system in the ground Born-Oppenheimer potential surface $U(\{\mathbf{u}_s(l)\})$ can be expanded to the quadratic order in the displacements from the equilibrium positions

$$U(\{\mathbf{u}_s(l)\})_{\text{harm}} = U(\{\mathbf{u}_s(l)\} = 0) + \frac{1}{2} \sum_{ls\alpha} \sum_{mt\beta} C_{st}^{\alpha\beta}(l, m) u_{s\alpha}(l) u_{t\beta}(m), \quad (3.3)$$

here α, β run over the three Cartesian coordinates x, y, z . As in simple case of one-dimensional chain, the elements of the interatomic force constants matrix are defined as the second derivative of $U(\{\mathbf{u}_s(l)\})$ evaluated at the equilibrium geometry

$$C_{st}^{\alpha\beta}(l, m) = \left. \frac{\partial^2 U}{\partial u_s^\alpha(l) \partial u_t^\beta(m)} \right|_0 = C_{st}^{\alpha\beta}(\mathbf{R}_l - \mathbf{R}_m). \quad (3.4)$$

By this definition, it is easy to observe that the matrix C is symmetric so that

$$C_{st}^{\alpha\beta}(l, m) = C_{ts}^{\beta\alpha}(m, l). \quad (3.5)$$

Besides, due to the translational invariance of the Bravais lattice, the dependence of the force constant on any pair of atoms is through the difference between their

equilibrium positions. This symmetry property can be described mathematically

$$C_{st}^{\alpha\beta}(l, m) = C_{st}^{\alpha\beta}(l', m') \quad \text{if} \quad \mathbf{R}_l - \mathbf{R}_m = \mathbf{R}_{l'} - \mathbf{R}_{m'} = \mathbf{R}. \quad (3.6)$$

It is natural to think that when all nuclei stay at their equilibrium positions or move with the identical displacement, the interatomic forces vanish, leading to the following “sum rule” that typically governs the matrix of the interatomic force constants

$$\sum_{mt} C_{st}^{\alpha\beta}(l, m) = 0. \quad (3.7)$$

The classical equations of motion for the dynamics of the nuclei against time τ is given by

$$M_s \frac{\partial^2 u_{s\alpha}(l, t)}{\partial \tau^2} = F_s^\alpha(l) = - \sum_{mt\beta} C_{st}^{\alpha\beta}(l, m) u_{t\beta}(m). \quad (3.8)$$

Assume the solutions to Eq. (3.8) have the form of plane waves

$$u_{s\alpha}(l, t) = u_{s\alpha}^\nu(\mathbf{q}) e^{i\mathbf{q}\cdot\mathbf{R}_l} e^{-i\omega^\nu(\mathbf{q})\tau}, \quad (3.9)$$

where ν denotes the index of normal mode with vibrational frequency ω . Substituting Eq. (3.9) into Eq. (3.8) gives

$$-M_s (\omega^\nu)^2 u_{s\alpha}^\nu(\mathbf{q}) = - \sum_{t\beta} \left(\sum_m C_{st}^{\alpha\beta}(l, m) e^{-i\mathbf{q}\cdot(\mathbf{R}_l - \mathbf{R}_m)} \right) u_{t\beta}^\nu(\mathbf{q}). \quad (3.10)$$

Define $\tilde{C}_{st}^{\alpha\beta}(\mathbf{q})$ as the Fourier transform of real-space interatomic force constants

$$\tilde{C}_{st}^{\alpha\beta}(\mathbf{q}) = \sum_m C_{st}^{\alpha\beta}(l, m) e^{-i\mathbf{q}\cdot(\mathbf{R}_l - \mathbf{R}_m)} = \frac{1}{N_c} \frac{\partial^2 U}{\partial u_s^{*\alpha}(\mathbf{q}) \partial u_t^\beta(\mathbf{q})}. \quad (3.11)$$

Note that U as defined in Eq. (2.13) represents the total energy of the infinite crystal

while U/N_c represents the total energy per unit cell. Thus we have

$$M_s(\omega^\nu)^2 u_{s\alpha}^\nu(\mathbf{q}) = \sum_{t\beta} \tilde{C}_{st}^{\alpha\beta}(\mathbf{q}) u_{t\beta}^\nu(\mathbf{q}). \quad (3.12)$$

Then the phonon frequencies $\omega(\mathbf{q})$ and displacement amplitudes $u(\mathbf{q})$ are determined by the secular equation of Eq. (3.12). Furthermore, the eigendisplacements satisfy the orthogonality relations

$$\sum_{s\alpha} M_s u_{s\alpha}^{\nu*}(\mathbf{q}) u_{s\alpha}^{\nu'}(\mathbf{q}) = M^\nu \delta_{\nu,\nu'}, \quad (3.13)$$

here M^ν denotes a mode effective mass. Notice that we may see in the literature that $\tilde{C}(\mathbf{q})$ is scaled by the nuclear masses with introduced notation, $\tilde{D}(\mathbf{q})$, the dynamical matrix of the crystal in reciprocal space

$$\tilde{D}_{st}^{\alpha\beta}(\mathbf{q}) = \frac{\tilde{C}_{st}^{\alpha\beta}(\mathbf{q})}{\sqrt{M_s M_t}}. \quad (3.14)$$

In this case, Eq. (3.12) becomes

$$(\omega^\nu)^2(\mathbf{q}) e_{s\alpha}^\nu(\mathbf{q}) = \sum_{t\beta} \tilde{D}_{s\alpha,t\beta}(\mathbf{q}) e_{t\beta}^\nu(\mathbf{q}), \quad (3.15)$$

where the phonon eigenvector

$$e_{s\alpha}^\nu(\mathbf{q}) = \sqrt{M_s} u_{s\alpha}^\nu(\mathbf{q}) \quad (3.16)$$

is normalized so that

$$\sum_{s\alpha} |e_\nu(\mathbf{q})|^2 = 1. \quad (3.17)$$

Since $\tilde{C}(\mathbf{q})$ and $\tilde{D}(\mathbf{q})$ are both $3N \times 3N$ matrices, and hence for each wavevector \mathbf{q} , Eq. (3.12) or the essentially equivalent Eq. (3.15) will produce $3N$ eigenmodes,

i.e. $3N$ dispersion curves. The so called longitudinal or transverse modes depend on how the displacement of atoms from their equilibrium position, represented by vector \mathbf{u} , relates to the propagation direction of the wave, represented by \mathbf{q} . In case of longitudinal mode, \mathbf{u} coincides with \mathbf{q} , whereas for transverse mode, atoms move perpendicular to \mathbf{q} . According to the sum rule Eq. (3.7), it follows that

$$\sum_t \tilde{C}_{st}^{\alpha\beta}(\mathbf{q} = 0) \equiv 0. \quad (3.18)$$

Multiplying both sides by the same quantity leads to

$$\sum_{t\beta} \tilde{C}_{st}^{\alpha\beta}(\mathbf{q} = 0)u_\beta \equiv 0, \quad (3.19)$$

which means that when $\mathbf{q} \rightarrow 0$, the phonon frequencies $\omega(\mathbf{q}) = 0$ with all the displacement basis $u_{t\beta} \equiv u_\beta$ in the Eq. (3.12), that is to say, the whole cell moves together with the same amplitude along any of the three directions under the long-wavelength limit $\mathbf{q} \rightarrow 0$. As a consequence, there are three normal modes that present the behavior of elastic waves, called acoustic branches, the solutions of the remaining $(3N - 3)$ optical branches describe the relative vibration of atoms in the unit cell. It is worth mentioning that the matrix of interatomic force constants Eq. (3.11) is known as the analytic contribution, calculated by ignoring the macroscopic electric field associated with the motion of charged atoms. More analysis for phonon modes in polar crystals is discussed in Section 3.3 and in Appendix B.

3.2 Density functional perturbation theory

There are two main first principles phonon calculations methods: the finite displacement method^{83,84} and the approach within the framework of density functional perturbation theory (DFPT).^{85–88} The first method, as used to evaluate those results

of Eq. (3.4), is also referred to be the frozen-phonon method. It starts with the equilibrium positions of the atoms in a supercell. For each atom, the self-consistent total electronic energy is calculated for small displacements in each direction.

This method is straightforward to implement, but the drawback is that it requires the simulation cell to be large enough to converge Eq. (3.4) for $\mathbf{R}_l - \mathbf{R}_m$, which makes the use of supercells dramatically increase the workload of computation, thereby greatly limiting the practicality of the method. In 1987, Baroni, Giannozzi, and Testa⁸⁵ proposed the method of DFPT for calculating dynamic lattice properties. Using the total ground-state energy estimated from DFT, the DFPT proceeds with the calculation of the linear response of the energy with respect to the nuclear displacements perturbation. Due to its powerful and flexible theoretical techniques, the DFPT method has been applied to a variety of complex systems to analyze materials properties.

In the section we discuss the approach of calculating the second derivative of the total energy with respect to an atomic displacement through the DFPT. Before we proceed further, it is convenient to rewrite here the Hellmann-Feynman force derived in Section 2.2

$$\mathbf{F}_I = -\frac{\partial U(\{\mathbf{R}\})}{\partial \mathbf{R}_I} = -\frac{\partial E(\{\mathbf{R}\})}{\partial \mathbf{R}_I} - \frac{\partial V_{\text{NN}}(\{\mathbf{R}\})}{\partial \mathbf{R}_I}, \quad (3.20)$$

where $E(\{\mathbf{R}\})$ is the ground-state energy of the electrons calculated from DFT

$$\begin{aligned} E(\{\mathbf{R}\}) = & \int \rho(\mathbf{r})V_{\text{ext}}(\mathbf{r})d\mathbf{r} - 2\frac{\hbar^2}{2m} \sum_n^{N/2} \int \psi_n^*(\mathbf{r})\nabla^2\psi_n(\mathbf{r})d\mathbf{r} \\ & + \frac{e^2}{2} \iint \frac{\rho(\mathbf{r})\rho(\mathbf{r}')}{|\mathbf{r} - \mathbf{r}'|}d\mathbf{r}d\mathbf{r}' + E_{\text{xc}}[\rho(\mathbf{r})]. \end{aligned} \quad (3.21)$$

Substituting Eq. (3.21) into Eq. (3.20), we see that the force acting on the I th

nucleus takes the form

$$\mathbf{F}_I = - \int \rho(\mathbf{r}) \frac{\partial V_{\text{ext}}(\mathbf{r})}{\partial \mathbf{R}_I} d\mathbf{r} - \frac{\partial V_{\text{NN}}(\{\mathbf{R}\})}{\partial \mathbf{R}_I}. \quad (3.22)$$

As defined in Eq. (3.4), the interatomic force constants can be accessed by differentiating the forces with respect to nuclear coordinates

$$\frac{\partial^2 U(\{\mathbf{R}\})}{\partial \mathbf{R}_I \partial \mathbf{R}_J} = - \frac{\partial F_I}{\partial \mathbf{R}_J} = \int \frac{\partial \rho(\mathbf{r})}{\partial \mathbf{R}_J} \frac{\partial V_{\text{ext}}(\mathbf{r})}{\partial \mathbf{R}_I} d\mathbf{r} + \delta_{IJ} \int \rho(\mathbf{r}) \frac{\partial^2 V_{\text{ext}}(\mathbf{r})}{\partial \mathbf{R}_I \partial \mathbf{R}_J} d\mathbf{r} + \frac{\partial^2 V_{\text{NN}}(\{\mathbf{R}\})}{\partial \mathbf{R}_I \partial \mathbf{R}_J}. \quad (3.23)$$

In the case of small atomic displacements, the change in the ground state electron density will have the form

$$\Delta \rho(\mathbf{r}) = 4 \text{Re} \sum_n \psi_n^*(\mathbf{r}) \Delta \psi_n(\mathbf{r}). \quad (3.24)$$

The variation in the Kohn-Sham wave function denoted by $\Delta \psi_n(\mathbf{r})$ is obtained by the first order perturbation theory⁸⁹ as follows

$$(H_{\text{eff}} - \epsilon_n) |\Delta \psi_n\rangle = - (\Delta V_{\text{eff}} - \Delta \epsilon_n) |\psi_n\rangle, \quad (3.25)$$

where H_{eff} is the unperturbed Kohn-Sham Hamiltonian for an electron

$$H_{\text{eff}} = - \frac{\hbar^2}{2m} \nabla^2 + V_{\text{eff}}(\mathbf{r}). \quad (3.26)$$

The corresponding effective potential V_{eff} is given by

$$V_{\text{eff}} = V_{\text{ext}}(\mathbf{r}) + e^2 \int \frac{\rho(\mathbf{r}')}{|\mathbf{r} - \mathbf{r}'|} d\mathbf{r}' + V_{\text{xc}}(\mathbf{r}). \quad (3.27)$$

The correction to the effective potential potential to the first order is

$$\Delta V_{\text{eff}}(\mathbf{r}) = \Delta V_{\text{ext}}(\mathbf{r}) + e^2 \int \frac{\Delta \rho(\mathbf{r}')}{|\mathbf{r} - \mathbf{r}'|} d\mathbf{r}' + \left. \frac{dV_{\text{xc}}(\rho)}{d\rho} \right|_{\rho=\rho(\mathbf{r})} \Delta \rho(\mathbf{r}). \quad (3.28)$$

The notation $\Delta \varepsilon_n$ represents the first order correction to the Kohn-Sham eigenvalue

$$\Delta \varepsilon_n = \langle \psi_n | \Delta V_{\text{eff}} | \psi_n \rangle. \quad (3.29)$$

The explicit expression for the change in the Kohn-Sham orbital will be

$$\Delta \psi_n(\mathbf{r}) = \sum_{m \neq n} \psi_m(\mathbf{r}) \frac{\langle \psi_m | \Delta V_{\text{eff}} | \psi_n \rangle}{\varepsilon_n - \varepsilon_m}, \quad (3.30)$$

where the sum runs over all the occupied and unoccupied states except the currently considered state. Then Eq. (3.24) becomes

$$\Delta \rho(\mathbf{r}) = 4 \sum_n \sum_{m \neq n} \psi_n^*(\mathbf{r}) \psi_m(\mathbf{r}) \frac{\langle \psi_m | \Delta V_{\text{eff}} | \psi_n \rangle}{\varepsilon_n - \varepsilon_m}. \quad (3.31)$$

Terms in the summation for m corresponding to an occupied state are canceled and hence make no net contribution, so that it needs only to include m corresponding to unoccupied states in the evaluation. Equations (3.28 - 3.31) constitute a complete loop for self-consistent calculations. Further details of calculation techniques are described in Baroni *et al.*⁸⁸

DFPT is especially suitable for calculating the force constant matrix in the reciprocal space through Eq. (3.11). The force constant matrix on a discrete grid of \mathbf{q} vectors, if known, can be used to interpolate the force constant matrix at any generic \mathbf{q} point by performing Fourier transforms and inverse Fourier transforms.

3.3 LO-TO splitting

Crystals containing more than two atoms in the unit cell generate branches of the optical wave, composed of one longitudinal optical (LO) phonon mode and two transverse optical (TO) phonon modes. Generally, these can be treated with the frozen phonon method or DFPT, excepting, however, the case where the $\mathbf{q} = 0$ in ionic crystals. In this section, we discuss the well-known effect of LO-TO splitting due to the interaction of the long-range Coulomb field with the LO vibrations. A detailed analysis of the coupling of phonon optical (both LO and TO) modes and photon in typical ionic crystals and the resulting phenomenon of discontinuous modes near the center of the Brillouin zone is discussed in Appendix B.

In the long wavelength limit $\mathbf{q} \rightarrow 0$, the dipoles created by the displacement of charges in the optical phonon modes induces an electric field with assumed form $\mathbf{E}(\mathbf{q}) = \mathbf{E}_0(\mathbf{q})e^{i\mathbf{q}\cdot\mathbf{r}-i\omega t}$ which results in an additional restoring force

$$\mathbf{F} = -M(\omega^\nu)^2\mathbf{u} + eZ^*\mathbf{E}, \quad (3.32)$$

where ω^ν denotes the frequency of pure phonon modes obtained by solving Eq. (3.12), and the site-dependent Z^* is Born effective charge caused by the force acting on ion arising from the macroscopic electric field. To be more specific, the Born effective tensor takes the following expression

$$eZ_{\alpha\beta}^{*s} = \left. \frac{\partial F_{s,\alpha}}{\partial E_\beta} \right|_{u_{s\alpha}=0} = - \left. \frac{\partial}{\partial E_\beta} \right|_{u_{s\alpha}=0} \left. \frac{\partial U_{SL}}{\partial u_{s\alpha}(\mathbf{q}=0)} \right|_{E_\beta=0} = - \left. \frac{\partial^2 U_{SL}}{\partial E_\beta \partial u_{s\alpha}(\mathbf{q}=0)} \right|_{u_{s\alpha}=0, E_\beta=0}, \quad (3.33)$$

where $U_{SL} = U/N_c$ represents the static energy per unit cell corresponding to the converged energy of the optimized crystal lattice. Eq. (3.33) implies that the tensor element, $Z_{\alpha\beta}^{*s}$, for s -type ions is essentially equal to the partial derivative of the macroscopic polarization in the β direction with respect to the α component of the displacement evaluated at zero electric field. Combining Eqs. (3.12) and (3.32), the

equation of motion Eq. (3.33) is modified to be

$$-M_s \omega^2 u_{s\alpha}^\nu(\mathbf{q}) = -M_s (\omega^\nu)^2 u_{s\alpha}^\nu(\mathbf{q}) + \sum_{\beta} e Z_{\alpha\beta}^{*s} E_{\beta}(\mathbf{q}). \quad (3.34)$$

In addition to the electronic contribution quantified by the electronic dielectric constant ε^∞ , the total displacement field should also take the ionic polarization resulting from the oscillating dipoles in the crystal into account

$$D_{\alpha}(\mathbf{q}) = \sum_{\beta} \varepsilon_{\alpha\beta} E_{\beta}(\mathbf{q}) = \sum_{\beta} \varepsilon_{\alpha\beta}^{\infty} E_{\beta}(\mathbf{q}) + \frac{4\pi e}{\Omega} \sum_{t\beta} Z_{\alpha\beta}^{*t} u_{t\beta}(\mathbf{q}), \quad (3.35)$$

where Ω is the volume of unit cell, and the notation ε without superscript denotes the frequency dependent dielectric tensor. Through Eq. (3.35), we can derive the relation between ε and high frequency ε^∞ as

$$\varepsilon_{\alpha\beta}(\omega) = \varepsilon_{\alpha\beta}^{\infty} + \frac{4\pi e^2}{\Omega} \sum_{\nu} \frac{\mathcal{R}_{\alpha}^{\nu} \mathcal{L}_{\beta}^{\nu}}{((\omega^\nu)^2 - \omega^2) M^{\nu}} \quad (3.36)$$

with the definitions

$$\mathcal{R}_{\alpha}^{\nu} \equiv \sum_{t\beta} Z_{\alpha\beta}^{*t} u_{t\beta}^{\nu}; \quad \mathcal{L}_{\beta}^{\nu} \equiv \sum_{s\alpha} (u_{s\alpha}^{\nu})^* Z_{\alpha\beta}^{*s}. \quad (3.37)$$

In order to find a solution for Eq. (3.34), we now consider the Maxwell's equations in the absence of external charges and currents for non-magnetic materials

$$\nabla \cdot \mathbf{D} = 0 \quad (3.38)$$

$$\nabla \times (\nabla \times \mathbf{E}) + \frac{1}{c^2} \frac{\partial^2 \mathbf{D}}{\partial t^2} = 0. \quad (3.39)$$

For the case of TO modes, $\mathbf{E} \perp \mathbf{q}$, *i.e.* $\mathbf{E} \cdot \mathbf{q} = 0$, Eq. (3.32) is reduced to $\mathbf{F}_T =$

$-M\omega^2\mathbf{u}$, and therefore for the pure TO mode

$$\omega_T^{1,2} = \omega^\nu, \quad (3.40)$$

which means the frequency of the doubly-degenerate TO modes is unshifted in the presence of electric field. While for the case of LO modes, $\mathbf{E} \cdot \mathbf{q} \neq 0$, causing an additional restoring force. In order to satisfy Eq. (3.38) we must have $\mathbf{D}_L = 0$, which is equivalent to require that longitudinal component $\varepsilon_{\alpha\beta}(\omega)$ in Eq. (3.36) vanishes

$$\varepsilon_{\alpha\beta}^\infty + \frac{4\pi e^2}{\Omega} \sum_\nu \frac{\mathcal{R}_\alpha^\nu \mathcal{L}_\beta^\nu}{((\omega^\nu)^2 - \omega^2) M^\nu} = 0. \quad (3.41)$$

To simplify the analysis, we assume there is only one LO modes having non-trivial values of \mathcal{R}_α^ν and \mathcal{L}_β^ν , then straightforwardly from Eq. (3.41) we can obtain the LO frequency in the range $\mathbf{q} \rightarrow 0$

$$\omega_L^2 = (\omega^\nu)^2 + \frac{1}{\varepsilon_{\alpha\beta}^\infty} \frac{4\pi e^2}{\Omega M^\nu} \mathcal{R}_\alpha^\nu \mathcal{L}_\beta^\nu, \quad (3.42)$$

which in fact is a q -independent quantity and upshifted in response to the dipole-dipole interaction. Up to now, we have quantified the phenomenon of LO-TO splitting to a certain degree: in spite of the symmetry of the polar crystals, the LO mode is accompanied by an additional restoring force due to the long-range nature of Coulomb interaction. This extra force then in turn inspires the motions of ions, leading to the frequency of the LO mode shift by an amount exactly equal to the second term of Eq. (3.42) on the right, and thus breaks the degeneracy between the LO mode and the two TO modes in a very narrow wavelength window close to $\mathbf{q} = 0$. Furthermore, it turns out in the simple case of the number of the coupled modes $n_L^\nu = 1$ the LO mode and the TO mode have the following connection, called Lyddane-Sachs-Teller

relation⁹⁰

$$\frac{\omega_L^2}{\omega_T^2} = \frac{\varepsilon^0}{\varepsilon^\infty}, \quad (3.43)$$

where the static dielectric tensor, ε^0 , is evaluated at $\omega = 0$ in Eq. (3.36) according to

$$\varepsilon_{\alpha\beta}^0 \equiv \varepsilon_{\alpha\beta}(\omega = 0) = \varepsilon_{\alpha\beta}^\infty + \frac{4\pi e^2}{\Omega} \sum_\nu \frac{\mathcal{R}_\alpha^\nu \mathcal{L}_\beta^\nu}{(\omega^\nu)^2 M^\nu}. \quad (3.44)$$

It can be immediately seen that the frequency discrepancy of the LO mode from that of the TO modes varies with the electronic contribution to the static dielectric constant; The higher the ratio of ε^0 to ε^∞ , the bigger the gap between ω_L and ω_T .

The analytic term of the interatomic force constant matrix Eq. (3.11) at exactly $\mathbf{q} = 0$ has been automatically included in the DFPT implementation of ab initio packages such as ABINIT and QUANTUM ESPRESSO, the non-analytic term for $\mathbf{q} \rightarrow 0$ needs to be added additionally so that the total second-order matrix takes the form

$$\text{tot} \tilde{C}_{st}^{\alpha\beta}(\mathbf{q} \rightarrow 0) = \text{AN} \tilde{C}_{st}^{\alpha\beta}(\mathbf{q} = 0) + \text{NA} \tilde{C}_{st}^{\alpha\beta}(\mathbf{q} \rightarrow 0), \quad (3.45)$$

where the non-analytic term is given by^{86,88}

$$\text{NA} \tilde{C}_{st}^{\alpha\beta} = \frac{4\pi e^2}{\Omega} \frac{(\mathbf{q} \cdot \mathbf{Z}^{*s})_\alpha (\mathbf{q} \cdot \mathbf{Z}^{*t})_\beta}{\sum_{\alpha\beta} q_\alpha \varepsilon_{\alpha\beta}^\infty q_\beta}. \quad (3.46)$$

Within the framework of DFPT, both Z^* and ε^∞ can be obtained via response to the perturbation of the non-periodic electric field. Eq. (3.46) shows in the practical calculation of including the coupling effect on LO modes for small q , and we need to specify the direction of \mathbf{q} along which this non-analytic correction is evaluated. This associated direction can be determined from the non-trivial displacement-dependent parameters \mathcal{R}_α^ν and \mathcal{L}_β^ν defined by Eq. (3.37). More details could be found in Chapter 6.

Chapter 4

Theory of ionic transport in solids

4.1 Common diffusion mechanisms

The active diffusion in the ionic conductor is carried out by means of thermal activation with the help of defects. To evaluate the performance of a solid electrolyte material as a practical ionic conductor, a necessary prerequisite is to understand the microscopic diffusion mechanisms of the mobile carriers.

In real crystals, atoms constantly vibrate at a small amplitude near their equilibrium positions. At low temperatures, the vibrational energy of each atom is not high enough to escape from its equilibrium site which we will reference as a “host” site. As a result, the diffusion of ions in the crystal depends mainly on the defects introduced by doping, which are called extrinsic defects. As the temperature rises gradually, the thermal vibration of the atoms becomes more intense. Some of them with sufficient vibrational energy may occasionally overcome quantum mechanical and Coulombic interactions with surrounding atoms and break away from the regular lattice sites, resulting in a number of intrinsic defects such as vacancies and interstitial ions in the crystal. During this process, the change in the Born-Oppenheimer energy profile within the crystal lattice, in turn, promotes the redistribution of atoms/defects.

The generation, movement, and reset of those defects ultimately determines the ionic conductivity of the material.

The equilibrium position of each atom in the crystal lattice corresponds to a potential energy valley. To jump from one site to the nearest neighboring one, an atom needs to surpass the barrier energy between the two positions. Every time an atom vibrates back and forth, it can be considered an attempt to cross the barrier. However, an active jump is likely to succeed only when the activation energy obtained by the thermal fluctuation is greater than the barrier energy (Note that the migration barrier here refers to the jumping of atoms between adjacent lattice positions). The conductivity property of a material is actually the macroscopic reflection of a series of microscopic jumping behaviors of ions between adjacent lattice points.

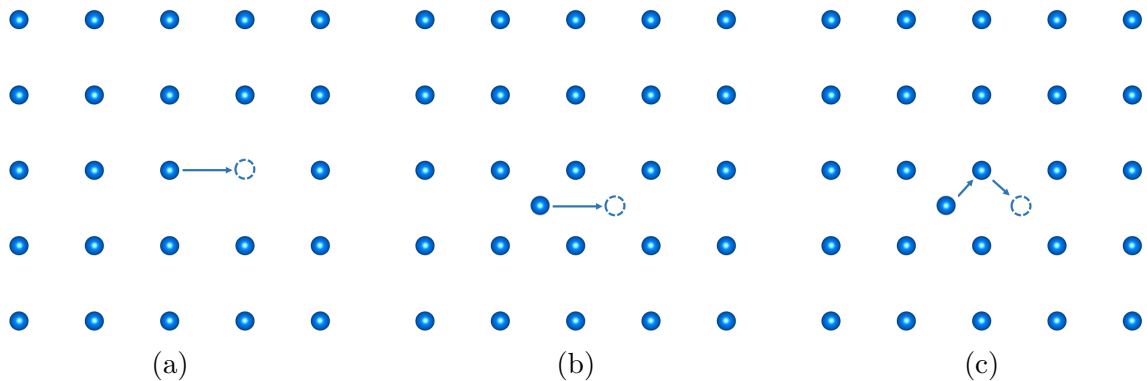


Figure 4.1: Schematic illustration of (a) vacancy, (b) interstitial, and (c) interstitialcy mechanism of diffusion. The solid blue sphere, empty sphere, and arrow represent current atomic position, to be occupied position, and hopping direction, respectively.

The energy barrier for atomic motion depends on many factors, such as crystal structure, compound composition, atomic binding energy, *etc.* Also, it is closely related to the diffusion mechanism of ions. In crystal with defects, the diffusion of the ions usually proceeds through the following three most often encountered mechanisms,

(1) Vacancy mechanism

Ion diffusion via a vacancy mechanism occurs by exchanging the position of an ion between a regular lattice site and neighboring vacancy. As illustrated in Fig. 4.1a,

in the case of a vacant site appearing in the crystal lattice, the nearest neighbor will preferentially jump into the available vacancy, thereby moving one step by transferring the vacancy from one lattice site to another. Besides the precondition of the presence of a vacancy in the vicinity, the ion must also gain enough energy to overcome the effective energy barriers due to interactions with surrounding ions and due to lattice distortions.

(2) Interstitial mechanism

In the interstitial mechanism of diffusion shown schematically in Fig. 4.1b, the ion hops from one interstitial position to the next one in the neighborhood without the participation of the regular lattice sites. Such a mechanism is most likely when the material has neighboring interstitial sites within the crystal structure. Although the interstitial ions in the three-dimensional lattice are always adjacent to multiple interstitial positions for jumping, the atomic activation energy must be sufficient for ions to be able to squeeze into the target position by crossing the gap of normal lattice sites.

(2) Interstitialcy mechanism

The diffusion process of the interstitialcy mechanism, also known as the kick-out mechanism, is schematically shown in Fig. 4.1c. Different from the elementary act of single-hop seen in the first two mechanisms, the movement of ions according to this mechanism is taking place by the cooperative hops of an interstitial ion and an ion at a normal lattice site. Specifically, the lattice ion hops to an adjacent interstitial position, leaving a vacancy that is subsequently being occupied by the nearby interstitial ion. The process is equivalent to an interstitial ion displacing the lattice ion by kicking it out to an empty interstitial site. When the involved one lattice and two interstitial sites are non-collinear, the initial and final states of the interstitially diffusion of ions of the same type are identical to the direct interstitial diffusion. However, the elementary diffusion attempt, which consists of two instead of

one single ionic hops, may result in a more energetically favorable migration pattern with relatively lower barrier energy. In fact, the concerted mechanisms of multiple ions have been identified in a number of very promising electrolyte materials by He *et al.*⁹¹

4.2 The Nernst-Einstein equation and the Haven ratio

As discussed in the previous section, the diffusion of ions in solid proceeds by means of thermal activation with ions hopping randomly to available vacancies and interstitial sites of the lattice structure. For the case that the hops of ions of the same type a are uncorrelated to each other, the single ion motion is described by the tracer diffusion coefficient D_{tr} ⁹²

$$D_{tr} = \lim_{t \rightarrow \infty} \frac{d}{dt} \left[\frac{1}{2dN_a} \left\langle \sum_{i=1}^{N_a} |\Delta \mathbf{R}_i(t)|^2 \right\rangle_t \right], \quad (4.1)$$

where $d = 3$ for three-dimensional system, N_a denotes the number of ions of type a , $\Delta \mathbf{R}_i(t) = \mathbf{R}_i(t) - \mathbf{R}_i(0)$ represents the displacement of the i -ion over the time interval t . As indicated by the bracket symbol, the ion travel distance in the time interval t is actually the statistical average over all the distances with same time duration in the ensemble.

The dependence of D_{tr} on temperature is usually described by Arrhenius relationship is

$$D_{tr} = D_0 e^{-E_a/k_B T}, \quad (4.2)$$

where D_0 is a constant, T the temperature in Kelvin, and k_B the Boltzmann constant. E_a represents the activation energy, which is numerically equivalent to the energy barrier that the mobile ion has to overcome to move through the crystal.

The ion conductivity, which is prompted by the movement of charged ions in the

crystalline solid, can be quantitatively described by the product of the mobile ion concentration, that is, the number of conductivity carriers per unit volume $\rho_a = N_a/V$, the charge of the mobile ions q , and mobility μ

$$\sigma = \rho_a q \mu. \quad (4.3)$$

At a fixed temperature, the ion mobility is expressed as

$$\mu = \frac{q D_\sigma}{k_B T}, \quad (4.4)$$

in which the proportional conductivity diffusivity D_σ is often used to measure the effectiveness of the collective diffusion of all mobile ions

$$D_\sigma = \lim_{t \rightarrow \infty} \frac{d}{dt} \left[\frac{1}{2dN_a} \left\langle \left| \sum_{i=1}^{N_a} \Delta \mathbf{R}_i(t) \right|^2 \right\rangle_t \right]. \quad (4.5)$$

Combining Eqs. (4.3) and (4.4) leads to the following expression for the ionic conductivity

$$\sigma = \frac{\eta q^2}{k_B T} D_\sigma. \quad (4.6)$$

So far, we have obtained the well-known Nernst-Einstein equation, which connects ionic conductivity with the conductivity diffusion coefficient.

The charge diffusion coefficient, by definition, can be divided into two terms

$$\begin{aligned} D_\sigma &= \lim_{t \rightarrow \infty} \frac{d}{dt} \left[\frac{1}{2dN_a} \left\langle \sum_{i=1}^{N_a} |\Delta \mathbf{R}_i(t)|^2 \right\rangle_t \right] + \lim_{t \rightarrow \infty} \frac{d}{dt} \left[\frac{1}{2dN_a} \left\langle \sum_{i=1}^{N_a} \sum_{j \neq i}^{N_a} |\Delta \mathbf{R}_i(t) \cdot \Delta \mathbf{R}_j(t)| \right\rangle_t \right] \\ &= D_{tr} + D_{co}, \end{aligned} \quad (4.7)$$

from which it is clear to see that the first part on the right-hand side is exactly the tracer diffusion coefficient of individual hops. The second cross-interaction term, denoted by D_{co} , comes from the contribution of the correlated motion between all

pairs of ions of the same type a but with different labels.

Typically, we introduce Haven ratio H_r to characterize the independent non-interacting diffusion relative to the integrated behavior of interparticle interactions. It is defined to be the ratio of tracer diffusivity to the conductivity diffusivity

$$H_r = \frac{D_{tr}}{D_\sigma} = \frac{D_{tr}}{D_{tr} + D_{co}}. \quad (4.8)$$

Straightforwardly, when there is no correlation between different particles, $D_\sigma = D_{tr}$.

Substituting D_{tr} in Eq. (4.2) for D_σ yields

$$\sigma = \frac{\eta q^2}{k_B T} \frac{D_{tr}}{H_r} = \frac{\eta q^2}{k_B T H_r} D_0 e^{-E_a/k_B T}. \quad (4.9)$$

The above equation is usually employed to analyze ionic conductivity from the results of molecular dynamics simulations at various temperatures. In addition to the factors such as temperature, carrier concentration, and so on, ion conductivity is also directly influenced by the dynamical correlations of ions movement. A lower value of H_r implies multiple ions that interact to hop collectively, which is conducive to improving the conduction of ions in solid electrolyte materials. However, it is a computational challenge to directly assess the coupled motions between migrating ions from H_r since a much longer simulation time is needed for the cross term D_{co} or the total diffusivity D_σ in Eq. (4.8) to achieve convergence. The practical technique we adopted for evaluating possible correlated hopping can be found in Chapter 9.

Generally, the crystal structure of a typical solid electrolyte with excellent performance is constructed by two sublattices nesting with each other. One conducting sublattice is composed of conducting ions, and the other forms the framework structure. While the conducting sublattice displays a highly disordered melting or liquid-like behavior, the framework sublattice must be frozen and rigid enough to ensure structural stability in response to the changes of the operating environment,

such as temperature and pressure. In addition, it should include suitable void space that allows the crystal to transfer ions through continuous pathways. Such diffusion channel is best to be two-dimensional or three-dimensional. It also expects that there are various locations for the mobile ions to occupy; that is, the defect sites outnumber the migrating ions themselves. Furthermore, the available positions for ions to hop should be similar in energy. Equally essential is that the migration barrier energy between the neighboring sites should be fairly low so that the ions can easily hop from one to another.

4.3 Modeling method of ionic transport

Within the first principles or ab initio theoretical framework of DFT, two reliable computer simulation techniques have been developed to understand the ionic transport properties of electrolyte materials. One is the Nudged Elastic Band (NEB) method, which is generally used to determine the barrier energy of the ion migration by finding the minimum energy path (MEP) between two metastable configurations. Another approach is molecular dynamic (MD) simulations, a powerful tool for calculating the statistical average of the macroscopic model by simulating the real-time dynamical motions of interactive particles with quantum features.

4.3.1 Nudged elastic band method

For some rare events with pretty low reaction probability, it is necessary to simulate about 10^{15} steps to observe the transition from reactants to products if using the conventional molecular dynamics approaches. However, by presetting the initial state and a known final state, the corresponding reaction path and energy barrier can be obtained within acceptable simulation steps using the nudged elastic band (NEB) method, which was proposed by the Jónsson group.⁵¹⁻⁵³ Specifically, NEB is a method

developed to locate the saddle points and the minimum energy path, *i.e.* the path with the highest transition probability, between two metastable states on a potential energy surface. It works by dividing the whole reaction path into several segments with the starting and ending configurations of each segment referred to as discrete “images” of the system. The “elastic bands” in this context mean any two adjacent images are connected by springs, forming a path of springs. While the word “nudge” implies that the spring forces act only along the band to maintain equal image spacing, and the component of the potential force is constrained to perpendicular to the band, hence in this way, each image tends to slide down toward the minimum energy path to minimize its potential energy.

Suppose a continuum reaction path is represented by a chain of $N_{\text{img}} + 1$ discrete images in total. Initially, the reaction coordinate of the i th image, \mathbf{R}_i , is determined by linear interpolation

$$\mathbf{R}_i = \mathbf{R}_0 + \frac{i}{N_{\text{img}}} (\mathbf{R}_N - \mathbf{R}_0), \quad (4.10)$$

here \mathbf{R}_0 and \mathbf{R}_N denote the positions of the initial and the final state, respectively. Define the normalized local tangent of the band at \mathbf{R}_i as

$$\hat{\boldsymbol{\tau}}_i = \frac{\boldsymbol{\tau}_i}{|\boldsymbol{\tau}_i|}, \quad (4.11)$$

where

$$\boldsymbol{\tau}_i = \frac{\mathbf{R}_i - \mathbf{R}_{i-1}}{|\mathbf{R}_i - \mathbf{R}_{i-1}|} + \frac{\mathbf{R}_{i+1} - \mathbf{R}_i}{|\mathbf{R}_{i+1} - \mathbf{R}_i|}. \quad (4.12)$$

To calculate the force acting on \mathbf{R}_i , only two terms, the elastic force that is parallel to the tangent and a perpendicular force due to the external potential, are taken into account

$$\mathbf{F}_i = \mathbf{F}_i^s|_{\parallel} + \mathbf{F}_i|_{\perp}, \quad (4.13)$$

here elastic force projected along the band is simply given by

$$\mathbf{F}_i^s|_{\parallel} = k [(\mathbf{R}_i - \mathbf{R}_{i-1}) - (\mathbf{R}_{i+1} - \mathbf{R}_i)] \cdot \hat{\boldsymbol{\tau}}_i \hat{\boldsymbol{\tau}}_i, \quad (4.14)$$

in which k is an artificial elastic constant, and therefore $\mathbf{F}|_{\parallel}$ is a fictitious elastic force designed for the purpose of numerical simulation. The second piece, the real external force projected orthogonally to the path direction, takes the form

$$\mathbf{F}_i|_{\perp} = \nabla U(\mathbf{R}_i)|_{\perp} = \nabla U(\mathbf{R}_i) - \nabla U(\mathbf{R}_i) \cdot \hat{\boldsymbol{\tau}}_i. \quad (4.15)$$

All of the intermediate images are being optimized simultaneously using various types of optimization schemes such as steepest descent⁹³ or Broyden's method⁹⁴ to find the lowest possible energy. The minimum energy path condition is satisfied when

$$\nabla U(\mathbf{R}_i)|_{\perp} = 0. \quad (4.16)$$

As illustrated in Eq. (4.14), the elastic constant k is set to be identical for all springs so that the images can keep uniform spacing when converging on the minimum energy path. However, usually there is no image that lands at the saddle point and the saddle point energy has to be estimated by interpolation, causing the activation energy obtained from the difference between the local minima and the saddle point energy much uncertainty. Later Henkelman⁹⁵ proposed a so called climbing image nudged elastic band method (CI-NEB) to constraint the convergence of a saddle point. Compared to the original formulation of the NEB method, the extended CI-NEB method redefines the force, $\mathbf{F}_{i_{\max}}$, acting on the image with the highest energy as follows

$$\begin{aligned} \mathbf{F}_{i_{\max}} &= - \left[\nabla U(\mathbf{R}_{i_{\max}}) - \nabla U(\mathbf{R}_{i_{\max}})|_{\parallel} \right] + \nabla U(\mathbf{R}_{i_{\max}})|_{\parallel} \\ &= -\nabla U(\mathbf{R}_{i_{\max}}) + 2\nabla U(\mathbf{R}_{i_{\max}}) \cdot \hat{\boldsymbol{\tau}}_{i_{\max}} \hat{\boldsymbol{\tau}}_{i_{\max}}. \end{aligned} \quad (4.17)$$

The above equation indicates that instead of being affected by the elastic force, the highest energy image experiences an inverted potential force along the band. The treatment allows the highest energy image to climb up to the transition state along the minimum energy path, giving a rigorous recognition of the saddle point.

In the perspective of ionic conductivity, the saddle point energy along the minimum energy path is the potential energy maximum which approximates the activation energy barrier E_a , a quantity of central importance for analyzing the migration mechanisms within transition state theory as adapted to ionic migration.

4.3.2 Ab initio molecular dynamics

The basic idea underlying molecular dynamics (MD) is that knowledge of the effective interaction potentials between particles in a system allows for simulation of the dynamic evolution behavior of the entire system. Unlike classical MD methods using empirical force fields, the approach of ab initio molecular dynamics (AIMD) uses the force field derived from quantum-mechanical Schrödinger wave equation and samples the atomic configurations over the simulation duration to accurately determine the equilibrium thermodynamic and dynamical properties of the studied system.^{96–98}

For the Born-Oppenheimer variant of AIMD, the theoretical framework is formed by unifying electronic structure calculations with the molecular dynamics of classically behaving nuclei. Compared with Eq. (2.6), the total wavefunction for the Schrödinger equation with time-dependent state of the nuclei is expanded to be

$$\Psi(\{\mathbf{r}\}; \{\mathbf{R}\}; t) = \Psi_{\mathbf{R}}(\{\mathbf{r}\})\chi(\{\mathbf{R}\}; t). \quad (4.18)$$

Due to adapting the slow nuclear motion adiabatically, the electronic structure at each instant step of MD simulations is reducible to a time-independent quantum problem. That is, the separation leads to a stationary Schrödinger equation for the

quickly varying electrons Eq. (2.9) and a Newtonian equation of motion for the slowly varying nuclei in an effective potential

$$M_I \ddot{\mathbf{R}}_I = \mathbf{F}_I = -\nabla_{\mathbf{R}} U(\{\mathbf{R}\}), \quad (4.19)$$

where $U(\{\mathbf{R}\})$ is the Born-Oppenheimer potential energy surface with the detailed discussion given in Section 2. From the perspective of the nuclei, the electron is always in the ground state, indicating the electronic structure problem has to be solved self-consistently to reach the minimum $\Psi_{\mathbf{R}}(\{\mathbf{r}\})$ at each AIMD step.

On the basis of the atomic forces $\mathbf{F}(\{\mathbf{R}\})$ evaluated from the Hellmann-Feynman theorem, it is crucial to formulate a numerical algorithm to integrate the equations of motion on the time scale given by nuclear motion. One of the simplest but effective integrators is originate with a Taylor series expansion to express the atomic positions at $t + \Delta t$ in the following form

$$\mathbf{R}_I(t + \Delta t) \approx \mathbf{R}_I(t) + \dot{\mathbf{R}}_I(t)\Delta t + \frac{\Delta t^2}{2!}\ddot{\mathbf{R}}_I(t) + \frac{\Delta t^3}{3!}\dddot{\mathbf{R}}_I(t) + O(\Delta t^4). \quad (4.20)$$

Replacing $\dot{\mathbf{R}}_I(t)$ and $\ddot{\mathbf{R}}_I(t)$ with the equivalent notations $\mathbf{v}_I(t)$ and $\mathbf{F}_I(t)/M_I$, respectively, Eq. (4.20) becomes

$$\mathbf{R}_I(t + \Delta t) \approx \mathbf{R}_I(t) + \mathbf{v}_I(t)\Delta t + \frac{\mathbf{F}_I(t)}{2M_I}\Delta t^2 + \frac{\Delta t^3}{3!}\ddot{\mathbf{R}}_I(t) + O(\Delta t^4). \quad (4.21)$$

Similarly, the application of the Taylor series for $\mathbf{R}_I(t - \Delta t)$ gives

$$\mathbf{R}_I(t - \Delta t) \approx \mathbf{R}_I(t) - \mathbf{v}_I(t)\Delta t + \frac{\mathbf{F}_I(t)}{2M_I}\Delta t^2 - \frac{\Delta t^3}{3!}\ddot{\mathbf{R}}_I(t) + O(\Delta t^4). \quad (4.22)$$

Adding Eqs. (4.20) and (4.22) we find immediately

$$\mathbf{R}_I(t + \Delta t) + \mathbf{R}_I(t - \Delta t) = 2\mathbf{R}_I(t) + \frac{\mathbf{F}_I(t)}{M_I} \Delta t^2 + O(\Delta t^4). \quad (4.23)$$

Rearranging the above equation yields the Verlet algorithm for numerically propagating the positions⁹⁹

$$\mathbf{R}_I(t + \Delta t) = 2\mathbf{R}_I(t) - \mathbf{R}_I(t - \Delta t) + \frac{\mathbf{F}_I(t)}{M_I} \Delta t^2 + O(\Delta t^4). \quad (4.24)$$

The local error in estimating the updated atomic position is 4th order Δt^4 . The atomic velocity, which plays no part in the above integration process, is simply derived from the forward and reverse trajectories using finite difference method

$$\mathbf{v}_I(t) = \frac{\mathbf{R}_I(t + \Delta t) - \mathbf{R}_I(t - \Delta t)}{2\Delta t} + O(\Delta t^2). \quad (4.25)$$

To directly involve velocity, it is convenient to devise a mathematically equivalent form of the Verlet algorithm. Note that the substitution of $(t - \Delta t) \rightarrow t$ and $t \rightarrow (t + \Delta t)$ in Eq. (4.22) allows to derive back the expression for $\mathbf{R}_I(t)$

$$\mathbf{R}_I(t) \approx \mathbf{R}_I(t + \Delta t) - \mathbf{v}_i(t + \Delta t)\Delta t + \frac{\mathbf{F}_I(t + \Delta t)}{2M_I} \Delta t^2. \quad (4.26)$$

By inserting Eq. (4.21) into Eq. (4.26), we obtain the updated velocity at one advancing time step $t + \Delta t$

$$\mathbf{v}_I(t + \Delta t) = \mathbf{v}_I(t) + \frac{\mathbf{F}_I(t) + \mathbf{F}_I(t + \Delta t)}{2M_I} \Delta t. \quad (4.27)$$

Equations (4.21) and (4.27) constructs the complete velocity variant of the velocity algorithm¹⁰⁰ which concurrently evolve the atomic positions and velocities. By recursively incorporating the velocity Verlet algorithm into Eq. (4.19) in a long time

MD simulations, it enables to improve stability of the numerical integration of the equations of motion with a high level of accuracy.¹⁰¹

AIMD simulations are typically carried out with the subjection of a statistical ensemble specified by a set of constraint equilibrium conditions. There are three commonly used ensembles for creating a target environment in solid electrolytes simulations. The microcanonical ensemble at the constant condition of the number of particles N , the volume V , and total energy E describes isolated systems free from an external force. In this ensemble, only those microstates or configurations forming conserved E hypersurface are allowed to count in the ensemble average of a quantity, for which the contribution of the qualified phase space points is equally probable according to the principle of equal a priori probability in statistical mechanics. The constant (N, V, T) condition of motion corresponds to the canonical ensemble. Typically, the fixed temperature T is attained by bringing the system of interest into contact with an external thermostat. As a result, the total energy of the simulated system may fluctuate for exchanging heat and work with the external system. A popular approach is the Nosé–Hoover algorithm^{102,103} to maintain the thermal equilibrium between the physical system and the surrounded heat reservoir or heat bath. Under equilibrium conditions of canonical ensemble, the probability of the simulated system being in a particular microstate is governed by Boltzmann distribution. As in the canonical ensemble, the isothermal-isenthalpic ensemble is used to treat the statistical distribution of a system held at a constant number of particles N and temperature T . The distinctive feature of this ensemble is that pressure P is also chosen as a control viable with invariant value preserved by allowing the change in the volume of the simulated system.

The AIMD simulation has been one of the most dominant theoretical tools to study various problems in computational fields of physics, chemistry, and biology, *etc.* Particularly for examining ionic transport in solid electrolyte materials, the

AIMD calculation at finite temperature offers the most convenient approach to directly observe the dynamic trajectories of mobile ions, which further allows relatively comprehensive analysis on the favorable migration mechanisms and the associated low-energy crystallographic sites that highly involved in the conducting process. In this regard, the AIMD method of modeling the unbiased and spontaneous motions of ions is able to reveal a great number of details compared to the NEB methodology applicable for evaluating hops with prespecified initial and final states. With elemental quantities measured numerous times at regular time intervals, the main characteristic of ionic conductor properties, such as diffusivity and ionic conductivity, are subsequently accessible via the formulas discussed in Chapter 4.2. However, the MD simulations are computationally expensive as large system sizes and sufficiently long time scales are required to yield useful results with physics significance. Nevertheless, these drawbacks are expected to be alleviated with progressive development in high-performance computing.

Part 2

Summary of Research Work

Chapter 5

First principles simulations of $\text{Li}_4\text{P}_2\text{S}_6$, and $\text{Na}_4\text{P}_2\text{S}_6$, and $\text{Li}_2\text{Na}_2\text{P}_2\text{S}_6$

5.1 Overview

The project was motivated by the experimental result of Hood *et al.*¹⁰⁴ Besides verifying the based-centered monoclinic structure $C2/m$ of $\text{Na}_4\text{P}_2\text{S}_6$, the new experiment also detected that the material has significant Na ion conductivity (3×10^{-6} S/cm) at room temperature. By contrast, its $\text{Li}_4\text{P}_2\text{S}_6$ analog, characterized with the space group $P321$ (later was determined to be $P\bar{3}m1$ in computer modeling), exhibits poor ionic conductivity properties. It was identified as a low conductivity decomposition product in the formation of lithium thiophosphate electrolytes. Using DFT with the harmonic phonon approximation, we found that the simulated stable structural patterns for $\text{Li}_4\text{P}_2\text{S}_6$ and $\text{Li}_4\text{P}_2\text{S}_6$ are consistent with those reported in the experiments. For $\text{Na}_4\text{P}_2\text{S}_6$, it was observed that the Na ion migrates most likely within the plane formed by h type sites via a vacancy mechanism, involving interstitial d type sites. We

also predicted that the Na ion conductivity could be enhanced by alloying $\text{Na}_4\text{P}_2\text{S}_6$ with Li to form $\text{Li}_2\text{Na}_2\text{P}_2\text{S}_6$ having the same $C2/m$ structure with compacted a and b lattice constants. The calculation of Helmholtz free energies suggests that the alloy material is stable for a range of temperatures at and above room temperature in terms of the energy difference $F(\text{Li}_2\text{Na}_2\text{P}_2\text{S}_6 + 2\text{Na}) - F(\text{Na}_4\text{P}_2\text{S}_6 + 2\text{Li}) \leq -0.35$ eV. Molecular dynamics simulations indicate that $\text{Li}_2\text{Na}_2\text{P}_2\text{S}_6$ has larger Na ion conductivity than does $\text{Na}_4\text{P}_2\text{S}_6$ and therefore is promising as a possible solid state electrolyte for all solid state Na ion batteries.

Prof. Holzwarth conceived the original idea of the work presented in this chapter. The numerical simulations and data analysis were performed by myself under the guidance of Prof. Holzwarth. The first draft of the manuscript was written in collaboration with Prof. Holzwarth. Dr. Hood reviewed and helped with the improvement of previous versions of the manuscript. All substantial corrections and revisions were completed by Prof. Holzwarth and me.

5.2 Published work

The work was published in *Physical Review Materials* 4, 045406 (2020) and the local copy can be found in Appendix A.

Chapter 6

Continuity of phonon dispersion curves of anisotropic ionic materials

6.1 Overview

The work presented in this chapter was inspired by the observation that phonon dispersion curves for ionic materials with hexagonal or other anisotropic structures appear to have discontinuities or mode disappearances near the Brillouin zone center. These discontinuities are related to the well-known coupling of some of the vibrational modes to long-wavelength electromagnetic waves within the material as described in 1951 by Huang.¹⁰⁵ Up to now, the full details of these discontinuities have not been carefully described in the literature.

In this paper, we review the coupled equations for ion displacements and electric fields in terms of the parameters obtained from DFT and DFPT derive expressions for their solutions. It shows that the solutions can be expressed as linear combinations of the pure phonon vibrational modes. This phonon basis expansion approach, while

not currently implemented in typical density functional codes (such as ABINIT and QUANTUM ESPRESSO), offers the benefits of efficiency and insight to polariton analyses. The paper illustrates the polariton solutions near zero wavevector for boron nitride (BN) in both cubic and hexagonal structures. The dispersion curves of the phonon-photon modes were found to continuously connect within the conventional phonon dispersion diagrams for these materials. This is especially interesting for the anisotropic case of h-BN. While typical density functional codes already treat the electromagnetic couplings to longitudinal modes, we show in this paper how to extend the analysis to the transverse modes.

The discontinuity of the phonon dispersion curves was firstly noticed for the materials studied in Chapter 5. We presented the phenomenon in the weekly condensed matter journal club discussions. At that time, Prof. Kerr proposed the initial conceptual idea of solving the phonon-photon coupling equations to understand the effect of the macroscopic electric field on the phonon frequencies. Prof. Holzwarth and I wrote the Fortran and Python codes to examine the newly developed theoretical formalism, respectively. The independent programming with the input taken from the calculation carried out in ABINIT gave identical results, which also agree very well with the ABINIT output produced using the so-called non-analytic correction to the dynamical matrix to correctly represent the modified longitudinal optical vibrational modes. The original draft was prepared in collaboration with Prof. Holzwarth. All authors were involved in helping shape the analysis and manuscript.

6.2 Published work

The work was published in *Journal of Physics: Condensed Matter* 32, 055402 (2019) and the local copy can be found in Appendix B.

Chapter 7

First principles simulations of Li_3BO_3 , Li_3BN_2 and doped materials

7.1 Overview

The work presented in this chapter consists of two companion papers: “Computational study of Li_3BO_3 and Li_3BN_2 I: Electrolyte properties of pure and doped crystals” (Paper I) and “Computational study of Li_3BO_3 and Li_3BN_2 II: Stability analysis of pure phases and of model interfaces with Li anodes” (Paper II).

While the two papers focus on different material properties, they constitute one complete computational study of similar materials Li_3BO_3 and Li_3BN_2 . Using first-principles modeling techniques based on DFT and DFPT, the detailed diffusion simulation and analysis in Paper I reveals that the Li ion migration in the monoclinic phases of Li_3BO_3 and $\beta\text{-Li}_3\text{BN}_2$ most likely proceeds via vacancy mechanisms. For Li_3BO_3 the Li ion migration primarily occurs in planes formed by the b and c axes, while for $\beta\text{-Li}_3\text{BN}_2$ the Li ion migration is largely one-dimensional along the a lattice

direction. Our simulations show that while perfect crystals of these materials exhibit essentially no conductivity, simulations with a Li vacancy ratio of 1/12 for Li_3BO_3 and 1/16 for Li_3BN_2 show reasonable agreement with several experimental conductivity measurements both reported in the literature and in the current study. The structural properties of Li_3BO_3 and all the three reported phases of Li_3BN_2 are investigated in Paper II. Within the harmonic phonon approximation, the single phase of Li_3BO_3 and the β and γ phases of Li_3BN_2 show good agreement between simulation and experimental analysis. However, the reported tetragonal phase of α - Li_3BN_2 was found to be unstable, as evidenced by imaginary phonon modes near the M point of its Brillouin zone. Our analysis finds that the real α phase of Li_3BN_2 has an orthorhombic structure with a unit cell having twice as many formula units and very small adjustments of the fractional coordinates compared with the original analysis. Quasi-harmonic phonon simulations of the orthorhombic structure at room temperature is in good agreement with experimental X-ray patterns reported in the literature. Also in Paper II, in anticipation of using the monoclinic forms of Li_3BO_3 and Li_3BN_2 as electrolyte or as stabilizing coating materials, we computationally analyzed the stability of the compounds with respect to decomposition and also modeled their reactivity with pure Li metal. The computational results suggest impressive chemical stability for these materials. Additionally, simulations of idealized interfaces of these materials with Li provide further evidence that these materials may be useful for the stabilization of pure Li metal anodes in all solid state batteries.

The interest in studying Li_3BO_3 and Li_3BN_2 originates from the recommendation of Dr. Hood to look into the borate family of materials for possible new electrolytes systems. With an initial review of the literature, we defined several research questions and came up with a preliminary plan for our calculations. The simulations were conceived and performed by myself. During the whole process, Prof. Holzwarth and I had been keeping close discussions on possible directions, challenges, and progress.

One of the most time-consuming sections is the quasi-harmonic analysis for Li_3BN_2 in the $Pm\bar{m}n$ structure. For each particular set of lattice constants of a uniform $3 \times 3 \times 4$ grid, the prerequisite dynamical matrices were evaluated on a discrete \mathbf{q} -grid that contains 12 unique points in the irreducible Brillouin zone of the crystal. The key coding for postprocessing Quantum Espresso data includes the interpolation of Helmholtz free energy on a refined grid of lattice constants using MATLAB. In terms of drafting the work, I wrote the first draft of both manuscripts. Revising and editing of the later versions were completed in collaboration with Prof. Holzwarth. Each manuscript benefits greatly from Dr. Hood's insightful feedback from the experimental perspective.

7.2 Published work

Paper I and II have been published in *Physical Review Materials* and the local copies can be found in Appendices C and D.

Chapter 8

First principles simulations of Li boracites $\text{Li}_4\text{B}_7\text{O}_{12}\text{Cl}$ and $\text{Li}_5\text{B}_7\text{O}_{12.5}\text{Cl}$

8.1 Overview

The mineral boracite $\text{Mg}_3\text{B}_7\text{O}_{13}\text{Cl}$ is characterized by a rigid framework of B-O bonds. That structure has led to Li ion conducting compounds such as lithium chloroboracite $\text{Li}_4\text{B}_7\text{O}_{12}\text{Cl}$. The material with fractionally occupied Li sites located in diffusion channels formed by a rigid B_7O_{12} framework possesses essential features of an ideal Li-ion conductor.

Early experimental work in 1977¹⁰⁶ identified three structural modifications of $\text{Li}_4\text{B}_7\text{O}_{12}\text{Cl}$ related to a face-centered cubic pattern. The room-temperature α form was suggested to have a rhombohedral distortion but was not fully characterized. Our first-principles calculations find the optimized structure of the α phase to have a face-centered rhombohedral structure with space group $R3c$ (No. 161) and structurally very similar to the higher temperature cubic structures of the β and γ forms

apart from the fractional occupancy patterns of the Li configurations. Using the convex hull approach, we estimate α - $\text{Li}_4\text{B}_7\text{O}_{12}\text{Cl}$ to be thermodynamically stable within the composition space of Li_2O , B_2O_3 , and LiCl . Our analysis of Li ion mechanisms indicates that a concerted process, involving two host Li sites and a neighboring unoccupied site based on the face-centered cubic structure, provides the most efficient ion transport in $\text{Li}_4\text{B}_7\text{O}_{12}\text{Cl}$. The room temperature ionic conductivity calculated from MD simulations is on the order of 10^{-4} S/cm, showing good agreement with the recent experimental measurement for pure polycrystalline samples of $\text{Li}_4\text{B}_7\text{O}_{12}\text{Cl}$.¹⁰⁷ The temperature-dependent occupancies of Li sites, as the main structural distinction of the three reported modifications of $\text{Li}_4\text{B}_7\text{O}_{12}\text{Cl}$, are also observed in the MD simulations performed at various temperatures.

Another boracite-type compound with compositions of $\text{Li}_5\text{B}_7\text{O}_{12.5}\text{Cl}$ crystallizes into an ordered cubic $F23$ structure.¹⁰⁸ The material has a high structural similarity to α - $\text{Li}_4\text{B}_7\text{O}_{12}\text{Cl}$ but a considerable difference in the occupancy parameters of the similar Li positions. In this context, we would like to explore the question of how the Li ion migration differs in the fully ordered $\text{Li}_5\text{B}_7\text{O}_{12.5}\text{Cl}$ and α - $\text{Li}_4\text{B}_7\text{O}_{12}\text{Cl}$ containing natural Li vacancies. The migration study indicates that, unlike the case of the α - $\text{Li}_4\text{B}_7\text{O}_{12}\text{Cl}$, the Li ions transport in the crystal of $\text{Li}_5\text{B}_7\text{O}_{12.5}\text{Cl}$ most likely via vacancy processes with rare involvement of the interstitial defects, resulting in poor ionic conductivity with the extrapolated room-temperature value lower than 10^{-10} S/cm.

In the extended work carried out in collaboration with Cory Lynch, who is a fellow graduate student in the group, we also predict that the Li ion conductivity can be enhanced by substituting chemically similar ions to form $\text{Li}_4\text{Al}_3\text{B}_4\text{O}_{12}\text{Cl}$, $\text{Li}_4\text{B}_7\text{S}_{12}\text{Cl}$, and $\text{Li}_4\text{Al}_3\text{B}_4\text{S}_{12}\text{Cl}$. The three analog compounds all have the same $R3c$ ground state structure but with expanded lattices. The preliminary studies show that they also have better Li conducting performance than $\text{Li}_4\text{B}_7\text{O}_{12}\text{Cl}$ and therefore are promising

to be used as solid-state electrolytes in all-solid-state Li-ion batteries.

Under the supervision of Prof. Holzwarth, this work was planned and executed by myself. The calculations were a little bit more challenging due to the disordered phase of crystalline $\text{Li}_4\text{B}_7\text{O}_{12}\text{Cl}$ and the large unit cells for long-time MD simulations. The manuscript, starting from my initial draft, is being revised and edited for publication.

8.2 Manuscripts in preparation

The submitted manuscript for the $\text{Li}_4\text{B}_7\text{O}_{12}\text{Cl}$ and $\text{Li}_5\text{B}_7\text{O}_{12.5}\text{Cl}$ systems can be found in Appendix E. The results for the additional paper on boracite extensions are not yet available at the time of the preparation of this dissertation.

Chapter 9

First principles simulations of idealized $\text{Li}_{7.5}\text{B}_{10}\text{S}_{18}\text{X}_{1.5}$ ($\text{X} = \text{Cl},$ Br, I)

9.1 Introduction

This project focuses on modeling a recently reported family of superadamantanoid lithium thioborate halide electrolytes which have the composition in the form of $\text{Li}_{7.5}\text{B}_{10}\text{S}_{18}\text{X}_{1.5}$ ($\text{X} = \text{Cl}, \text{Br}, \text{I}$).³ The manuscript is being prepared, and this current chapter describes some of the key points. The three materials, all experimentally characterized by having the monoclinic space group symmetry $C2/c$ (No. 15) with highly disordered Li and X sites arranged in the spacious cavity formed by a rigid $\text{B}_{10}\text{S}_{18}$ framework. The measured room-temperature ionic conductivity is on the order of magnitude of 1 mS/cm, qualifying themselves as the Li superionic conductors.

The chloride compound $\text{Li}_{7.5}\text{B}_{10}\text{S}_{18}\text{Cl}_{1.5}$ has some common features with the previously discussed lithium sulfide boracite $\text{Li}_4\text{B}_7\text{S}_{12}\text{Cl}$, theoretically predicated by substituting S for O ions in the original boracite. In terms of similarities, the two materials

systems, both showing favorable Li ionic conductivity, all have the same elemental constituents with Cl and mobile Li ions residing in the large voids formed by B-S framework in the crystalline structure of each material. In terms of difference, the experimentally realized superionic chlorine material $\text{Li}_{7.5}\text{B}_{10}\text{S}_{18}\text{Cl}_{1.5}$ is predicated to be chemically stable, while as far as we know, the proposed boracite material $\text{Li}_4\text{B}_7\text{S}_{12}\text{Cl}$ has not been realized in the experiment, and, according to our calculations, has some chemical stability issues. The B-S framework of the known superadamantanoid material is composed of a network of supertetrahedral BS_4 . In contrast, the boracite material has both tetrahedral and planar B-S units to make the framework. The symmetry of the newly found superionic material is rather low with monoclinic $C2/c$ space group, whereas the boracite structures are based on a highly ordered rhombohedral $R3c$ structure. Although both have big cavities, the void region of the boracite case is smaller and more structured.

Our current computational study focuses on understanding the overall stability and Li ion migration mechanisms of the group of thioborate materials $\text{Li}_{7.5}\text{B}_{10}\text{S}_{18}\text{X}_{1.5}$ ($\text{X} = \text{Cl}, \text{Br}, \text{I}$). By optimizing many possible stoichiometric crystalline configurations, we found ordered ground state realizations of the materials for the three halides $\text{X} = \text{Cl}, \text{Br}, \text{I}$. The evaluations of possible decomposition reactions suggest that all those electrolytes are chemically stable. Molecular dynamics simulations based on the initially ordered structures at various temperatures show significant Li ion hopping within the void channels of the structures at temperatures as low as $T = 400 \text{ K}$. Further examination found the Li ion diffusion proceeds most likely via concerted migration of multiple Li ions. Our preliminary results are in general consistent with the experimental findings of Kaup *et al.*,³ indicating that these materials are very promising solid electrolytes for possible use in all-solid-state Li ion batteries.

9.2 Computational methods

The computational methods used in this work are based on density functional theory^{44,45} using the PBEsol exchange-correlation functional and the projector augmented wave (PAW) formalism. The atomic datasets with PAW basis and projector functions were generated by the ATOMPAW code.⁵⁶ All simulations were carried out using the QUANTUM ESPRESSO package⁵⁵ for the primitive cell of the $C2/c$ structure of four $\text{Li}_{7.5}\text{B}_{10}\text{S}_{18}\text{X}_{1.5}$ ($\text{X} = \text{Cl}, \text{Br}, \text{I}$) units (148 atoms). The structural optimization calculations were performed with plane wave expansions of the wave function including $|\mathbf{k} + \mathbf{G}|^2 \leq 81 \text{ Bohr}^{-2}$ and a uniform grid of $2 \times 2 \times 2$ Bloch vectors of \mathbf{k} . For long-time molecular dynamics simulations, the number of plane waves and Brillouin zone sampling was reduced to 64 Bohr^{-2} and a single zone-centered \mathbf{k} point, respectively. Results of crystal structures and ions mobility were reported in the conventional cell setting of 296 atoms. The VESTA software package¹⁰⁹ was used to construct diagrams of crystal structures. Python¹¹⁰ and MATLAB¹¹¹ codings were employed for calculating and visualizing the ion probability densities, using data generated from molecular dynamics simulations. The symmetry properties of the optimized structures were identified using the FINDSYM program.¹¹²

9.3 Crystal structures

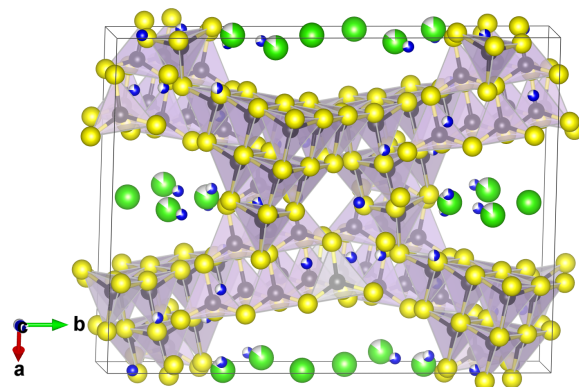
Our calculations start from the experimental crystallographic data of $\text{Li}_{7.5}\text{B}_{10}\text{S}_{18}\text{Cl}_{1.5}$ obtained from X-ray diffraction measurement of single-crystal samples at room temperature. The reported crystal structure was characterized to have monoclinic space group $C2/c$ consisting of eight formula units of 296 atoms per conventional cell. While the B and O sites are fully occupied, the Li and Cl sites are highly disordered. More specifically, the Li ions fractionally locate at eight symmetrically distinctive sites while the Cl ions are partially placed in three inequivalent positions. To build up a

reasonably good candidate for the idealized ordered structure of $\text{Li}_{7.5}\text{B}_{10}\text{S}_{18}\text{Cl}_{1.5}$, we adjusted the fractional occupancies by assuming that all the Li sites and only two of three Cl sites have 100% occupancy. However, even so, it was necessary to find one or more distinct positions for accommodating the remaining eight Li ions, for the reason that such atomic coordinates were not identified in the experimental analysis.

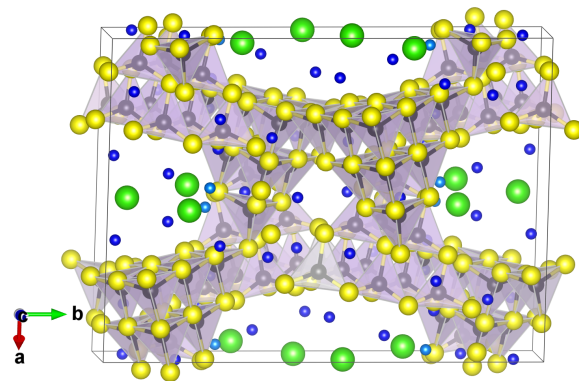
To reduce the computational burden, all simulations were carried out using a primitive cell model with half the number of atoms of the conventional cell for this particular symmetry. In this case, it was necessary to find four additional optimized Li sites. By optimizing a sizable number of initial guesses with the possible missing Li sites associated with $4f$ or $2e$ type points of a coarse grid, we found a relatively lower energy ordered structure consistent with the $C2/c$ symmetry. The structure with the missing Li ions sitting at $4f$ position (0.036, 0.267, 0.062) is calculated to have an energy of at least 0.06 eV per primitive cell lower than the energies of the other candidate structures.

Comparing the polyhedral drawings shown in Fig. 9.1 for the experimental and optimized crystal structures, we find that the placements of the B-S framework in the two crystals are remarkably similar. To some extent, our ideal model has position profiles of Li and Cl ions similar to those of experimental measurements, except that the Li ions are more dispersed and uniformly distributed in the ordered representative structure.

Since the three crystalline halides $\text{Li}_{7.5}\text{B}_{10}\text{S}_{18}\text{X}_{1.5}$ ($\text{X} = \text{Cl}, \text{Br}, \text{I}$) have the same space group symmetry with similar lattice parameters and atomic positions, it is reasonable to construct the initial configurations for the rest of halide materials simply by substituting Br or I ions for Cl ions in the idealized $\text{Li}_{7.5}\text{B}_{10}\text{S}_{18}\text{Cl}_{1.5}$ structure, instead of using the corresponding reported crystallographic data with diverse fractional occupancy on the Li and X sites. The optimized ordered structural models for all the three different halides, together with the drawings of experimental structures,



(a)



(b)

Figure 9.1: Polyhedral diagrams of conventional cells of $\text{Li}_{7.5}\text{B}_{10}\text{S}_{18}\text{Cl}_{1.5}$, comparing (a) experimental structure deduced from diffraction data with (b) the optimized structure of this work. The Li, B, S, and Cl ions are represented by blue, black, yellow, and green balls, respectively.

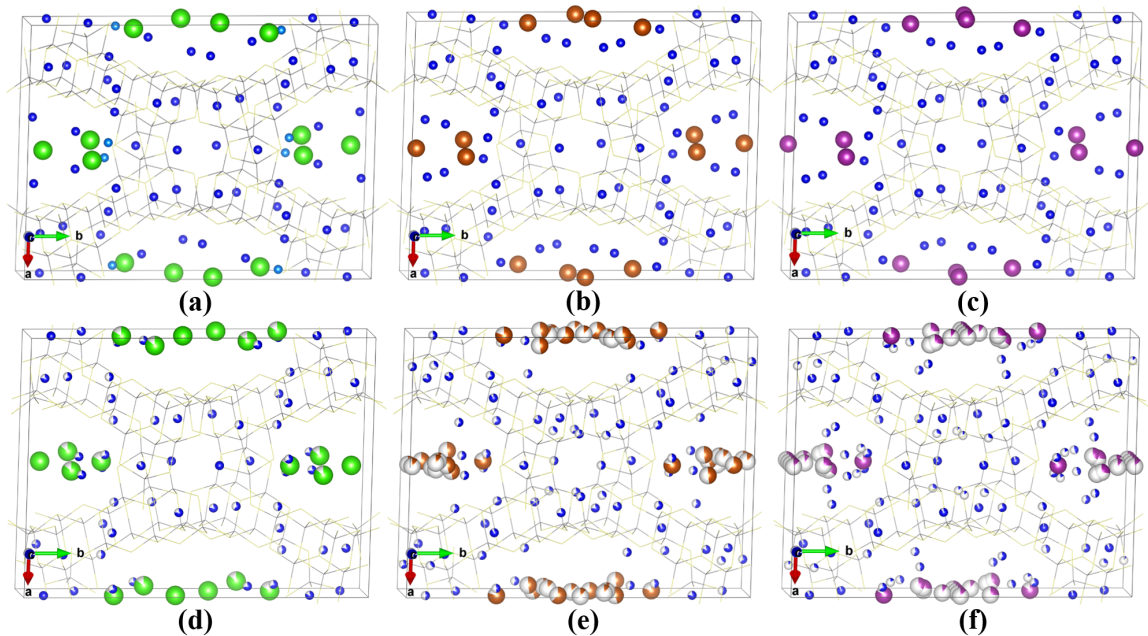


Figure 9.2: Summary of results for the three different halides $\text{Li}_{7.5}\text{B}_{10}\text{S}_{18}\text{X}_{1.5}$ with $\text{X} = \text{Cl}$ (a and d), Br (b and e), I (c and f), comparing computationally optimized structures on the top row with the structures deduced by Kaup *et al.*³ on the bottom row. The color conventions are the same as in Fig. 9.1 except that the B-O framework is indicated with thin stick.

are shown in Fig. 9.2. In order to visualize this a little bit better, we represent the B-S framework with a thin stick so that we can easily see the Li and halide positions. It is not out of our expectation to find the general likeness between those diagrams, although there are indeed some differences in, for example, the arrangement patterns of Li and X ions.

Table 9.1 summarizes the lattice parameters and the fractional coordinates of the inequivalent Li and X atoms for the $\text{Li}_{7.5}\text{B}_{10}\text{S}_{18}\text{X}_{1.5}$ with $\text{X} = \text{Cl}$, Br , I . It is worth mentioning that the lattice parameters are calculated to be around 0.2 - 0.5 Å different from the experimental values. The slight discrepancy is perhaps due to the lattice distortion when transforming from disordered to ordered representations. In particular, the converged results of lattice parameters are somewhat surprising given the radius consideration. Intuitively, the lattice volume would gradually expand from the composition with Cl to the one with I. Further examination is required to provide

a more detailed explanation.

Table 9.1: Summary of lattice parameters and inequivalent fractional positions of Li and X ions for the most stable ordered phases of $\text{Li}_{7.5}\text{B}_{10}\text{S}_{18}\text{X}_{1.5}$ with $\text{X} = \text{Cl}, \text{Br}, \text{I}$. The experiment data were taken from Kaup *et al.*³

		X = Cl (cal./exp.)	X = Br (cal./exp.)	X = I (cal./exp.)
a (Å)		20.96/21.16	20.88/21.21	21.09/21.32
b (Å)		21.66/22.23	21.19/21.25	21.40/21.27
c (Å)		16.02/16.13	16.07/16.26	16.08/16.21
$\alpha = \gamma$ (deg)		90.00/90.00	90.00/90.00	90.00/90.00
β (deg)		128.75/128.92	128.43/128.82	128.70/128.77
Volume (Å ³)		5672.62/5638.31	5572.37/5708.07	5664.13/5731.36

		Fractional coordinates (x, y, z)		
Atom	Wyck	X = Cl (cal.)	X = Br (cal.)	X = I (cal.)
Li(1)	4 e	(0.000, 0.830, 0.250)	(0.000, 0.834, 0.250)	(0.000, 0.833, 0.250)
Li(2)	4 e	(0.000, 0.063, 0.250)	(0.000, 0.067, 0.250)	(0.000, 0.066, 0.250)
Li(3)	8 f	(0.666, 0.446, 0.453)	(0.672, 0.445, 0.456)	(0.669, 0.445, 0.455)
Li(4)	8 f	(0.427, 0.143, 0.724)	(0.407, 0.101, 0.741)	(0.397, 0.092, 0.723)
Li(5)	8 f	(0.375, 0.021, 0.587)	(0.396, 0.047, 0.548)	(0.389, 0.038, 0.532)
Li(6)	8 f	(0.315, 0.374, 0.783)	(0.327, 0.376, 0.792)	(0.325, 0.374, 0.789)
Li(7)	4 c	(0.250, 0.250, 0.000)	(0.250, 0.250, 0.000)	(0.250, 0.250, 0.000)
Li(8)	8 f	(0.357, 0.259, 0.555)	(0.367, 0.247, 0.557)	(0.359, 0.252, 0.555)
Li(9)	8 f	(0.036, 0.267, 0.062)	(0.048, 0.281, 0.047)	(0.055, 0.283, 0.048)
X(1)	8 f	(0.035, 0.311, 0.383)	(0.028, 0.341, 0.404)	(0.028, 0.345, 0.403)
X(2)	4 e	(0.000, 0.450, 0.250)	(0.000, 0.482, 0.250)	(0.000, 0.503, 0.250)

The experimental report also includes analysis of the neutron scattering in terms of the pair distribution function, which we have reproduced in Fig. 9.3(a). To examine our idealized structures, the pair distribution can also be simulated from our MD data according to the expression

$$G(r) = \frac{1}{4\pi r^2 N \rho} \left\langle \sum_{i=1}^N \sum_{j \neq i}^N \delta(r - |\mathbf{R}_i(t) - \mathbf{R}_j(t)|) \right\rangle_t, \quad (9.1)$$

here N is the number of ions in the simulation cell which has a number density of ρ . In practice, the summation over j includes periodic images of the simulation cell. The above form is particular for describing the correlations of distinctive ions as the terms $j = i$ are excluded from the summation. The angular brackets in the expression imply the averaging over the duration of the time frame t . For our purpose, the difference in atomic positions indicated by $\mathbf{R}_i(t) - \mathbf{R}_j(t)$ is only calculated for motions at same time step. The finite time evolution behavior is not considered in the current calculation.

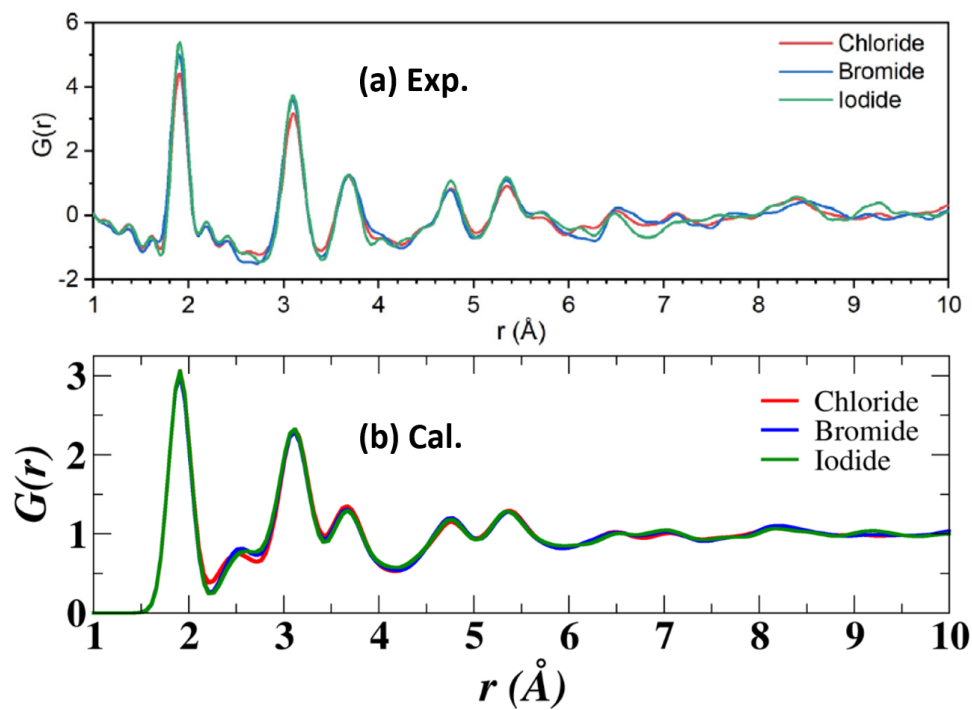


Figure 9.3: Plots of the pair distribution functions for $\text{Li}_{7.5}\text{B}_{10}\text{S}_{18}\text{X}_{1.5}$ with $\text{X} = \text{Cl}$ (red), Br (blue), I (green), comparing results deduced from (a) the experimental neutron diffraction by Kaup *et al.*³ with results (b) calculated from MD simulations at $\langle T \rangle \approx 400$ K, averaged over 30 ps of simulation time.

Figure 9.3(b) shows that the profiles of calculated pair distribution with respect to the spatial distance are remarkably similar for $\text{Li}_{7.5}\text{B}_{10}\text{S}_{18}\text{X}_{1.5}$ ($\text{X} = \text{Cl}, \text{Br}, \text{I}$). The first few main peaks located at 1.9, 2.6, 3.1, 3.7, 4.8, 5.4 Å correspond to the separation of distinctive ions that are most likely to present in these crystal structures. Comparatively, the experimental values of Kaup *et al.*³ obtained by manually digitizing the published graph shown also in Fig. 9.3(a), are 1.9, 3.1, 3.7, 4.8, 5.3 Å. Perhaps because the dominating effects are coming from the robust B-S framework, the experimental and the calculated results for the three halides, in general, are very similar. It is therefore viable to use those ordered representative models to study the properties of this group of materials.

9.4 Stability analysis

To address the likely stability of the lithium thioborate halide $\text{Li}_{7.5}\text{B}_{10}\text{S}_{18}\text{X}_{1.5}$ with $\text{X} = \text{Cl}, \text{Br}, \text{I}$, we proposed several one-to-one analogous decomposition reactions for the three materials as listed in the first column of Table 9.2. The reaction energies are determined from the simple density functional static lattice analysis for each material involved in the reactions. The positive values of the results, estimated by subtracting the left (products) from the right hand side (reactants) energies, indicate that the lithium thioborate halides are energetically more stable than the sum of the given decomposition productions for these cases. Although the present theoretical investigation is not the whole story, it does indicate the reasonable stability of the three halide materials in terms of their chemistry.

9.5 Molecular dynamics simulations for Li ions

The trajectories $\mathbf{R}_i^u(t)$ of each ion i of type u at evolution time t from molecular dynamics simulations provide us the most essential starting point to access the motions

Table 9.2: Computed energy differences ($\Delta U_{SL} = U_{SL}^P - U_{SL}^R$) between reactants (R) and products (P) for reactions indicated by the first column. All energies are given in eV units.

Reaction: $R \rightarrow P$	$\Delta U_{SL}(X = \text{Cl})$	$\Delta U_{SL}(X = \text{Br})$	$\Delta U_{SL}(X = \text{I})$
$\text{Li}_{7.5}\text{B}_{10}\text{S}_{18}\text{X}_{1.5} \rightarrow 1.5 \text{ LiX} + 6 \text{ Li} + 10 \text{ B} + 18 \text{ S}$	25.54	25.63	25.71
$\text{Li}_{7.5}\text{B}_{10}\text{S}_{18}\text{X}_{1.5} \rightarrow 1.5 \text{ LiX} + 6 \text{ Li} + 5 \text{ B}_2\text{S}_3 + 3 \text{ S}$	13.12	13.20	13.28
$\text{Li}_{7.5}\text{B}_{10}\text{S}_{18}\text{X}_{1.5} \rightarrow 1.5 \text{ LiX} + 2 \text{ Li}_3\text{BS}_3 + 4 \text{ B}_2\text{S}_3$	0.99	1.08	1.16
$\text{Li}_{7.5}\text{B}_{10}\text{S}_{18}\text{X}_{1.5} \rightarrow 1.5 \text{ LiX} + 3 \text{ Li}_2\text{S} + 5 \text{ B}_2\text{S}_3$	0.83	0.92	1.00

of the mobile Li and X ions in the lithium thioborate halides. In this work, we adapted the ideas of He *et al.*¹¹³ to determine a probability density in the form

$$P^u(\mathbf{r}) = \frac{1}{k_{\max}} \sum_{k=1}^{k_{\max}} \sum_{i \in u} \delta(\mathbf{r} - \mathbf{R}_i^u(t_k)), \quad (9.2)$$

here \mathbf{r} denotes a lattice position that a u type ion visits, k_{\max} represents the number of time steps, t_k is the sampling time. By definition, the integral of $P^u(\mathbf{r})$ through the crystal cell is the total number of u type ions N^u . In practice, the evaluation is based on the molecular dynamics trajectories in the conventional simulation cell. And the delta function in the definition is approximated by an isotropic three-dimensional Gaussian shape

$$\delta(\mathbf{s}) \approx \frac{1}{(2\pi\sigma^2)^{3/2}} e^{-s^2/2\sigma^2} \quad (9.3)$$

with σ chosen as 0.2 \AA .

Figure 9.4 shows the colored isosurfaces of constant probability values superposed on the optimized structural diagrams, plotting separately for Li in the top row and (X = Cl, Br, I) ions in the bottom row. It is evident that there are remarkably similar shapes between the three halides. By rotating the visualization to other directions, we found that most Li ions contribute to ionic current as they are observed to move extensively within the crystal along three-dimensional migration pathways. More information we can perceive is that the relatively easy conduction of Li ions in each material is attributed to the low barrier energy between neighboring sites. It is

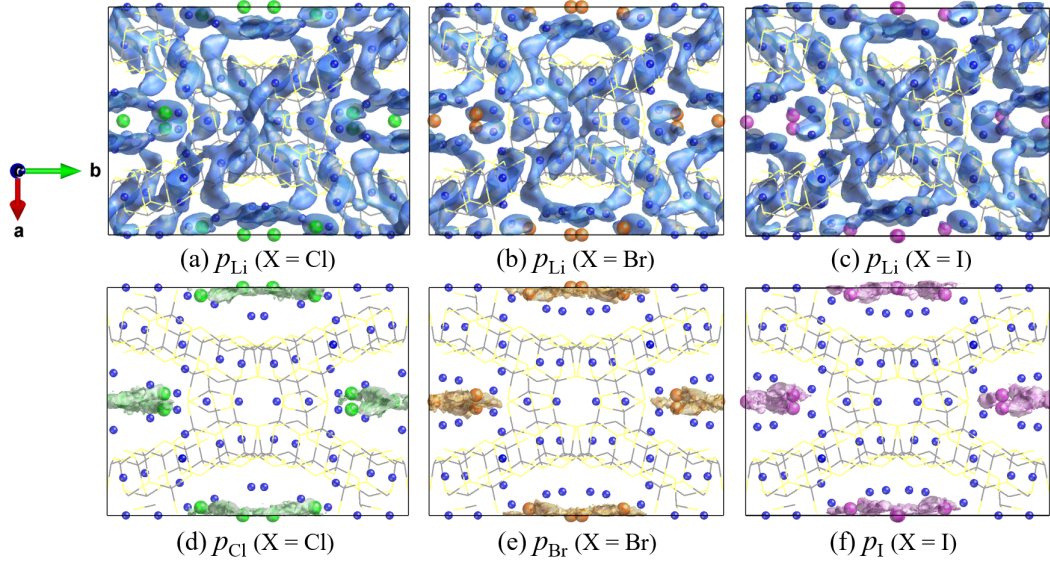


Figure 9.4: Isosurface plots of $P^u(\mathbf{r}) = 0.04\text{\AA}^{-3}$ for Li (a, b, and c) and X (d, e, and f) ions in $\text{Li}_{7.5}\text{B}_{10}\text{S}_{18}\text{X}_{1.5}$ with $X = \text{Cl}, \text{Br}, \text{I}$, visualized along the c -axis. The results are determined from molecular dynamics simulations at $\langle T \rangle = 768, 775,$ and 779 K, respectively. The $\text{B}_{10}\text{S}_{18}$ units are represented by the thin sticks.

reasonable to speculate that the disorder within the Li ion sublattice in these systems is a critical determinant to the superior Li conducting behavior. By contrast, the motions of halogens X ($X = \text{Cl}, \text{Br}, \text{I}$) are confined within the void channels of each of the crystals, presenting distribution patterns actually compatible with those disordered arrangements of X ions of experiment structures shown in Fig. 9.1.

A more quantitative picture of Li ion diffusional properties is provided by the mean squared displacements (MSD). For an MD simulation at average temperature T

$$\text{MSD}(\tau, T) = \frac{1}{N^{\text{Li}}} \left\langle \sum_{i=1}^{N^{\text{Li}}} |\mathbf{R}_i(t + \tau) - \mathbf{R}_i(t)|^2 \right\rangle_t, \quad (9.4)$$

which is related to the tracer diffusion $D_{tr}(T)$ which is defined as

$$D_{tr}(T) = \lim_{\tau \rightarrow \infty} \left(\frac{1}{6\tau} \text{MSD}(\tau, T) \right). \quad (9.5)$$

The dependence of the tracer diffusion coefficient on temperature follows an Arrhenius

behavior

$$D_{tr}(T) = D_{ref}e^{-E_a/k_B T}, \quad (9.6)$$

here k_B is Boltzmann constant, the prefactor D_{ref} and activation energy E_a are deduced from the intercept and slope of the logarithmic plot of $D_{tr}(T)$ vs $1/T$, respectively. Also, from those diffusion coefficients for various temperatures, we can approximate the conductivity of Li ions based on the Nernst-Einstein relationship

$$\sigma(T) = \frac{N^{Li}}{V} \frac{e^2 D_{tr}(T)}{k_B T H_r}, \quad (9.7)$$

where V is the volume of the simulation cell, the elemental charge $e = 1.6 \times 10^{-19}$ Coulombs for Li ions, H_r is Haven ratio typically used to estimate the coupling motions between different Li ions.

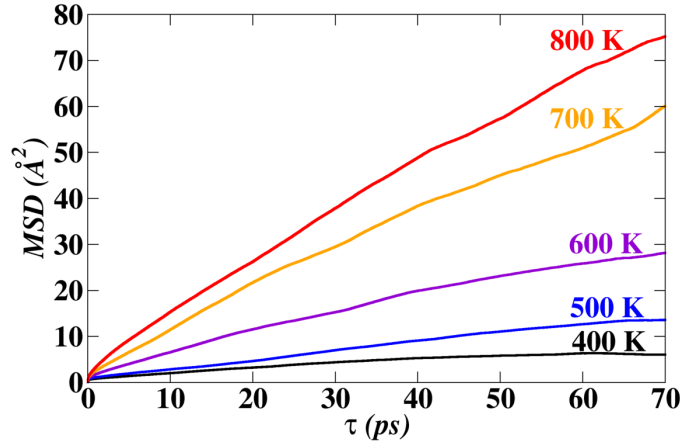


Figure 9.5: MSD plot for Li ions of $\text{Li}_{7.5}\text{B}_{10}\text{S}_{18}\text{Cl}_{1.5}$ at various simulation temperatures as indicated by the text near each curve.

Figure 9.5 shows the MSD results on $\text{Li}_{7.5}\text{B}_{10}\text{S}_{18}\text{Cl}_{1.5}$ averaged over time intervals of up to 70 ps for five different average temperatures from 400 K to 800 K. It is impressive to observe that there is appreciable Li ions migration at temperature as low as 400 K. As the temperature increases, the diffusion coefficient increases as Li ions gain more thermal energy to overcome the migration barriers to move a greater distance.

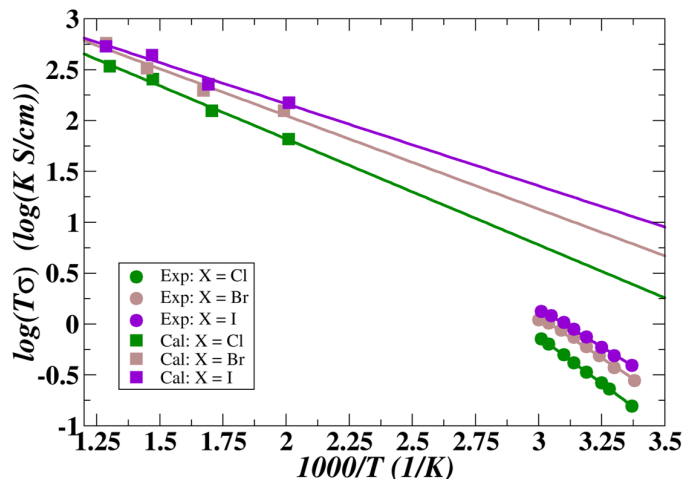


Figure 9.6: Plots of Li ion conductivity from MD simulations in comparison with experimental conductivity measurements.

Figure 9.6 presents the Li ion conductivities for the iodine, bromine, and Cl materials, estimated from the MD results, comparing with the experimental measurements reported by Kaup and co-workers.³ The general trend of the computational results is that the iodide material displays the best ionic conductivity performance, followed by the bromide and the chloride materials. The qualitative feature is consistent with the experimental results superposed on this diagram here. However, the quantitative comparison between the experiment and the calculation shows a significant discrepancy. For example, the measured room temperature ionic conductivities for the three halides are found to be about 1 mS/cm, while the simulated results are overestimated by more than a factor of 10. The partial reason for the far less agreement between the theory and the experiment can be ascribed to the simplistic approximation for the Haven ratio. The simulation results assumed $H_r = 1$, which corresponds to the notion of uncorrelated effects of Li ion migrations in the transport process. However, it is the usual case that the Li ion hopping events are not independent as observed for other classes of superionic conductors.

Since the known fact that the convergence of cross correlation term between conducting ions with different labels takes longer simulation time, it is not convenient

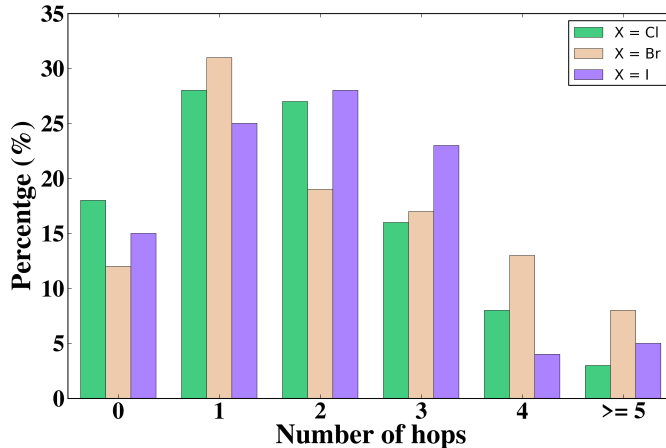


Figure 9.7: Frequency distribution of number of hopping events of Li ions in time interval of 0.5 ps for $\text{Li}_{7.5}\text{B}_{10}\text{S}_{18}\text{X}_{1.5}$ with $X = \text{Cl}$ (green), Br (brown), and I (violet). The values of vertical axes are obtained from MD simulations of 50 ps duration using primitive cell models at $\langle T \rangle = 768, 775,$ and 779 K, respectively.

to analyze the correlated motion by directly calculating the haven ratio. One practical method is to track the motions of each migrating Li ion and tabulate the time of the ion arriving at a new vacant equilibrium site of the optimized lattice. The corresponding ground state configuration of $\text{Li}_{7.5}\text{B}_{10}\text{S}_{18}\text{X}_{1.5}$ ($X = \text{Cl}, \text{Br}, \text{I}$) contains nine distinctive host sites for Li ions, ranging from $\text{Li}(1)$ to $\text{Li}(9)$ as the positions listed in Table 9.1. For the convenience of later analysis, we mark those $\text{Li}(1)$ -type perfect lattice sites at Wyckoff position $4e$ with labels s_1^i ($i = 1, 2, 3, 4$). For the case of this particular space group, the number of symmetrically equivalent sites of each unique site type is reduced by half in a primitive cell setting. The label definition for other host sites works in the same way. At each time step of MD simulations, each individual Li ion was always appropriately labeled for the sake of tracking their migration pathways within the crystal. Considering it is rare for the Li ion to get the exact position of a host site, the arrival time of a Li ion was indicated when it reached the shortest distance from its equilibrium site within a sphere of 1 \AA about that site. By definition, the difference between two consecutive arrival times measures the time the Li ion takes for a hopping event to occur. The arrival times and related hopping

details are accumulated for all the Li ions in the simulation cell. The collected information allows us to analyze, for example, how many hopping events occurred within a certain time period. Based on this model, we examined 100 time intervals of 0.5 ps, and each was analyzed in terms of the number of hopping events that occurred. The resulting histogram of numbers of Li ion hops, comparing between the three halides, is presented in Fig. 9.7. The figure shows that for each material case, the percentage of time intervals experiencing 0 or 1 hops is less than the intervals experiencing 2 or more hops, suggesting the fast Li ion diffusion in $\text{Li}_{7.5}\text{B}_{10}\text{S}_{18}\text{X}_{1.5}$ ($\text{X} = \text{Cl}, \text{Br}, \text{I}$) are likely attributed to the multi-ion concerted migration mechanism.

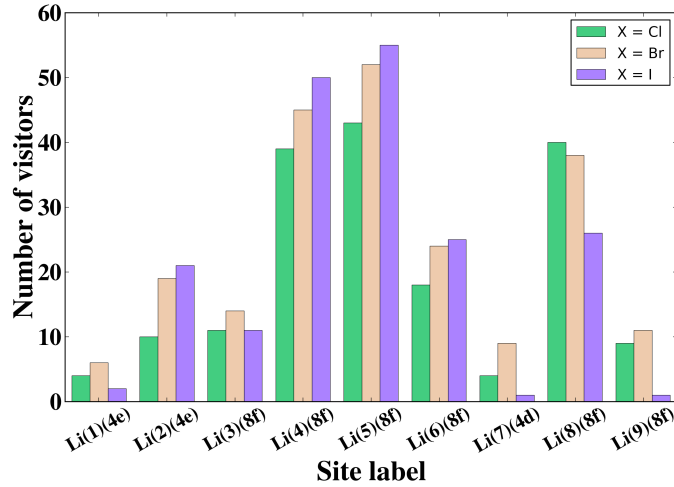


Figure 9.8: Histograms of the number of visitors of each host site type with label indicated on the horizontal axes for $\text{Li}_{7.5}\text{B}_{10}\text{S}_{18}\text{X}_{1.5}$ with $\text{X} = \text{Cl}$ (green), Br (brown), and I (violet). The values of vertical axes are obtained from MD simulations of 50 ps duration using primitive cell models at $\langle T \rangle = 768, 775, \text{ and } 779 \text{ K}$, respectively.

It also would be interesting to explore the degree of involvement of the host Li sites in transporting Li ions in each material. For this purpose, we accumulated the occupation times of different unique sites for each material and produced the histogram plot as shown in Fig. 9.8. To be specific, the number of visitors of a given site type counts when the mobile Li ions hop into any of its equivalent sites from a nearest-neighbor site. In this sense, the comparisons of Fig. 9.8 indicate that the Li(4) and Li(5) type sites, located within the large void cavities, are most attractive

as they are visited by plenty of Li ions. To gain an insight into the vacancy formation sites, we calculated the vacancy energy for each distinct host site of Li ions. The results, obtained by relaxing the ideal lattice geometry with one absent Li ion on the vacant position and one compensating charge of opposite sign, are summarized in Table 9.3.

Table 9.3: Vacancy energies E_v (in eV/formula unit) for unique vacancy sites in $\text{Li}_{7.5}\text{B}_{10}\text{S}_{18}\text{X}_{1.5}$ ($\text{X} = \text{Cl}, \text{Br}, \text{and I}$). The zero of energy was taken to be the lowest vacancy energy.

Site	Wyck	E_v (X = Cl)	E_v (X = Br)	E_v (X = I)
Li(1)	4 e	0.166932	0.147793	0.136162
Li(2)	4 e	0.141463	0.095707	0.100984
Li(3)	8 f	0.177265	0.138379	0.127997
Li(4)	8 f	0.000030	0.000000	0.010037
Li(5)	8 f	0.000000	0.000002	0.010034
Li(6)	8 f	0.175595	0.144719	0.133384
Li(7)	4 c	0.212470	0.176451	0.159958
Li(8)	8 f	0.000083	0.002882	0.000000
Li(9)	8 f	0.075308	0.143022	0.129700

It is encouraging to note that those most popular sites are exactly the ones Li(4), Li(5), and Li(8) with relatively lower vacancy energies, as given in Table 9.3. On the one hand, the agreement corroborates our proposed scheme for analyzing Li ion hopping events. On the other hand, it implies that the most probable conduction path of Li ions is formed by the energetically favorable sites with approximately similar energies. Such phenomenon observed for $\text{Li}_{7.5}\text{B}_{10}\text{S}_{18}\text{X}_{1.5}$ ($\text{X} = \text{Cl}, \text{Br}, \text{and I}$) is compatible with the common features of fast ionic conductors.

Chapter 10

Conclusions

In this work, we carried out first principles modeling of a number of solid electrolyte materials intending to advance our understanding of their fundamental and technological properties, such as stability of the ideal bulk forms, the interface behavior with anodes, and the underlying conduction mechanisms of the mobile ions. In general, our computational results on each particular materials system under consideration are compatible with the experimental measurements. It is also expected that some simulation analysis on the predicated materials could provide critical insight for experimentalists for further possible investigations.

In terms of computational challenges, the first principles molecular dynamics simulation is usually limited to moderate-sized systems containing a few hundreds of atoms. Typical MD runs demand above 500000 times steps of about 2 fs integration interval to achieve converged statistics of diffusion processes. Even with the aid of parallel supercomputers, it may take weeks or months to obtain sufficient sampling. Besides, the quantity of interest evaluated starting from the immediate MD output likely depends on numerical approximations. For example, the ionic conductivity is commonly deduced from the Nernst-Einstein relation without considering the correlated motions by assuming the Haven ratio $H_r = 1$. However, when coupled transport

of ions is significant, the simplification can lead to a deviation of several orders of magnitude from the experimental data. For that reason, more elaborate approaches must be applied for not missing essential physical effects. Another challenge is the systematically modeling of crystalline solids with structural disorders. Although it is straightforward to convert a crystallographic structure with fractionally occupied atomic sites to stoichiometric supercell configurations suitable for simulations, reasonable sampling strategies are required because for highly disordered phases, the number of permutations of atoms and available lattice sites may be way too high to process.

As new electrolyte materials frequently appear in the experimental literature, the established computational methods will continue to be powerful tools in comprehensively understanding the basic properties of target materials. Nevertheless, there is always plenty of space for refining the existing approaches as well as for developing innovative ones to meet more specific and realistic needs.

Appendices

Appendix A

Computational and experimental
(re)investigation of the structural
and electrolyte properties of
 $\text{Li}_4\text{P}_2\text{S}_6$, and $\text{Na}_4\text{P}_2\text{S}_6$, and
 $\text{Li}_2\text{Na}_2\text{P}_2\text{S}_6$

Computational and experimental (re)investigation of the structural and electrolyte properties of $\text{Li}_4\text{P}_2\text{S}_6$, $\text{Na}_4\text{P}_2\text{S}_6$, and $\text{Li}_2\text{Na}_2\text{P}_2\text{S}_6$

Yan Li¹, Zachary D. Hood² and N. A. W. Holzwarth¹

¹Department of Physics, Wake Forest University, Winston-Salem, North Carolina 27109, USA

²Department of Materials Science and Engineering, Massachusetts Institute of Technology, Cambridge, Massachusetts 02139, USA



(Received 28 January 2020; accepted 24 March 2020; published 21 April 2020)

The ionic materials $\text{Li}_4\text{P}_2\text{S}_6$ and $\text{Na}_4\text{P}_2\text{S}_6$ are both based on the same building blocks of the dimer ions $(\text{P}_2\text{S}_6)^{4-}$. Motivated by new experimental structural and ion conductivity studies, we computationally examine this family of materials, finding $\text{Na}_4\text{P}_2\text{S}_6$ and its modification $\text{Li}_2\text{Na}_2\text{P}_2\text{S}_6$ to be promising Na ion electrolytes. Using first-principles calculations based on density functional theory and density functional perturbation theory within the harmonic phonon approximation, we show that vibrational effects provide nontrivial contributions to the structural stabilization of these materials. Computed nonresonant Raman phonon spectra and temperature-dependent ionic conductivity for $\text{Na}_4\text{P}_2\text{S}_6$ are both found to be in reasonable agreement with experiment. First-principles analysis of ionic conductivity in both $\text{Na}_4\text{P}_2\text{S}_6$ and $\text{Li}_2\text{Na}_2\text{P}_2\text{S}_6$ indicates that Na ions move primarily within the interlayer region between the $(\text{P}_2\text{S}_6)^{4-}$ layers, efficiently proceeding via direct or indirect hops between vacancy sites, with indirect processes involving intermediate interstitial sites.

DOI: [10.1103/PhysRevMaterials.4.045406](https://doi.org/10.1103/PhysRevMaterials.4.045406)

I. INTRODUCTION

There is growing interest in developing all-solid-state batteries for stable and efficient energy storage applications. For example, a recent review [1] notes that inorganic solid electrolytes “lie at the heart of the solid-state battery concept,” stressing the importance of basic research for expanding our knowledge of the fundamental properties of these materials. As particular examples, alkali metal hexathiohypodiphosphate materials $\text{Li}_4\text{P}_2\text{S}_6$ and $\text{Na}_4\text{P}_2\text{S}_6$ and their modifications are of interest to the effort of developing all solid-state batteries. While $\text{Li}_4\text{P}_2\text{S}_6$ has been found to have very small ionic conductivity [2–4], and is cited [5] as a decomposition product in the preparation of lithium thiophosphate electrolytes, $\text{Na}_4\text{P}_2\text{S}_6$ [6] appears to be a competitive electrolyte for sodium ion batteries. Recent experiments [6,7] have provided new structural and electrochemical results which prompt a reexamination of previous computational studies on these materials [2,8] and also prompt an investigation of their modifications, resulting in the prediction of a new promising Na ion electrolyte having the composition $\text{Li}_2\text{Na}_2\text{P}_2\text{S}_6$.

$\text{Li}_4\text{P}_2\text{S}_6$ and $\text{Na}_4\text{P}_2\text{S}_6$ have very similar chemical and structural properties based on the same building blocks of $(\text{P}_2\text{S}_6)^{4-}$ (hexathiohypodiphosphate) complex ions which have D_{3d} point symmetry and typically align along the crystallographic *c* axis. The crystal structure of $\text{Li}_4\text{P}_2\text{S}_6$ was analyzed by Mercier *et al.* in 1982 [9], finding a disordered lattice with space group $P6_3/mcm$ (No. 193) [10]. Hood *et al.* [2] showed that the disordered Mercier structure could be explained by the energetic insensitivity of the system to the detailed layer arrangements of the $(\text{P}_2\text{S}_6)^{4-}$ complex ions. In that paper, the disordered Mercier structure was categorized in terms of the placements of the $(\text{P}_2\text{S}_6)^{4-}$ ions along the hexagonal *c* axes using the labels \mathbf{P}_\uparrow and \mathbf{P}_\downarrow . For the few

example structures we investigated, the lowest-energy structures were those with 50% \mathbf{P}_\uparrow and 50% \mathbf{P}_\downarrow , while the structure with 100% \mathbf{P}_\uparrow has the higher-symmetry space group $P\bar{3}1m$ (No. 162) [10], with an energy of 0.03 eV per formula unit higher than the lowest-energy structures. More recently, Neuberger *et al.* [7] showed that it is possible to prepare more highly crystalline samples. These samples, when analyzed with a combination of x-ray analysis and nuclear magnetic resonance (NMR) measurements, were found to have an ordered structure with two inequivalent P sites and to be characterized with the space group $P321$ (No. 150) [10] with three formula units per unit cell. This new analysis provides an explanation of how twinning and poor crystallinity may result in samples consistent with the disordered Mercier structure [9]. The Neuberger analysis supersedes the incorrect analysis of Dietrich *et al.* [3] and approximately corresponds to a Mercier-type structure with $\frac{1}{3}\mathbf{P}_\uparrow$ and $\frac{2}{3}\mathbf{P}_\downarrow$. However, for reasons discussed below, we will reference the Neuberger structure in terms of the $P\bar{3}m1$ space group (No. 164) [10].

Meanwhile, the analogous sodium ion material $\text{Na}_4\text{P}_2\text{S}_6$ was synthesized by Kuhn *et al.* [11] and shown to be characterized by an ordered based-centered monoclinic structure with space group $C2/m$ (No. 12) [10]. Simulations by Rush *et al.* [8] suggested that the $C2/m$ structure may be metastable with respect to lower-energy configurations analogous to the $\text{Li}_4\text{P}_2\text{S}_6$ materials. However, recent experimental results of Hood *et al.* [6] on $\text{Na}_4\text{P}_2\text{S}_6$ find its ground-state structure to be the $C2/m$ structure of Kuhn [11] and also find that it has very promising ionic conductivity.

In view of the new experimental findings, this paper reports a reexamination of our earlier work on $\text{Li}_4\text{P}_2\text{S}_6$ and $\text{Na}_4\text{P}_2\text{S}_6$ and also considers a possible mixed-ion material with the composition $\text{Li}_2\text{Na}_2\text{P}_2\text{S}_6$. Our goal is to determine whether modified and enhanced computational methods can explain

the observed ground-state structures of these materials and to explore mechanisms of Na ion conductivity in $\text{Na}_4\text{P}_2\text{S}_6$ and $\text{Li}_2\text{Na}_2\text{P}_2\text{S}_6$. The remainder of the paper is organized as follows. Section II presents the formalism and computational methods used in this work. Section III presents the computational results for the structural analysis of $\text{Li}_4\text{P}_2\text{S}_6$ and $\text{Na}_4\text{P}_2\text{S}_6$, including the static lattice results in Sec. III A and the effects of phonon energies within the harmonic approximation in Sec. III B. Section III B 1 presents the phonon dispersion curves and comparison between the calculated and measured Raman phonon spectrum for $\text{Na}_4\text{P}_2\text{S}_6$, while Sec. III B 2 presents the phonon dispersion curves for $\text{Li}_4\text{P}_2\text{S}_6$. Results for the phonon contributions to the stabilization of the crystalline phases of both $\text{Na}_4\text{P}_2\text{S}_6$ and $\text{Li}_4\text{P}_2\text{S}_6$ are presented in Sec. III C. Section IV presents results on the most stable structure of $\text{Li}_2\text{Na}_2\text{P}_2\text{S}_6$. Section V examines the Na ion conductivity properties of $\text{Na}_4\text{P}_2\text{S}_6$ and $\text{Li}_2\text{Na}_2\text{P}_2\text{S}_6$. Section VI contains the discussion and conclusions.

II. CALCULATIONAL METHODS

A. General formalism and software implementation

The calculations in this study were based on density functional theory (DFT) [12,13] and density functional perturbation theory (DFPT) [14–18] implemented in the ABINIT [19] and QUANTUM ESPRESSO [20] codes, using the projector augmented plane-wave (PAW) [21] method and using atomic data sets generated with the ATOMPAW code [22]. These data sets were generated with the most recent version of the ATOMPAW code which has been modified for better compatibility with the QUANTUM ESPRESSO formalism [23]. The software packages VESTA [24] and XCRYSDEN [25] were used for visualizations of structural configurations and FINDSYM [26] helped with the space-group analysis of the structures. The MERCURY software package [27] was used to simulate x-ray patterns from calculation results and from published structural data. Additionally, the Bilbao Crystallographic Server [28] was used to help with the symmetry analysis.

Our previous simulation studies of ion conducting materials [2,8] used the exchange-correlation functional of the local density approximation (LDA) [29] because of its generally good representation of vibrational properties of materials [30]. However, in this work, it is necessary to reexamine these previous simulations. Encouraged by recent reports by Petretto *et al.* [31] and by He *et al.* [32] in simulating structural and vibrational spectra for a wide range of inorganic materials in reasonable agreement with experiment, we were motivated to adopt the exchange-correlation functional based on a modified generalized gradient formulation known as PBEsol [33].

B. Formalism for evaluating phase stability

1. First-principles estimation of the Helmholtz free energy

For a system held at constant temperature T and volume V , the equilibrium state is described by a minimum of the Helmholtz free-energy function $F(T, V)$. Within the framework of the Born-Oppenheimer approximation [34] and the harmonic phonon approximation [14,35], $F(T)$ is determined

by a sum of two terms¹

$$F(T) = F_{\text{SL}}(T) + F_{\text{vib}}(T), \quad (1)$$

where the subscript “SL” denotes the static lattice energy at equilibrium and the subscript “vib” denotes the harmonic phonon contribution. For insulating materials in their ground state,

$$F_{\text{SL}}(T) \approx U_{\text{SL}}, \quad (2)$$

the static lattice Helmholtz free energy is approximately temperature independent and determined by the internal energy U_{SL} which is well approximated by the total energy of the system determined from DFT [12,13], optimized with respect to the crystalline lattice vectors and atomic positions. In fact, our previous simulation studies of the materials [2,8] considered only this static lattice contribution. In this work, U_{SL} was evaluated using both ABINIT using a plane-wave cutoff for representing the valence wave functions of $|\mathbf{k} + \mathbf{G}|^2 \leq 50$ Ry and QUANTUM ESPRESSO using a slightly larger plane-wave cutoff of $|\mathbf{k} + \mathbf{G}|^2 \leq 64$ Ry. Here, \mathbf{k} and \mathbf{G} represent an electronic wave vector and reciprocal lattice vector, respectively. For calculations using primitive unit cells, the Brillouin zone sampling of the electronic Bloch wave vector \mathbf{k} used Monkhorst-Pack grids [36] of $3 \times 3 \times 4$ for the $P\bar{3}m1$ structure and $6 \times 6 \times 6$ for the $C2/m$ and $P\bar{3}1m$ structures. For calculations using supercells, the Brillouin zone sampling was adjusted accordingly.

For evaluating the contribution to the Helmholtz free energy due to phonon vibrations in the harmonic phonon approximation [14] we use DFPT which has been implemented in both ABINIT and QUANTUM ESPRESSO. We follow a procedure similar to that described in several references including one by Howard *et al.* [37], as summarized briefly as follows. The harmonic phonon approximation is based on the assumption that it is sufficiently accurate to describe variations of the equilibrium atomic geometry of the static lattice by a Taylor series of small deviations in the atomic displacements of U_{SL} up to quadratic order. This approximation does not include any effects of thermal expansion, and the vibrational frequencies derived from the analysis are independent of temperature. The corresponding vibrational Helmholtz free energy $F_{\text{vib}}(T)$ is explicitly given by the equation

$$F_{\text{vib}}(T) = \int_0^\infty d\omega f_{\text{vib}}(\omega, T), \quad (3)$$

where the weighted phonon density of states factor $f_{\text{vib}}(\omega, T)$ is defined as [35]

$$f_{\text{vib}}(\omega, T) = k_B T \ln \left[2 \sinh \left(\frac{\hbar\omega}{2k_B T} \right) \right] g(\omega). \quad (4)$$

Here, k_B is the Boltzmann constant and $g(\omega)$ denotes the phonon density of states normalized to $3N$ for a material with N atoms in the unit cell. The weighted phonon density of states factor $f_{\text{vib}}(\omega, T)$ is derived from the distribution

¹For notational simplicity, the Helmholtz free energy is written $F(T)$, suppressing the volume dependence in order to focus on the temperature dependence.

of quantum mechanical harmonic oscillator states [35]. In order to assess the contributions of various phonon modes to the vibrational free energy, it is also convenient to define an integrated weighted phonon density of states factor

$$f_{\text{vib}}^{\text{int}}(\omega, T) \equiv \int_0^\omega f_{\text{vib}}(\omega', T) d\omega'. \quad (5)$$

The phonon density of states $g(\omega)$ is determined from a knowledge of the frequencies of the normal modes of vibration $\omega_\nu(\mathbf{q})$ as a function of phonon wave vector \mathbf{q} :

$$g(\omega) = \frac{V}{(2\pi)^3} \int d^3q \sum_{\nu=1}^{3N} \delta(\omega - \omega_\nu(\mathbf{q})), \quad (6)$$

where the integral is taken throughout the unit cell. For our three-dimensional systems, the integral of Eq. (6) is equal to the total number of normal modes of the evaluation cell ($3N$) which is 108, 36, and 36 for the $P\bar{3}m1$, $C2/m$, and $P\bar{3}1m$ structures, respectively.

2. Normal-mode analysis

The normal-mode frequencies $\omega_\nu(\mathbf{q})$ are found by solving eigenvalue problems of the form

$$M_s \omega_\nu^2(\mathbf{q}) u_{si}^v(\mathbf{q}) = \sum_{tj} \tilde{C}_{si,tj}(\mathbf{q}) u_{tj}^v(\mathbf{q}). \quad (7)$$

Here, the indices s, t, \dots denote atoms within the unit cell and the indices i, j, \dots denote Cartesian directions (x, y, z). M_s denotes the atomic mass of the atom at site s . The matrix $\tilde{C}_{si,tj}(\mathbf{q})$ is the Fourier transform of the matrix of second derivatives of the static lattice energy U_{SL} with respect to small displacements of atoms in the unit cell. Explicitly, the analytic part of the second derivative matrix is given by

$$\tilde{C}_{si,tj}(\mathbf{q}) = \sum_m \frac{\partial^2 U_{\text{SL}}(\{\mathbf{u}\})}{\partial u_{si}(\mathbf{R}_l) \partial u_{tj}(\mathbf{R}_m)} e^{-i\mathbf{q} \cdot (\mathbf{R}_l - \mathbf{R}_m)}, \quad (8)$$

where \mathbf{R}_l and \mathbf{R}_m represent the positions of the l th and the m th unit cells in the crystal, respectively. Because of the translational symmetry of the lattice, the summation over \mathbf{R}_m in Eq. (8) spans all translation vectors of the unit cell and the result does not depend upon \mathbf{R}_l . The parameters $u_{si}(\mathbf{R}_l)$ represent the displacement in the i direction of atom s from its equilibrium position ($\boldsymbol{\tau}_s + \mathbf{R}_l$) in cell l . For a normal-mode analysis of the system characterized by phonon wave vector \mathbf{q} , $u_{si}(\mathbf{R}_l)$ is related to the normal-mode amplitude $u_{si}^v(\mathbf{q})$ according to

$$u_{si}(\mathbf{R}_l) = u_{si}^v(\mathbf{q}) e^{i\mathbf{q} \cdot \mathbf{R}_l}. \quad (9)$$

Within the framework of DFPT, Eq. (8) can be evaluated as in terms of the displacement amplitudes $u_{si}(\mathbf{q})$ according to

$$\tilde{C}_{si,tj}(\mathbf{q}) = \frac{\partial^2 U_{\text{SL}}}{\partial u_{si}^*(\mathbf{q}) \partial u_{tj}(\mathbf{q})}. \quad (10)$$

For ionic materials in the $\mathbf{q} \rightarrow 0$ limit, in addition to the analytic contribution to the dynamical matrix (10), effects due to the coupling of ion motions to long-wavelength electromag-

netic fields [14–18,34,38] must be taken into account. These long-wavelength electromagnetic field couplings lead to the frequency splitting of transverse optical (TO) and longitudinal optical (LO) modes at $\mathbf{q} = 0$ and for hexagonal and other layered geometries as considered in this work, they lead to apparent discontinuities in the phonon dispersion curves $\omega_\nu(\mathbf{q})$ for some of the normal modes [38].

It is convenient to define an atomic weight factor which represents the contribution of each atom type a among the sites s to the mode ν according to

$$W_a^v(\mathbf{q}) \equiv \sum_{s \in a, i} |e_{si}^v(\mathbf{q})|^2, \quad (11)$$

where the normalized eigenvectors are defined according to

$$e_{si}^v(\mathbf{q}) = \sqrt{M_s} u_{si}^v(\mathbf{q}) \quad \text{where} \quad \sum_{si} |e_{si}^v(\mathbf{q})|^2 = 1. \quad (12)$$

Using atomic weight factors given by Eq. (11) for each normal mode, a projected density of phonon modes function (PJIDOS) for each atomic type can then be defined according to

$$g^a(\omega) \equiv \frac{V}{(2\pi)^3} \int d^3q \sum_{\nu=1}^{3N} (\delta(\omega - \omega_\nu(\mathbf{q})) W_a^v(\mathbf{q})). \quad (13)$$

Defined in this way, it is apparent that

$$\sum_a g^a(\omega) = g(\omega). \quad (14)$$

In practice, it is of interest to examine the dispersion of the normal-mode frequencies $\omega_\nu(\mathbf{q})$ plotted along various lines within the Brillouin zone. In order to facilitate analysis of the phonon dispersion curves $\omega_\nu(\mathbf{q})$ and projected densities of states $g^a(\omega)$ functions, both ABINIT and QUANTUM ESPRESSO use interpolations based on Eq. (8) evaluated from the DFPT results of the unique \mathbf{q} points on a coarser Brillouin zone sampling grid. In this work the coarse Brillouin zone sampling grids for the phonon wave vectors \mathbf{q} were based on Monkhorst-Pack grids [36] using $3 \times 3 \times 4$ for the $P\bar{3}m1$ structure and $3 \times 3 \times 3$ for the $C2/m$ and $P\bar{3}1m$ structures. All of these quantities provide insight into the factors which contribute to minimizing the Helmholtz free energy [Eq. (1)] which thus determine the most stable phase at any given temperature.

3. Analysis of nonresonant Raman spectra

For purposes of validation, it is helpful to compare computed and measured results whenever possible. In this case, nonresonant Raman spectra have been measured for samples of $\text{Na}_4\text{P}_2\text{S}_6$ [6]. Furthermore, with an updated version of ABINIT [39], it is now possible to make a first-principles estimate of Raman spectra within the PAW formalism [21], although restricted only to the local density approximation (LDA) [29] exchange-correlation functionals. Accordingly, for this portion of the calculation only, we used atomic data sets generated by ATOMPAW [22] with the LDA exchange-correlation functions. Past experience [40] shows that this functional generally gives excellent results for phonon frequencies while systematically underestimating lattice equilibrium lattice constants in terms of agreement with experimental measurements.

There have been a number of papers in the literature detailing the equations for first-principles estimations of Raman spectra. In this work we follow the work and approximate the notation of Umari *et al.* [41], Veithen *et al.* [42], and Prosandeev *et al.* [43]. We assume that the sample is composed of randomly oriented crystals and that the measured spectrum is unpolarized. For the Stokes shifted spectrum with an assumed Lorentzian line shape, the Raman intensity $I(\omega)$ as a function of frequency ω can be expressed according to

$$I(\omega) = \sum_{\nu} \left\langle \frac{d\sigma}{d\Omega} \right\rangle^{\nu} \frac{\Gamma^{\nu}}{(\omega - \omega_{\nu})^2 + \Gamma^{\nu 2}}. \quad (15)$$

Here, the sum over ν includes all of the Raman active normal modes with frequencies ω_{ν} . Γ^{ν} represents a linewidth parameter that is estimated empirically. The orientationally averaged Raman power cross section is given by [41]

$$\left\langle \frac{d\sigma}{d\Omega} \right\rangle^{\nu} = \mathcal{V} \frac{\hbar(\omega_I - \omega_{\nu})^4 [n_{\nu}(T) + 1]}{2\omega_{\nu} c^4} |\langle \alpha_{ij}^{\nu} \rangle|^2. \quad (16)$$

Here, \mathcal{V} represents the volume of the scattering sample, c is the speed of light, ω_I denotes the frequency of the incident laser light, and $n_{\nu}(T)$ represents the temperature-dependent Bose-Einstein distribution of the mode ν :

$$n_{\nu}(T) = \frac{1}{e^{\hbar\omega_{\nu}/k_B T} - 1}. \quad (17)$$

The Raman matrix element for scattered light direction i and incident light direction j for mode ν is given in terms of the displacement derivative of the electronic dielectric matrix ϵ_{ij}^{∞} according to

$$\alpha_{ij}^{\nu} = \frac{\sqrt{\mathcal{V}}}{4\pi} \sum_{sk} \frac{\partial \epsilon_{ij}^{\infty}}{\partial \tau_{sk}} u_{sk}^{\nu}. \quad (18)$$

Here, the summation goes over all atoms s in the unit cell and all Cartesian directions k . τ_{sk} denotes the k th component of the equilibrium position of atom s within a unit cell and u_{sk}^{ν} denotes the k th component of atom s of phonon eigenvector of Eq. (7) evaluated for $\mathbf{q} = 0$. The orientational averaging can be expressed in terms of invariants of $|\langle \alpha_{ij}^{\nu} \rangle|^2$ according to [43,44]

$$|\langle \alpha_{ij}^{\nu} \rangle|^2 = \frac{1}{30} (10G_{\nu}^{(0)} + 5G_{\nu}^{(1)} + 7G_{\nu}^{(2)}), \quad (19)$$

where

$$\begin{aligned} G_{\nu}^{(0)} &= \frac{1}{3} (\alpha_{xx}^{\nu} + \alpha_{yy}^{\nu} + \alpha_{zz}^{\nu})^2 \\ G_{\nu}^{(1)} &= \frac{1}{2} ((\alpha_{xy}^{\nu} - \alpha_{yx}^{\nu})^2 + (\alpha_{xz}^{\nu} - \alpha_{zx}^{\nu})^2 + (\alpha_{yz}^{\nu} - \alpha_{zy}^{\nu})^2) \\ G_{\nu}^{(2)} &= \frac{1}{2} ((\alpha_{xy}^{\nu} + \alpha_{yx}^{\nu})^2 + (\alpha_{xz}^{\nu} + \alpha_{zx}^{\nu})^2 + (\alpha_{yz}^{\nu} + \alpha_{zy}^{\nu})^2) \\ &\quad + \frac{1}{3} ((\alpha_{xx}^{\nu} - \alpha_{yy}^{\nu})^2 + (\alpha_{xx}^{\nu} - \alpha_{zz}^{\nu})^2 + (\alpha_{yy}^{\nu} - \alpha_{zz}^{\nu})^2). \end{aligned} \quad (20)$$

C. Formalism for modeling ionic conductivity

1. Nudged elastic band (NEB) calculations

As in previous work [2,8], the ‘‘nudged elastic band’’ (NEB) approach [45–47] was used to estimate the Na ion migration energy E_m . For both $\text{Na}_4\text{P}_2\text{S}_6$ and $\text{Li}_2\text{Na}_2\text{P}_2\text{S}_6$ in the $C2/m$ structure, simulations were performed on supercells constructed from primitive cells multiplied by $2 \times 1 \times 2$. In addition to simulating the energy path diagram for Na ion vacancies between adjacent host lattice sites in order to estimate E_m , this same supercell was used to estimate the formation energy E_f as the static lattice energy difference from the perfect supercell and one with a host lattice Na ion placed in an interstitial position, forming a vacancy-interstitial pair. From these results we can infer that the activation energy E_a for Na ion conductivity can be estimated as

$$E_m \leq E_a^{\text{NEB}} \leq E_m + \frac{1}{2} E_f. \quad (21)$$

Here, the upper estimate represents the case for a well-formed sample with few native vacancies, while the lower estimate represents the case for a sample with a significant population of vacancies. It is generally expected that the temperature (T) dependence of the conductivity is described by an Arrhenius relationship

$$\sigma(T) = \frac{A}{T} e^{-E_a^{\text{NEB}}/k_B T}, \quad (22)$$

where A is a temperature-independent constant and k_B denotes the Boltzmann constant.

2. Molecular dynamics simulations

First-principles molecular dynamics simulations were performed by using QUANTUM ESPRESSO [20], focusing on the investigation of Na ion diffusion in both $\text{Na}_4\text{P}_2\text{S}_6$ and $\text{Li}_2\text{Na}_2\text{P}_2\text{S}_6$. For each material, the simulations were carried out for a supercell constructed with $2 \times 1 \times 2$ conventional unit cells and eight formula units, using a minimal zero-center \mathbf{k} -point sampling grid $1 \times 1 \times 1$. The plane-wave expansion included $|\mathbf{k} + \mathbf{G}| \leq 64$ Ry and the energy tolerance of the self-consistent field was set to 10^{-8} Ry. Each simulation used a time step of $\Delta t = 2.4$ fs in a microcanonical ensemble (NVE) and the Verlet algorithm [48] was chosen to integrate the equation of motion. Since the equations of motion conserve the simulation energy E , the average temperature can be determined for each ensemble from the average kinetic energy of the simulation. Due to the temperature fluctuations within each simulation, the temperature cannot be precisely set by this procedure, but the approximate temperature can be controlled by setting the initial conditions of each simulation. This approach and choice of parameters gave good results in previous molecular dynamics studies of ionic conductors by our group [37]. Compared to the NEB approach for studying ion hops along a presumed migration pathway, the molecular dynamics simulations model the dynamics of motions of the ensemble of ions within the femtosecond timescale. Thus, it is possible to display more diffusion pathways and reveal new diffusion mechanisms.

In order to quantify the molecular dynamics results in terms of Na ion conductivity, we use the approximate treatment based on the mean-squared displacements (MSD)

of the mobile Na ions. Denoting by $\mathbf{r}_s(t)$ the trajectory of the s th ion as a function of time t , the MSD is given by

$$\text{MSD}(t, T) \equiv \frac{1}{N_{\text{Na}}} \left\langle \sum_{s=1}^{N_{\text{Na}}} |\mathbf{r}_s(t) - \mathbf{r}_s(0)|^2 \right\rangle_T. \quad (23)$$

Here, N_{Na} represents the number of Na ions in the simulation cell. The angular brackets represent an ensemble average which in practice is achieved by averaging the expression over multiple trajectories with the same time interval t [49]. The subscript T denotes the average temperature of the simulation. In the limit of long simulation times, the MSD is related to the tracer diffusion $D_{\text{tr}}(T)$ which in turn has an Arrhenius dependence on the simulation temperature T . For a three-dimensional system,

$$D_{\text{tr}}(T) = \frac{1}{6} \lim_{t \rightarrow \infty} \left(\frac{\text{MSD}(t, T)}{t} \right) = D_0 e^{-E_a^{\text{MSD}}/k_B T}. \quad (24)$$

For this system, the Nernst-Einstein relationship between the electrical conductivity and the tracer diffusion coefficient [50,51] is given by

$$\sigma(T) = \frac{N_{\text{Na}} e^2 D_{\text{tr}}(T)}{V k_B T H_r}. \quad (25)$$

Here, V represent the volume of the simulation cell and H_r denotes the Haven ratio [52,53] which provides a measure of the correlation in the motions of the conducting ions. Comparing the constant coefficients in Eqs. (24) and (22) and assuming that the two activation energies are comparable, we find the Arrhenius constants have the relationship

$$A = \frac{N_{\text{Na}} e^2 D_0}{V k_B H_r}. \quad (26)$$

Here, we see that the molecular dynamics analysis does provide an estimate of the magnitude of ionic conductivity up to the unknown Haven ratio H_r , while the NEB approach does not. In general, the activation energy E_a^{MSD} estimates the ensemble average of single ion processes, while E_a^{NEB} estimates the activation energy for hopping between idealized local minima in Na ion vacancy potential energy surface.

III. ANALYSIS OF STABLE CRYSTAL STRUCTURES OF $\text{Li}_4\text{P}_2\text{S}_6$ and $\text{Na}_4\text{P}_2\text{S}_6$

A. Computed optimized static lattice structures

Based on previous computational experience and new experimental analysis outlined in the Introduction (Sec. I), we focus on three different structures for analyzing the structural properties of $\text{Li}_4\text{P}_2\text{S}_6$ and $\text{Na}_4\text{P}_2\text{S}_6$. These are the trigonal Neuberger structure [7] analyzed for well-crystallized samples of $\text{Li}_4\text{P}_2\text{S}_6$ having three formula units per unit cell, the base-centered monoclinic Kuhn structure [11] analyzed for crystals of $\text{Na}_4\text{P}_2\text{S}_6$ having one formula unit per primitive cell, and the trigonal reference structure having space group $P\bar{3}1m$ which is based on a subgroup of the Mercier structure of $\text{Li}_4\text{P}_2\text{S}_6$ [9] having one formula unit per primitive unit cell. While the $P\bar{3}1m$ structure has not been observed for these materials, it does present a useful reference related to the $C2/m$ structure.

TABLE I. Summary of static lattice results. Lattice constants for the primitive unit cells are listed in units of Å and angles in degrees. The static lattice energy differences ΔU_{SL} are listed as eV/(formula unit) referenced to the energy of the $P\bar{3}1m$ structure.

$\text{Li}_4\text{P}_2\text{S}_6$	a	b	c	α	β	γ	ΔU_{SL}
$P\bar{3}1m^a$	10.42	10.42	6.54	90.0	90.0	120.0	0.00
$C2/m^b$	6.08	6.08	6.89	97.9	97.9	119.1	0.31
$P\bar{3}1m$	6.03	6.03	6.48	90.0	90.0	120.0	0.04
$\text{Na}_4\text{P}_2\text{S}_6$	a	b	c	α	β	γ	ΔU_{SL}
$P\bar{3}1m$	11.10	11.10	7.25	90.0	90.0	120.0	0.00
$C2/m^c$	6.51	6.51	7.52	98.5	98.5	117.6	0.00
$P\bar{3}1m$	6.45	6.45	7.13	90.0	90.0	120.0	0.09

^aCorresponding experimental values quoted from Ref. [7] are $a = b = 10.51$ Å, $c = 6.59$ Å, assuming the closely related space group $P321$.

^bLattice parameters for conventional unit cell are $a_c = 6.17$ Å, $b_c = 10.48$ Å, $c_c = 6.89$ Å, and $\beta_c = 105.8^\circ$.

^cLattice parameters for conventional unit cell are $a_c = 6.74$ Å, $b_c = 11.13$ Å, $c_c = 7.52$ Å, and $\beta_c = 106.5^\circ$. The corresponding experimental values quoted from Ref. [11] are $a_c = 6.725$ Å, $b_c = 11.222$ Å, $c_c = 7.542$ Å, and $\beta_c = 107.03^\circ$.

Table I summarizes the lattice constants and angles computed for these structures. From this table, it is apparent that the calculated structural parameters are very close to the available experimental values, differing by at most 0.1 Å and 1° for the lattice constants and angles. Figures 1(a)–1(c) show the ball and stick models of the three structures. The unique fractional coordinates are given in the Appendix.

In the course of optimizing the Neuberger structure using the experimentally analyzed [7] fractional coordinates for $\text{Li}_4\text{P}_2\text{S}_6$ as a guide, we find that the optimized structure has an additional inversion center compared with $P321$ space group, resulting in the space group $P\bar{3}1m$ (No. 164) [10]. This slightly contradicts the results of Neuberger *et al.* [7], presented in their Supplemental Materials. On the other hand, the x-ray diffraction patterns of the $P\bar{3}1m$ and $P321$ structures, which are shown in Fig. 2, appear to be very similar. In this paper we will refer to the Neuberger structure in terms of the $P\bar{3}1m$ space group.

For the centered monoclinic unit cell $C2/m$ structure of $\text{Na}_4\text{P}_2\text{S}_6$ analyzed by Kuhn *et al.* [11], it is convenient to use the primitive cell vectors (\mathbf{a} , \mathbf{b} , \mathbf{c}) which can be related to the conventional monoclinic cell parameters (a_c , b_c , c_c , β_c) according to [54,55]

$$\begin{aligned} \mathbf{a} &= \frac{1}{2}a_c\hat{\mathbf{x}} - \frac{1}{2}b_c\hat{\mathbf{y}}, \\ \mathbf{b} &= \frac{1}{2}a_c\hat{\mathbf{x}} + \frac{1}{2}b_c\hat{\mathbf{y}}, \\ \mathbf{c} &= c_c \cos \beta_c \hat{\mathbf{x}} + c_c \sin \beta_c \hat{\mathbf{z}}. \end{aligned} \quad (27)$$

Analyzed in terms of the primitive cell parameters, it is apparent from Table I and Figs. 1(b) and 1(c) that the primitive cell form of Kuhn structure is very similar to the simple hexagonal $P\bar{3}1m$ structure.

Also listed in Table I are the static lattice energies ΔU_{SL} referenced to the energy of the $P\bar{3}1m$ structure.

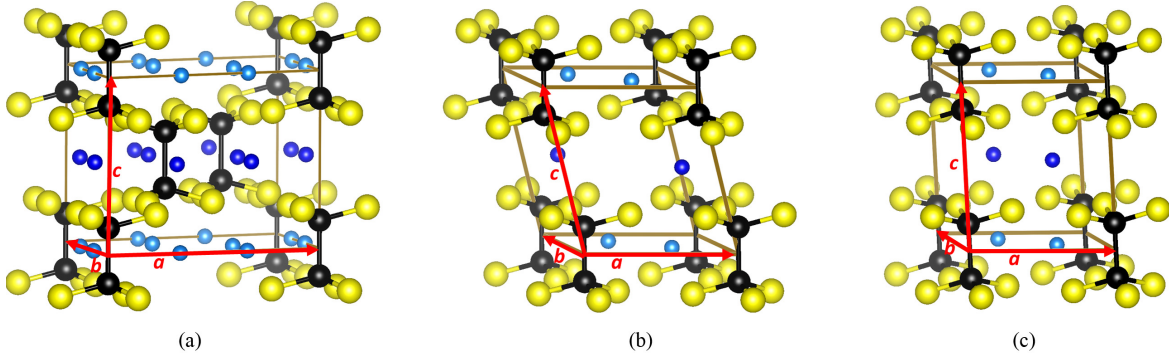


FIG. 1. Ball and stick visualizations of $\text{Li}/\text{Na}_4\text{P}_2\text{S}_6$ in the (a) $P\bar{3}m1$, (b) $C2/m$, and (c) $P\bar{3}1m$ structures showing axes of primitive cell (brown lines and red arrows) with Li/Na, P, and S represented by blue, black, and yellow balls, respectively. Two shades of blue are used to indicate the two inequivalent Li/Na sites in each structure.

The results for the materials in the $C2/m$ and $P\bar{3}1m$ structures are somewhat different from the earlier results by Rush [8] obtained using the LDA exchange-correlation functional. The current results using the PBEsol exchange-correlation functional find the lowest static lattice energy of $\text{Li}_4\text{P}_2\text{S}_6$ in the $P\bar{3}m1$ structure which is consistent with the LDA results which found the related Mercier structures to have the lowest static lattice energies. For $\text{Na}_4\text{P}_2\text{S}_6$, the PBEsol exchange-correlation functional finds the lowest static lattice energies for both the $P\bar{3}m1$ and $C2/m$ structures, while the LDA results found the stability pattern for $\text{Na}_4\text{P}_2\text{S}_6$ to be similar to that of $\text{Li}_4\text{P}_2\text{S}_6$.

B. Phonon contributions

1. $\text{Na}_4\text{P}_2\text{S}_6$

In order to further analyze the structures, we computed the phonon normal modes as explained in Sec. IIB using

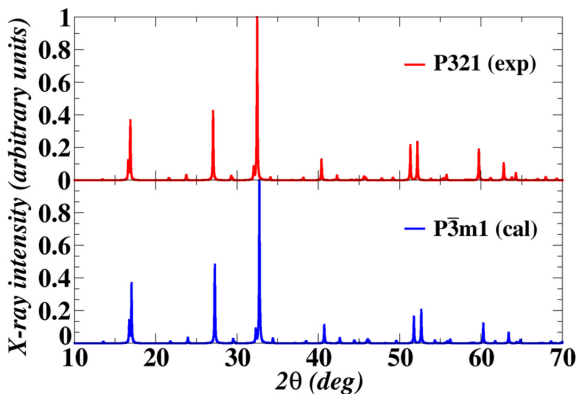


FIG. 2. Comparison of x-ray diffraction patterns for wavelength $\lambda = 1.54 \text{ \AA}$ for $\text{Li}_4\text{P}_2\text{S}_6$ generated from the MERCURY software package [27]. The upper (red) curve represents the experimental analysis [7] analyzed with the $P321$ space group; the lower (blue) curve represents the simulation results having the $P\bar{3}m1$ space group.

DFPT in both the ABINIT and QUANTUM ESPRESSO codes. While the equations in Secs. IIB1–IIB3 reference the phonon frequencies in units of rad/s , the results presented here are instead quoted as $\omega/(2\pi c)$ in units of cm^{-1} (where c denotes the speed-of-light constant). Figure 3 shows the phonon dispersion curves along with the corresponding atom type projected density of states $[g^a(\omega)]$ for $\text{Na}_4\text{P}_2\text{S}_6$, comparing results in three considered structures. For each structure, the associated path of high-symmetry \mathbf{q} points is selected as recommended for the type of Bravais lattice with diagrams shown in Figs. 3(d) and 3(e), reproduced from Ref. [56]. In view of the fact that the phonon frequencies throughout the Brillouin zone are real, each structure is predicted to be dynamically stable. The figure shows considerable similarity between the phonon dispersions $\omega_v(\mathbf{q})$ and atom type projected density of states $g^a(\omega)$, for the three structures. While vibrational amplitudes on the S sites occur throughout the frequency range, the Na amplitudes contribute to mode frequencies in the range of $0\text{--}300 \text{ cm}^{-1}$. Vibrations in the range $300\text{--}600 \text{ cm}^{-1}$ generally correspond to modes associated with the $(\text{P}_2\text{S}_6)^{4-}$ dimer ions. In particular, all three structures have two modes per formula unit which are independent of \mathbf{q} , indicating pure internal dimer vibrations. For example, for the $C2/m$ structure, these internal vibrational modes occur near the frequencies $\omega^{30}(\mathbf{q}) = 370 \text{ cm}^{-1}$ and $\omega^{32}(\mathbf{q}) = 540 \text{ cm}^{-1}$ and occur at similar frequencies for the other two structures. For the $P\bar{3}m1$ structure having three formula units per primitive cell, these internal dimer vibrations occur in two groups of three modes each, with a small splitting within each group due to a slight inequivalence of one-third of the $(\text{P}_2\text{S}_6)^{4-}$ placements. The three phonon band plots in Figs. 3(a)–3(c) display the apparent dispersion discontinuities at the Γ point mentioned in Sec. IIB2 [38].

Since the Raman spectrum of $\text{Na}_4\text{P}_2\text{S}_6$ in the $C2/m$ structure has been measured [6], it is useful to examine its Raman active phonon vibrational modes theoretically and computationally. According to group theory analysis [28] of the $\mathbf{q} = 0$ normal modes for this system which is characterized by the C_{2h} point group, the 36 vibrational modes are distributed among the 4 distinct representations according

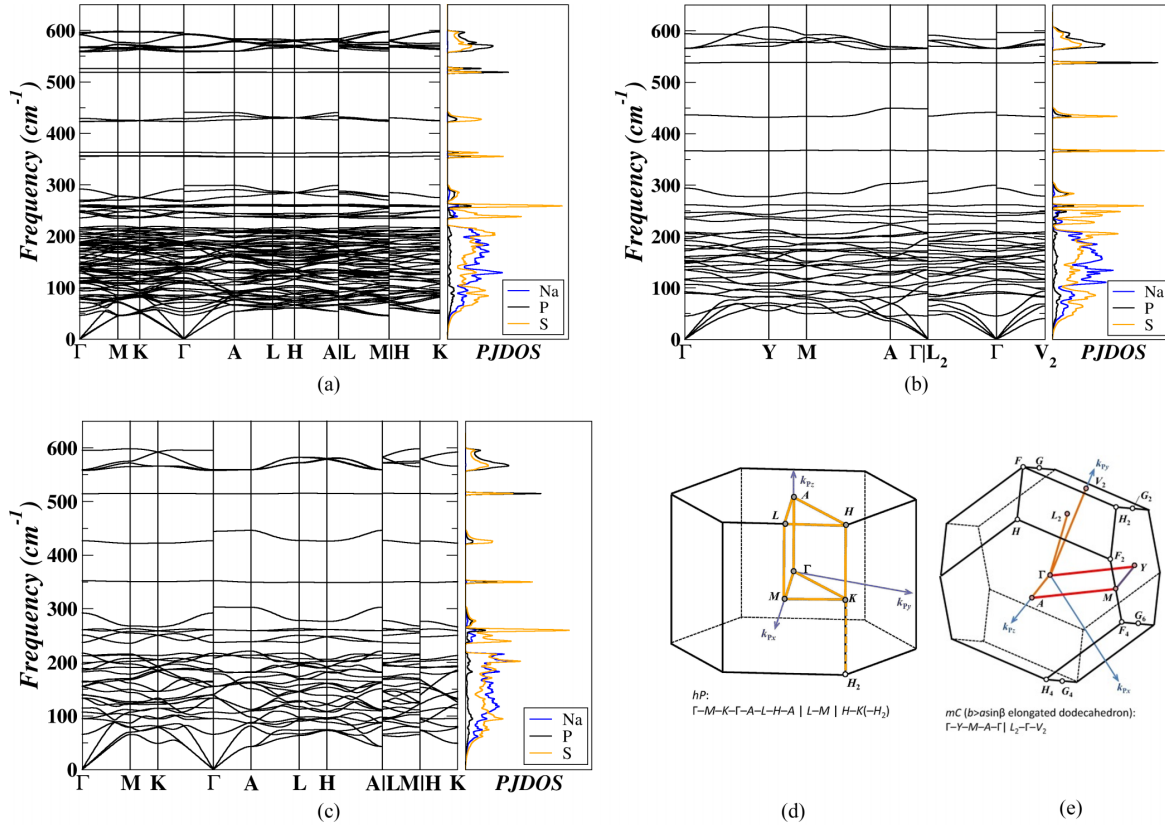


FIG. 3. For $\text{Na}_4\text{P}_2\text{S}_6$, plots of phonon normal-mode frequencies $\omega(\mathbf{q})$ in units of cm^{-1} for (a) $P\bar{3}m1$, (b) $C2/m$, and (c) $P\bar{3}1m$ structures all in their primitive unit cells plotted along various lines within the Brillouin zone. The atom type projected density of states [$g^a(\omega)$, PJDOS] are plotted using the same frequency scale along the right panel of each dispersion plot. Brillouin zone diagrams (d) for the trigonal $P\bar{3}m1$ and $P\bar{3}1m$ structures and diagram (e) for the monoclinic $C2/m$ structure are reproduced from Hinuma *et al.* in Ref. [56] with permission from the publisher.

to $9A_g + 7A_u + 9B_g + 11B_u$. Here, the infrared active modes have symmetry $7A_u + 11B_u$ and the remaining symmetries $9A_g + 9B_g$ are Raman active.

As mentioned in Sec. IIB3, the ABINIT code [39] has not yet implemented the Raman intensity analysis for the PBEsol [33] exchange-correlation functional, but only for the LDA [29] functional. Consequently, it is important to assess how sensitive are the computed phonon frequencies to the choice of exchange-correlation functional. For this test, we used PAW data sets generated with the ATOMPAW [22] code and, as a further check, also use optimized norm-conserving (ONC) developed by Haman [57] which are available from the PSEUDODOJO project [58]. In Fig. 4 we compare the spectra of Raman active mode frequencies computed using the LDA and PBEsol exchange-correlation functionals using both the PAW and ONC data sets. The results show that the phonon frequencies generated with the LDA exchange-correlation functional using the ONC and PAW data sets are essentially identical, while those generated with the PBEsol exchange-correlation functional and the PAW data sets, used in the majority of this paper, are usually shifted to lower frequencies in the range of 5–15 cm^{-1} .

Using DFPT to estimate the Raman spectra of $\text{Na}_4\text{P}_2\text{S}_6$ in the $C2/m$ structure as described in Sec. IIB3 we can make a quantitative comparison with the measured spectrum which

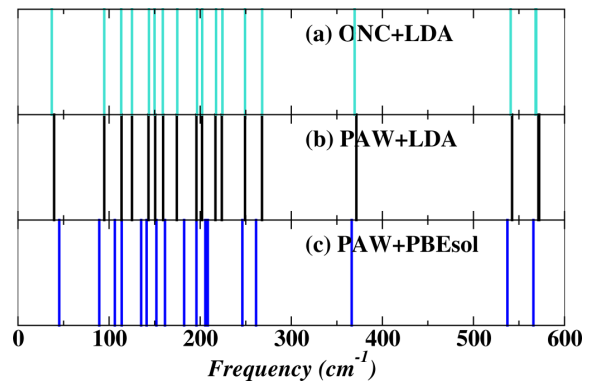


FIG. 4. Frequencies of $\mathbf{q} = 0$ Raman active modes of $\text{Na}_4\text{P}_2\text{S}_6$ in the $C2/m$ structure. Comparing results of (a) ONC, (b) PAW, both using LDA, to the results of (c) PAW using PBEsol.

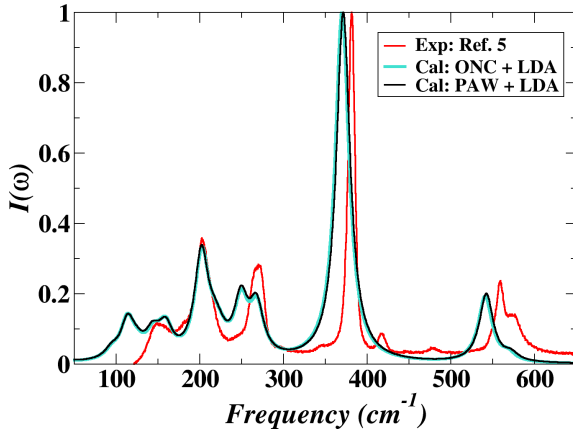


FIG. 5. Calculated Raman intensities for the $C2/m$ structure of $\text{Na}_4\text{P}_2\text{S}_6$ using ONC (turquoise) and PAW (black), in comparison to the experimental spectrum (red) [6] resulting from an incident light wavelength of 532 nm. The calculated spectra used the LDA exchange-correlation functional and were evaluated at $T = 300$ K. For each mode, the Lorentzian linewidth Γ^ν was chosen to be 10 cm^{-1} .

is presented in Fig. 5. For this simulation, we used the LDA exchange-correlation functional and both ONC and PAW data sets. The computed spectra assumed that $T = 300$ K and assumed a constant Lorentzian linewidth of $\Gamma^\nu = 10 \text{ cm}^{-1}$. The computed and experimental intensities were adjusted so that their peak intensities were each scaled to a value of 1. The computed intensity curves using the ONC and PAW are essentially superposed one on another validating both the code implementations of the two formalisms and also validating these ONC and PAW data sets. The results also show a close agreement between the computed and experimental values. For example, both the experiment and calculation observe the highest intensity peak at about 383 and 371 cm^{-1} , respectively. More specifically, this peak corresponds to a normal mode of A_g symmetry associated with the internal stretching motions of the $(\text{P}_2\text{S}_6)^{4-}$ ions. This mode also corresponds to the lowest frequency nondispersive mode mentioned in Sec. III B 1 and shown in Fig. 3(b). In future work, it may be appropriate to further investigate the sensitivity of the computed spectra on the Lorentzian linewidth parameter Γ^ν .

2. $\text{Li}_4\text{P}_2\text{S}_6$

Since the Neuberger [7] preparation of $\text{Li}_4\text{P}_2\text{S}_6$, corresponds to the $P\bar{3}m1$ structure, it is useful to compare its vibrational spectrum with that of $\text{Na}_4\text{P}_2\text{S}_6$ shown in Fig. 3(a) in order to get a sense of the difference caused by replacing Na by Li within the lattice of the same symmetry as shown in Fig. 6. The comparison shows that the vibrational spectra for the two materials are very similar; the main differences are that the Li amplitude motions extend to higher frequencies, 370 cm^{-1} , compared with the corresponding Na amplitude motions.

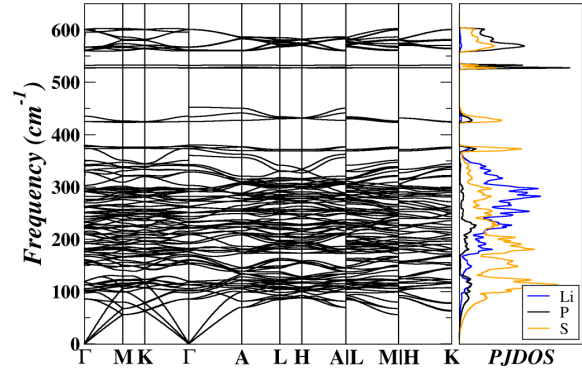


FIG. 6. Phonon band structure and the corresponding projected density of states for $\text{Li}_4\text{P}_2\text{S}_6$ in the $P\bar{3}m1$ structure. See Fig. 3(d) for the Brillouin zone diagram of the hexagonal structure.

C. Helmholtz free energy and stability of crystalline phases

The total Helmholtz free energy of $\text{Na}_4\text{P}_2\text{S}_6$ in each of the three model structures, as evaluated from Eqs. (1)–(3), are shown Fig. 7(a) in comparison with those of $\text{Li}_4\text{P}_2\text{S}_6$ analogs as plotted in Fig. 7(b). The corresponding vibrational free energies F_{vib} near the room temperature are inserted in each subfigure for comparing the contributions to the stability of the crystal. As implied by the overlapped black and purple curves in the inserted figures, the phonon contributions from the two hexagonal structures $P\bar{3}m1$ and $P\bar{3}1m$ are almost identical with energy value higher than that of $C2/m$ structure throughout the temperature range for both materials. In the case of $\text{Na}_4\text{P}_2\text{S}_6$, the lowest Helmholtz free energy of the $C2/m$ structure indicates that the vibrational free energy contributes to the stabilization of this phase. While for $\text{Li}_4\text{P}_2\text{S}_6$, although the $C2/m$ structure possesses the lowest vibrational free energy, it is the static energy U_{SL} that plays a dominant role in stabilizing in the $P\bar{3}m1$ structure.

We present the summary of simulation energies at $T = 300$ K in Table II to detail the relationships between the competing energies. It is interesting to note that at this temperature, $F_{\text{vib}} < 0$ for all of the $\text{Na}_4\text{P}_2\text{S}_6$ structures while $F_{\text{vib}} > 0$ for all of the $\text{Li}_4\text{P}_2\text{S}_6$ structures. It is also interesting to note that the vibrational contributions to the stabilization

TABLE II. Summary of simulation energies for $\text{Na}_4\text{P}_2\text{S}_6$ and $\text{Li}_4\text{P}_2\text{S}_6$ at $T = 300$ K. Results given in units of eV/(formula unit); for each material, the energy zero is set at the static lattice energy U_{SL} for the $P\bar{3}m1$ structure.

$\text{Na}_4\text{P}_2\text{S}_6$	ΔU_{SL}	$F_{\text{vib}} (300 \text{ K})$	$F (300 \text{ K})$
$P\bar{3}m1$	0.00	-0.04	-0.04
$C2/m$	0.00	-0.08	-0.08
$P\bar{3}1m$	0.09	-0.04	0.05
$\text{Li}_4\text{P}_2\text{S}_6$	ΔU_{SL}	$F_{\text{vib}} (300 \text{ K})$	$F (300 \text{ K})$
$P\bar{3}m1$	0.00	0.19	0.19
$C2/m$	0.31	0.12	0.43
$P\bar{3}1m$	0.04	0.20	0.24

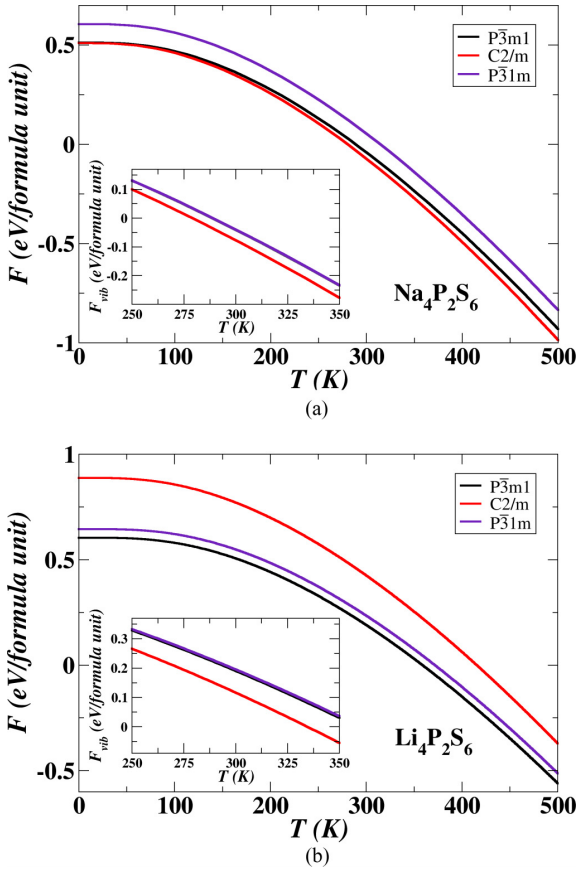


FIG. 7. Plot of Helmholtz free energy and the vibrational free energy (inset) for (a) $\text{Na}_4\text{P}_2\text{S}_6$ and (b) $\text{Li}_4\text{P}_2\text{S}_6$, comparing results for the $P\bar{3}m1$ (black), $C2/m$ (red), and the $P\bar{3}1m$ (purple) structures. In both sets of curves the zero of energy is taken by setting $U_{\text{SL}}(P\bar{3}m1) = 0$.

of these materials are substantial. For both materials at $T = 300$ K, the $C2/m$ structure has the lowest value of F_{vib} . This stabilizes the $\text{Na}_4\text{P}_2\text{S}_6$ in the $C2/m$ structure relative to the other two structures. However, for $\text{Li}_4\text{P}_2\text{S}_6$, the $P\bar{3}m1$ structure has the smallest value of $F = 0.19$ eV/formula unit benefiting from contributions of static lattice energy. Overall, our results on each material are consistent with the corresponding experimental analysis [6,7,11] in terms of structural stability.

In order to further understand how the phonon normal modes contribute to the vibrational Helmholtz free energy $F_{\text{vib}}(T)$, it is helpful to examine the weighted phonon density of states factor defined in Eq. (4) and its integral defined in Eq. (5) as well as the phonon density of states $g(\omega)$ defined by Eq. (6) which are all plotted in Fig. 8 for the functions evaluated at $T = 300$ K representing $\text{Na}_4\text{P}_2\text{S}_6$ (a) and $\text{Li}_4\text{P}_2\text{S}_6$ (b), both in their $C2/m$ structures. Here, we see that while $g(\omega) \geq 0$ for all frequencies ω , $f_{\text{vib}}(\omega, T)$ changes sign from negative to positive when $2 \sinh[\hbar\omega/(2k_B T)] = 1$. For $T = 300$ K, and for ω in units of cm^{-1} , this sign change occurs at

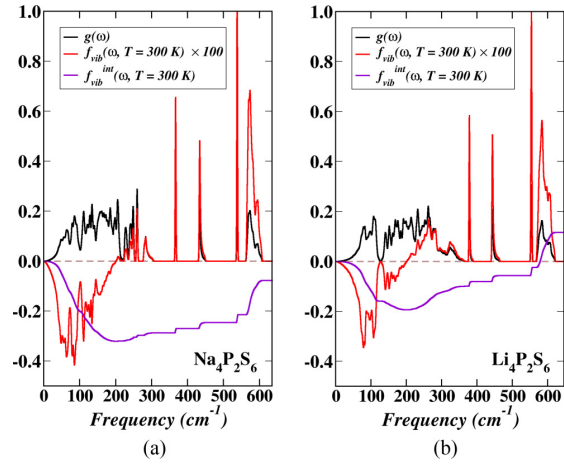


FIG. 8. Details of the vibrational stabilization at $T = 300$ K for (a) $\text{Na}_4\text{P}_2\text{S}_6$, (b) $\text{Li}_4\text{P}_2\text{S}_6$ in the $C2/m$ structure. In each subplot, the black curve indicates the phonon density of states $g(\omega)$, the red curve represents the weighted phonon density of states $f_{\text{vib}}(\omega, T = 300 \text{ K})$ scaled by a factor of 100, and the purple curve gives the integrated weighted phonon density of states factor $f_{\text{vib}}^{\text{int}}(\omega, T = 300 \text{ K})$ as defined in Eqs. (6), (4), and (5), respectively. In these plots the corresponding vertical scales are in units of states/ cm^{-1} for $g(\omega)$, $\text{eV}/(\text{formula unit})/\text{cm}^{-1}$ for f_{vib} , and $\text{eV}/(\text{formula unit})$ for $f_{\text{vib}}^{\text{int}}$.

$\omega \approx 201 \text{ cm}^{-1}$. Figure 8 shows that in the frequency range $0 \leq \omega \leq 201 \text{ cm}^{-1}$, $\text{Na}_4\text{P}_2\text{S}_6$ has a greater phonon density of states than does $\text{Li}_4\text{P}_2\text{S}_6$, which numerically explains why the vibrational Helmholtz free energy of $\text{Na}_4\text{P}_2\text{S}_6$ is much lower than that of $\text{Li}_4\text{P}_2\text{S}_6$. Qualitatively, the fact that $\text{Na}_4\text{P}_2\text{S}_6$ has a greater phonon density of states at low frequencies could be explained by low-frequency vibrations of the more massive Na ions compared with those of the less massive Li ions.

IV. PREDICTION OF A MIXED-ION ELECTROLYTE

$\text{Li}_2\text{Na}_2\text{P}_2\text{S}_6$

A. Optimized structure

In addition to the reexamination of known crystalline materials $\text{Na}_4\text{P}_2\text{S}_6$ and $\text{Li}_4\text{P}_2\text{S}_6$, we also examined the possibilities for mixed-ion material $\text{Li}_2\text{Na}_2\text{P}_2\text{S}_6$ based on the idea of ionic substitution. For example, starting with the $C2/m$ structure of crystalline $\text{Na}_4\text{P}_2\text{S}_6$, we consider the possibility of modifying the structure by substituting two Li ions for two Na ions in the setting of the primitive cell. The $C2/m$ structure of $\text{Na}_4\text{P}_2\text{S}_6$ has two crystallographically distinct Na sites with Wyckoff labels g and h . These are indicated by light blue and dark blue shades in Fig. 1(b), respectively. From this viewpoint, we intuitively construct two likely geometries of atomic arrangements for $\text{Li}_2\text{Na}_2\text{P}_2\text{S}_6$. For the configuration R_g^{Li} illustrated in Fig. 9(a), we replace all equivalent Na ions in $\text{Na}_4\text{P}_2\text{S}_6$ of type g with Li ions. For the configuration R_h^{Li} illustrated in Fig. 9(b), we replace all Na ions of type h with Li ions. After optimization using variable cell techniques, both proposed structures retain their space-group symmetry of

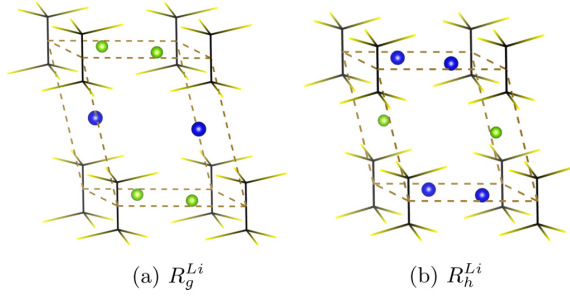


FIG. 9. Diagrams of two possible arrangements of ions for primitive crystalline unit cells of $\text{Li}_2\text{Na}_2\text{P}_2\text{S}_6$ in their optimized $C2/m$ structures with Li, Na, and the building block $(\text{P}_2\text{S}_6)^{4-}$ units represented by green balls, blue balls, and wire frames, respectively. Li ions in (a) are located at the equivalent g sites while in (b) Li ions are located at h sites.

$C2/m$ with the optimized lattice parameters for each potential structure being listed in Table III. Given that R_g^{Li} results in a low-energy structure having relative static lattice energy of -0.16 eV with respect to R_h^{Li} , this configuration is determined to be the ground structure of $\text{Li}_2\text{Na}_2\text{P}_2\text{S}_6$ and will be used in subsequent analysis and simulations. It is also worth mentioning that the equilibrium volume of $\text{Li}_2\text{Na}_2\text{P}_2\text{S}_6$ in the R_g^{Li} structure has approximately 10% less volume than that of $\text{Na}_4\text{P}_2\text{S}_6$, which is not surprising because the Li ion has a smaller radius than does the Na ion.

In the case of having Na as well as Li ions vibrating in the same lattice, it would be interesting to compare the vibrational features of $\text{Li}_2\text{Na}_2\text{P}_2\text{S}_6$ with those of the pure material $\text{Na}_4\text{P}_2\text{S}_6$ in terms of phonon dispersion relations which are given in Figs. 10 and 3(b), respectively. The comparison shows that the dispersion curves of the two materials are very similar with the same number of modes covering an almost identical range of frequencies. The fact that the harmonic phonon analysis of the ground-state structure of $\text{Li}_2\text{Na}_2\text{P}_2\text{S}_6$ results in all phonon modes having real frequencies, provides evidence of its dynamical stability.

TABLE III. Comparison of the optimized lattice parameters for $\text{Li}_2\text{Na}_2\text{P}_2\text{S}_6$ in the R_g^{Li} and R_h^{Li} structures. Also listed are the static lattice energy differences ΔU_{SL} referenced to the energy of the R_h^{Li} structure in units of eV/formula unit.

		R_g^{Li}	R_h^{Li}
Primitive cell:	$a = b$ (Å)	6.18	6.46
	c (Å)	7.50	7.01
	$\alpha = \beta$ (deg)	97.77	97.88
	γ (deg)	119.21	118.43
Conventional cell:	a_c (Å)	6.26	6.61
	b_c (Å)	10.67	11.10
	c_c (Å)	7.50	7.01
	β_c (deg)	105.50	105.54
	ΔU_{SL} (eV/FU)	-0.16	0.00

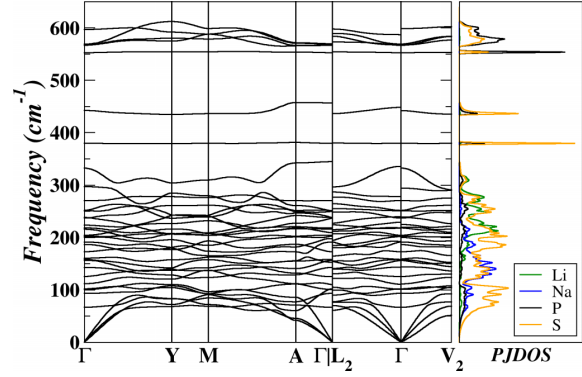
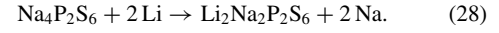


FIG. 10. Phonon band structure and the corresponding projected density of states for $\text{Li}_2\text{Na}_2\text{P}_2\text{S}_6$ (in the stable R_g^{Li} structure). See Fig. 3(e) for the Brillouin zone diagram of the $C2/m$ structure.

B. Possible reaction pathways

To the best of our knowledge, the crystal $\text{Li}_2\text{Na}_2\text{P}_2\text{S}_6$ has not been yet observed experimentally. However, with predictive capabilities of first-principles calculations, we can quantitatively evaluate the plausibility of synthesizing the material by considering a number of reactions. Perhaps the simplest reaction involves replacing Na with Li in $\text{Na}_4\text{P}_2\text{S}_6$ according to



In this reaction (28) we assume that both $\text{Na}_4\text{P}_2\text{S}_6$ and $\text{Li}_2\text{Na}_2\text{P}_2\text{S}_6$ are in their ground-state $C2/m$ structures and Li and Na are in their metallic body-centered-cubic structures. The reaction energy of the products P and the reactants R is then estimated from

$$\Delta F(T) = \Delta U_{\text{SL}} + \Delta F_{\text{vib}}(T) + \Delta F_{\text{elec}}^{\text{metal}}(T). \quad (29)$$

The reaction energy $\Delta F(T)$ calculated in this way represents the net energy of the process, typically referenced to room temperature ($T = 300$ K) and does not account for possible reaction barriers. Nevertheless, $\Delta F(T)$ is useful for assessing stabilities; $\Delta F(T) > 0$ implies that the reactants are more stable than the products, while $\Delta F(T) < 0$ implies that the products are more stable than the reactants at temperature T . Here, $\Delta U_{\text{SL}} = U_{\text{SL}}^{\text{P}} - U_{\text{SL}}^{\text{R}}$ represents the static lattice energy difference between the left-side reactants and the right-side products of the reaction as determined from ground-state (zero-temperature) density functional calculations. Similarly, we denote $\Delta F_{\text{vib}}(T) = F_{\text{vib}}^{\text{P}}(T) - F_{\text{vib}}^{\text{R}}(T)$ in the harmonic phonon approximation, as the vibrational energy change during the reaction process. For this reaction which involves metallic constituents, there is in principle a contribution $\Delta F_{\text{elec}}^{\text{metal}}(T)$ due to temperature-dependent electronic excitations of metallic Li and Na. However, our calculations indicate these contributions are numerically small ($\sim 10^{-3}$ eV) and can be neglected. Graphs of $\Delta F(T)$ and separately of the Helmholtz free energies of the reactants and products as a function of temperature T are presented in Fig. 11. For this reaction, $\Delta F(T) < 0$ for the computed temperature range and at $T = 300$ K, $\Delta F(T = 300 \text{ K}) = -0.35$ eV. This suggests

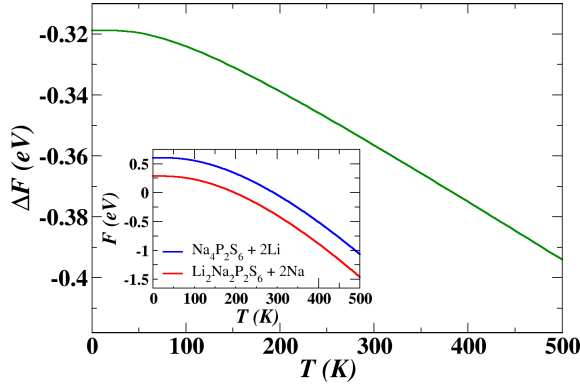


FIG. 11. Plot of the reaction energy of Eq. (28) as a function of temperature. The inner plot presents the comparison of the Helmholtz free energy of the reactants (blue curve) with that of products (red curve) for the predicted reaction.

that it is energetically favorable for Li to replace Na according to reaction (28) over a significant temperature range.

While reaction (28) provides a possible synthesis route producing the mixed-ion electrolyte with an excess Na metal coating, there are a number of other possible reactions one can imagine to produce the pure mixed-ion electrolyte $\text{Li}_2\text{Na}_2\text{P}_2\text{S}_6$. We have analyzed some of these according to Eq. (29), neglecting the $\Delta F_{\text{elec}}^{\text{metal}}(T)$ contributions. The results are summarized together with the results for reaction [(28) or No. 1] in Table IV. From this table, we see that the only reaction that has a positive ΔF is No. 3, suggesting that $\text{Li}_2\text{Na}_2\text{P}_2\text{S}_6$ is unstable relative to the phase-separated mixture of $\text{Na}_4\text{P}_2\text{S}_6$ and $\text{Li}_4\text{P}_2\text{S}_6$. On the other hand, knowing that $\text{Li}_4\text{P}_2\text{S}_6$ forms at very high temperature [2,7,9] suggests that there may be a large activation barrier to the formation of $\text{Li}_4\text{P}_2\text{S}_6$. It is possible that a low-temperature synthesis process that keeps the reaction energy below the energy of the

reaction barrier to form $\text{Li}_4\text{P}_2\text{S}_6$ could provide a successful pathway to the synthesis of $\text{Li}_2\text{Na}_2\text{P}_2\text{S}_6$. Perhaps some of the reactions mentioned in Table IV (other than No. 3) are worth investigating for this purpose.

V. IONIC CONDUCTIVITIES

A. Nudged elastic band (NEB) analysis

In order to understand mechanisms of Na ion conductivity in $\text{Na}_4\text{P}_2\text{S}_6$ and $\text{Li}_2\text{Na}_2\text{P}_2\text{S}_6$ in the $C2/m$ structure, it is helpful to visualize part of simulation cell (composed of $2 \times 1 \times 2$ conventional monoclinic cells) as illustrated in Fig. 12(a). Previously reported analysis of Na ion conductivity in $\text{Na}_4\text{P}_2\text{S}_6$ in the $C2/m$ structure [8] found the most energetically favorable migration to occur with a vacancy mechanism within planes containing Na ions at the crystallographic h sites between $(\text{P}_2\text{S}_6)^{4-}$ layers. One example zigzag path is illustrated in Fig. 12(a) showing net migration along the \mathbf{a} axis. Using the NEB methods discussed in Sec. IIC1, the energy path diagrams for Na ion vacancy migration along neighboring h sites for $\text{Na}_4\text{P}_2\text{S}_6$ and $\text{Li}_2\text{Na}_2\text{P}_2\text{S}_6$ are compared in Fig. 12(b). The results indicate that E_m is significantly smaller for $\text{Li}_2\text{Na}_2\text{P}_2\text{S}_6$ compared with that of $\text{Na}_4\text{P}_2\text{S}_6$ which correlates with the shortened distance between neighboring h sites by approximately 0.2 Å.

The Na ion vacancy mechanism for the macroscopic ion conductivity depends upon a population of Na ion vacancies. For a highly ordered crystal, this population depends on the “formation” of interstitial-vacancy pairs. In previous work [8], the most favorable interstitial sites were found to be located at the crystallographic d sites which are close to and in the same plane as the h sites as shown in Fig. 12(a). The results of this work using the PBEsol exchange-correlation function are qualitatively similar but numerically different from the previous work [8] which used the LDA functional. In this work, we find the following values (in units of eV): $E_m = 0.25$ and 0.16 and $E_f = 0.18$ and 0.13 for $\text{Na}_4\text{P}_2\text{S}_6$ and $\text{Li}_2\text{Na}_2\text{P}_2\text{S}_6$, respectively, suggesting that $\text{Li}_2\text{Na}_2\text{P}_2\text{S}_6$ may

TABLE IV. Computed energy differences [Eq. (29)] for indicated reactions in eV units, evaluated at $T = 300$ K and neglecting electronic excitation contributions. $\text{Na}_4\text{P}_2\text{S}_6$ and $\text{Li}_2\text{Na}_2\text{P}_2\text{S}_6$ are assumed to have the optimized $C2/m$ structures discussed in this paper, $\text{Li}_4\text{P}_2\text{S}_6$ is assumed to have the optimized $P\bar{3}m1$ structure discussed in this paper, Na and Li are assumed to have the optimized bcc [space group $Im\bar{3}m$ (No. 229)] structures, while the assumed structures of all other constituents are referenced in the footnotes.

No.	Reaction: $R \rightarrow P$	ΔU_{SL}	ΔF_{vib}	ΔF
1	$\text{Na}_4\text{P}_2\text{S}_6 + 2 \text{Li} \rightarrow \text{Li}_2\text{Na}_2\text{P}_2\text{S}_6 + 2 \text{Na}$	-0.29	-0.06	-0.35
2	$2 \text{Li} + 2 \text{Na} + 2 \text{P}^{\text{a}} + 6 \text{S}^{\text{b}} \rightarrow \text{Li}_2\text{Na}_2\text{P}_2\text{S}_6$	-10.62	0.06	-10.56
3	$\frac{1}{2} \text{Na}_4\text{P}_2\text{S}_6 + \frac{1}{2} \text{Li}_4\text{P}_2\text{S}_6 \rightarrow \text{Li}_2\text{Na}_2\text{P}_2\text{S}_6$	0.13	-0.03	0.10
4	$\frac{1}{2} \text{Na}_4\text{P}_2\text{S}_6 + \frac{2}{3} \text{Li}_3\text{PS}_4^{\text{c}} + \frac{1}{12} \text{P}_4\text{S}_4^{\text{d}} \rightarrow \text{Li}_2\text{Na}_2\text{P}_2\text{S}_6$	-0.24	-0.02	-0.26
5	$\frac{2}{3} \text{Na}_3\text{PS}_4^{\text{e}} + \frac{2}{3} \text{Li}_3\text{PS}_4^{\text{c}} + \frac{1}{6} \text{P}_4\text{S}_4^{\text{d}} \rightarrow \text{Li}_2\text{Na}_2\text{P}_2\text{S}_6$	-0.48	-0.00	-0.48
6	$\frac{2}{3} \text{Na}_3\text{PS}_4^{\text{e}} + \frac{1}{3} \text{P}_4\text{S}_{10}^{\text{f}} + 2 \text{Li} \rightarrow \text{Li}_2\text{Na}_2\text{P}_2\text{S}_6$	-5.01	0.06	-4.95
7	$\frac{2}{3} \text{Li}_3\text{PS}_4^{\text{c}} + \frac{1}{3} \text{P}_4\text{S}_{10}^{\text{f}} + 2 \text{Na} \rightarrow \text{Li}_2\text{Na}_2\text{P}_2\text{S}_6$	-4.70	0.07	-4.63

^aBlack phosphorous with space group $Cmce$ (No. 64); from Ref. [59].

^bOrthorhombic (α -S₈) with space group $Fddd$ (No. 70); from Ref. [60].

^c γ -Li₃PS₄ with space group $Pmn2_1$ (No. 31); from Ref. [61].

^d α -P₄S₄ with space group $C2/c$ (No. 15); from Ref. [62].

^e α -Na₃PS₄ with space group $P\bar{4}2_1c$ (No. 114); from Ref. [63].

^fP₄S₁₀ with space group $P\bar{1}$ (No. 2); from Ref. [64].

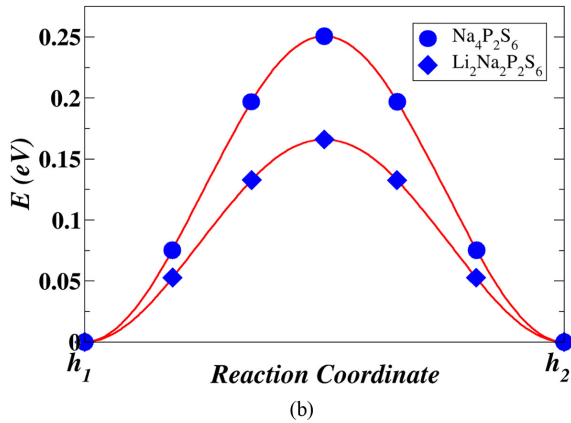
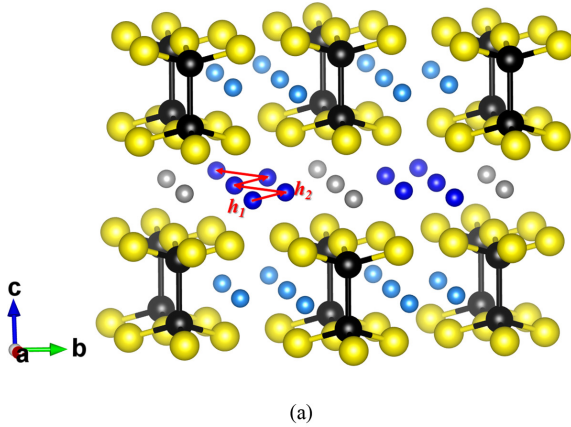


FIG. 12. (a) Ball and stick diagram of a portion of the simulation cell used to study Na ion conductivity in $\text{Na}_4\text{P}_2\text{S}_6$ and $\text{Li}_2\text{Na}_2\text{P}_2\text{S}_6$ with the same ball color conventions as used in the diagrams shown in Sec. III. Dark blue balls indicate Na ions with Wyckoff labels h , light blue balls indicate Na or Li ions with Wyckoff labels g , and gray balls indicate interstitial sites with Wyckoff labels d . The red arrows indicate the most likely Na ion vacancy migration pathway between adjacent h sites. (b) Configuration energy diagram results of NEB calculation of Na ion vacancy migration along one step of the indicated pathway, comparing results for $\text{Na}_4\text{P}_2\text{S}_6$ and $\text{Li}_2\text{Na}_2\text{P}_2\text{S}_6$.

have promising Na ion conductivity. These and related results will be summarized in Table V.

B. Molecular dynamics simulations

First-principles molecular dynamics simulations were performed using supercells of $\text{Na}_4\text{P}_2\text{S}_6$ and $\text{Li}_2\text{Na}_2\text{P}_2\text{S}_6$ as described in Sec. IIC2. In order to collect statistically significant numbers of hopping events within reasonable simulation times, it was necessary to use high temperatures for the simulations; typically the temperature averaged over the simulation time was $\langle T \rangle > 900$ K. It is expected that the high-temperature simulation results can be extrapolated to more physical temperatures in a simplified accelerated dynamics

TABLE V. NEB and MD results on $\text{Na}_4\text{P}_2\text{S}_6$ and $\text{Li}_2\text{Na}_2\text{P}_2\text{S}_6$ calculated with the PBEsol exchange-correlation functional, in comparison to those of previous work obtained using the LDA exchange-correlation functional and available experimental data. All energies are given in eV units.

Materials	Analysis	E_m	E_f	E_a
$\text{Na}_4\text{P}_2\text{S}_6$	LDA + NEB ^a	0.30	0.24	0.42
	PBEsol + NEB	0.25	0.18	0.34
	PBEsol + MD			0.41
	Experiment ^b			0.39
$\text{Li}_2\text{Na}_2\text{P}_2\text{S}_6$	PBEsol + NEB	0.16	0.13	0.23
	PBEsol + MD			0.30

^aReference [8].

^bReference [6].

algorithm [65]. This approach follows the pioneering work of Mo *et al.* [66].

The results offer additional perspectives on the Na ion migration mechanisms of these materials. In particular, by directly observing the ion trajectories, we find that the most significant ion motion occurs within planes containing Na ions (located at the Wyckoff labeled h sites at equilibrium) between $(\text{P}_2\text{S}_6)^{4-}$ layers, consistent with the NEB analysis discussed above. For simplicity, we will refer to this plane as the inter-layer plane. We found that there is essentially no conduction path along the c axis of these materials. We also examined the Li ion motion for $\text{Li}_2\text{Na}_2\text{P}_2\text{S}_6$. At equilibrium, the ions are located at the Wyckoff sites labeled g which are within the $(\text{P}_2\text{S}_6)^{4-}$ layer planes. We found the Li ion trajectories to be characterized by oscillations about their equilibrium positions resulting in a high degree of site localization and essentially no diffusion. Similar behavior was observed for the g -site Na ions in $\text{Na}_4\text{P}_2\text{S}_6$.

In order to visualize the significant Na ion motion in these materials, Fig. 13 shows the superposed snapshots of the ion positions in a volume containing the interlayer plane. The snapshots were taken each time interval of $20\Delta t$, where Δt denotes the Verlet time integration parameter, for the first 30 ps of the MD simulations. For $\text{Na}_4\text{P}_2\text{S}_6$ the average temperature was $\langle T \rangle = 955$ K and for $\text{Li}_2\text{Na}_2\text{P}_2\text{S}_6$ the average temperature was $\langle T \rangle = 973$ K. At the beginning of the calculation, there are eight Na ions with labels from Na(1) to Na(8) corresponding to their respective host lattice h sites ($h_1 - h_8$) in the simulation cell. The notations ($d_1 - d_4$) indicate the interstitial d sites within the supercell. More labels with superscript “prime” were placed in each subfigure representing sites in neighboring cells.

Figure 13 shows that in contrast to the predictions of the NEB analysis which focused on ion vacancy migration along the a axis, the molecular dynamics results suggest that ion migration occurs throughout the interlayer plane due to involvement of the interstitial d sites. Additionally, the results qualitatively show that, compared to the case for $\text{Na}_4\text{P}_2\text{S}_6$, it is evident that the Na ions hop more frequently in $\text{Li}_2\text{Na}_2\text{P}_2\text{S}_6$, presenting a more extensive network of diffusional channels. Some general observations of the hopping events are as follows. The migration of Na ions is either via direct vacancy

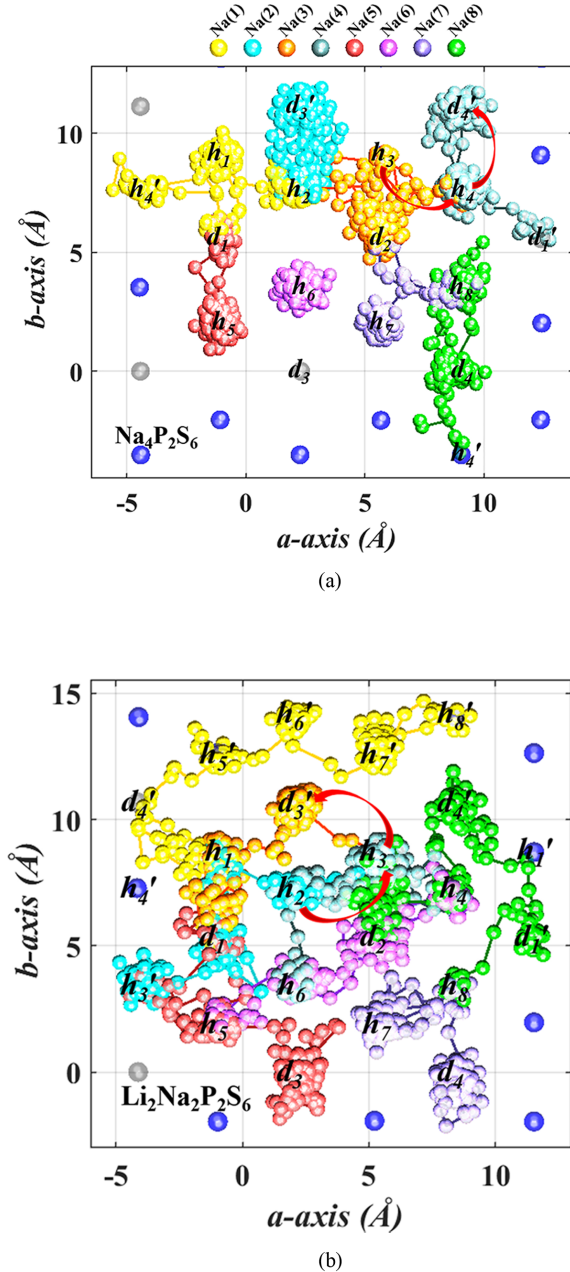


FIG. 13. Superposed snapshots of 30-ps molecular dynamics simulations visualized within slices of the simulation cells containing an interlayer plane for (a) $\text{Na}_4\text{P}_2\text{S}_6$ with average temperature $\langle T \rangle = 955$ K and (b) $\text{Li}_2\text{Na}_2\text{P}_2\text{S}_6$ with average temperature $\langle T \rangle = 973$ K. The time interval between snapshots is $20\Delta t = 0.048$ ps. The blue balls represent the host h sites and the gray balls represent the interstitial d sites. Each distinct Na ion is represented with a unique color in order to follow its motion throughout the simulation. The red arrows indicate particular examples of Na ion jumps between sites with the tail and head of each arrow consistent with the time sequence of the jump.

mechanism between the host $h \leftrightarrow h$ sites or via indirect vacancy mechanism between $h \leftrightarrow d$ sites. Specifically, the diffusion process can be triggered by one Na ion at a host h site jumping into the nearest-neighbor d site, leaving a vacancy that is available to be occupied by another Na ion from a nearby h site. For these simulations, no migrations between the $d \leftrightarrow d$ sites were observed. This suggests that for these materials, the Na ion migration processes involve both direct vacancy hops and indirect vacancy hops with interstitial intermediates, but direct interstitial mechanisms were not identified in these data sets. For example, in Fig. 13(a) the first hop in the simulation occurs for Na(4) at $t = 0.60$ ps, jumping from site h_4 to site d'_4 . Later at $t = 1.57$ ps, the Na(3) ion jumps from site h_3 to fill the vacancy h_4 . A similar initial process is observed in Fig. 13(b) in a faster timescale where $t = 0.60$ ps, the Na(3) ion jumps from site h_3 into the site d'_3 , and subsequently at $t = 0.97$ ps, the Na(2) ion jumps from its h_2 site into the vacant h_3 site.

In order to quantify these effects, we can analyze the nearest-neighbor hopping events as a function of time. In particular, for $t > 0$, we can determine the average number of hops between nearest-neighbor (nn) h sites [$H_{h \leftrightarrow h}(t)$] and the average number of hops between nearest-neighbor (nn) $h \leftrightarrow d$ sites [$H_{h \leftrightarrow d}(t)$] in the following way. Within the simulation cell there are 2 interlayer planes containing a total of 16 Na ions, each with a label s . At each time t , we assign each of these s mobile ions to the nearest host lattice site h_k where within each plane, $1 \leq k \leq 8$ or interstitial site d_l where within each plane $1 \leq l \leq 4$. Then, for each time $t > 0$, we compute the hop counter functions according to the comparison of the site assignments at time $t - \Delta t$ and t :

$$C_{h \leftrightarrow h}^s(t) = \begin{cases} C_{h \leftrightarrow h}^s(t - \Delta t), & \text{no config. change} \\ C_{h \leftrightarrow h}^s(t - \Delta t) + 1, & h \leftrightarrow \text{nn } h \end{cases} \quad (30)$$

$$C_{h \leftrightarrow d}^s(t) = \begin{cases} C_{h \leftrightarrow d}^s(t - \Delta t), & \text{no config. change} \\ C_{h \leftrightarrow d}^s(t - \Delta t) + 1, & \{h, d\} \leftrightarrow \text{nn } \{d, h\} \end{cases}$$

with $C_{h \leftrightarrow h}^s(t = 0) = 0 = C_{h \leftrightarrow d}^s(t = 0)$. The algorithm must be adapted to take into account hops across the simulation cell boundaries. From these hop counter results we can then compute the accumulated and averaged hop functions according to

$$H_{h \leftrightarrow h}(t) = \frac{1}{16} \sum_{s=1}^{16} C_{h \leftrightarrow h}^s(t),$$

$$H_{h \leftrightarrow d}(t) = \frac{1}{16} \sum_{s=1}^{16} C_{h \leftrightarrow d}^s(t). \quad (31)$$

The results of this analysis are illustrated in Fig. 14. As expected, the accumulated hop function for $\text{Li}_2\text{Na}_2\text{P}_2\text{S}_6$ is larger than the corresponding function for $\text{Na}_4\text{P}_2\text{S}_6$ for both $h \leftrightarrow d$ and $h \leftrightarrow h$ events. A less intuitive result of this analysis is that $H_{h \leftrightarrow d}(t) > H_{h \leftrightarrow h}(t)$ for both materials, indicating the importance of the intermediate interstitial processes for ion migration in these materials.

In order to connect the simulations with ion conductivity, molecular dynamics runs with simulation times of 50–70 ps were performed at various average temperatures. For $\text{Na}_4\text{P}_2\text{S}_6$ the average temperatures were $\langle T \rangle = 955, 1051, 1143$, and

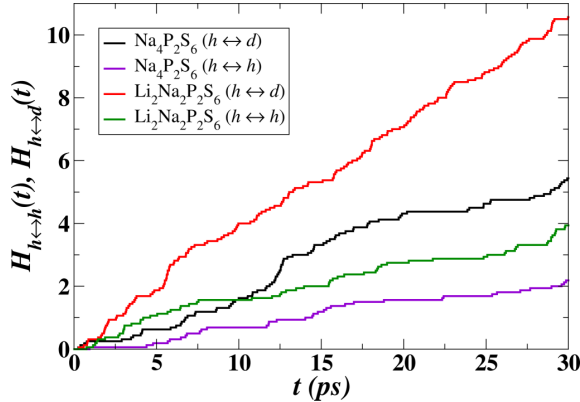


FIG. 14. Plots of the accumulated hop functions $H_{h \leftrightarrow h}(t)$ and $H_{h \leftrightarrow d}(t)$ as a function of the simulations time t . The results for $\text{Na}_4\text{P}_2\text{S}_6$ are shown in black and purple and the results for $\text{Li}_2\text{Na}_2\text{P}_2\text{S}_6$ are shown in red and green. The data from the simulations illustrated in Fig. 13 were used for this analysis.

1287 K, while for $\text{Li}_2\text{Na}_2\text{P}_2\text{S}_6$ the average temperatures were $\langle T \rangle = 994, 1060, 1193,$ and 1260 K. The results, assuming the Haven ratio $H_r = 1$, together with the available experimental measurements are presented in Fig. 15, plotting $\log(T\sigma)$ vs $1/T$. On the basis of Eqs. (24) and (25), the activation energy is obtained from the slope of the corresponding fit line. For the case of $\text{Na}_4\text{P}_2\text{S}_6$, it shows that the calculated tracer activation energy $E_a^{\text{MSD}} = 0.41$ eV is in reasonably good agreement with the experimental value of $E_a^{\text{expt}} = 0.39$ eV. The discrepancy between experiment and computation may be due to the rough approximation of the Haven ratio. Other possible reasons for the discrepancy include the choice of statistical ensemble for modeling the system and the simulation time may also affect the accuracy

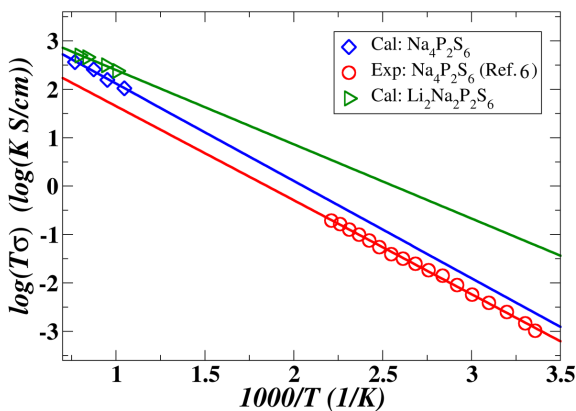


FIG. 15. Plots of the ionic conductivity with the calculated values for $\text{Na}_4\text{P}_2\text{S}_6$ (blue diamonds) and $\text{Li}_2\text{Na}_2\text{P}_2\text{S}_6$ (green triangles) evaluated using Eq. (25) with $H_r = 1$. The experimental value for $\text{Na}_4\text{P}_2\text{S}_6$ (red circles) was obtained by refitting the data in Ref. [6]. The straight lines represent the best fit of the computational or the experimental analysis.

of the numerical analysis. The tracer activation energy of $\text{Li}_2\text{Na}_2\text{P}_2\text{S}_6$ is $E_a^{\text{MSD}} = 0.30$ eV. Consistent with the NEB analysis, we again see that $\text{Li}_2\text{Na}_2\text{P}_2\text{S}_6$ presents better ionic conductivity than $\text{Na}_4\text{P}_2\text{S}_6$. The results for both NEB and molecular dynamics analyses are summarized in Table V. Here, we note that for these systems, $E_a^{\text{NEB}} \neq E_a^{\text{MSD}}$ because of their different treatments of the effects of interstitial (d) sites. The NEB analysis presented here only considered direct hops between nearest-neighbor vacancy sites, including the interstitial sites only in the estimation of the population of vacancies via the Boltzmann factor due to the formation energy E_f of the interstitial-vacancy pair. The molecular dynamics analyses indicate significant contributions of hops between vacancy and interstitial sites, presenting a plausibly more physical picture of the Na ion migration processes.

VI. DISCUSSION AND CONCLUSIONS

The three focuses of this work are (1) a comprehensive (re)examination of the crystal structures and stabilities of $\text{Li}_4\text{P}_2\text{S}_6$ and $\text{Na}_4\text{P}_2\text{S}_6$, (2) a prediction and analysis of a mixed-ion electrolyte $\text{Li}_2\text{Na}_2\text{P}_2\text{S}_6$, and (3) an assessment of the Na ion conductivity properties of $\text{Na}_4\text{P}_2\text{S}_6$ and of the mixed-ion material $\text{Li}_2\text{Na}_2\text{P}_2\text{S}_6$.

The results of the structural analyses are presented in Sec. III with the numerical results evaluated at $T = 300$ K summarized in Table II. Here we see that, within the harmonic phonon approximation [14,35], the Helmholtz free energy due to vibrations plays a nontrivial role in stabilizing the materials. Using plots of the weighted phonon density of states factor and its integral in Fig. 8, it is possible to understand the vibrational stabilization of the more massive Na ions relative to the corresponding Li ion vibrations in these materials. Additionally, we found that computations using the PBEsol exchange-correlation functional [33] contributed to the better agreement with the experimental results compared with previous calculations [2,8] which used the LDA exchange-correlation functional [29]. The present computational results are consistent with the latest structural analyses, finding the stable structures at $T = 300$ K to be the Neuberger structure [7] for $\text{Li}_4\text{P}_2\text{S}_6$ and the Kuhn structure [11] for $\text{Na}_4\text{P}_2\text{S}_6$. For the Neuberger structure, we offered computational evidence of a slight correction to structural analysis, suggesting that the space group should be $P\bar{3}m1$ (No. 164) rather than the reported space group of $P321$. Further evidence of computational consistency with experiment was obtained in comparing experimental and computational nonresonant Raman phonon spectra of $\text{Na}_4\text{P}_2\text{S}_6$ shown in Fig. 4. Here, the most intense signal was identified as due to the internal stretching mode of the $(\text{P}_2\text{S}_6)^{4-}$ complex ions.

The results of analyzing the structure and stability of the possible mixed-ion electrolyte $\text{Li}_2\text{Na}_2\text{P}_2\text{S}_6$ are presented in Sec. IV. We found that two Li ions can substitute for the two intralayer Na ions of $\text{Na}_4\text{P}_2\text{S}_6$ in the $C2/m$ structure. Here, “intralayer” refers to the layers containing the $(\text{P}_2\text{S}_6)^{4-}$ building blocks of the structure. Compared with the original $\text{Na}_4\text{P}_2\text{S}_6$ structure, the resulting $\text{Li}_2\text{Na}_2\text{P}_2\text{S}_6$ crystal maintains the $C2/m$ space group with contracted lattice constants in the layer planes. Both $\text{Na}_4\text{P}_2\text{S}_6$ and $\text{Li}_2\text{Na}_2\text{P}_2\text{S}_6$ have similar interlayer Na ions arranged at equilibrium on sites with Wyckoff

TABLE VI. Comparison of the fractional coordinates of Li/Na₄P₂S₆ based on the Neuberger structure [7]. The column labeled “Wyck” lists the conventional cell multiplicity and Wyckoff labels based on the $P\bar{3}m1$ space group. The “Experiment” column lists the coordinates from the $P321$ analysis [7] which in general is in one-to-one correspondence except that the $6g$ sites of the $P\bar{3}m1$ structure map to two distinct $3e$ sites of the $P321$ structure and $6h$ sites of the $P\bar{3}m1$ structure map to two distinct $3f$ sites of the $P321$ structure as indicated.

Li ₄ P ₂ S ₆		Calculated			Experiment		
Atom	Wyck	<i>x</i>	<i>y</i>	<i>z</i>	<i>x</i>	<i>y</i>	<i>z</i>
Li	6 <i>g</i>	0.666	0.000	0.000	0.625/−0.683	0.000	0.0000
Li	6 <i>h</i>	0.667	0.000	$\frac{1}{2}$	0.631/−0.671	0.000	$\frac{1}{2}$
P	2 <i>c</i>	0.000	0.000	0.171	0.000	0.000	0.170
P	2 <i>d</i>	$\frac{1}{3}$	$\frac{2}{3}$	0.663	$\frac{1}{3}$	$\frac{2}{3}$	0.668
P	2 <i>d</i>	$\frac{1}{3}$	$\frac{2}{3}$	0.324	$\frac{1}{3}$	$\frac{2}{3}$	0.335
S	6 <i>i</i>	0.110	0.220	0.242	0.108	0.217	0.241
S	6 <i>i</i>	0.114	0.557	0.254	0.122	0.561	0.250
S	6 <i>i</i>	0.447	0.224	0.259	0.452	0.226	0.255
Na ₄ P ₂ S ₆		Calculated			Experiment		
Atom	Wyck	<i>x</i>	<i>y</i>	<i>z</i>	<i>x</i>	<i>y</i>	<i>z</i>
Na	6 <i>g</i>	0.659	0.000	0.000			
Na	6 <i>h</i>	0.676	0.000	$\frac{1}{2}$			
P	2 <i>c</i>	0.000	0.000	0.157			
P	2 <i>d</i>	$\frac{1}{3}$	$\frac{2}{3}$	0.660			
P	2 <i>d</i>	$\frac{1}{3}$	$\frac{2}{3}$	0.342			
S	6 <i>i</i>	0.102	0.205	0.229			
S	6 <i>i</i>	0.129	0.564	0.271			
S	6 <i>i</i>	0.463	0.231	0.264			

label *h*. Table IV lists reaction energies as estimated from differences in the Helmholtz free energies in the harmonic phonon approximation evaluated at $T = 300$ K for several possible reaction pathways. While we find that Li₂Na₂P₂S₆ is unstable with respect to $\frac{1}{2}(\text{Li}_4\text{P}_2\text{S}_6 + \text{Na}_4\text{P}_2\text{S}_6)$, we reasonably argue that since Li₄P₂S₆ forms at high temperature (typically 900° C) [2,7,9], it may be possible to stabilize

Li₂Na₂P₂S₆ with low-temperature reactions such as perhaps some of those listed in Table IV.

Results relating to simulations of Na ion conductivity in Na₄P₂S₆ and Li₂Na₂P₂S₆ are presented in Sec. V. Both NEB and molecular dynamics simulations find the dominant ionic conductivity to be due to Na ion motions in the interlayer planes. Because of its contracted lattice, it is predicted that

TABLE VII. Calculated fractional atomic coordinates of Li/Na₄P₂S₆ in the Kuhn structure [11] based on the conventional unit cell compared with the Kuhn structure [11] listed in the “Experiment” column. The column labeled “Wyck” lists the conventional cell multiplicity and Wyckoff label.

Li ₄ P ₂ S ₆		Calculated			Experiment		
Atom	Wyck	<i>x</i>	<i>y</i>	<i>z</i>	<i>x</i>	<i>y</i>	<i>z</i>
Li	4 <i>g</i>	0.000	0.668	0.000			
Li	4 <i>h</i>	0.000	0.823	0.500			
P	4 <i>i</i>	0.055	0.000	0.168			
S	4 <i>i</i>	0.769	0.000	0.260			
S	8 <i>j</i>	0.734	0.336	0.238			
Na ₄ P ₂ S ₆		Calculated			Experiment		
Atom	Wyck	<i>x</i>	<i>y</i>	<i>z</i>	<i>x</i>	<i>y</i>	<i>z</i>
Na	4 <i>g</i>	0.000	0.662	0.000	0.0000	0.6627	0.0000
Na	4 <i>h</i>	0.000	0.816	0.500	0.0000	0.8153	0.5000
P	4 <i>i</i>	0.053	0.000	0.157	0.0532	0.0000	0.1561
S	4 <i>i</i>	0.794	0.000	0.244	0.7942	0.0000	0.2414
S	8 <i>j</i>	0.722	0.347	0.230	0.7233	0.3499	0.2312

TABLE VIII. Fractional coordinates of Li/Na₄P₂S₆ simulated in the $P\bar{3}1m$ structure. The column labeled “Wyck” lists the conventional cell multiplicity and Wyckoff label.

Atom	Wyck	Li ₄ P ₂ S ₆			Na ₄ P ₂ S ₆		
		x	y	z	x	y	z
Li/Na	2 <i>c</i>	$\frac{1}{3}$	$\frac{2}{3}$	0.000	$\frac{1}{3}$	$\frac{2}{3}$	0.000
Li/Na	2 <i>d</i>	$\frac{1}{3}$	$\frac{2}{3}$	$\frac{1}{2}$	$\frac{1}{3}$	$\frac{2}{3}$	$\frac{1}{2}$
P	2 <i>e</i>	0.000	0.000	0.174	0.000	0.000	0.163
S	6 <i>k</i>	0.329	0.000	0.247	0.304	0.000	0.238

Li₂Na₂P₂S₆ has larger conductivity and lower activation barriers compared with Na₄P₂S₆. The analysis of the molecular dynamics trajectories suggests that both Na ion vacancy migration and indirect participation of interstitial sites contribute to the conductivity throughout the interlayer plane. Analyzing the Na ion trajectories in terms of the MSD(*t*, *T*) [Eq. (23)] and using the Nernst-Einstein equation (25) with the assumption of the Haven ratio $H_v = 1$, the simulated ion conductivity could be compared with the experimental measurements for Na₄P₂S₆ as shown in Fig. 15. There is reasonable agreement between the simulations and experimental results. If it becomes possible to stabilize the mixed-ion material Li₂Na₂P₂S₆, our simulations suggest that it will have a very promising Na ion conductivity.

ACKNOWLEDGMENTS

This work was supported by NSF Grant No. DMR-1507942. Computations were performed on the Wake Forest University DEAC cluster, a centrally managed resource with support provided in part by the University. Helpful discussions with A. Lachgar and D. Kondipudi from the WFU Department of Chemistry are gratefully acknowledged. Experimental work was conducted at the Center for Nanophase Materials Sciences, which is a Department of Energy Office of Science User Facility.

APPENDIX A: DETAILS OF THE NEUBERGER STRUCTURES OF Li₄P₂S₆ AND Na₄P₂S₆

The simulated structure corresponding to the structure analyzed by Neuberger [7] is detailed in Table VI. We use the space-group analysis of the $P\bar{3}1m$ structure rather than of the $P321$ structure of the Neuberger paper [7]. The P positions for the two space groups have the same Wyckoff labels, while the S positions of the $P321$ structure having the 6*g* multiplicity and label are equivalent to the 6*i* multiplicity and label of the $P\bar{3}1m$ structure. For the Li/Na sites, the pairs of 3*e* and 3*f* sites of the $P321$ structure correspond to the 6*g* and 6*h* multiplicities and labels of the $P\bar{3}1m$ structure.

APPENDIX B: DETAILS OF KUHN STRUCTURES OF Li₄P₂S₆ AND Na₄P₂S₆

The simulated fractional atomic coordinates of Li₄P₂S₆ and Na₄P₂S₆ are detailed in Table VII based on the conventional unit cell in the $C2/m$ structure and compared with the experimental results reported by Ref. [11] from x-ray

measurements on single-crystal samples. The results are very similar to those reported earlier by Rush *et al.* [8] simulated using the LDA exchange-correlation functional.

APPENDIX C: DETAILS OF THE $P\bar{3}1m$ REFERENCE STRUCTURES OF Li₄P₂S₆ AND Na₄P₂S₆

Table VIII lists the fractional coordinates of Li/Na₄P₂S₆ found in these simulations for the metastable $P\bar{3}1m$ structure. The corresponding lattice parameters are listed in Table I and the results are very similar to those reported earlier by Rush *et al.* [8] simulated using the LDA exchange-correlation functional.

APPENDIX D: DETAILS OF THE PREDICTED STRUCTURE OF CRYSTALLINE Li₂Na₂P₂S₆

Table IX lists the fractional coordinates of Li₂Na₂P₂S₆ for the ground-state R_g^{Li} structure in comparison with the results for the metastable R_h^{Li} structure. The initial configurations of these two structures were constructed based on the optimized primitive cell parameters of Kuhn structure for Na₄P₂S₆.

TABLE IX. Calculated fractional coordinates of Li₂Na₂P₂S₆ in the R_g^{Li} and the R_h^{Li} structures based on the conventional unit cell of $C2/m$ symmetry. The column labeled “Wyck” lists the conventional cell multiplicity and Wyckoff label.

Li ₂ Na ₂ P ₂ S ₆		R_g^{Li}		
Atom	Wyck	x	y	z
Li	4 <i>g</i>	0.000	0.668	0.000
Na	4 <i>h</i>	0.000	0.817	0.500
P	4 <i>i</i>	0.053	0.000	0.154
S	4 <i>i</i>	0.768	0.000	0.236
S	8 <i>j</i>	0.732	0.339	0.217
Li ₂ Na ₂ P ₂ S ₆		R_h^{Li}		
Atom	Wyck	x	y	z
Li	4 <i>h</i>	0.000	0.843	0.500
Na	4 <i>g</i>	0.000	0.664	0.000
P	4 <i>i</i>	0.052	0.000	0.167
S	4 <i>i</i>	0.786	0.000	0.263
S	8 <i>j</i>	0.718	0.346	0.251

- [1] T. Famprakis, P. Canepa, J. A. Dawson, M. S. Islam, and C. Masquelier, *Nat. Mater.* **18**, 1278 (2019).
- [2] Z. D. Hood, C. Kates, M. Kirkham, S. Adhikari, C. Liang, and N. A. W. Holzwarth, *Solid State Ionics* **284**, 61 (2016).
- [3] C. Dietrich, M. Sadowski, S. Siculo, D. A. Weber, S. J. Sedlmaier, K. S. Weldert, S. Indris, K. Albe, J. Janek, and W. G. Zeier, *Chem. Mater.* **28**, 8764 (2016).
- [4] Ö. U. Kudu, T. Famprakis, B. Fleutot, M.-D. Braidia, T. Le Mercier, M. S. Islam, and C. Masquelier, *J. Power Sources* **407**, 31 (2018).
- [5] K. Minami, A. Hayashi, and M. Tatsumisago, *J. Ceram. Soc. Jpn.* **118**, 305 (2010).
- [6] Z. D. Hood, H. Wang, X. Liu, A. S. Pandian, R. Peng, J. K. Keum, and M. Chi (unpublished).
- [7] S. Neuberger, S. P. Culver, H. Eckert, W. G. Zeier, and J. Schmedt auf der Günne, *Dalton Trans.* **47**, 11691 (2018).
- [8] L. E. Rush Jr. and N. A. W. Holzwarth, *Solid State Ionics* **286**, 45 (2016).
- [9] R. Mercier, J. P. Malugani, B. Fahys, J. Douglanle, and G. Robert, *J. Solid State Chem.* **43**, 151 (1982).
- [10] *International Tables for Crystallography, Volume A: Space-group symmetry, Fifth revised edition*, edited by T. Hahn (Kluwer Academic, Boston, 2002).
- [11] A. Kuhn, R. Eger, J. Nuss, and B. V. Lotsch, *Z. Anorg. Allg. Chem.* **640**, 689 (2014).
- [12] P. Hohenberg and W. Kohn, *Phys. Rev.* **136**, B864 (1964).
- [13] W. Kohn and L. J. Sham, *Phys. Rev.* **140**, A1133 (1965).
- [14] P. Giannozzi, S. de Gironcoli, P. Pavone, and S. Baroni, *Phys. Rev. B* **43**, 7231 (1991).
- [15] X. Gonze, *Phys. Rev. B* **55**, 10337 (1997).
- [16] X. Gonze and C. Lee, *Phys. Rev. B* **55**, 10355 (1997).
- [17] S. Baroni, S. De Gironcoli, A. Dal Corso, and P. Giannozzi, *Rev. Mod. Phys.* **73**, 515 (2001).
- [18] P. Giannozzi and S. Baroni, in *Handbook of Materials Modeling*, edited by S. Yip (Springer, Berlin, 2005), pp. 195–214.
- [19] X. Gonze, F. Jollet, F. A. Araujo, D. Adams, B. Amadon, T. Applencourt, C. Audouze, J.-M. Beuken, J. Bieder, A. Bokhanchuk, E. Bousquet, F. Bruneval, D. Caliste, M. Côté, F. Dahm, F. D. Pieve, M. Delaveau, M. D. Gennaro, B. Dorado, C. Espejo *et al.*, *Comput. Phys. Commun.* **205**, 106 (2016), available at <http://www.abinit.org>
- [20] P. Giannozzi, O. Andreussi, T. Brumme, O. Bunau, M. Buongiorno Nardelli, M. Calandra, R. Car, C. Cavazzoni, D. Ceresoli, M. Cococcioni, N. Colonna, I. Carnimeo, A. Dal Corso, S. de Gironcoli, P. Delugas, R. A. DiStasio, A. Ferretti, A. Floris, G. Fratesi, G. Fugallo *et al.*, *J. Phys.: Condens. Matter* **29**, 465901 (2017), available at <http://www.quantum-espresso.org>
- [21] P. E. Blöchl, *Phys. Rev. B* **50**, 17953 (1994).
- [22] N. A. W. Holzwarth, A. R. Tackett, and G. E. Matthews, *Comput. Phys. Commun.* **135**, 329 (2001), available at <http://pwpaw.wfu.edu>
- [23] N. A. W. Holzwarth, *Comput. Phys. Commun.* **243**, 25 (2019).
- [24] K. Momma and F. Izumi, *Appl. Crystallogr.* **44**, 1272 (2011), code available at <http://jp-minerals.org/vesta/en/>
- [25] A. Kokalj, *Comput. Mater. Sci.* **28**, 155 (2003), code available at <http://www.xcrysden.org>
- [26] H. T. Stokes and D. M. Hatch, *J. Appl. Crystallogr.* **38**, 237 (2008), available at <http://iso.byu.edu/iso/isotropy.php>
- [27] MERCURY 3.5.1 (2014), developed and distributed by the Cambridge Crystallographic Data Centre, <http://www.ccdc.cam.ac.uk/mercury/>
- [28] M. I. Aroyo, J. M. Perez-Mato, D. Orobengoa, E. Tasci, G. De La Flor, and A. Kirov, *Bulg. Chem. Commun.* **42**, 183 (2011), available at <http://www.cryst.ehu.es/>
- [29] J. P. Perdew and Y. Wang, *Phys. Rev. B* **45**, 13244 (1992).
- [30] Y. A. Du and N. A. W. Holzwarth, *Phys. Rev. B* **76**, 174302 (2007).
- [31] G. Petretto, S. Dwaraknath, H. P.C. Miranda, D. Winston, M. Giantomassi, M. J. van Setten, X. Gonze, K. A. Persson, G. Hautier, and G.-M. Rignanese, *Sci. Data* **5**, 180065 (2018).
- [32] L. He, F. Liu, G. Hautier, M. J. T. Oliveira, M. A. L. Marques, F. D. Vila, J. J. Rehr, G.-M. Rignanese, and A. Zhou, *Phys. Rev. B* **89**, 064305 (2014).
- [33] J. P. Perdew, A. Ruzsinszky, G. I. Csonka, O. A. Vydrov, G. E. Scuseria, L. A. Constantin, X. Zhou, and K. Burke, *Phys. Rev. Lett.* **100**, 136406 (2008).
- [34] M. Born and K. Huang, *Dynamical Theory of Crystal Lattices* (Oxford University Press, Oxford, 1954).
- [35] A. A. Maradudin, E. W. Montroll, G. H. Weiss, and I. P. Ipatova, *Theory of Lattice Dynamics in the Harmonic Approximation*, 2nd ed., *Solid State Physics: Supplement* (Academic, New York, 1971), Vol. 3.
- [36] H. J. Monkhorst and J. D. Pack, *Phys. Rev. B* **13**, 5188 (1976).
- [37] J. Howard, Z. D. Hood, and N. A. W. Holzwarth, *Phys. Rev. Mater.* **1**, 075406 (2017).
- [38] Y. Li, W. C. Kerr, and N. A. W. Holzwarth, *J. Phys.: Condens. Matter* **32**, 055402 (2019).
- [39] X. Gonze, B. Amadon, G. Antonius, F. Arnardi, L. Baguet, J.-M. Beuken, J. Bieder, F. Bottin, J. Bouchet, E. Bousquet, N. Brouwer, F. Bruneval, G. Brunin, T. Cavignac, J.-B. Charraud, W. Chen, M. Côté, S. Cottenier, J. Denier, G. Geneste *et al.*, *Comput. Phys. Commun.* **248**, 107042 (2019).
- [40] Y. A. Du and N. A. W. Holzwarth, *ECS Trans.* **25**, 27 (2010).
- [41] P. Umari, A. Pasquarello, and A. Dal Corso, *Phys. Rev. B* **63**, 094305 (2001).
- [42] M. Veithen, X. Gonze, and P. Ghosez, *Phys. Rev. B* **71**, 125107 (2005).
- [43] S. A. Prosandeev, U. Waghmare, I. Levin, and J. Maslar, *Phys. Rev. B* **71**, 214307 (2005).
- [44] H. Hamaguchi, in *Advances in Infrared and Raman Spectroscopy*, edited by R. J. H. Clark and R. E. Hester (Wiley, New York, 1985), Vol. 12, pp. 273–310.
- [45] H. Jónsson, G. Mills, and K. W. Jacobsen, in *Classical and Quantum Dynamics in Condensed Phase Simulations*, edited by B. J. Berne, G. Ciccotti, and D. F. Coker (World Scientific, Singapore, 1998), pp. 385–404.
- [46] G. Henkelman, B. P. Uberuaga, and H. Jónsson, *J. Chem. Phys.* **113**, 9901 (2000).
- [47] G. Henkelman and H. Jónsson, *J. Chem. Phys.* **113**, 9978 (2000).
- [48] L. Verlet, *Phys. Rev.* **159**, 98 (1967).
- [49] X. He, Y. Zhu, A. Epstein, and Y. Mo, *npj Comput. Mater.* **4**, 18 (2018).
- [50] G. E. Murch, *Solid State Ionics* **7**, 177 (1982).
- [51] J. D. Howard and N. Holzwarth, *Solid State Ionics* **325**, 80 (2018).
- [52] K. Campaan and Y. Haven, *Trans. Faraday Soc.* **54**, 1498 (1958).

- [53] Y. Haven and B. Verkerk, *Phys. Chem. Glasses* **6**, 38 (1965).
- [54] D. Hicks, M. J. Mehl, E. Gossett, C. Toher, O. Levy, R. M. Hanson, G. Hart, and S. Curtarolo, *Comput. Mater. Sci.* **161**, S1 (2019).
- [55] M. J. Mehl, D. Hicks, C. Toher, O. Levy, R. M. Hanson, G. Hart, and S. Curtarolo, *Comput. Mater. Sci.* **136**, S1 (2017).
- [56] Y. Hinuma, G. Pizzi, Y. Kumagai, F. Oba, and I. Tanaka, *Comput. Mater. Sci.* **128**, 140 (2017).
- [57] D. R. Hamann, *Phys. Rev. B* **88**, 085117 (2013).
- [58] M. van Setten, M. Giantomassi, E. Bousquet, M. Verstraete, D. Hamann, X. Gonze, and G.-M. Rignanese, *Comput. Phys. Commun.* **226**, 39 (2018), data sets available at <http://www.pseudo-dojo.org/>
- [59] A. Brown and S. Rundqvist, *Acta Crystallogr.* **19**, 684 (1965).
- [60] S. J. Rettig and J. Trotter, *Acta Crystallogr., Sect. C: Cryst. Struct. Commun.* **43**, 2260 (1987).
- [61] K. Homma, M. Yonemura, T. Kobayashi, M. Nagao, M. Hirayama, and R. Kanno, *Solid State Ionics* **182**, 53 (2011).
- [62] P. C. Minshall and G. M. Sheldrick, *Acta Crystallogr. B* **34**, 1326 (1978).
- [63] M. Jansen and U. Henseler, *J. Solid State Chem.* **99**, 110 (1992).
- [64] A. Vos, R. Olthof, F. van Bolhuis, and R. Botterweg, *Acta Crystallogr.* **19**, 864 (1965).
- [65] M. R. Sørensen and A. F. Voter, *J. Chem. Phys.* **112**, 9599 (2000).
- [66] Y. Mo, S. P. Ong, and G. Ceder, *Chem. Mater.* **24**, 15 (2012).

Appendix B

Continuity of phonon dispersion curves in layered ionic materials

PAPER

Continuity of phonon dispersion curves in layered ionic materials

To cite this article: Yan Li *et al* 2020 *J. Phys.: Condens. Matter* **32** 055402

View the [article online](#) for updates and enhancements.



IOP | ebooks™

Bringing you innovative digital publishing with leading voices to create your essential collection of books in STEM research.

Start exploring the collection - download the first chapter of every title for free.

This content was downloaded from IP address 152.17.143.184 on 01/11/2019 at 13:46

Continuity of phonon dispersion curves in layered ionic materials

Yan Li¹, W C Kerr¹ and N A W Holzwarth¹

Physics Department, Wake Forest University, Winston-Salem, NC, United States of America

E-mail: natalie@wfu.edu

Received 1 August 2019, revised 26 September 2019

Accepted for publication 10 October 2019

Published 1 November 2019



Abstract

The coupling of lattice vibrations with macroscopic electric fields in ionic crystals is examined from first principles based on density functional theory and density functional perturbation theory. Our analyses show that the coupled optical phonon–photon modes are well represented by using the pure phonon modes evaluated at $\mathbf{q} = 0$ as a basis. In addition, we find that apparent ‘discontinuities’ and mode ‘disappearances’ in the phonon dispersion curves of ionic materials for $\mathbf{q} \rightarrow 0$ in hexagonal and other anisotropic materials are caused by the directional dependence of the Born effective charge tensor which is responsible for this coupling. The full dispersion curves, including the phonon–photon transverse modes are shown to be continuous functions of wavevector. Our work in this report provides a promising tool for first principles evaluation of phonon polaritons that may be accessible to experiment. Explicit examples are explored for cubic and hexagonal BN; the calculated results are in good agreement with previous computational values and available experimental measurements.

Keywords: phonon-polariton, first principles calculations, ionic crystals

(Some figures may appear in colour only in the online journal)

1. Introduction

Intuitively, physical quantities are expected to be continuous functions of their variables, so it is a surprise to find discontinuities in phonon dispersion curves. Figure 1 shows a typical representation of phonon dispersion, where the normal mode frequencies $\omega^\nu(\mathbf{q})$ are plotted as a function of phonon wavevector \mathbf{q} along special directions of the Brillouin zone for boron nitride in the zincblende structure¹. For this cubic structure, the phonon dispersion curves $\omega^\nu(\mathbf{q})$ appear to be continuous functions of \mathbf{q} . By contrast, in examining phonon dispersion curves for ionic materials having hexagonal or other layered structures [1], we often find apparent discontinuities or mode disappearances near the Γ point of the Brillouin zone. For example, figure 2 shows the phonon dispersion curves for boron nitride in the hexagonal structure. For this hexagonal structure, two of the optic phonon dispersion curves with wavevector \mathbf{q} pointing in a direction within

a layer plane ($\mathbf{M} \rightarrow \Gamma$) end abruptly at the Γ point and seem to have no presence in the phonon band diagram for the wavevector \mathbf{q} pointing in the perpendicular direction ($\Gamma \rightarrow \mathbf{A}$). In reality, the phonon band diagram represents the same number of vibrational modes (in this case 12) throughout the Brillouin zone.

The physical reasons for these discontinuities were explained in 1951 by Huang [2] and are detailed in several textbooks [3–6]. The explanation is based on the analysis of the coupling of some of the vibrational modes to long wavelength electromagnetic waves within the material including the effects of Maxwell’s equations on the system. In this report, we show how the dispersion curves of the coupled phonon–photon modes can be calculated from first principles and can be included in a modified phonon band diagram in the $|\mathbf{q}| \rightarrow 0$ range. The photon-phonon normal modes of cubic and hexagonal BN are examined as examples.

The remainder of this paper is organized as follows. Section 2 details the general formalism. Section 3 presents the results for BN, including a description of the first principles methods (section 3.1) and results for the phonon–photon dispersions in the vicinity of $\mathbf{q} \rightarrow 0$ range for cubic and

¹ Following usual practices, for plotting and tabulation purposes, instead of representing frequencies in radians per second, we use throughout the manuscript $\omega^\nu(\mathbf{q})/(2\pi c)$ in units of (cm^{-1}) . Here c denotes the speed of light in vacuum.

hexagonal BN (section 3.2). Section 4 contains the summary and conclusions.

2. Formalism

The first principles formalism for evaluating vibrational modes of periodic solids within the framework of the Born–Oppenheimer approximation [3] and density functional theory [8, 9], has been developed using density functional perturbation theory (DFPT) by a number of authors [10–14]. This formalism has been implemented in several electronic structure code packages such as ABINIT [15] and Quantum ESPRESSO [16]. In the following, we approximately follow the notation of [13] and [14], using Gaussian units.

The starting point of the analysis is a self-consistent density functional calculation to find the optimized total energy of the crystalline material, finding the optimized lattice vectors \mathbf{a} , \mathbf{b} , and \mathbf{c} , the optimized coordinates τ_s of the N atoms labeled s within the unit cell, and the corresponding static lattice energy per unit cell U_{SL} . Here τ_s represents the equilibrium position within a unit cell and any given cell within the material can be represented relative to the origin by a translation vector $\mathbf{R}_l = l_1\mathbf{a} + l_2\mathbf{b} + l_3\mathbf{c}$ where l_i denote integer values. Consider that an optimized atomic position in unit cell at position \mathbf{R}_l is displaced by a small vector $\mathbf{u}_s(l)$.

$$\mathbf{R}_l + \tau_s \rightarrow \mathbf{R}_l + \tau_s + \mathbf{u}_s(l). \quad (1)$$

It is convenient to perform the analysis in phonon wavevector space. For a given phonon wavevector \mathbf{q} within the Brillouin zone,

$$\mathbf{u}_s(l) = \mathbf{u}_s(\mathbf{q})e^{i\mathbf{q}\cdot\mathbf{R}_l}, \quad (2)$$

where $\mathbf{u}_s(\mathbf{q})$ represents the complex amplitude of the atomic displacement associated with atom s and wavevector \mathbf{q} . Then, within the harmonic approximation, and using DFPT, it is possible to evaluate the analytic part of the second derivative matrix

$$\tilde{C}_{s\alpha,t\beta}(\mathbf{q}) = \frac{\partial^2 U_{SL}}{\partial u_{s\alpha}^*(\mathbf{q}) \partial u_{t\beta}(\mathbf{q})}. \quad (3)$$

Here, α and β denote the Cartesian coordinate directions x , y , or z . For most of the Brillouin zone where $|\mathbf{q}| > 0$, and within the Born–Oppenheimer approximation [3], the ion motion can be determined from the classical equations of motion in terms of the harmonic restoring force represented by the second derivative matrix (equation (3)) according to the equation

$$M_s \frac{\partial^2 u_{s\alpha}(\mathbf{q})}{\partial t^2} = - \sum_{t\beta} \tilde{C}_{s\alpha,t\beta}(\mathbf{q}) u_{t\beta}(\mathbf{q}). \quad (4)$$

Here, M_s denotes the mass of atom s . In this analysis, we have assumed that the displacement is a continuous function of time t according to $\mathbf{u}_s(\mathbf{q}) \rightarrow \mathbf{u}_s(\mathbf{q}, t) \rightarrow \mathbf{u}_s(\mathbf{q})e^{-i\omega t}$, where the last expression includes the further assumption of a harmonic time dependence. Typically these equations are solved in terms of normal modes of vibration with eigenfrequencies ω^ν and eigendisplacements $u_{s\alpha}^\nu$:

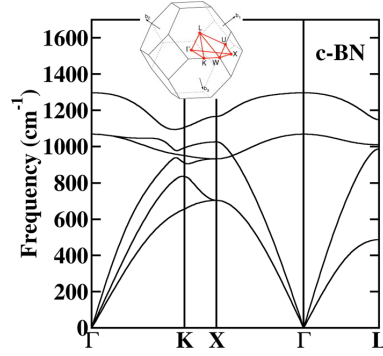


Figure 1. Phonon dispersion curves ($\omega^\nu(\mathbf{q})$) for cubic BN. The inset Brillouin zone diagram was reprinted from Setyawan *et al* [7], copyright (2010), with permission from Elsevier.

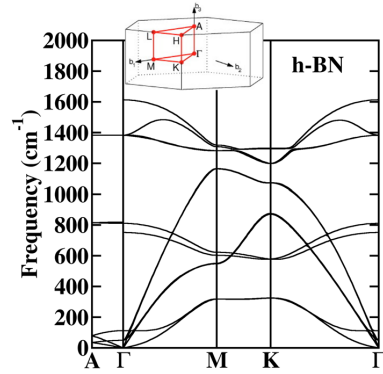


Figure 2. Phonon dispersion curves ($\omega^\nu(\mathbf{q})$) for hexagonal BN. The inset Brillouin zone diagram was reprinted from Setyawan *et al* [7], copyright (2010), with permission from Elsevier.

$$(\omega^\nu(\mathbf{q}))^2 M_s u_{s\alpha}^\nu(\mathbf{q}) = \sum_{t\beta} \tilde{C}_{s\alpha,t\beta}(\mathbf{q}) u_{t\beta}^\nu(\mathbf{q}), \quad (5)$$

where ν labels each of the $3N$ normal mode solutions corresponding to a unit cell with N atoms. It is convenient to normalize the eigendisplacements according to

$$\sum_{s\alpha} |u_{s\alpha}^\nu(\mathbf{q})|^2 = 1. \quad (6)$$

Note that the eigendisplacements satisfy an orthogonality condition

$$\sum_{s\alpha} M_s (u_{s\alpha}^{\nu'}(\mathbf{q}))^* u_{s\alpha}^\nu(\mathbf{q}) = M^\nu \delta_{\nu'\nu}, \quad (7)$$

where M^ν denotes a mode effective mass.

However, in the long wavelength limit as $\mathbf{q} \rightarrow 0$, the ionic motion couples to the macroscopic electric field. The coupling depends on the Born effective charge tensor for each atom [17] which can be calculated by evaluating the response of the system to an electric field using DFPT. A convenient expression for the Born effective charge tensor is

$$eZ_{\alpha\beta}^{*s} = - \left. \frac{\partial^2 U_{SL}}{\partial u_{s\alpha}(\mathbf{q}=0) \partial E_\beta} \right|_{u_{s\alpha}=0, E_\beta=0}. \quad (8)$$

Here e denotes the elementary charge and E_β denotes an electric field in the β direction and the derivative is evaluated in the limit of zero field value. We note the asterisk in the notation (equation (8)) does not imply complex conjugation [12]. It can be shown [12, 18] that the Born effective charge tensor satisfies the relation for each combination of $\alpha\beta$

$$\sum_s Z_{\alpha\beta}^{*s} = 0. \quad (9)$$

On the other hand, the tensor properties of $Z_{\alpha\beta}^{*s}$ depend on the site symmetry of atom s and for some materials it is possible that the Born effective charge tensor is not symmetric such that [19]

$$Z_{\alpha\beta}^{*s} \neq Z_{\beta\alpha}^{*s}. \quad (10)$$

Because of the coupling of the ion motion to the long wavelength electric field, in the $\mathbf{q} \rightarrow 0$ range, the ionic displacements are described by the modified equations of motion determined by both the harmonic restoring force represented by the second derivative matrix (equation (3)) and the coupling due to the Born effective charge tensor (equation (8)) to an electric field.

$$M_s \frac{\partial^2 w_{s\alpha}(\mathbf{q})}{\partial t^2} = - \sum_{t\beta} \tilde{C}_{s\alpha,t\beta}(\mathbf{q}) w_{t\beta}(\mathbf{q}) + \sum_{\beta} e Z_{\alpha\beta}^{*s} E_\beta(\mathbf{q}). \quad (11)$$

Here we introduced the notation $\mathbf{w}_s(\mathbf{q}) \rightarrow \mathbf{w}_s(\mathbf{q}, t) \rightarrow \mathbf{w}_s(\mathbf{q})e^{-i\omega t}$ to represent the atomic displacements coupled to the electric field in order to distinguish them from their uncoupled counter parts $\mathbf{u}_s(\mathbf{q})$. In turn, the related electric displacement field $\mathbf{D}(\mathbf{q})$ is composed of electric field $\mathbf{E}(\mathbf{q})$ screened by the electronic response as characterized by the electronic part of the dielectric permittivity tensor which is often denoted as $\epsilon_{\alpha\beta}^\infty$ and the additional polarization field introduced by the vibrating ions according to:

$$D_\alpha(\mathbf{q}) = \sum_{\beta} \epsilon_{\alpha\beta}^\infty E_\beta(\mathbf{q}) + \frac{4\pi e}{\Omega} \sum_{t\beta} Z_{\alpha\beta}^{*t} w_{t\beta}(\mathbf{q}). \quad (12)$$

Here Ω denotes the volume of the unit cell.

We assume that our material is insulating and neutral so that the sourceless Maxwell's equations apply. We also assume that there are no magnetic dipolar effects so that the two relations for the electric and displacement fields in the $\mathbf{q} \rightarrow 0$ range resulting from Maxwell's equations are given by

$$\nabla \cdot \mathbf{D} = 0, \quad (13)$$

and

$$\nabla \times (\nabla \times \mathbf{E}) + \frac{1}{c^2} \frac{\partial^2 \mathbf{D}}{\partial t^2} = 0. \quad (14)$$

In this $\mathbf{q} \rightarrow 0$ range, we approximate the lattice displacements as continuous functions of position responding to the macroscopic electric and magnetic fields within the material, seeking plane-wave-like solutions with

$$\mathbf{w}_s(t) \rightarrow \mathbf{w}_s^0(\mathbf{q})e^{i\mathbf{q}\cdot\mathbf{r}-i\omega t} \quad \text{and} \quad \mathbf{E}(\mathbf{q}) = \mathbf{E}^0(\mathbf{q})e^{i\mathbf{q}\cdot\mathbf{r}-i\omega t}. \quad (15)$$

In order to solve the coupled equations (11), (13) and (14), it is reasonable to assume that the amplitude of the displacements can be expressed as a linear combination of the pure vibrational normal modes with unknown amplitudes U^ν

$$w_{s\alpha}^0(\mathbf{q}) = \sum_{\nu} U^\nu(\mathbf{q}) u_{s\alpha}^\nu(\mathbf{q}). \quad (16)$$

Since the analysis is performed in the $\mathbf{q} \rightarrow 0$ limit the amplitude and eigenvectors can be evaluated at $\mathbf{q} = 0$. Accordingly we will drop the \mathbf{q} argument in most of the following analysis. The coupling effects of the atomic motions and the electric field are controlled by the sum of the Born effective charges multiplied by the normal mode displacements which can be evaluated for each normal mode. It is convenient to define two summations according to

$$\mathcal{R}_\alpha^\nu \equiv \sum_{t\beta} Z_{\alpha\beta}^{*t} u_{t\beta}^\nu \quad (17)$$

and

$$\mathcal{L}_\beta^\nu \equiv \sum_{s\alpha} (u_{s\alpha}^\nu)^* Z_{\alpha\beta}^{*s}. \quad (18)$$

For many modes ν , the Born coupling parameters are trivial; $\mathcal{L}_\beta^\nu = \mathcal{R}_\beta^\nu = 0$. Non-trivial values of \mathcal{L}_β^ν and \mathcal{R}_β^ν indicate that for this mode, the displacement eigenvector creates an oscillating electrical polarization which typically interacts with external infrared radiation. For nontrivial modes, the two coupling parameters \mathcal{L}_β^ν and \mathcal{R}_β^ν need not be related. However for crystalline materials having atomic sites with high symmetry such that relationships in equation (10) are equalities, the two coefficients are related according to $\mathcal{R}_\alpha^\nu = (\mathcal{L}_\alpha^\nu)^*$. By using the expansion (equation (16)) to evaluate the equation of motion for the displacements (equation (11)), we find that the amplitudes U^ν are proportional to the electric field according to

$$U^\nu = \frac{e}{((\omega^\nu)^2 - \omega^2) M^\nu} \sum_{\beta} \mathcal{L}_\beta^\nu E_\beta^0. \quad (19)$$

These amplitudes can be used in equation (12) to evaluate the frequency-dependent electric displacement field and the corresponding frequency-dependent dielectric tensor according to

$$\epsilon_{\alpha\beta}(\omega) = \epsilon_{\alpha\beta}^\infty + \frac{4\pi e^2}{\Omega} \sum_{\nu} \frac{\mathcal{R}_\alpha^\nu \mathcal{L}_\beta^\nu}{((\omega^\nu)^2 - \omega^2) M^\nu}. \quad (20)$$

This expression is equivalent to a similar analysis by Gonze and Lee [12] and some of the ideas are presented in textbooks such as Maradudin *et al* [5]. Equation (20) is valid for frequencies ω small enough such that $\hbar\omega < E_g$, where E_g represents the electronic band gap. This restriction is consistent with the assumption that the electronic dielectric contribution $\epsilon_{\alpha\beta}^\infty$ is constant. The estimation of the static dielectric constant, $\epsilon_{\alpha\beta}^0$, evaluated by setting $\omega \rightarrow 0$ is expected to be well justified by the expression

$$\epsilon_{\alpha\beta}^0 \equiv \epsilon_{\alpha\beta}(\omega = 0) = \epsilon_{\alpha\beta}^\infty + \frac{4\pi e^2}{\Omega} \sum_\nu \frac{\mathcal{R}_\alpha^\nu \mathcal{L}_\beta^\nu}{(\omega^\nu)^2 M^\nu}. \quad (21)$$

It is interesting to mention that equation (20) is consistent with a Drude-like model of the ionic contributions to the dielectric function, where $(\mathcal{R}_\alpha^\nu \mathcal{L}_\beta^\nu)/(M^\nu/m_e)$ represents an oscillator strength, with m_e denoting the electron mass. Missing from the analysis and from equation (20) are considerations of damping processes that may more fully describe the driven oscillator system. Using the notation γ^ν to represent the damping coefficient for mode ν , equation (20) would be modified with an imaginary contribution with alteration of the denominator

$$\left((\omega^\nu)^2 - \omega^2\right) \rightarrow \left((\omega^\nu)^2 - \omega^2 - i\omega\gamma^\nu\right). \quad (22)$$

However, these damping effects are outside the scope of the present study.

In order to now solve Maxwell's equations (equations (13) and (14)) in the long wavelength limit, we consider two cases in terms of the orientation of the wavevector \mathbf{q} relative to the electric field orientation. For the case of a longitudinal electric field, the electric field is along the wavevector direction as represented by the unit vector $\hat{\mathbf{q}}$; $E_L^0 = \mathbf{E}^0 \cdot \hat{\mathbf{q}}$. For the case of a transverse electric field, it is convenient to define the propagation direction $\hat{\mathbf{q}}$ and two perpendicular transverse directions denoted by unit vectors $\hat{\mathbf{T}}_1$ and $\hat{\mathbf{T}}_2$. In this case the electric field \mathbf{E}_T^0 is in the plane spanned by \mathbf{T}_1 and \mathbf{T}_2 . For example, the longitudinal and transverse matrix elements of the electronic dielectric tensor can be written

$$\epsilon_{LL}^\infty \equiv \sum_{\alpha\beta} \hat{q}_\alpha \epsilon_{\alpha\beta}^\infty \hat{q}_\beta \quad \text{and} \quad \epsilon_{T_i T_j}^\infty \equiv \sum_{\alpha\beta} \hat{T}_{i\alpha} \epsilon_{\alpha\beta}^\infty \hat{T}_{j\beta}, \quad (23)$$

where $i, j = 1, 2$. Similarly, we can define longitudinal and transverse components of the Born coupling parameters such as

$$\mathcal{R}_L^\nu \equiv \sum_\alpha \mathcal{R}_\alpha^\nu \hat{q}_\alpha \quad \text{and} \quad \mathcal{L}_L^\nu \equiv \sum_\beta \mathcal{L}_\beta^\nu \hat{q}_\beta \quad (24)$$

for the longitudinal Born coupling parameters, and similar expressions can be written for the transverse coupling parameters.

In the following analysis, we assume that the dielectric tensor (equation (20)) is block diagonal in the directions $\hat{\mathbf{q}}$, $\hat{\mathbf{T}}_1$, and $\hat{\mathbf{T}}_2$. Mixed longitudinal and transverse solutions will not be considered in this analysis.

For the longitudinal solutions, the \mathbf{E} and \mathbf{D} fields both are along the direction $\hat{\mathbf{q}}$. However, Maxwell's equations (equations (13) and (14)) require that the longitudinal component of the frequency-dependent dielectric tensor (equation (20)) vanishes:

$$\epsilon_{LL} = \epsilon_{LL}^\infty + \frac{4\pi e^2}{\Omega} \sum_\nu \frac{\mathcal{R}_L^\nu \mathcal{L}_L^\nu}{\left((\omega^\nu)^2 - \omega^2\right) M^\nu} = 0. \quad (25)$$

Here, the summation is taken only over nontrivial modes ν . For any given longitudinal direction $\hat{\mathbf{q}}$, the number n_L of

nontrivial values of longitudinal Born coupling parameters \mathcal{R}_L^ν and \mathcal{L}_L^ν is less than the total number of normal modes ($3N$). The general solution of equation (25) requires the solution of a n_L^{th} order polynomial in the variable ω^2 . In the special case that $n_L = 1$ and the nontrivial mode is written with index ν , the solution to equation (25) takes the form

$$\omega^2 \equiv \omega_L^2 = (\omega^\nu)^2 + \frac{1}{\epsilon_{LL}^\infty} \frac{4\pi e^2}{\Omega M^\nu} \mathcal{R}_L^\nu \mathcal{L}_L^\nu. \quad (26)$$

This longitudinal 'LO' mode does not depend on \mathbf{q} .

An alternative approach was developed by Giannozzi and others [10, 12, 13] and included in the ABINIT and QUANTUM ESPRESSO codes, for example, combining the longitudinal component of equation (12) with the longitudinal component of equation (11) to directly solve for the $\mathbf{q} \rightarrow 0$ longitudinal modes according to the equation

$$\omega^2 M_s w_{s\alpha}^0(\mathbf{q}) = \sum_{i\beta} \tilde{C}_{s\alpha, i\beta}^{\text{tot}}(\mathbf{q}) w_{i\beta}^0(\mathbf{q}). \quad (27)$$

Here

$$\tilde{C}_{s\alpha, i\beta}^{\text{tot}}(\mathbf{q}) = \tilde{C}_{s\alpha, i\beta}(\mathbf{q}) + \frac{4\pi e^2}{\Omega \epsilon_{LL}^\infty} Z_{L\alpha}^{*s} Z_{\beta L}^{*i}. \quad (28)$$

The second term of equation (28) is usually referenced as the non-analytic contribution to the second derivative matrix. The direct solution of equation (27) gives the corrected eigenmodes of the longitudinal atomic displacements in the $\mathbf{q} \rightarrow 0$ range. Note that for this longitudinal case, even though the long wavelength electrical field is polarized in the longitudinal direction, some of the atomic displacements may have components in other directions. It has been noted by Gonze and Lee [12] that the eigenvectors of equation (27) are not necessarily the same as the eigenvectors of equation (5). In fact, if we use the pure phonon mode basis to represent the atomic displacements in equation (27) as in equation (16), we see that the non-analytic term can cause mixing of the pure phonon modes. It is possible to determine the n_L eigenvalues ω_L^2 of equation (27) by diagonalizing a $n_L \times n_L$ matrix $\mathcal{G}_{\nu\nu'}^L$ in the pure phonon mode basis.

$$\sum_{\nu'} \mathcal{G}_{\nu\nu'}^L U^{\nu'} = \omega_L^2 U^\nu. \quad (29)$$

The matrix elements are given by

$$\mathcal{G}_{\nu\nu'}^L = (\omega^\nu)^2 \delta_{\nu\nu'} + \frac{1}{\epsilon_{LL}^\infty} \frac{4\pi e^2}{\Omega M^\nu} \mathcal{L}_L^\nu \mathcal{R}_L^{\nu'}. \quad (30)$$

This is equivalent to solving the polynomial equation implied by equation (25) or to directly solving equation (27). However, the advantage of solving the eigenvalue problem of equation (29) is that for each eigenvalue ω_L^2 , one can also determine the corresponding eigenvector in terms of the amplitudes U^ν of the n_L coupled pure phonon modes.

For the transverse solutions, Maxwell's equation (13) is always satisfied since the wavevector is perpendicular the electric field direction, while Maxwell's equation (14) describes another \mathbf{q} -dependent coupling relationship between

the fields and ion motions. The solutions $\omega^2 = \omega_T^2$ must satisfy Maxwell's equations for the transverse case according to the following relationships:

$$\sum_{T_i} \left(q^2 c^2 \delta_{T_i T_i} - \omega_T^2 \left(\epsilon_{T_i T_i}^\infty + \frac{4\pi e^2}{\Omega} \sum_{\nu'} \frac{\mathcal{R}_{T_i}^\nu \mathcal{L}_{T_i}^\nu}{(\omega^\nu)^2 - \omega_T^2} \mathbf{M}^\nu \right) \right) E_{T_i}^0 = 0. \quad (31)$$

For any given choice of transverse directions $\hat{\mathbf{T}}_i$ and $\hat{\mathbf{T}}_j$, the number n_T of nontrivial values of the transverse Born coupling parameters $\mathcal{R}_{T_i}^\nu$ and $\mathcal{L}_{T_i}^\nu$ is less than the total number of normal modes ($3N$). The general solutions of equation (31) requires the solution of a $2n_T^{\text{th}}$ order polynomial in the variable ω^2 . In the special case that $n_T = 1$, the transverse electronic dielectric tensor $\epsilon_{T_i T_i}^\infty$ is diagonal, and the nontrivial mode is written with index ν , the solution to equation (31) for a given value of the wavevector q , takes the form

$$\omega_{T_i \pm}^2(\mathbf{q}) = \frac{q^2 c^2 + (\omega^\nu)^2 \epsilon_{T_i T_i}^\infty + \mathcal{A}^\nu}{2\epsilon_{T_i T_i}^\infty} (1 \pm \mathcal{S}^\nu(\mathbf{q})). \quad (32)$$

Here,

$$\mathcal{S}^\nu(\mathbf{q}) \equiv \sqrt{1 - \frac{4q^2 c^2 (\omega^\nu)^2 \epsilon_{T_i T_i}^\infty}{(q^2 c^2 + (\omega^\nu)^2 \epsilon_{T_i T_i}^\infty + \mathcal{A}^\nu)^2}}, \quad (33)$$

and

$$\mathcal{A}^\nu \equiv \frac{4\pi e^2}{\Omega M^\nu} \mathcal{R}_{T_i}^\nu \mathcal{L}_{T_i}^\nu. \quad (34)$$

In the neighborhood of $\mathbf{q} = 0$, the '+' branch of the transverse modes takes the value

$$\omega_{T_i+}^2(\mathbf{q} \approx 0) = (\omega^\nu)^2 + \frac{1}{\epsilon_{T_i T_i}^\infty} \frac{4\pi e^2}{\Omega M^\nu} \mathcal{R}_{T_i}^\nu \mathcal{L}_{T_i}^\nu + S q^2 c^2. \quad (35)$$

The value of $\omega_{T_i+}^2(\mathbf{q} = 0)$ is numerically the same as the longitudinal solution in equation (26) when the electric field directions are geometrically the same. For $q > 0$, the dispersion is that of a photon mode with quadratic coefficient $S = 1/\epsilon_{T_i T_i}^\infty - 1/\epsilon_{T_i T_i}^0$. The '-' branch of the transverse modes in the $\mathbf{q} \rightarrow 0$ range have linear dispersion with the form $\omega_{T_i-}(\mathbf{q}) = qc/\sqrt{\epsilon_{T_i T_i}^0}$ for $\mathbf{q} \approx 0$. For larger values of wavevector, $\mathbf{q} \gg \omega^\nu c/\sqrt{\epsilon_{T_i T_i}^\infty}$, the frequency of the transverse modes is asymptotic to $\omega_{T_i-}(\mathbf{q}) = \omega^\nu$, the normal mode frequency without electric field effects and identifies as a 'TO' mode. In summary, the solution for $\omega_{T_i-}(\mathbf{q})$ is photon-like at very small values of q and becomes phonon-like, at larger values of q . The expressions discussed in this section will be illustrated for the example of BN in section 3.2. More general analysis for choices of the transverse directions $\hat{\mathbf{T}}_i$ have been worked out for the case of α -GaN by Irmer *et al* [20] which isostructural to hexagonal BN.

It is also possible to write the general equations for the transverse modes for the case $n_T > 1$ in the pure phonon basis similarly to equation (29). The general expression can be written in terms of a generalized eigenvalue problem of the form

$$\sum_{\nu'} \mathcal{G}_{\nu\nu'}^T U^{\nu'} = \omega_T^2 U^\nu, \quad (36)$$

where the $n_T \times n_T$ matrix $\mathcal{G}_{\nu\nu'}^T$ is given by

$$\mathcal{G}_{\nu\nu'}^T \equiv (\omega^\nu)^2 \delta_{\nu\nu'} + \frac{4\pi e^2}{\Omega M^\nu} \sum_{T_i T_j} \left(\epsilon_{T_i T_i}^\infty - \frac{q^2 c^2}{\omega_T^2} \mathbf{1} \right)_{T_i T_j}^{-1} \mathcal{L}_{T_i}^\nu \mathcal{R}_{T_j}^{\nu'}. \quad (37)$$

This is not a usual eigenvalue problem since the eigenvalue ω_T^2 appears in the expression of the matrix $\mathcal{G}_{\nu\nu'}^T$; however iterative methods can be used to solve equation (36). Because of this, there are generally two solutions for each value of \mathbf{q} corresponding to the $\omega_{T\pm}(\mathbf{q})$ branches. The limiting values of the results for $q = 0$ and $q \gg \omega^\nu c/\sqrt{\epsilon_{T_i T_i}^\infty}$ derived for the simple case can be seen from the form of equation (37).

Note that in all of these expressions, the value of the phonon-photon coupling is controlled by Born coupling parameters defined in equations (17) and (18) \mathcal{R}_α^ν and \mathcal{L}_α^ν , where α is the direction of the atomic displacements for the pure phonon mode ν . Whether the full solution to the coupled phonon-photon equations is longitudinal or transverse depends on the direction of the wavevector \mathbf{q} relative to the direction α . Because of the form of the non-trivial Born coupling parameters \mathcal{L}_β^ν and \mathcal{R}_β^ν , the modes ν are often labeled as 'optical' modes 'LO' or 'TO' corresponding to longitudinal or transverse, respectively. The ω_{LO} frequencies are shifted relative to the frequencies ω^ν of the pure phonon vibrations according to equations (29) and (30) due to their coupling to the long wavelength electric fields. However the ω_{TO} frequencies correspond to $\omega_{T-}(q \gg \omega^\nu c/\sqrt{\epsilon_{T_i T_i}^\infty}) = \omega^\nu$, that is having the same magnitude as the uncoupled transverse Γ point phonon vibrations. While the ABINIT and QUANTUM ESPRESSO codes do not explicitly consider the coupled transverse phonon-photon modes, all of the necessary parameters are calculated in order to evaluate equations (30) and (37).

3. Example results for cubic and hexagonal BN

While the equations presented in section 2 apply generally to all insulating ionic crystals, it is useful to illustrate the results for the simple and well-studied example of boron nitride so that we can compare with a large literature of experimental [21–28] and computational [29–38] reports.

3.1. Computational methods

The structural optimizations were based on density functional theory (DFT) [8, 9] and the phonon frequencies and eigenvectors of normal vibrational modes were obtained by diagonalizing the dynamical matrix using density functional perturbation theory (DFPT) [10–14]. The computations used the projector augmented wave (PAW) [39] formalism. The PAW basis and projector functions were generated by the ATOMPAW [40] code. The local density approximation (LDA) [41] functional was chosen to treat the exchange-correlation effects. The calculations were carried out by using

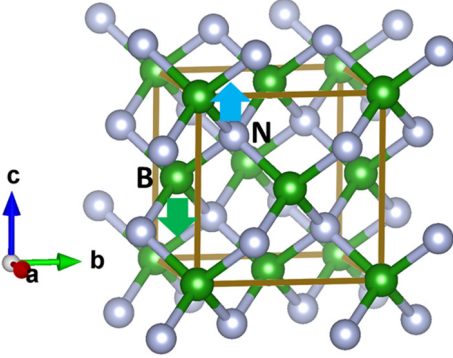


Figure 3. Ball and stick drawing of conventional unit cell of cubic BN (space group $F\bar{4}3m$ [44]) indicating one B and one N site within a primitive cell. The arrows indicate the vibrational directions of the atoms for one of the three degenerate optical modes at $\mathbf{q} = 0$ (Γ point).

Table 1. Comparison of experimental and calculated optical properties of cubic (zincblende) BN, including the electronic (ϵ^∞) and static (ϵ^0) dielectric constants, Born effective charges ($Z^{*B} = -Z^{*N}$), and frequencies of TO (ω_{TO}) and LO vibrational modes (ω_{LO}) (in units of cm^{-1}).

ϵ^∞	ϵ^0	Z^{*B}	ω_{TO}	ω_{LO}	Reference
4.55	6.70	1.87	1069	1297	Calc. (Present)
4.5	7.1		1065	1340	Exp. ([22])
4.46	6.80		1056	1305	Exp. ([25])
4.54		1.93	1040	1285	Calc. ([29])
4.54	6.74	1.89	1062	1295	Calc. ([31])
4.52	6.93		1027	1269	Calc. ([34])

the ABINIT package [15] and checked with the Quantum ESPRESSO [16] package. Visualizations were constructed using the XCrySDEN [42] and VESTA [43] software packages.

The results were obtained using very tight convergence tolerances and dense sampling parameters beyond what was actually necessary for convergence. The plane wave expansion of the electronic wavefunctions included wavevectors with $|\mathbf{k} + \mathbf{G}|^2 \leq (2m_e/\hbar^2)E_{\text{cut}}$ with $E_{\text{cut}} = 80$ Ry. The electronic structure was sampled on a uniform grid of $16 \times 16 \times 16$ and $12 \times 12 \times 8$ \mathbf{k} -points within the Brillouin zone for the cubic and hexagonal structures respectively.

The optimized lattice constant for the cubic cell of BN (space group $F\bar{4}3m$; #216 in the International table of crystallography [44]), was found to be 3.58 Å which compares well with the experimental value [45] of 3.6159 Å measured at room temperature. The optimized lattice constants for the hexagonal cell of BN (space group $P6_3/mmc$; #194 in the International table of crystallography [44]) were found to be $a = 2.49$ Å and $c = 6.49$ Å which compare well with the experimental values [46] of $a = 2.50399$ Å and $c = 6.6612$ Å measured at room temperature.

The phonon analysis was performed using density functional perturbation theory, sampling the phonon dispersion on a uniform grid of $4 \times 4 \times 4$ and $6 \times 6 \times 2$ \mathbf{q} -points for

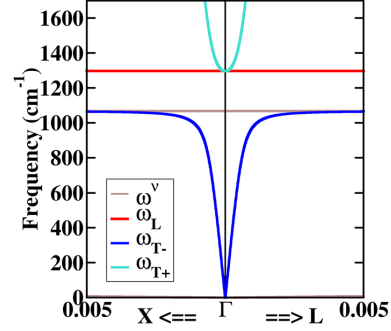


Figure 4. Phonon and phonon–photon dispersion curves in the vicinity of the Γ point of the Brillouin zone for cubic BN. The plot includes \mathbf{q} points in the direction $\Gamma \rightarrow X$ and in the direction $\Gamma \rightarrow L$ with the 0.005 tick marks indicating the value of \mathbf{q} in units of the length of the $\Gamma \rightarrow X$ distance. The end points of the graph correspond to $|\mathbf{q}| = 1.4 \times 10^5 \text{ cm}^{-1}$. The curves for ω^v represent the modes calculated by ABINIT from equation (5) corrected for the TO–LO splitting as shown in figure 1. The coupled longitudinal modes are plotted in red while the coupled transverse modes are plotted in turquoise for upper branch and blue for lower branch as indicated.

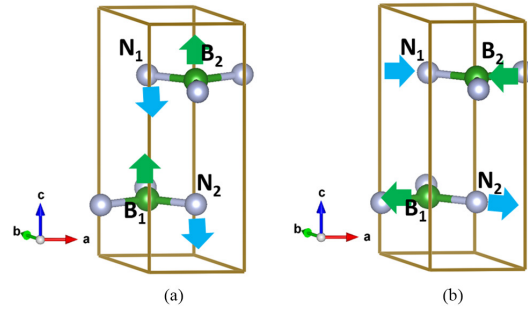


Figure 5. Ball and stick drawing of unit cell of hexagonal BN (space group $P6_3/mmc$ [44]) indicating the four B and N sites. The arrows indicate the vibrational directions of the atoms for $\mathbf{q} = 0$ (Γ point) mode # 7 (a) and for mode # 11 (b).

the cubic and hexagonal structures respectively. These values were used in the ABINIT code to generate the phonon dispersion curves presented in figures 1 and 2; these are consistent with previous calculations in the literature [29, 30, 32, 35].

3.2. Examples of phonon–photon dispersion curves

3.2.1. BN in a cubic structure. Figure 3 shows a diagram of a conventional unit cell of BN in the cubic structure (zincblende with space group $F\bar{4}3m$) with two atoms per primitive unit cell. The corresponding six phonon dispersion curves $\omega^v(\mathbf{q})$ are presented in figure 1. The upper three curves near the Γ point are optical modes. At the Γ point ($\mathbf{q} = 0$), the single ω_{LO} mode is computed to have frequency 1298 cm^{-1} while the doubly degenerate ω_{TO} modes are computed to have the frequency 1069 cm^{-1} . These were determined using the ABINIT and QUANTUM ESPRESSO codes which use the ‘non-analytic’ corrections to the second derivative matrix given in

Table 2. Comparison of experimental and simulated optical properties of hexagonal ($P6_3/mmc$) BN, including the electronic (ϵ_{xx}^∞ , ϵ_{zz}^∞) and static (ϵ_{xx}^0 , ϵ_{zz}^0) dielectric constants and Born effective charges ($Z_{xx}^{*B} = -Z_{xx}^{*N}$, $Z_{zz}^{*B} = -Z_{zz}^{*N}$). Here x refers to the hexagonal plane and z refers to the c axis direction. Also listed are the lower and higher frequency optical mode frequencies in units of cm^{-1} .

ϵ_{xx}^∞	ϵ_{zz}^∞	ϵ_{xx}^0	ϵ_{zz}^0	Z_{xx}^{*B}	Z_{zz}^{*B}	$\omega_{\text{TO}}^{\text{low}}$	$\omega_{\text{LO}}^{\text{low}}$	$\omega_{\text{TO}}^{\text{high}}$	$\omega_{\text{LO}}^{\text{high}}$	Reference
4.88	2.85	6.65	3.39	2.70	0.81	752	820	1383	1614	Calc. (Present)
4.95	4.10	7.04	5.09			783	828	1367	1610	Exp. [21]
4.85	2.84	6.61	3.38	2.71	0.82	754	823	1382	1614	Calc. [31]
4.87	2.95	6.71	3.57			746	819	1372	1610	Calc. [34]

equation (27). Because of the high symmetry of this crystal, the dielectric tensors $\epsilon_{\alpha\beta}^\infty$ and $\epsilon_{\alpha\beta}^0$ are diagonal and isotropic as are the Born effective charge tensors $Z_{\alpha\beta}^{*B} = -Z_{\alpha\beta}^{*N}$. The results computed in the present work are presented in table 1 where it is seen that they agree well with both experimental measurements and with previous calculations in the literature.

In this case, the pure phonon eigenstate solutions to equation (5) at $\mathbf{q} = 0$ for $\nu = 4, 5, 6$ are degenerate, with $\omega^\nu(\mathbf{q} = 0) = 1069 \text{ cm}^{-1}$ and with Born coupling parameters $\mathcal{R}_\alpha^\nu = \mathcal{L}_\alpha^\nu = 2.63$ for $\alpha = x, y$, or z . For each choice of wavevector $\hat{\mathbf{q}}$ which defines the longitudinal direction and choice of transverse directions $\hat{\mathbf{T}}_1$ and $\hat{\mathbf{T}}_2$, there are three phonon–photon modes with frequencies $\omega_L(\mathbf{q})$ (from equation (26)), and $\omega_{T\pm}(\mathbf{q})$ (from equation (32)). In order to represent the phonon–photon modes in a conventional phonon band diagram, we must choose the wavevector values near $\mathbf{q} = 0$ along the special directions of the Brillouin zone. Because of the high symmetry of this crystal, the values of the electronic dielectric function $\epsilon_{\alpha\alpha}^\infty$ and the Born coupling parameter $\mathcal{R}_\alpha^\nu = \mathcal{L}_\alpha^\nu$ are the same for all directions α , the dispersion curves of $\omega_L(\mathbf{q})$ and $\omega_{T\pm}(\mathbf{q})$ have the same shape in each of the plotting directions, although their meanings differ. For example, consider the plot for $\Gamma \rightarrow \mathbf{X}$ direction in the phonon band diagram. In this case, the longitudinal direction is $\hat{\mathbf{q}} = \hat{\mathbf{x}}$ while the transverse directions can be $\hat{\mathbf{T}}_1 = \hat{\mathbf{y}}$ and $\hat{\mathbf{T}}_2 = \hat{\mathbf{z}}$ or an equivalent permutation. As another example, consider the plot for $\Gamma \rightarrow \mathbf{L}$ ($\langle 111 \rangle$ direction) in the phonon band diagram. In this case, the longitudinal direction is along the $\langle 111 \rangle$ direction, while the transverse directions are any two directions perpendicular to $\langle 111 \rangle$. Similarly, plotting the dispersions in the $\Gamma \rightarrow \mathbf{K}$ ($\langle 110 \rangle$ direction) in the phonon band diagram means that the longitudinal mode is along the $\langle 110 \rangle$ direction while the transverse directions are perpendicular to $\langle 110 \rangle$. The phonon–photon dispersion curves are plotted in figure 4 in the $\Gamma \rightarrow \mathbf{X}$ and $\Gamma \rightarrow \mathbf{L}$ directions together with the pure phonon modes in a small range ($1.4 \times 10^4 \text{ cm}^{-1}$) of the Brillouin zone near $\mathbf{q} = 0$.

3.2.2. BN in a hexagonal structure. Figure 5 represents ball and stick diagrams of primitive cells of h-BN having the $P6_3/mmc$ structure and 4 atoms per primitive unit cell. The corresponding 12 phonon dispersion curves $\omega^\nu(\mathbf{q})$ as calculated by ABINIT were presented in figure 2. This structure of BN has less symmetry than that of the cubic phase but the dielectric tensors and Born effective charge tensors are diagonal having the form $Q_{xx} = Q_{yy}$ for tensor components representing the hexagonal layers and distinct values Q_{zz} representing

components along the c -axis. Values of the dielectric tensor components, Born effective charge tensor components, and values of $\omega_{\text{TO}}(\mathbf{q} \gg \omega^\nu c / \sqrt{\epsilon_{T_i, T_i}^\infty})$ and $\omega_{\text{LO}}(\mathbf{q} = 0)$ are listed in table 2 where they are compared with experiments and computations. In general, the present calculations are in good agreement with the literature except for the experimental values of ϵ_{zz} reported by Geick *et al* [21].

For hexagonal BN, it turns out that of the 12 normal modes at $\mathbf{q} = 0$, only three have nontrivial values of $\mathcal{R}_\alpha^\nu = \mathcal{L}_\alpha^\nu$. The lowest frequency mode that has a nontrivial value of \mathcal{R}_α^ν is mode #7 with calculated frequency $\omega^\nu(\mathbf{q} = 0) = 752 \text{ cm}^{-1}$ and $\alpha = z$. The relative atomic displacements for this mode are illustrated in figure 5(a). In this case the non-zero Born coupling parameter is found to have the magnitude $\mathcal{R}_z^\nu = \mathcal{L}_z^\nu = 1.61$. The longitudinal mode is therefore along the $\hat{\mathbf{z}}$ axis, $\hat{\mathbf{q}} = \hat{\mathbf{z}}$, and the longitudinal frequency calculated from equation (26) is $\omega_L = 820 \text{ cm}^{-1}$ which can be plotted as a horizontal line on the phonon band diagram in the $\Gamma \rightarrow \mathbf{A}$ direction. The corresponding transverse modes associated with this vibration can have the electric field along the $\hat{\mathbf{T}}_1 = \hat{\mathbf{z}}$ direction so that $\hat{\mathbf{q}}$ and $\hat{\mathbf{T}}_2$ are oriented along $\hat{\mathbf{x}}$ and $\hat{\mathbf{y}}$. In the conventional phonon band diagram, the two dispersive transverse modes $\omega_{T\pm}(\mathbf{q})$ could then be plotted along the $\Gamma \rightarrow \mathbf{M}$ and $\Gamma \rightarrow \mathbf{K}$ directions.

The other two normal modes with nontrivial values of $\mathcal{R}_\alpha^\nu = \mathcal{L}_\alpha^\nu$ are the doubly degenerate modes #11 and #12 with $\alpha = x$ and $\alpha = y$. The relative atomic displacements for one of these modes are indicated in figure 5(b). In this case, $\omega^\nu(\mathbf{q} = 0) = 1383 \text{ cm}^{-1}$ and the non-zero Born coupling parameter is found to have the magnitude $\mathcal{R}_\alpha^\nu = \mathcal{L}_\alpha^\nu = 5.35$ where $\alpha = x$ or $\alpha = y$. The nondispersive longitudinal frequency of this LO mode is calculated (via equation (26)) to be $\omega_L = 1614 \text{ cm}^{-1}$ and can be plotted along the $\Gamma \rightarrow \mathbf{M}$ and $\Gamma \rightarrow \mathbf{K}$ directions. For the case that $\alpha = x$, the corresponding transverse modes associated with this vibration have the electric field direction along the $\hat{\mathbf{T}}_1 = \hat{\mathbf{x}}$ direction so that $\hat{\mathbf{q}}$ and $\hat{\mathbf{T}}_2$ are oriented along $\hat{\mathbf{y}}$ and $\hat{\mathbf{z}}$. For the case that $\alpha = y$, the corresponding transverse modes associated with this vibration have the electric field direction along the $\hat{\mathbf{T}}_1 = \hat{\mathbf{y}}$ direction so that $\hat{\mathbf{q}}$ and $\hat{\mathbf{T}}_2$ are oriented along $\hat{\mathbf{z}}$ and $\hat{\mathbf{x}}$. Therefore, in the conventional phonon band diagram, the two dispersive transverse modes $\omega_{T\pm}(\mathbf{q})$ are then plotted along the $\Gamma \rightarrow \mathbf{A}$ ($\hat{\mathbf{x}}$ or $\hat{\mathbf{y}}$ transverse to $\hat{\mathbf{z}}$) and $\Gamma \rightarrow \mathbf{K}$ ($\hat{\mathbf{x}}$ transverse to $\hat{\mathbf{y}}$) or $\Gamma \rightarrow \mathbf{M}$ ($\hat{\mathbf{y}}$ transverse to $\hat{\mathbf{x}}$), accordingly. For all three of the coupled phonon–photon modes, the analytical formulas of equations (26) and (32) apply. The results are plotted in figure 6 in a small range of \mathbf{q} points near the Γ point of the Brillouin zone ($3.9 \times 10^4 \text{ cm}^{-1}$).

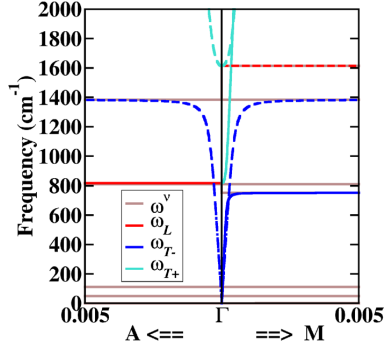


Figure 6. Phonon and phonon–photon dispersion curves in the vicinity of the Γ point of the Brillouin zone for h-BN. The plot includes \mathbf{q} points in the direction $\Gamma \rightarrow \mathbf{A}$ and in the direction $\Gamma \rightarrow \mathbf{M}$ with the 0.005 tick marks indicating the value of \mathbf{q} in units of the length of the $\Gamma \rightarrow \mathbf{A}$ distance. The end points of the graph correspond to $|\mathbf{q}| = 3.9 \times 10^4 \text{ cm}^{-1}$. The curves for ω^ν represent the modes calculated by ABINIT from equation (5) corrected for the TO-LO splitting as shown in figure 2. The coupled longitudinal modes are plotted in red while the coupled transverse modes are plotted in blue or turquoise as indicated. Dashed lines are used to distinguish curves associated with modes #11 and #12 from those associated with mode #7 drawn with full lines.

4. Summary and conclusions

In this report we set out to investigate the detailed origin of apparent discontinuities and mode disappearances in phonon band diagrams of ionic materials having hexagonal and other anisotropic structures. This resulted in a synthesis of the work of Huang [2, 3], Giannozzi *et al* [10], Gonze *et al* [12], Baroni *et al* [13], and others to derive the coupled equations for the ion motion and long wavelength electric fields using results from density functional theory and density functional perturbation theory. Current codes such as ABINIT and QUANTUM ESPRESSO include the effects on the longitudinal optical modes by introducing the so-called non-analytic correction to the second derivative matrix (equation (28)). In this work, we extend the analysis to include the transverse phonon–photon modes as well. The combination of the longitudinal and transverse phonon–photon mode dispersions are continuous functions of the wavevector \mathbf{q} as has been demonstrated for cubic and hexagonal BN in figures 4 and 6, respectively. In principle, it should be possible to experimentally explore the transverse mode dispersions near $\mathbf{q} \rightarrow 0$. For example, Henry and Hopfield [47] showed that Raman spectroscopy can be used in a small angle scattering geometry to couple to the polariton. In a more recent example, heterostructures including hexagonal BN have been developed and measured with infrared microscopy to map the phonon–photon dispersion modes [48].

As a practical consideration, it may be useful to further explore the use of the $\mathbf{q} = 0$ pure phonon mode basis (equation (16)) in order to analyze the longitudinal and transverse eigenvalues and eigenvectors as in equations (29), (30) and (36), (37).

Acknowledgments

This work was supported by NSF Grant DMR-1507942. Computations were performed on the Wake Forest University DEAC cluster, a centrally managed resource with support provided in part by the University. We would like to thank Fabien Bruneval and Josef Zwanziger for help with ABINIT commands.

Appendix. Some practical details

In practice, the phonon dispersion curves are usually evaluated not directly in units of angular frequency ω (rad/sec) but in units of wave number $\tilde{\omega} \equiv \omega/(2\pi c)$ (cm^{-1}), where c denotes the speed of light in vacuum. Therefore in order to evaluate the constants in equation (26) for example:

$$\frac{4\pi e^2}{\Omega M^\nu} \rightarrow \frac{1}{(2\pi c)^2} \frac{4\pi e^2}{\Omega M^\nu} \equiv 16\pi \left(\frac{e_H}{hc}\right)^2 \frac{1}{\Omega/a_B^3} \frac{1}{M^\nu/m_e}. \quad (\text{A.1})$$

Here e_H denotes the ground state energy of a H atom, h denotes Planck’s constant, a_B denotes the Bohr radius, and m_e denotes the electron mass.

ORCID iDs

Yan Li <https://orcid.org/0000-0001-8253-7802>
W C Kerr <https://orcid.org/0000-0002-1281-8761>
N A W Holzwarth <https://orcid.org/0000-0001-5492-0660>

References

- [1] Li Y, Hood Z D and Holzwarth N A W 2019 Manuscript in preparation
- [2] Huang K 1951 *Proc. R. Soc. A* **A208** 352–65
- [3] Born M and Huang K 1954 *Dynamical Theory of Crystal Lattices* (Oxford: Oxford University Press)
- [4] Kittel C 1963 *Quantum Theory of Solids* (New York: Wiley)
- [5] Maradudin A A, Montroll E W, Weiss G H and Ipatova I P 1971 *Theory of Lattice Dynamics in the Harmonic Approximation (Solid State Physics: Supplement vol 3)* 2nd edn (New York: Academic)
- [6] Böttger H 1983 *Principles of the Theory of Lattice Dynamics* (Weinheim: Physik Verlag)
- [7] Setyawan W and Curtarolo S 2010 *Comput. Mater. Sci.* **49** 299–312
- [8] Hohenberg P and Kohn W 1964 *Phys. Rev.* **136** B864–71
- [9] Kohn W and Sham L J 1965 *Phys. Rev.* **140** A1133–8
- [10] Giannozzi P, De Gironcoli S, Pavone P and Baroni S 1991 *Phys. Rev. B* **43** 7231
- [11] Gonze X 1997 *Phys. Rev. B* **55** 10337–54
- [12] Gonze X and Lee C 1997 *Phys. Rev. B* **55** 10355–68
- [13] Baroni S, De Gironcoli S, Dal Corso A and Giannozzi P 2001 *Rev. Mod. Phys.* **73** 515
- [14] Giannozzi P and Baroni S 2005 Density-functional perturbation theory *Handbook of Materials Modeling* ed S Yip (Berlin: Springer) p 195–214
- [15] Gonze X *et al* 2016 *Comput. Phys. Commun.* **205** 106–31

- [16] Giannozzi P et al 2017 *J. Phys.: Condens. Matter* **29** 465901
- [17] Ghosez P and Gonze X 2000 *J. Phys.: Condens. Matter* **12** 9179–88
- [18] Pick R M, Cohen M H and Martin R M 1970 *Phys. Rev. B* **1** 910–20
- [19] Ghosez P, Michenaud J P and Gonze X 1998 *Phys. Rev. B* **58** 6224
- [20] Irmer G, Röder C, Himcinski C and Kortus J 2013 *Phys. Rev. B* **88** 104303
- [21] Geick R, Perry C H and Rupprecht G 1966 *Phys. Rev.* **146** 543–7
- [22] Gielisse P J, Mitra S S, Plendl J N, Griffis R D, Mansur L C, Marshall R and Pascoe E A 1967 *Phys. Rev.* **155** 1039–46
- [23] Hoffman D M, Doll G L and Eklund P C 1984 *Phys. Rev. B* **30** 6051–6
- [24] Jäger S, Bewilogua K and Klages C P 1994 *Thin Solid Films* **245** 50–4
- [25] Eremets M I, Gauthier M, Polian A, Chervin J C, Besson J M, Dubitskii G A and Semenova Y Y 1995 *Phys. Rev. B* **52** 8854–63
- [26] Reich S, Ferrari A C, Arenal R, Loiseau A, Bello I and Robertson J 2005 *Phys. Rev. B* **71** 205201
- [27] Kutsay O et al 2010 *Diam. Relat. Mater.* **19** 968–71
- [28] Cuscó R, Gil B, Cassabois G and Artús L 2016 *Phys. Rev. B* **94** 155435
- [29] Karch K and Bechstedt F 1997 *Phys. Rev. B* **56** 7404–15
- [30] Kern G, Kresse G and Hafner J 1999 *Phys. Rev. B* **59** 8551–9
- [31] Ohba N, Miwa K, Nagasako N and Fukumoto A 2001 *Phys. Rev. B* **63** 115207
- [32] Yu W J, Lau W M, Chan S P, Liu Z F and Zheng Q Q 2003 *Phys. Rev. B* **67** 014108
- [33] Liu L, Feng Y P and Shen Z X 2003 *Phys. Rev. B* **68** 104102
- [34] Cai Y, Zhang L, Zeng Q, Cheng L and Xu Y 2007 *Solid State Commun.* **141** 262–6
- [35] Hamdi I and Meskini N 2010 *Physica B* **405** 2785–94
- [36] Michel K H and Verberck B 2011 *Phys. Rev. B* **83** 115328
- [37] Ontaneda J, Singh A, Waghmare U V and Grau-Crespo R 2018 *J. Phys.: Condens. Matter* **30** 185701
- [38] Gruber T and Grüneis A 2018 *Phys. Rev. B* **98** 134108
- [39] Blöchl P E 1994 *Phys. Rev. B* **50** 17953–79
- [40] Holzwarth N A W, Tackett A R and Matthews G E 2001 *Comput. Phys. Commun.* **135** 329–47
- [41] Perdew J P and Wang Y 1992 *Phys. Rev. B* **45** 13244–9
- [42] Kokalj A 2003 *Comput. Mater. Sci.* **28** 155–68
- [43] Momma K and Izumi F 2011 *Appl. Crystallogr.* **44** 1272–6
- [44] Hahn T (ed) 2002 *International Tables for Crystallography, Volume A: Space-Group Symmetry, Fifth Revised Edition* (Boston, MA: Kluwer Academic)
- [45] Eichhorn K, Kirfel A, Grochowski J and Serda P 1991 *Acta Crystallogr. B* **47** 843–8
- [46] Pease R S 1952 *Acta Crystallographica* **5** 356–61
- [47] Henry C H and Hopfield J J 1965 *Phys. Rev. Lett.* **15** 964–6
- [48] Yang X, Zhai F, Hu H, Hu D, Liu R, Zhang S, Sun M, Sun Z, Chen J and Dai Q 2016 *Adv. Mater.* **28** 2931–8

Appendix C

Computational study of Li_3BO_3
and Li_3BN_2 I: Electrolyte
properties of pure and doped
crystals

Computational study of Li_3BO_3 and Li_3BN_2 I: Electrolyte properties of pure and doped crystalsYan Li ¹, Zachary D. Hood ², and N. A. W. Holzwarth ¹¹Department of Physics, Wake Forest University, Winston-Salem, North Carolina 27109, USA²Applied Materials Division, Argonne National Laboratory, Argonne, Illinois 60439, USA

(Received 22 June 2021; accepted 29 July 2021; published 17 August 2021)

Both Li_3BO_3 and Li_3BN_2 materials have promising properties for use in all-solid-state batteries and other technologies dependent on electrolytes with significant ionic conductivity. As the first of a two-part study, this paper reports the analysis of detailed simulations of Li ion diffusion in the monoclinic forms of these materials. Using both NEB and MD methods, it is clear that Li ion migration via vacancy mechanisms provides the most efficient ion transport in each material. While the results suggest that interstitial defects in these materials do not play a direct role in Li ion migration, their relative stability seems to enhance vacancy production via the formation of Frenkel-type defects. This may partially explain why the Li ion conductivities computed from MD simulations of samples initially containing a single Li ion vacancy are in reasonable agreement with measured values of this work for Li_3BO_3 and those reported in the literature for poorly crystalline samples of both materials. The possibility of increasing vacancy concentrations by substitutional doping (F for O in Li_3BO_3 and C for B in Li_3BN_2) is also examined, finding simulated conductivities comparable to those of the ideal vacancy model.

DOI: [10.1103/PhysRevMaterials.5.085402](https://doi.org/10.1103/PhysRevMaterials.5.085402)

I. INTRODUCTION

There has been considerable progress in developing inorganic Li ion conducting solid electrolytes for a variety of technologies such as all-solid-state lithium ion batteries for energy storage and delivery and for thin film sensors, as evidenced in a number of recent reviews [1–8]. Some of the current challenges for materials science include optimizing the ion conductivity and stability of solid electrolytes and stabilizing the interfaces between solid electrolytes and electrodes, particularly working toward stabilizing metallic Li as a very efficient anode. For example, nitride and oxide electrolytes such as lithium oxynitride (LIPON) are known [9–12] to show excellent stability with Li metal anodes and cathodes. Rather than developing a single material that meets all of the technological requirements, one promising approach has been to develop composite materials and coatings such as described by Richards *et al.* [13]. In the search for further optimization, boron-based materials have been gaining considerable interest because of their general availability, nontoxicity, and demonstrated success in related technologies such as high-strength borosilicate glass. Additionally, from a technical viewpoint, it is known that boron-based materials are likely to be adaptable to efficient processing techniques such as atomic layer deposition, sol-gel-based processes, and spray coating procedures. In this paper and in the companion paper (Paper II [14]), we examine two boron-based materials which have been identified as good Li ion conductors— Li_3BO_3 and Li_3BN_2 —with possible applications as Li ion electrolytes or coatings.

The literature reports promising electrolyte properties of Li_3BO_3 and Li_3BN_2 . Ohta *et al.* [15] reported the use of

Li_3BO_3 as an intermediate electrolyte to stabilize the interface between a LiCoO_2 cathode and a lithium garnet oxide electrolyte in an all-solid-state battery. Li_3BO_3 was found to provide a structurally stable contact between the cathode and the garnet electrolyte. In the context of solid electrolytes, the experimental studies [16–23] show Li_3BO_3 -based glass and glass-ceramic solid electrolytes exhibit relatively high ionic conductivities in the range of $10^{-7} - 10^{-5}$ S/cm at room temperature. Li_3BN_2 is a ternary compound similar to Li_3BO_3 . In addition to its electrolyte properties, several other applications have been explored. For example, the material was explored as a promising material for hydrogen storage applications [24,25] and it was also studied as solvent catalyst for synthesizing the cubic BN from hexagonal BN [26–28]. There has also been some work exploring α - Li_3BN_2 as a cathode material for Li ion batteries [29]. The present paper focuses on the performance of Li_3BN_2 as a potential solid electrolyte or coating material. In the 1987 paper by Yamane *et al.* [30], two crystalline phases of Li_3BN_2 were prepared from Li_3N and BN binary compounds. The measured ionic conductivity for a polycrystalline sample at 400 K was reported to be 3×10^{-7} S/cm. Shigeno *et al.* [31] recently showed that a “glass-ceramic” form of Li_3BN_2 , with a similar x-ray pattern to monoclinic β - Li_3BN_2 , has a room temperature conductivity of 1.1×10^{-7} S/cm, several orders of magnitude higher than the room-temperature conductivity of crystalline α - Li_3BN_2 .

Li_3BO_3 and Li_3BN_2 share some common features. For both, the relatively high conducting phase has a monoclinic $P2_1/c$ (space group No. 14) [32,33] structure (α form for Li_3BO_3 and β form for Li_3BN_2). However, to the best of our knowledge, the detailed mechanisms of the Li-ion diffusion in these materials has not yet been reported in the literature.

A comprehensive computational study of Li_3BO_3 and Li_3BN_2 is presented in two papers. This paper (Paper I) focuses on analyzing Li ion mobilities, important for electrolyte functionality, and is organized as follows. Section II presents the computation methods used in this paper. The models of pure and doped materials for Li ion migration are discussed in Sec. III. Sections IV and V analyze Li ion diffusion mechanisms using the nudged elastic band (NEB) method [34–36] and molecular dynamics (MD) simulations, respectively. Exploring possibilities for optimizing ionic conductivity, vacancy, and interstitial mechanisms in the bulk pure and doped models of Li_3BO_3 and Li_3BN_2 , are investigated. A summary and conclusions of this paper are given in Sec. VI. Paper II [14] analyzes the structural and chemical stabilities of bulk Li_3BO_3 and Li_3BN_2 and their interfaces with ideal metallic Li.

II. CALCULATIONAL METHODS

The computational methods for this paper are based on density functional theory [37,38] using the projector augmented plane wave [39] formalism with the data sets generated by the ATOMPAW code [40]. All calculations in this paper were performed using the QUANTUM ESPRESSO [41,42] package with the modified generalized gradient formulation known as PBEsol [43] to describe the exchange-correlation effects. In this paper, all simulations are based on the monoclinic structures optimized as described in Paper II [14]. For this paper, focusing on transport, convergence parameters could be slightly less stringent compared with those used in Paper II. Here we used the plane wave expansion cutoff $2m|\mathbf{k} + \mathbf{G}|^2/\hbar^2 \leq 64$ Ry. Interestingly, while the two materials have the same space group, their dimensions are quite different. For simulating Li ion diffusion in Li_3BO_3 , simulations were performed using a $3 \times 1 \times 1$ supercell of the conventional cell having 84 atoms and approximately equal lattice lengths (9.73, 9.17, and 8.24 Å) for the a , b , and c directions, respectively. The ionic transport properties investigated for $\beta\text{-Li}_3\text{BN}_2$ are based on a $2 \times 2 \times 1$ supercell containing 96 atoms with similar lattice lengths (10.22, 14.00, and 6.71 Å) for the a , b , and c directions, respectively. For the MD and NEB simulations in these relatively large supercells, the k-point sampling could be reduced from that described in Paper II which focused on detailed energetics and structures. Here, the k-point sampling could be reduced to a few or even a single sampling point as evidenced by convergence studies on representative NEB calculations.

The structural configurations were visualized using the VESTA [44] and XCRYSDEN [45] programs.

III. MODELS FOR LI ION MIGRATION

As discussed in Paper II [14], both Li_3BO_3 and Li_3BN_2 in their $P2_1/c$ monoclinic (space group No. 14) [32,33] structures are well-ordered. They both are densely packed with limited space available for Li ion motion. Analysis of Li ion migration necessarily involves identifying metastable defects including interstitials and vacancies.

To estimate the metastable interstitial positions in the ideal crystals, we searched for the lowest energy optimized

structures of supercells of the ideal crystals augmented with an additional Li ion (and with a uniform distribution of compensating charge). In this study, we found one such ideal interstitial I-int site for each material based on a $3 \times 1 \times 1$ supercell for Li_3BO_3 and a $2 \times 2 \times 1$ supercell for Li_3BN_2 . These I-int sites are also useful for estimating the energy to form a vacancy-interstitial pair defect, E_f , from the energy difference of the lowest nontrivial energy for an optimized vacancy-interstitial structure relative to its corresponding perfect supercell.

In this paper, we considered two types of vacancy defects. An ideal vacancy defect I-vac was modeled using optimized structures of supercells of the ideal crystals diminished with a missing Li ion (and with a uniform distribution of compensating charge). We also considered various ion substitutions in the supercell to model a neutral Li ion vacancy material. These are referenced as a F-doped vacancy for Li_3BO_3 and as a C-doped vacancy for Li_3BN_2 . The choice of F substituting for O in Li_3BO_3 and C substituting for B in Li_3BN_2 represent exploratory design possibilities for increasing ionic conductivity following similar strategies described in the literature [46–48], including other possibilities for these materials [21,49,50].

To estimate defect-induced atomic distortions relative to the perfect crystal structure, we followed the approach of Lepley and Holzwarth [51] to calculate the averaged atomic distortion parameter,

$$\bar{D}^a = \frac{1}{N^a} \sum_{i=1, \in N^a}^{N^a} |\Delta \mathbf{R}_i^a|, \quad (1)$$

and the maximum distortion parameter,

$$D_{\max}^a = \max_{i \in N^a} |\Delta \mathbf{R}_i^a|. \quad (2)$$

In these equations, N^a denotes the number of ions of type a and $\Delta \mathbf{R}_i^a$ denotes the difference in the position of the i th ion of type a in the optimized structure of the defective lattice relative to its position in the ideal lattice. For the case of vacancy defects, the vacancy site is omitted from the analysis in Eqs. (1) and (2). For the F-doped and C-doped models, we allowed only one substitutional site in the supercell so the corresponding $N^a = 1$ and the average and maximum distortion measures are equal: $D^a = D_{\max}^a$.

A. Defect models for Li_3BO_3

The lowest energy metastable interstitial sites are visualized with green balls in Fig. 1 in the $3 \times 1 \times 1$ supercell. Referenced to the unit cell of the $P2_1/c$ structure, these I-int sites map closely to the multiplicity and Wyckoff label $2b$ with example fractional coordinates (0.5, 0.5, 0.5). The corresponding vacancy-interstitial pair formation energy is estimated to be $E_f = 1.25$ eV. Because of this high formation energy and relatively large distance between I-int sites within the crystal structure (>3.24 Å), we expect that interstitial mechanisms play a minimal role in Li ion migration for Li_3BO_3 .

There are three inequivalent Li ion sites in Li_3BO_3 and correspondingly three distinct I-vac energies. The site labels in Fig. 1 indicate a possible Li ion vacancy migration path in the $3 \times 1 \times 1$ supercell in terms of an I-vac site moving

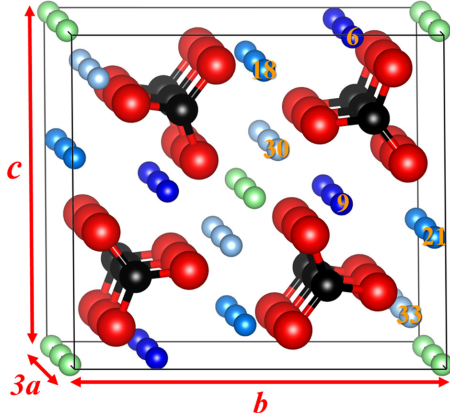


FIG. 1. Ball and stick diagram of Li_3BO_3 with Li, B, and O represented by three shades of blue, black, and red balls, respectively. Dark, medium, and light blue shades correspond to Li(1), Li(2), and Li(3) types, respectively. Equivalent I-int sites are shown with green balls.

successively according to the labels $6 \rightarrow 18 \rightarrow 30 \rightarrow 9 \rightarrow 21 \rightarrow 33 \rightarrow 6$. In this case, the geometrically equivalent sites are $9 \equiv 6$, $21 \equiv 18$, and $33 \equiv 30$. These correspond to the Li(1)-, Li(2)-, and Li(3)-type labels discussed in Paper II [14], respectively. From the optimized structures of the geometrically distinct Li sites, we find that the I-vac energies are very similar. It is convenient to set the I-vac energy of site $18 \equiv 21$ to be zero. The results, together with the distortion measures, are summarized in Table I, given below. The table shows that for these I-vac defects, the largest average distortion is 0.07 Å or less and the Li host lattice sites experience the largest maximum distortions of 0.43 Å or less.

Because of the large vacancy-interstitial pair formation energy E_f , it is advantageous to consider electrolytes formed from Li_3BO_3 materials modified to have a native concentration Li ion vacancies. One way to accomplish this is to substitute x O ions with x F ions while removing x Li ions forming $\text{Li}_{3-x}\text{BO}_{3-x}\text{F}_x$. For the $3 \times 1 \times 1$ supercell, $x = 1/12$ and Table I also reports the results for optimized structures this model system, compared with the corresponding I-vac models. For the F-doped models, the Li vacancy energies are no longer equal, with the vacancy configuration on the

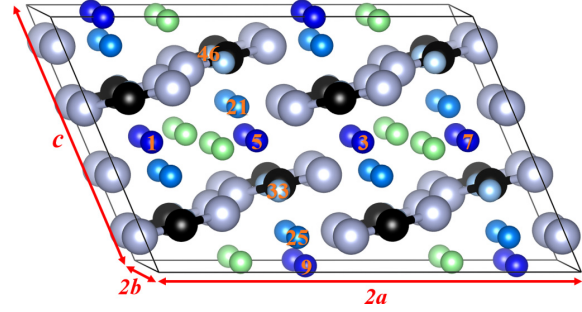
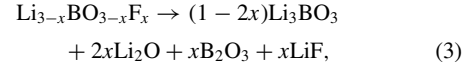


FIG. 2. Ball and stick diagram of Li_3BN_2 with Li, B, and N represented by three shades of blue, black, and gray balls, respectively. Dark, medium, and light blue shades correspond to Li(1), Li(2), and Li(3) types, respectively. Equivalent I-int sites are shown with green balls.

site closest to the substitutional F site (in this case, site 33) having the lowest energy and set to 0. For the F-doped models [illustrated in Fig. 3(a) below], the distortion measures are all larger than for the I-vac models, with the largest increases for the Li sites.

To estimate the stability of F-doped Li_3BO_3 , we considered the following possible decomposition reaction:



where $x = 1/12$ in this simulation. For simplicity, the reaction energy ΔU_{SL} , estimated on the basis of the static lattice energies only, was calculated from the energy of $\text{Li}_{3-x}\text{BO}_{3-x}\text{F}_x$ minus the energy of the products on the right-hand side of Eq. (3). The product LiF has a cubic structure with space group $Fm\bar{3}m$ (No. 225) and the information for the rest of the products can be found in Paper II. The minimum value of the six vacancy configurations considered (for the vacancy on site 33) was found to be $\Delta U_{\text{SL}} = -0.06$ eV. This negative value suggests that F-doped Li_3BO_3 is stable at least with respect to the modeled decomposition.

B. Defect models for Li_3BN_2

While Li_3BN_2 (in its β phase) has the same space group as Li_3BO_3 , the atomic arrangement is quite distinct, as discussed

TABLE I. The relative vacancy energies in eV and distortion parameters (in Å) as calculated according to Eqs. (1) and (2) for the I-vac and F-doped Li_3BO_3 . The labels in the first column refer to the vacancies displayed in Fig. 1, the column dis (in Å) gives the distance between the F substitutional site and the corresponding Li vacancy, measured from the host sites in the perfect crystal before relaxation.

Label	I-vac				F-doped				
	E_v	$\bar{D}^{\text{Li}}/D_{\text{max}}^{\text{Li}}$	$\bar{D}^{\text{B}}/D_{\text{max}}^{\text{B}}$	$\bar{D}^{\text{O}}/D_{\text{max}}^{\text{O}}$	E_v/dis	$\bar{D}^{\text{Li}}/D_{\text{max}}^{\text{Li}}$	$\bar{D}^{\text{B}}/D_{\text{max}}^{\text{B}}$	$\bar{D}^{\text{O}}/D_{\text{max}}^{\text{O}}$	$\bar{D}^{\text{F}}/D_{\text{max}}^{\text{F}}$
No. 6	0.04	0.05/0.29	0.03/0.09	0.05/0.21	0.30/3.93	0.11/0.83	0.06/0.14	0.07/0.24	0.15/0.15
No. 18	0.00	0.07/0.43	0.04/0.14	0.05/0.19	0.24/4.71	0.12/1.02	0.06/0.13	0.07/0.22	0.09/0.09
No. 30	0.02	0.07/0.34	0.04/0.13	0.06/0.24	0.40/5.60	0.10/0.35	0.06/0.17	0.07/0.25	0.08/0.08
No. 9	0.04	0.05/0.29	0.03/0.09	0.05/0.21	0.41/4.93	0.09/0.35	0.05/0.15	0.06/0.21	0.05/0.05
No. 21	0.00	0.07/0.43	0.04/0.14	0.05/0.19	0.23/3.30	0.10/0.41	0.06/0.17	0.07/0.18	0.07/0.07
No. 33	0.02	0.07/0.34	0.04/0.13	0.06/0.24	0.00/1.96	0.08/0.34	0.05/0.13	0.06/0.23	0.14/0.14

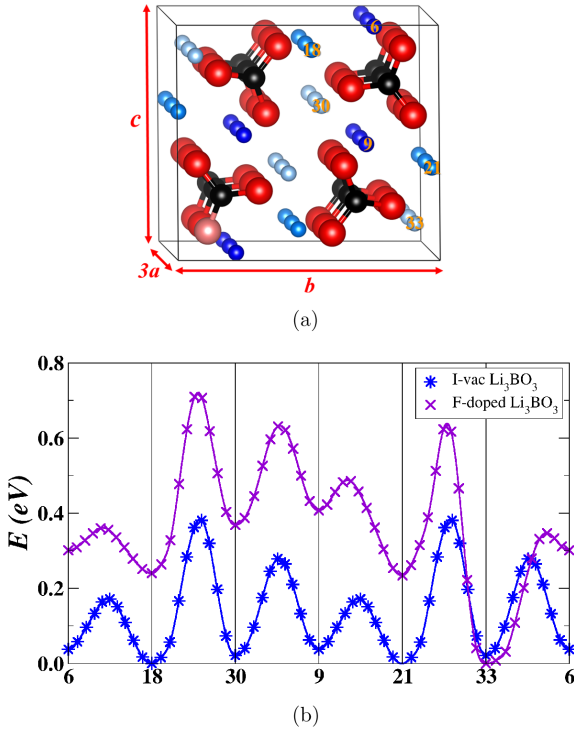


FIG. 3. (a) Ball and stick diagram for vacancy migration in Li_3BO_3 with Li, B, O, and F represented by three shades of blue, black, red, and pink balls, respectively. Labels indicate vacancy sites for migration pathway. (b) Configuration energy diagram results of NEB calculation of Li ion vacancy migration along the indicated pathway. The energies for these diagrams are adjusted for the lowest energy of the considered configurations, consistent with Table I.

in Paper II [14]. The lowest energy metastable interstitial sites are visualized with green balls in Fig. 2 in the $2 \times 2 \times 1$ supercell. Referenced to the unit cell of the $P2_1/c$ structure, these I-int sites map closely to the multiplicity and Wyckoff label $4e$ with example fractional coordinates (0.560, 0.279,

0.978). The corresponding vacancy-interstitial pair formation energy is estimated to be $E_f = 1.23$ eV. Although this is a relatively high formation energy, because of the relatively small distances between I-int sites within the crystal structure (2.91 Å), we expect that interstitial mechanisms may play a role in Li ion migration for Li_3BN_2 .

There are three inequivalent Li ion host sites in Li_3BN_2 and correspondingly three distinct I-vac energies. The site labels in Fig. 2 indicate two possible Li ion vacancy migration paths in the $2 \times 2 \times 1$ supercell which will be considered in Sec. IV B below. From the optimized structures of the geometrically distinct Li sites, we find that the I-vac energies for sites Li(1) and Li(2) are very similar, while I-vac energy for site Li(3) (light blue balls in Fig. 2) are 0.51 eV higher, which might be attributed to its strong Coulomb interactions with neighboring $(\text{BN}_2)^{-3}$ ions. It is convenient to set the I-vac energy of site $21 \equiv 25$ to be zero. The results together with the distortion measures are summarized in Table II given below. The table shows that for these I-vac defects, the largest average distortion is 0.07 Å or less and the Li host lattice sites experience the largest maximum distortions of 0.62 Å or less.

As for Li_3BN_2 , it is reasonable to expect that it is advantageous to consider electrolytes formed from Li_3BN_2 materials modified to have native concentration Li ion vacancies. One way to accomplish this is to substitute x B ions with x C ions and to remove x Li ions, forming $\text{Li}_{3-x}\text{B}_{1-x}\text{C}_x\text{N}_2$. For the $2 \times 2 \times 1$ supercell, $x = 1/16$ and Table II also reports the results for the optimized structures of this model system, compared with the corresponding I-vac models. For the C-doped models, the Li vacancy energies are no longer equal, with the vacancy configuration having the lowest energy (site 25) set to 0. For the C-doped models [illustrated in Fig. 4(a) below], the distortion measures for the Li sites are all larger than those for the I-vac models.

Analogous to the case of the F-doped Li_3BO_3 , the replacement of B with C breaks the symmetry of the original structure of the Li_3BN_2 , resulting in multiply inequivalent Li vacancies with the lowest metastable energy occurring for the vacancy configuration at site 25, which is 3.19 Å away from the position of the C dopant. As indicated in Table II, the C dopant

TABLE II. The relative vacancy energies in eV and distortion parameters (in Å) as calculated according to Eqs. (1) and (2) for the I-vac and C-doped Li_3BN_2 . The labels in the first column refer to the vacancies displayed in Fig. 2, the column dis (in Å) gives the distance between the C substitutional site and the corresponding Li vacancy, measured from the host sites in the perfect crystal before relaxation.

Label	I-vac				C-doped				
	E_v	$\bar{D}^{\text{Li}}/D_{\text{max}}^{\text{Li}}$	$\bar{D}^{\text{B}}/D_{\text{max}}^{\text{B}}$	$\bar{D}^{\text{N}}/D_{\text{max}}^{\text{N}}$	E_v/dis	$\bar{D}^{\text{Li}}/D_{\text{max}}^{\text{Li}}$	$\bar{D}^{\text{B}}/D_{\text{max}}^{\text{B}}$	$\bar{D}^{\text{C}}/D_{\text{max}}^{\text{C}}$	$\bar{D}^{\text{N}}/D_{\text{max}}^{\text{N}}$
No. 1	0.03	0.07/0.62	0.03/0.09	0.06/0.22	0.11/2.38	0.07/0.46	0.40/0.11	0.02/0.02	0.07/0.20
No. 5	0.03	0.07/0.62	0.03/0.09	0.06/0.22	0.06/3.10	0.07/0.35	0.03/0.09	0.11/0.11	0.06/0.23
No. 3	0.03	0.07/0.62	0.03/0.09	0.06/0.22	0.28/5.00	0.08/0.57	0.04/0.08	0.05/0.05	0.07/0.23
No. 7	0.03	0.07/0.62	0.03/0.09	0.06/0.22	0.17/4.05	0.08/0.58	0.04/0.09	0.04/0.04	0.07/0.23
No. 46	0.51	0.06/0.40	0.04/0.08	0.06/0.18	0.91/7.92	0.09/0.39	0.05/0.10	0.02/0.02	0.08/0.39
No. 21	0.00	0.06/0.35	0.04/0.10	0.07/0.27	0.33/5.66	0.08/0.42	0.05/0.09	0.03/0.03	0.09/0.28
No. 33	0.51	0.06/0.40	0.04/0.08	0.06/0.18	0.56/2.60	0.07/0.43	0.04/0.10	0.06/0.06	0.06/0.23
No. 25	0.00	0.06/0.35	0.04/0.10	0.07/0.27	0.00/3.19	0.07/0.27	0.03/0.05	0.11/0.11	0.07/0.25
No. 9	0.03	0.07/0.62	0.03/0.09	0.06/0.22	0.38/5.72	0.10/0.65	0.04/0.10	0.02/0.02	0.08/0.23

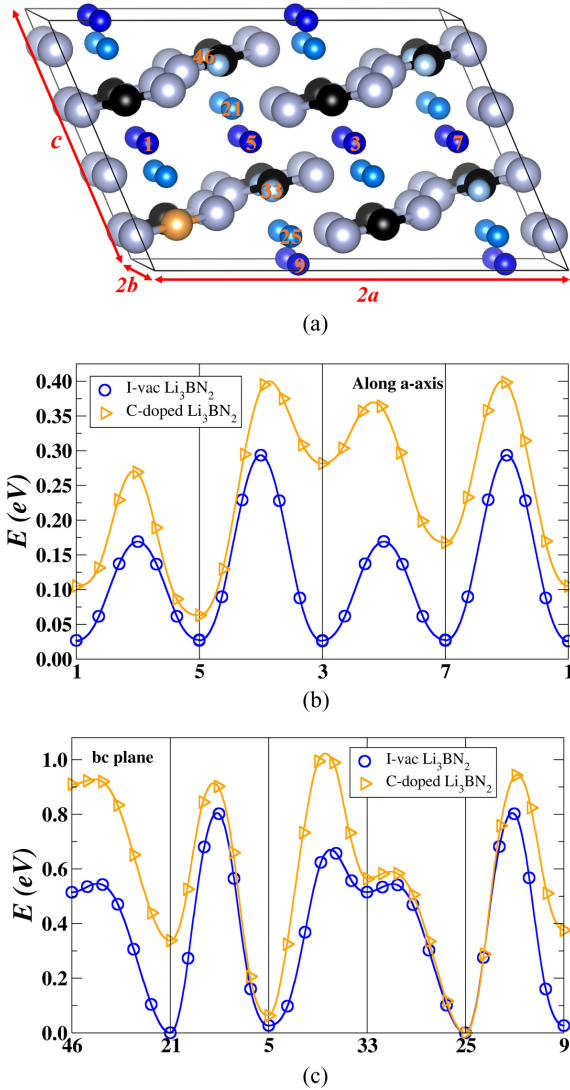
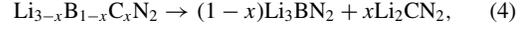


FIG. 4. (a) Ball and stick diagram for vacancy migration in Li₃BN₂ with Li, B, C, and N ions represented by three shades of blue, black, brown, and gray balls, respectively. Labels indicate vacancy sites for migration pathways. The configuration energy diagrams from NEB calculations for Li ion vacancy migrations along the **a** axis and within **bc** plane are shown in (b) and (c), respectively. The energies for these diagrams are adjusted for the lowest energy of the considered configurations, different for the I-vac and C-doped models and consistent with Table II.

tends to reduce the energy of the defect structure in which the vacancy is close to it, and at the same time undergoes greater deformation during optimization. However, it is evident that the vacancy energy pattern for the C-doped model is affected by more than proximity to the C site. For example, site 1 is closest to the C site with a distance of 2.38 Å but has an energy of 0.11 eV while the vacancy at site 33 is 2.60 Å away from the C site but its energy is up to 0.56 eV.

To estimate the stability of C-doped Li₃BN₂, we considered the following possible decomposition reaction:



where $x = 1/16$ in this simulation. For simplicity, the reaction energy ΔU_{SL} was estimated from the static lattice contributions of Li_{3-x}B_{3-x}C_xN₂ minus the energy of the productions on the right-hand side of Eq. (4). The structure for the product Li₂CN₂ has space group symmetry *I4/mmm* (No. 139) and was optimized based on the experimental data reported in Ref. [52]. The minimum value of the nine vacancy configurations considered (for the vacancy on site 25) was found to be $\Delta U_{\text{SL}} = +0.05$ eV. This positive value suggests that C-doped Li₃BN₂ may need special treatment to actually synthesize. However, since the doped structure is computationally stable, we include the simulation results for reference. In practice, it is known that Li₃BN₂ samples are sensitive to surface oxygen degradation.

IV. LI ION MIGRATION ANALYSIS VIA THE ELASTIC BAND METHOD

The NEB method [34–36] has been well developed to evaluate the temperature (T) dependence ion diffusion coefficient $D(T)$ according to the Arrhenius form

$$D(T) = D_0 e^{-E_a^{\text{NEB}}/k_B T}, \quad (5)$$

where k_B denotes the Boltzmann constant and D_0 is the temperature-independent pre-exponential factor. For the NEB analysis, the ion migration energy barrier E_m^{NEB} for a predefined migration path is determined from the highest energy found along the constructed NEB path relative to a reference defect energy of the supercell. The relationship of the activation energy E_a^{NEB} to E_m^{NEB} depends on the system under consideration. In general, we expect that the activation energy varies in a range:

$$\epsilon_{\min} \leq E_a^{\text{NEB}} \leq \epsilon_{\max}. \quad (6)$$

In this paper, we consider two types of systems—defective and ideal materials. Substitutionally doped materials, or materials prepared with poor crystallinity, are expected to have a substantial population of defects, so the activation energy for ionic diffusion is expected to be close to the minimum:

$$\epsilon_{\min} = E_m^{\text{NEB}} = \max(\Delta E_m + E_d^0). \quad (7)$$

Here, ΔE_m denotes the energy barrier calculated from the NEB formalism for a single hop step and E_d^0 represents the lowest defect energy such as listed in Tables I and II for the particular migration path. The E_d^0 contribution comes from the expectation that there is a temperature-dependent probability associated with the particular path, determined by the equilibrium population of the lowest energy defect sites as determined by a Boltzmann distribution [53]. For more ideal samples not having a population of vacancies or interstitials, it is assumed that the migration process is initiated by moving one Li ion at a host lattice site into an interstitial site, the activation energy for ionic conductivity E_a^{NEB} therefore additionally includes the defect formation energy E_f which is associated with a formation of vacancy-interstitial pair with

TABLE III. Vacancy hopping energies ΔE_m for Li_3BO_3 for the I-vac and F-doped models. The step labels refer to the position labels in Fig. 3(a). The distances (measured from the perfect crystal sites before defect optimization) are given in units of Å and energies are given in eV units.

Step	Distance	ΔE_m	
		I-vac	F-doped
6 \leftrightarrow 18	2.51	0.17	0.12
18 \leftrightarrow 30	2.69	0.38	0.48
30 \leftrightarrow 9	2.48	0.26	0.26
9 \leftrightarrow 21	2.51	0.17	0.25
21 \leftrightarrow 33	2.69	0.38	0.64
33 \leftrightarrow 6	2.48	0.26	0.35

the maximum value [54]:

$$\epsilon_{\max} = E_m^{\text{NEB}} + \frac{1}{2}E_f = \max(\Delta E_m + E_d^0) + \frac{1}{2}E_f. \quad (8)$$

A. NEB analysis for Li_3BO_3

As illustrated in Fig. 3, we identified the main diffusion path to be composed of sites 6 \leftrightarrow 18 \leftrightarrow 30 \leftrightarrow 9 \leftrightarrow 21 \leftrightarrow 33 \leftrightarrow 6 in both the I-vac and the F-doped Li_3BO_3 . The labels and energies correspond to the vacancy energies and distortion parameters listed in Table I. While this path is not the only possibility, it illustrates an efficient migration pathway within the **bc** plane.

The configuration path diagram shows that for the I-vac model, we see that the highest barrier for Li vacancy migration occurs between sites 18 and 30 or equivalently between sites 21 and 33 involving type Li(1) and Li(2) sites. By contrast, the F-doped model shows that the substitutional F ion tends to trap a Li ion vacancy in its vicinity (site 33 in this case). However, vacancy sites further away from the substitutional F site appear to resemble the I-vac energy path, shifted by approximately 0.2 eV. It is presumed that the simulations in larger supercells would converge more accurately to the I-vac energy profile.

The quantitative comparison between vacancy diffusion in Li_3BO_3 is summarized in Table III. For the I-vac crystal, the diffusion path consists of two symmetrically equivalent paths 6 \leftrightarrow 18 \leftrightarrow 30 \leftrightarrow 9 and 9 \leftrightarrow 21 \leftrightarrow 33 \leftrightarrow 6, resulting in two periodically repeated energy profiles with maximum step barrier of $\Delta E_m = 0.38$ eV occurring for 18 \leftrightarrow 30 and 21 \leftrightarrow 33. The energy barrier of each path segment in the F-doped crystal is comparable to that of the I-vac crystal. However, the hop between sites 21 \leftrightarrow 33 requires a higher energy of $\Delta E_m = 0.64$ eV compared to $\Delta E_m = 0.38$ eV in the I-vac structure, suggesting the F dopant tends to trap the vacancy close to the doping site. For path 30 \leftrightarrow 9 which is furthest from the F site, the doping effect is negligible with the same hopping energy of $\Delta E_m = 0.26$ eV as for the I-vac structure. From this analysis, we can estimate the activation energies for Li ion migration. According to Eq. (7), we find that $E_m^{\text{NEB}} = 0.38$ eV for the ideal I-vac model, compared with $E_m^{\text{NEB}} = E_a^{\text{NEB}} = 0.72$ eV for the F-doped model. For a stoichiometric and well-crystallized sample without presence of any defects, the vacancy-interstitial pair formation energy

E_f energy enters according to Eq. (7), resulting in the estimate $E_a^{\text{NEB}} = 1.00$ eV. While the F-doped model tends to trap the Li ion vacancy near the doping site, the estimate of the activation for Li ion migration energy is lower than that of the perfect crystal. As a consequence, doping with substitutional F provides an encouraging approach to improve the ionic conductivity properties of the pure Li_3BO_3 crystal. Alternatively, a stoichiometric but poorly crystalline sample would be expected to be represented by the I-vac model with an activation energy of $E_m^{\text{NEB}} = E_a^{\text{NEB}} = 0.38$ eV.

B. NEB analysis for Li_3BN_2

Among several possible migration paths of I-vac and C-doped models of Li_3BN_2 crystals, we present two representative Li ion vacancy migrations along the **a** axis and within a **bc** plane as illustrated in Fig. 4, with corresponding vacancy energies and distortion parameters listed in Table II. It is worth mentioning that the zero of energy was taken separately for the I-vac and C-doped models. The pure Li_3BN_2 contains three inequivalent Li sites: Li(1), Li(2), and Li(3) as indicated by three shades of blue balls in Fig. 4(a), consequently there are three distinct metastable vacancy configurations. For this I-vac case, the migration energy of each NEB channel was referenced to the energy of configuration with Li(2)-type vacancy at site 21 and its equivalent 25. For the C-doped model, site 25 has the lowest energy of the configurations considered and is set to zero energy, while sites further from the substitutional C site start to resemble the I-vac profile shifted to higher energy by approximately 0.3 eV.

The NEB energy diagrams for the I-vac and C-doped structures are shown in Fig. 4(b) for a path involving Li(1) vacancies sites moving along the **a** axis and Fig. 4(c) for a path involving alternating Li(1), Li(2), and Li(3) vacancy sites within in a **bc** plane. The quantitative analysis of vacancy diffusion in Li_3BN_2 is summarized in terms of the hopping energy barrier ΔE_m in Table IV based on the highest barrier for each indicated step. Since the supercell of the I-vac model of Li_3BN_2 consists of two replicas of the conventional unit cell along the **a** axis, the four-step path 1 \leftrightarrow 5 \leftrightarrow 3 \leftrightarrow 7 \leftrightarrow 1 involves two periodic energy profiles between nearest-neighbor sites of the same Li(1)-type: 1 \leftrightarrow 5 \leftrightarrow 3 and 3 \leftrightarrow 7 \leftrightarrow 1. Dominated by the migration path between 5 \leftrightarrow 3 (7 \leftrightarrow 1), the maximum energy barrier that a Li ion has to overcome for consecutive hops along this one-dimensional channel is $\Delta E_m = 0.27$ eV, together with the minimum defect energy $E_d^0 = 0.03$ eV, it can determine the migration energy of $E_m^{\text{NEB}} = 0.30$ eV for this path of the I-vac model from Eq. (7). Taking into account the estimated vacancy-interstitial pair formation energy of $E_f = 1.23$ eV, the activation energy for the perfect crystal is calculated to be $E_a^{\text{NEB}} = 0.62$ eV according to Eq. (8). Generally, the migration barrier for Li ion diffusion in the C-doped Li_3BN_2 not only depends on the position of the C dopant but also depends on the surrounding environment experienced by the mobile Li ions. For example, for the C-doped model, the corresponding **a** axis vacancy migration path finds the controlling barrier for the overall process to be the step 5 \leftrightarrow 3 with $\Delta E_m = 0.34$ eV, which together with the reference defect energy of $E_d^0 = 0.06$ eV, estimates $E_a^{\text{NEB}} = E_m^{\text{NEB}} = 0.40$ eV according to Eq. (7).

TABLE IV. Defect hopping energies ΔE_m for I-vac, C-doped, and I-int models of Li_3BN_2 . The step labels refer to the position labels in Fig. 4(a) for I-vac and C-doped models or the inset figure in Fig. 5 for the I-int models. The distances (measured from the corresponding perfect crystal sites before defect optimization) are given in units of \AA and energies are given in eV units.

Mechanism	Step	Distance	ΔE_m	
			I-vac	C-doped
Vacancy along a axis	1 \rightarrow 5	2.57	0.14	0.21
	5 \rightarrow 3	2.57	0.27	0.34
	3 \rightarrow 7	2.57	0.14	0.20
	7 \rightarrow 1	2.57	0.27	0.30
Vacancy in bc plane	46 \rightarrow 21	2.49	0.55	0.59
	21 \rightarrow 5	3.38	0.81	0.85
	5 \rightarrow 33	2.51	0.64	0.96
	33 \rightarrow 25	2.49	0.55	0.59
Kick out	I3 \rightarrow 1 \rightarrow I1	–	0.52	–
	I1 \rightarrow 21 \rightarrow I4	–	0.30	–
	I4 \rightarrow 2 \rightarrow I2	–	0.52	–

The Li ion diffusion in the **bc** plane of the I-vac and C-doped models of Li_3BN_2 involves a series of zigzag steps between adjacent inequivalent vacancy sites $46 \leftrightarrow 21 \leftrightarrow 5 \leftrightarrow 33 \leftrightarrow 25 \leftrightarrow 9$. The barriers for each step are summarized in Table IV. For the I-vac model of Li_3BN_2 , the path $46 \leftrightarrow 21 \leftrightarrow 5$ is symmetrically equivalent to the path $33 \leftrightarrow 29 \leftrightarrow 9$ with a hopping energy of $\Delta E_m = 0.81$ eV. This suggests that for a poorly crystalline sample of stoichiometric Li_3BN_2 , the activation energy would be $E_a^{\text{NEB}} = E_m^{\text{NEB}} = 0.81$ eV while for a well-crystallized sample the activation energy would be $E_a^{\text{NEB}} = 1.43$ eV, according to Eqs. (7) and (8), respectively. The corresponding hopping energies for the C-doped model are comparable, but because of the greater stability of the vacancy at site 46 near the C substitutional site, the largest hopping barrier is found to be $\Delta E_m = 0.96$ eV for the $5 \leftrightarrow 33$ step. The activation energies for this path in the **bc** plane is computed from Eq. (7) to be $E_a^{\text{NEB}} = 1.02$ eV. Generally, the Li ion migration barriers in the **bc** plane are significantly larger than those in along the **a** axis.

Also listed in Table IV are results from NEB analyses involving the equivalent lowest energy metastable interstitial sites. Figure 5 shows the corresponding local ball and stick diagram containing four equivalent nearest-neighboring interstitial sites I1–I4 surrounded by Li ions at host sites of types Li(1) and Li(2) together with the corresponding energy path diagram. Although direct hopping between interstitial sites seems to be unlikely on the basis of geometric considerations, kick-out or interstitialcy processes may be possible. This was examined using the results from the I-int models discussed in Sec. III B to model $2 \times 2 \times 1$ supercells of Li_3BN_2 containing one charge-compensated interstitial Li ion. The corresponding hopping energies ΔE_m are listed at the bottom of Table IV. Here the notation I3 \rightarrow 1 \rightarrow I1 means that an initial I-int configuration at the interstitial site I3 (visualized in the inset of Fig. 5) transitions to replace the host Li ion at site 1, which then moves to I-int configuration at the interstitial site I1. The

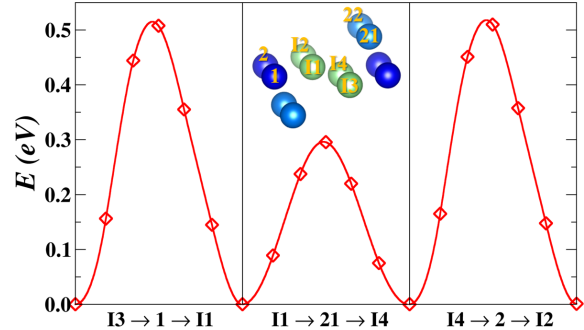


FIG. 5. Configuration energy diagram for the kick-out mechanism in Li_3BN_2 together with an inset diagram of the involved sites. In the diagram, Li ions at host sites are represented using the same convention as in Fig. 4(a) while interstitial sites are represented with green balls.

subsequent step of I1 \rightarrow 21 \rightarrow I4 is geometrically equivalent to the initial configuration in this supercell. Proceeding with this kick-out process, Li ions can consecutively hop between equivalent interstitial sites with the exchange of host ions along the **b** axis. The maximum hopping energy for the path I3 \rightarrow 1 \rightarrow I1 \rightarrow 21 \rightarrow I4 is $\Delta E_m = 0.52$ eV. According to Eqs. (7) and (8), the activation energy for this process is expected to be $E_a^{\text{NEB}} = 0.52$ or 1.14 eV for a poorly crystalline or highly crystalline sample, respectively.

In summary, the NEB analysis suggests that the most efficient Li ion conductivity in Li_3BN_2 occurs via a vacancy mechanism along the **a** axis of the crystal.

V. MOLECULAR DYNAMICS SIMULATIONS

MD simulations based on density-functional evaluations of the ideal and defective supercells were performed to understand the dynamic and statistical nature of Li ion migrations. The simulations approximated a microcanonical NVE ensemble, using a velocity Verlet algorithm [55] with a time integration step of $\Delta t = 2.4$ fs. Here NVE refers to a constant number of atoms N_{atom} in the supercell held at constant volume V and a constant energy which corresponds to $U_{\text{SL}} + E_{\text{kin}}^{\text{ion}}$, the total density functional static lattice energy plus the classical mechanics ion kinetic energy at each time step. The initial distribution of velocities of ions in the relaxed simulation cell is taken from Boltzmann distribution for twice the target temperature. Without controlling the temperature via any velocity rescaling scheme, this procedure is found to equilibrate for simulation times $t > t_{\text{eq}}$, with fluctuating instantaneous temperatures around the target temperature. For most of the simulations in this paper, $t_{\text{eq}} \approx 0.02$ ps. Typically, the average temperature for a given run is determined by averaging the temperature from the ion classical kinetic energy at each time step t' according to

$$\langle T \rangle = \frac{2}{3(N_{\text{atom}} - 1)k_B} \frac{1}{(t_{\text{max}} - t_{\text{eq}})} \int_{t_{\text{eq}}}^{t_{\text{max}}} E_{\text{kin}}^{\text{ion}}(t') dt'. \quad (9)$$

In this paper, a sufficiently high temperature is required to simulate significant hopping events in the model structures. We find that although $\langle T \rangle$ is generally close to the target temperature, it is somewhat dependent on the setting of the initial velocity distribution. The ionic conductivity for each system under consideration is obtained after a MD duration of 100–120 ps.

In this paper, the ionic motion is analyzed with the simplifying assumption that independent ion motion dominates, focusing on the so-called tracer diffusion process which depends on the mean-squared displacement (MSD) [56,57]. With equally probable microscopic states at each time step, the MSD, defined by the following relation, is introduced to track the dynamical evolution of Li ions over a time window of t for a simulated temperature T :

$$\text{MSD}(t, T) \equiv \frac{1}{N_{\text{Li}}} \left\langle \sum_{i=1}^{N_{\text{Li}}} |\mathbf{R}_i(t) - \mathbf{R}_i(0)|^2 \right\rangle_t, \quad (10)$$

where N_{Li} indicates the number of mobile Li ions in the simulation and $\mathbf{R}_i(t)$ denotes the position of the Li ion with label i at time t . During the simulations over the total time duration, there are many time intervals with the same period t but with different starting and ending times to improve the ensemble sampling to get more accurate diffusional properties, the MSD as a function of t is obtained by averaging over all the squared displacements with the same time interval as indicated by the angular brackets in the expression.

The quantitative information on the diffusion of Li ions is implied by the slope of the MSD or the so-called tracer diffusion coefficient D_{tr} at a sufficient calculation time,

$$D_{\text{tr}}(T) = \frac{1}{6} \lim_{t \rightarrow \infty} \frac{1}{(t - t_{\text{eq}})} \text{MSD}(t - t_{\text{eq}}, T). \quad (11)$$

Here the subscript tr specifies the self-diffusion process for noninteracting Li ions.

By definition, the diffusion coefficient relates to the capacity of a Li ion to move a distance over a time interval, and such diffusive behavior is subjected to a thermally activated process, customarily we can describe this temperature-dependent diffusion coefficient in terms of an Arrhenius relationship analogous to the diffusion modeled by the NEB approach of Eq. (5),

$$D_{\text{tr}}(T) = D_0 e^{-E_a^{\text{MD}}/k_B T}, \quad (12)$$

where D_0 is a temperature-independent pre-exponential factor, k_B is the Boltzmann constant, and E_a^{MD} is the activation energy of motion which can be deduced from the Arrhenius plot of $\ln(D_{\text{tr}}(T))$ versus $1/T$. In general, we expect that the activation energies deduced from the MD and the NEB analyses to differ because differing physical and mathematical approximations.

The ionic conductivity is related to the diffusion process via the Nernst-Einstein equation:

$$\sigma(T) = \rho q^2 \frac{D_{\text{tr}}(T)}{k_B T H_r}. \quad (13)$$

Here $\rho = N_{\text{Li}}/V$ denotes the ratio of the number of Li ions within the simulation cell to its volume V , q represents the charge of the Li ion (presumed to be +1, in units of the

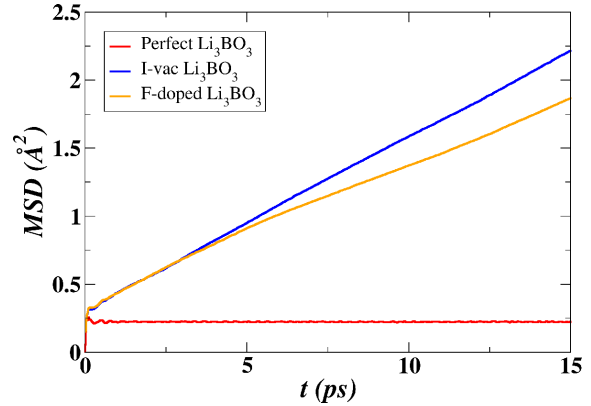


FIG. 6. Plots of $\text{MSD}(t, \langle T \rangle)$ from Eq. (10) in units of Å^2 as a function of time in units of picoseconds for the stoichiometric, I-vac, and F-doped models of Li_3BO_3 at average temperatures of $\langle T \rangle = 968, 998,$ and 996 K, respectively.

elementary charge unit e), H_r is the Haven ratio [58] which accounts for the effect of the correlation and collectivity effects of ionic motion. For our system, we take $H_r = 1$ with assumption of independent migrations of Li ions.

A. Molecular dynamics simulations for Li_3BO_3

Results for the MSDs of Li ions in $3 \times 1 \times 1$ supercells of pure Li_3BO_3 as well as I-vac and F-doped models are presented in Fig. 6 for simulation temperatures of approximately 1000 K, evaluated according to Eq. (10). As the nearly horizontal MSD curve for pure Li_3BO_3 shows, the full ordering of Li ions in this material greatly limits their displacements, resulting in extremely low ionic mobility. It is expected that the Li ion mobility can be improved by introducing Li vacancies sites. In fact, this is seen in Fig. 6 in terms of the substantial slopes of the MSD curves for the I-vac and F-doped models.

To visualize the Li ion motions in the I-vac and F-doped models, in Fig. 7 we show the ball and stick diagrams for the initial B and O sites with superposed Li ion positions for the first 70 ps of the simulation with a time interval of 0.24 ps. The time sequence of the superposed images is missing from this visualization, however, it is clear that there is considerable motion of the Li ions during the course of the simulation. Interestingly, the pattern of superposed Li ion sites look very similar for the I-vac and F-doped models, each without obvious occupancy of interstitial sites. To the extent that there are a significant number of images between all of the host lattice Li sites, one can conclude that all of the Li ions [types Li (1), (2), and (3)] participate in ion migration, consistent with the predicted diffusion pathway in NEB calculations shown in Fig. 3. It is therefore encouraging and provides some confidence that the Li ion migrations in our simulated crystals are likely to occur via vacancy mechanisms.

Figure 8 summarizes the results for the Li ion conductivity of Li_3BO_3 versus $1000/T$. The calculated MD results were estimated using Eq. (13) with $H_r = 1$. In the present paper, the measurement of the ionic conductivity for the pure Li_3BO_3 with sample preparation described in Paper II [14]

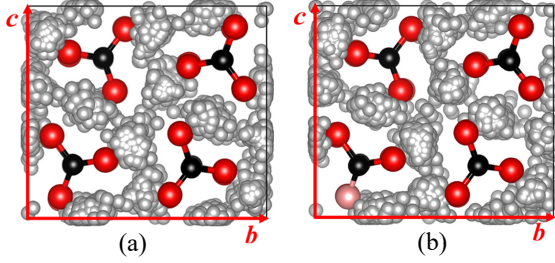


FIG. 7. Ball and stick diagrams of MD simulations for (a) I-vac Li_3BO_3 at temperature (T) = 996 K and (b) F-doped Li_3BO_3 at temperature (T) = 998 K. B, O, and F are shown at their initial positions with black red, and pink balls, respectively. Li positions of the initial configuration and 290 subsequent positions at time intervals of 0.24 ps are indicated with gray balls. Simulations were performed using microcanonical NVE ensembles in $3 \times 1 \times 1$ supercells. The diagram represents a projection onto the bc plane.

were conducted with gold blocking electrodes sputtering onto each side of the pellet sample for electrochemical impedance spectroscopy (EIS). EIS measurements were performed on a BioLogic SP-200 from 1 MHz to 100 MHz with an amplitude of 100 mV at temperatures ranging from 20 – 80 °C. Figure 8 also includes the experimental data analyzed from the published work of Ohta *et al.* [15] and Shigeno *et al.* [31] using digitizing software. All the straight lines represent the linear fit of the discrete values, the slope of which determines the deduced activation energy based on the Nernst-Einstein and Arrhenius relationships given in Eqs. (13) and (12), as listed in Table V. It is interesting to note that the experimental measurements plotted here show a range of values that are roughly in the same range of the MD simulation results.

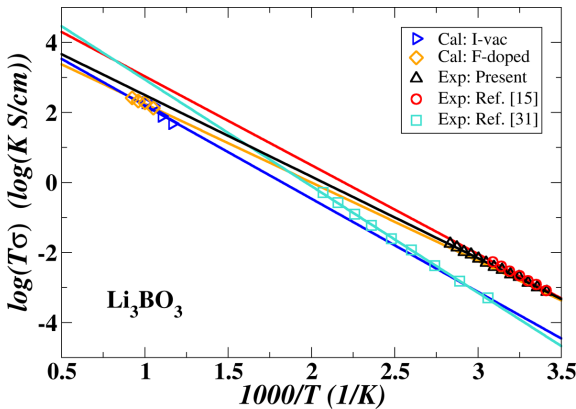


FIG. 8. Plot of computational and experimentally measured values of $\log_{10}(\sigma T)$ versus $1000/T$ for the I-vac and the F-doped models of Li_3BO_3 . The computed values of σ were determined from Eq. (13). Lines represent least squares fits to the $\log_{10}(\sigma T)$ data. The experimental results for polycrystalline Li_3BO_3 (red circles) were obtained by refitting the data in Ref. [15] and for glassy Li_3BO_3 (green squares) were obtained by refitting the data in Ref. [31].

TABLE V. Results of activation energy on Li_3BO_3 . The MD data in units of eV is determined from the slope of the straight line in Fig. 8, and the corresponding conductivity in units of S/cm is extrapolated to $T = 300$ K. The experimental results are listed as reported at $T = 25$ Celsius.

Material	Analysis	E_a	$\sigma(T = 300 \text{ K})$
I-vac Li_3BO_3	MD	0.53	3.2×10^{-7}
	NEB	0.38	—
F-doped Li_3BO_3	MD	0.45	3.4×10^{-6}
	NEB	0.72	—
Polycrystalline Li_3BO_3	Exp ^a	0.46	3.8×10^{-6}
Polycrystalline Li_3BO_3	Exp ^b	0.51	2.0×10^{-6}
Glassy Li_3BO_3	Exp ^c	0.60	3.4×10^{-7}

^aThe present experimental measurement.

^bExperimental data from Ref. [15].

^cExperimental data from Ref. [31].

In Table V, we list the results of NEB and MD simulations together with the experimental measurements. The larger estimated room-temperature conductivity and slightly lower activation energy of the F-doped Li_3BO_3 relative to the I-vac Li_3BO_3 suggests that substitutional doping of O with F creates an enabling environment for Li ion migration processes. While due to the trapping effect, the NEB results on the F-doped Li_3BO_3 are strongly influenced by the Li ion hops near the F site. The more physical picture is expected to be provided by MD simulations with an effective barrier evaluated over the hopping events of all mobile Li ions. The simulations on crystals with Li vacancies and the fitted results from the experiment shows good agreement, particularly the room-temperature conductivities of the calculated value and the experimental measurement are in the same order of magnitude $10^{-7} - 10^{-6}$ S/cm. Although our experimental measurements on the phase-pure Li_3BO_3 and the experimental papers [15,31] do not mention intentional doping in their sample preparation, the simulation results suggest that vacancy populations are likely to be present in the current experimental samples and the samples reported in Refs. [15,31] as well. This speculation is motivated both by the MD simulations near $T = 1000$ K, showing negligible Li MSDs for simulations on initially perfect configurations in contrast to simulations on initial configurations containing a single vacancy in the supercell shown in Fig. 6, and by the estimate of the interstitial-vacancy pair energy of $E_f = 1.25$ eV for this system. These results suggest that, while the bottleneck for vacancy formation is too high to generate conductivity in an ideal crystal, perhaps a small number of such Frenkel defects are typically formed during synthesis of these materials.

B. Molecular dynamics simulations for Li_3BN_2

To explore the performance of Li_3BN_2 as an ionic conductor, in Fig. 9 we plot the MSDs as a function of simulation time for MD simulations at average temperatures near 1300 K. Here we compare models of stoichiometric Li_3BN_2 having fully occupied host sites in the initial configuration, with the I-int model initially having an extra Li at one of the

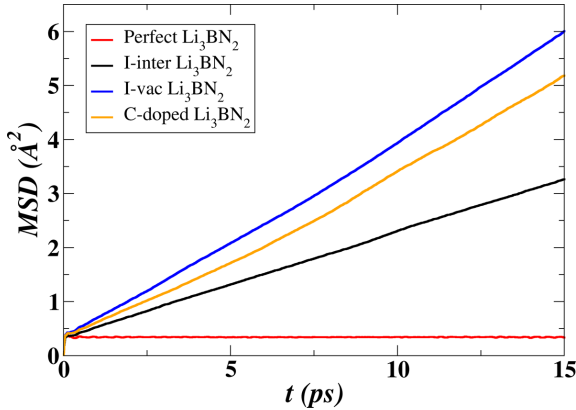


FIG. 9. Plots of $MSD(t, \langle T \rangle)$ from Eq. (10) in units of \AA^2 as a function of time in units of picosecond for $2 \times 2 \times 1$ supercells of Li_3BN_2 for the stoichiometric, I-int, I-vac, and C-doped models at average temperatures of $\langle T \rangle = 1272, 1259, 1254,$ and 1261 K, respectively.

metastable interstitial sites, with the I-vac model initially having a missing Li ion, and the C-doped model having a C ion substituting for one B ion together with a missing Li ion. For the C-doped models, we observed that the N–C–N bond is robust; showing no evidence of breaking throughout the simulation at each considered temperature. From the figure, we see that the Li ions of the stoichiometric model present trivial displacements with a flat MSD curve, indicating very high activation energy for triggering the diffusion process. By contrast, the three different defect configurations display measurable diffusivity with comparable slopes for a similar temperature. For the I-int model, we found that the interstitial Li ion only jumps back and forth between adjacent interstitial sites, causing a very localized and short-ranged migration in terms of a pure interstitial mechanism. Consistent with the kick-out process discussed above using the NEB analysis, the vacancy mechanism is found to be significant for the I-int model. For these high temperature simulations, it is interesting that the MSD curves predict that diffusivity of the I-vac model to be almost twice that of the I-int model, with the C-doped model predicted to have a diffusivity in between but more similar to that of the I-vac model.

To examine the role of Li ion vacancies in determining ion mobility, we can follow the Li ion trajectories $\mathbf{R}_i(t)$ to estimate the fraction of vacancy sites at any given time step t . For our constant volume simulations of the $2 \times 2 \times 1$ supercell, the location of each of the $N_h = 48$ host lattice sites are known. They are analyzed as occupied at time t if a Li ion is found within 1 \AA of the site; otherwise it is vacant. In this way, the number of vacancies at each time step $N_v(t)$ and the ratio $N_v(t)/N_h$ can be calculated. Not surprisingly, the vacancy ratio increases over time and with temperature. An example of vacancy fraction analysis for the I-vac model at two different temperatures is shown in Fig. 10. Similar results were obtained from the C-doped model. Here we see that at these temperatures, the vacancy fraction steadily rises, increasing more rapidly at the higher temperature. In each case,

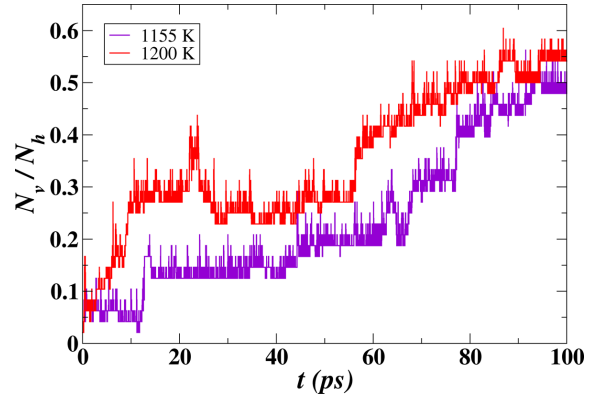


FIG. 10. Plots of fractions of vacancies with respect to simulation time in units of picosecond for I-vac Li_3BN_2 at $\langle T \rangle = 1155$ K (purple) and 1200 K (red).

we found that the most of the Li ions leaving the normal host sites did not hop into the interstitial defect positions but tended to hover at the intermediate sites between the host sites that constitute the main vacancy conducting path. On one hand, because of the growing number of unoccupied host sites as time progresses, the structure becomes increasingly defective and disordered, which may promote the ion diffusion. On the other hand, as suggested by Fig. 4 of the NEB analysis, the single hop barrier energies between neighboring host sites are unevenly distributed with relatively high values, thus slowing down the conduction of Li ions even with considerable vacant sites available to be occupied.

Using a similar approach to quantify the time-dependent occupancy of interstitial sites finds that the interstitial sites

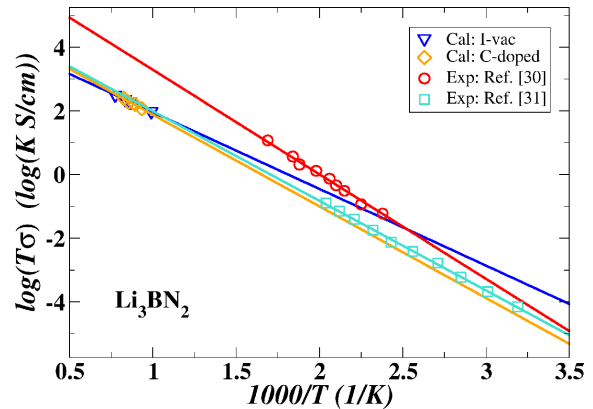


FIG. 11. Plots of $\log_{10}(\sigma T)$ vs $1000/T$ for the I-vac Li_3BN_2 (blue) and the C-doped Li_3BN_2 (orange). The data points were gathered from MD simulations and the straight line is a linear fit of the points with the slope determining the activation energy. The experimental results for polycrystalline Li_3BN_2 (red circles) were obtained by refitting the data in Ref. [30] and for glass-ceramic Li_3BN_2 (green squares) were obtained by refitting the data in Ref. [31].

TABLE VI. Results of conductivity simulations in comparison with the available experimental data. Energies are given in eV and the ionic conductivities are in units of S/cm. The experimental conductivities are listed as reported at (or extrapolated to) $T = 25$ Celsius.

Materials	Analysis	E_a	$\sigma(T = 300 \text{ K})$
I-vac Li_3BN_2	MD	0.48	7.2×10^{-7}
	NEB	0.30 (a)/0.81 (bc)	—
C-doped Li_3BN_2	MD	0.57	4.8×10^{-8}
	NEB	0.40 (a)/1.02 (bc)	—
Polycrystalline Li_3BN_2	Exp ^a	0.66	1.4×10^{-7}
Glass-ceramic Li_3BN_2	Exp ^b	0.56	1.1×10^{-7}

^aExperimental data from Ref. [30].

^bExperimental data from Ref. [31].

are found to play a minor role in the Li ion mobility in these systems.

From this insight, we focus on studying the ionic conductivity for the I-vac and C-doped models of Li_3BN_2 using Eq. (13) with $H_r = 1$ to analyze MD simulations with average temperatures ranging between 1000 – 1300 K. The results are shown in Fig. 11. The experimental data were analyzed from the published work of Yamane *et al.* [30] and Shigeno *et al.* [31] using digitizing software. The Li ion activation energies, as listed in Table VI, are deduced from the slopes of the linear fit lines of the discrete values according to the Nernst-Einstein and Arrhenius relationships given in Eqs. (13) and (12). It is also noticeable that the plots of the experimental measurements and the MD simulations are in the same range of values over the explored temperature range.

According to the results listed in Table VI, the activation energy for the C-doped model is 0.57 eV compared to 0.48 eV for the I-vac model. In general, the calculated MD results for the activation energy and room-temperature ionic conductivity are comparable with the experimental measurements. Following the MD trajectories, we find that the first diffusion channel formed in each structure is along the **a** axis, consisting of the most energetically favorable path identified in NEB calculations. Also, it is reasonable to see that for each model, the calculated activation energy from MD simulations falls in between the NEB data of the lowest barrier channel along the **a** axis and the NEB results of **bc** plane in which the massive Li ion diffusions are less likely to occur.

VI. SUMMARY AND CONCLUSIONS

Using NEB methods and MD simulations, we have studied the Li ion migration mechanisms of crystalline Li_3BO_3 and

Li_3BN_2 , both having monoclinic structure with space group symmetry $P2_1/c$. The two materials were found to be similar in terms of the Li ions positioning themselves within BO_3^{3-} or BN_2^{3-} anion frameworks as well as their Li ion conductivity mechanisms being characterized by vacancy processes. For both materials, the NEB analysis was able to identify the main Li ion vacancy migration pathways which turned out to be qualitatively consistent with the MD trajectories such as shown in Fig. 7 for Li_3BO_3 . For Li_3BO_3 , the migration path is two-dimensional within the **bc** plane, involving all of the Li ion sites. By contrast, the migration is one-dimensional along the **a** axis for Li_3BN_2 , involving only Li ion sites of type Li(1). In addition, the MD simulations show the Li ion to spend a significant amount of its time at a distance of more than 1 Å away from its equilibrium host site. This is shown qualitatively in Fig. 7 for Li_3BO_3 and more quantitatively in Fig. 10 for Li_3BN_2 .

Using MSD analysis of the MD results and approximating the Haven ratio to be 1, the ionic conductivity could be calculated from Eq. (13). The results for Li_3BO_3 shown in Fig. 8 and the results for Li_3BN_2 shown in Fig. 11 suggest very similar outcomes for simulations using supercells with an ideal vacancy or a vacancy due to substitutional doping. Moreover, simulation for both materials at high temperature extrapolate with respect to $1000/T$ to values that are close to data available from experimental measurements, including measurements on Li_3BO_3 generated for this paper. The Li ion conductivity at 300 K is $10^{-7} - 10^{-6}$ S/cm for Li_3BO_3 and $10^{-8} - 10^{-7}$ S/cm for Li_3BN_2 . It is interesting to speculate about possible sources of Li ion vacancies needed for the conduction processes in the experimental samples since these were prepared without intentional doping. One possibility might be that stable vacancy-interstitial defect pairs, usually known as Frenkel defects, are present in these samples. Our simulations show that while perfect crystals exhibit no conductivity, simulations with a Li vacancy ratio of 1/12 for Li_3BO_3 and 1/16 for Li_3BN_2 show reasonable agreement with the experiment.

ACKNOWLEDGMENTS

This work was supported by NSF Grant No. DMR-1940324. Computations were performed on the Wake Forest University DEAC cluster, a centrally managed resource with support provided in part by the university. Z.D.H. was supported by Laboratory Directed Research and Development (LDRD) funding from Argonne National Laboratory, provided by the Director, Office of Science, of the U.S. Department of Energy under Contract No. DE-AC02-06CH11357.

- [1] D. Campanella, D. Belanger, and A. Paoletta, *J. Power Sources* **482**, 228949 (2021).
 [2] M. Balaish, J. C. Gonzalez-Rosillo, K. J. Kim, Y. Zhu, Z. D. Hood, and J. L. M. Rupp, *Nat. Energy* **6**, 227 (2021).
 [3] Y. Zhu, J. C. Gonzalez-Rosillo, M. Balaish, Z. D. Hood, K. J. Kim, and J. L. M. Rupp, *Nat. Rev. Mater.* **6**, 313 (2020).

- [4] K. J. Kim, M. Balaish, M. Wadaguchi, L. Kong, and J. L. M. Rupp, *Adv. Energy Mater.* **11**, 2002689 (2020).
 [5] M. V. Reddy, C. M. Julien, A. Mauger, and K. Zaghbi, *Nanomaterials* **10**, 1606 (2020).
 [6] M. M. Ioanniti, F. Hu, and W. E. Tenhaeff, *J. Vac. Sci. Technol. A* **38**, 060801 (2020).

- [7] X. Miao, H. Wang, R. Sun, C. Wang, Z. Zhang, Z. Li, and L. Yin, *Energy Environ. Sci.* **13**, 3780 (2020).
- [8] Z. Tong, S.-B. Wang, Y.-K. Liao, S.-F. Hu, and R.-S. Liu, *ACS Appl. Mater. Interfaces* **12**, 47181 (2020).
- [9] J. Li, C. Ma, M. Chi, C. Liang, and N. J. Dudney, *Adv. Energy Mater.* **5**, 1401408 (2015).
- [10] W. C. West, Z. D. Hood, S. P. Adhikari, C. Liang, A. Lachgar, M. Motoyama, and Y. Iriyama, *J. Power Sources* **312**, 116 (2016).
- [11] Y. Zhu, X. He, and Y. Mo, *Adv. Sci.* **4**, 1600517 (2017).
- [12] Z. D. Hood, X. Chen, R. L. Sacci, X. Liu, G. M. Veith, Y. Mo, J. Niu, N. J. Dudney, and M. Chi, *Nano Lett.* **21**, 151 (2021).
- [13] W. D. Richards, L. J. Miara, Y. Wang, J. C. Kim, and G. Ceder, *Chem. Mater.* **28**, 266 (2016).
- [14] Y. Li, Z. D. Hood, and N. A. W. Holzwarth, *Phys. Rev. Materials* **5**, 085403 (2021).
- [15] S. Ohta, S. Komagata, J. Seki, T. Saeki, S. Morishita, and T. Asaoka, *J. Power Sources* **238**, 53 (2013).
- [16] M. He, H. Okudera, J. Fleig, A. Simon, X. Chen, and J. Maier, *J. Solid State Chem.* **178**, 680 (2005).
- [17] H. Yamada, *J. Indian Inst. Sci.* **96**, 315 (2016).
- [18] M. Tatsumisago, R. Takano, K. Tadanaga, and A. Hayashi, *J. Power Sources* **270**, 603 (2014).
- [19] M. Eom, S. Choi, S. Son, L. Choi, C. Park, and D. Shin, *J. Power Sources* **331**, 26 (2016).
- [20] K. Nagao, A. Hayashi, and M. Tatsumisago, *J. Ceram. Soc. Jpn.* **124**, 915 (2016).
- [21] K. Nagao, M. Nose, A. Kato, A. Sakuda, A. Hayashi, and M. Tatsumisago, *Solid State Ionics* **308**, 68 (2017).
- [22] M. Tatsumisago, R. Takano, M. Nose, K. Nagao, A. Kato, A. Sakuda, K. Tadanaga, and A. Hayashi, *J. Ceram. Soc. Jpn.* **125**, 433 (2017).
- [23] K. Nagao, A. Sakuda, A. Hayashi, and M. Tatsumisago, *J. Power Sources* **424**, 215 (2019).
- [24] H. W. Langmi and G. S. McGrady, *J. Alloys Compd.* **466**, 287 (2008).
- [25] H. Yamane, T. Kano, A. Kamegawa, M. Shibata, T. Yamada, M. Okada, and M. Shimada, *J. Alloys Compd.* **402**, L1 (2005).
- [26] M. Kagamida, H. Kanda, M. Akaishi, A. Nukui, T. Osawa, and S. Yamaoka, *J. Cryst. Growth* **94**, 261 (1989).
- [27] S. Nakano, H. Ikawa, and O. Fukunaga, *Diamond Relat. Mater.* **3**, 75 (1993).
- [28] O. Fukunaga and S. Takeuchi, *Int. J. Refract. Met. Hard Mater.* **55**, 54 (2016).
- [29] S. Emani, C. Liu, M. Ashuri, K. Sahni, J. Wu, W. Yang, K. Németh, and L. L. Shaw, *ChemElectroChem* **6**, 320 (2019).
- [30] H. Yamane, S. Kikkawa, and M. Koizumi, *J. Solid State Chem.* **71**, 1 (1987).
- [31] M. Shigeno, K. Nagao, M. Deguchi, C. Hotehama, H. Kowada, A. Sakuda, A. Hayashi, and M. Tatsumisago, *Solid State Ionics* **339**, 114985 (2019).
- [32] *International Tables for Crystallography, Volume A: Space-Group Symmetry*, 5th revised ed., edited by T. Hahn (Kluwer Academic Publishers, Boston, 2002).
- [33] M. I. Aroyo, J. M. Perez-Mato, D. Orobengoa, E. Tasci, G. De La Flor, and A. Kirov, *Bulg. Chem. Commun.* **43**, 183 (2011), <http://www.cryst.ehu.es/>.
- [34] H. Jónsson, G. Mills, and K. W. Jacobsen, in *Classical and Quantum Dynamics in Condensed Phase Simulations*, edited by B. J. Berne, G. Ciccotti, and D. F. Coker (World Scientific, Singapore, 1998), pp. 385–404.
- [35] G. Henkelman, B. P. Uberuaga, and H. Jónsson, *J. Chem. Phys.* **113**, 9901 (2000).
- [36] G. Henkelman and H. Jónsson, *J. Chem. Phys.* **113**, 9978 (2000).
- [37] P. Hohenberg and W. Kohn, *Phys. Rev.* **136**, B864 (1964).
- [38] W. Kohn and L. J. Sham, *Phys. Rev.* **140**, A1133 (1965).
- [39] P. E. Blöchl, *Phys. Rev. B* **50**, 17953 (1994).
- [40] N. A. W. Holzwarth, A. R. Tackett, and G. E. Matthews, *Comput. Phys. Commun.* **135**, 329 (2001), <http://pwpaw.wfu.edu>.
- [41] P. Giannozzi, O. Andreussi, T. Brumme, O. Bunau, M. Buongiorno Nardelli, M. Calandra, R. Car, C. Cavazzoni, D. Ceresoli, M. Cococcioni, N. Colonna, I. Carnimeo, A. Dal Corso, S. de Gironcoli, P. Delugas, R. A. DiStasio, A. Ferretti *et al.*, and *J. Phys.: Condens. Matter* **29**, 465901 (2017), <http://www.quantum-espresso.org>.
- [42] P. Giannozzi, O. Baseggio, P. Bonfà, D. Brunato, R. Car, I. Carnimeo, C. Cavazzoni, S. de Gironcoli, P. Delugas, F. Ferrari Ruffino, A. Ferretti, N. Marzari, I. Timrov, A. Urru, and S. Baroni, *J. Chem. Phys.* **152**, 154105 (2020), <http://quantum-espresso.org>.
- [43] J. P. Perdew, A. Ruzsinszky, G. I. Csonka, O. A. Vydrov, G. E. Scuseria, L. A. Constantin, X. Zhou, and K. Burke, *Phys. Rev. Lett.* **100**, 136406 (2008).
- [44] K. Momma and F. Izumi, *Appl. Crystallogr.* **44**, 1272 (2011), code available from <http://jp-minerals.org/vesta/en/>.
- [45] A. Kokalj, *Comput. Mater. Sci.* **28**, 155 (2003), code available at <http://www.xcrysden.org>.
- [46] Y.-W. Hu, I. D. Raistrick, and R. A. Huggins, *J. Electrochem. Soc.* **124**, 1240 (1977).
- [47] V. Thangadurai and W. Weppner, *Ionics* **8**, 281 (2002).
- [48] J. C. Bachman, S. Muy, A. Grimaud, H.-H. Chang, N. Pour, S. F. Lux, O. Paschos, F. Maglia, S. Lupart, P. Lamp, L. Giordano, and Y. Shao-Horn, *Chem. Rev.* **116**, 140 (2016).
- [49] E. Kazyak, K.-H. Chen, A. L. Davis, S. Yu, A. J. Sanchez, J. Lasso, A. R. Bielinski, T. Thompson, J. Sakamoto, D. J. Siegel, and N. P. Dasgupta, *J. Mater. Chem. A* **6**, 19425 (2018).
- [50] S. H. Jung, K. Oh, Y. J. Nam, D. Y. Oh, P. Brüner, K. Kang, and Y. S. Jung, *Chem. Mater.* **30**, 8190 (2018).
- [51] N. D. Lepley and N. A. W. Holzwarth, *J. Electrochem. Soc.* **159**, A538 (2012).
- [52] M. G. Down, M. J. Haley, P. Hubberstey, R. J. Pulham, and A. E. Thunder, *J. Chem. Soc. Dalton Trans.* 1407(10) (1978).
- [53] In principle, both vacancy and interstitial defects can be analyzed in this way. However, in the present paper, multiple vacancy defect and single interstitial defect configurations were considered for each system.
- [54] A. R. West, *Basic Solid State Chemistry*, 2nd ed. (John Wiley & Sons, Ltd., Hoboken, NJ, 1999).
- [55] W. D. Swope, H. C. Andersen, P. H. Berens, and K. R. Wilson, *J. Chem. Phys.* **76**, 637 (1982).
- [56] J. D. Howard and N. Holzwarth, *Solid State Ionics* **325**, 80 (2018).
- [57] X. He, Y. Zhu, A. Epstein, and Y. Mo, *npj Comput. Mater.* **4**, 18 (2018).
- [58] Y. Haven and B. Verkerk, *Phys. Chem. Glasses* **6**, 38 (1965).

Appendix D

Computational study of Li_3BO_3
and Li_3BN_2 II: Stability analysis of
pure phases and of model
interfaces with Li anodes

Computational study of Li_3BO_3 and Li_3BN_2 II: Stability analysis of pure phases and of model interfaces with Li anodes

Yan Li ¹, Zachary D. Hood ², and N. A. W. Holzwarth ¹

¹Department of Physics, Wake Forest University, Winston-Salem, North Carolina 27109, USA

²Applied Materials Division, Argonne National Laboratory, Argonne, Illinois 60439, USA



(Received 22 June 2021; accepted 29 July 2021; published 17 August 2021)

Both Li_3BO_3 and Li_3BN_2 materials have promising properties for use in all solid-state batteries and other technologies dependent on electrolytes with significant ionic conductivity. As the second of a two-part study, the structural properties of Li_3BO_3 and three reported phases of Li_3BN_2 are investigated using first-principles modeling techniques. For α - Li_3BN_2 , the tetragonal $P4_2/mnm$ structure reported in the literature is found to be unstable as evidenced by imaginary phonon modes near the M point of its Brillouin zone. Our simulations within the harmonic approximation suggest that the real α phase has the orthorhombic space group symmetry $Pmnm$ formed with twice as many formula units and tiny adjustments of the equivalent lattice parameters and fractional coordinates. Extending the analysis of the $Pmnm$ α - Li_3BN_2 structure to the quasiharmonic approximation improves the agreement between the room-temperature x-ray pattern reported in the literature and the corresponding simulation results. In anticipation of the use of the monoclinic phases of Li_3BO_3 and Li_3BN_2 in Li ion conducting applications, chemical stability is investigated in terms of free-energy differences of possible decomposition and Li reaction processes, finding encouraging results. As further investigations of Li_3BO_3 and β - Li_3BN_2 as electrolyte or coating materials, particularly for use with Li metal anodes, idealized electrolyte/Li interfaces were investigated in terms of their geometric, energetic, and electronic properties. The results find the electrolyte/Li interfaces to be quite favorable, perhaps comparable to the pioneering LiPON/Li system.

DOI: [10.1103/PhysRevMaterials.5.085403](https://doi.org/10.1103/PhysRevMaterials.5.085403)

I. INTRODUCTION

The companion paper (Paper I) [1] presents the results of first-principles computational methods used to investigate the detailed mechanisms of Li ion diffusion in the monoclinic forms of lithium borate Li_3BO_3 and boron-nitride Li_3BN_2 , finding encouraging results for ionic conductivity with the introduction of vacancies by disorder and doping. In the present paper, we examine the stability properties of pure Li_3BO_3 and Li_3BN_2 , including the stability of the crystalline materials and the stability of possible interface configurations with an ideal lithium anode in anticipation of possible applications as electrolytes or as coatings in solid-state batteries and other technologies.

The outline of this paper is as follows. Section II details the computational methods used in this paper. Section III presents the structural properties of Li_3BO_3 and three reported phases of Li_3BN_2 , including the calculated lattice parameters of the crystal structures and vibrational analyses using the harmonic phonon approach. To improve the physical treatment, in Sec. IV, the quasiharmonic approximation is applied to better represent the corrected structure of α - Li_3BN_2 . Section V discusses the stabilities of the materials in terms of possible decompositions and reactions with Li metal. In Sec. VI, we investigated the interface properties of the potential electrolyte materials, Li_3BO_3 and β - Li_3BN_2 , with Li metal. A summary of the results and some conclusions are given in Sec. VII.

II. CALCULATIONAL METHODS

The computational methods for this paper are based on density functional theory (DFT) [2,3] using the projector augmented plane wave (PAW) [4] formalism with the data sets generated by the ATOMPAW code [5]. The exchange-correlation terms were represented by the modified generalized gradient formulation known as PBEsol [6]. Density functional perturbation theory [7–11] was used to evaluate derivatives of the density functional energies. The computations were performed using both the ABINIT [12,13] and QUANTUM ESPRESSO [14,15] packages interchangeably. For reasons of convenience and efficiency, ABINIT was used to perform the calculations reported in Secs. III and V while QUANTUM ESPRESSO was used to perform the calculations reported in Secs. IV and VI. The two codes use slightly different internal algorithms to evaluate the system energies, so it was necessary to use slightly different calculational parameters. For example, for each Bloch wave vector \mathbf{k} , the summations over reciprocal lattice vectors \mathbf{G} included all terms such that $|\mathbf{k} + \mathbf{G}|^2 \leq 2m\epsilon_{\text{cut}}/\hbar^2$ (where m denotes the electron mass). By choosing ϵ_{cut} to be 50 and 81 Ry for ABINIT and QUANTUM ESPRESSO, respectively, equivalent results were obtained. On the other hand, other parameters such as the Brillouin zone sampling worked equally well in the two codes. For static lattice calculations, performed in the conventional cells, Brillouin-zone sampling grids [16]

were set to $12 \times 4 \times 4$ for Li_3BO_3 and $12 \times 12 \times 12$, $6 \times 6 \times 8$, $12 \times 12 \times 12$, and $6 \times 6 \times 8$ for Li_3BN_2 in the $P2_1/c$, $I4_1/amd$, $P4_2/mnm$, and $Pmnm$ structures, respectively. For interface calculations described in Sec. VI, larger supercells were constructed and the Brillouin zone sampling was adjusted accordingly.

The phonon calculations were performed in the primitive unit cells, following the approach described in previous work [17] using phonon wave-vector grids sufficient to represent the dynamical matrices at high symmetry \mathbf{q} points to obtain accurate phonon densities of states using interpolation methods. The \mathbf{q} -point grids were chosen to be $6 \times 2 \times 2$ for Li_3BO_3 , and $4 \times 4 \times 4$, $3 \times 3 \times 3$, $4 \times 4 \times 4$, and $3 \times 3 \times 4$ for the four considered structures of Li_3BN_2 .

In Sec. IV MATLAB [18] and Python [19] were used to aid the calculations, particularly for evaluating interpolation algorithms.

Visualizations of the structural configurations were obtained using the VESTA [20] and XCRYSDEN [21] programs. The software FINDSYM [22] helped in space-group analysis of the optimized structures. The MERCURY software package [23] was used to analyze x-ray patterns.

III. STRUCTURAL STABILITY IN THE HARMONIC APPROXIMATION

To evaluate the dynamical stability of the materials under consideration, we adopted the methodologies used in previous work [17] based on DFT [2,3] to represent the electronic ground state and the Born-Oppenheimer approximation [24] and the harmonic phonon approximation [7,25] to estimate the vibrational contribution to the Helmholtz free energy. The detailed equations are presented in Ref. [17], but some of the equations are given as follows. Self-consistent DFT performed on a unit cell of the material, optimizing the lattice parameters and internal coordinates, provides an excellent representation of the equilibrium static lattice internal energy U_{SL} of the system. Comparing the computed optimized lattice parameters and internal coordinates with experimentally measured values offers a quantitative estimate of the validity of the calculation and the measurement.

Since the materials of interest are electronically insulating, there are no temperature-dependent electronic contributions, so the equilibrium static lattice free energy is also temperature independent and well-approximated by U_{SL} . To estimate the contributions to the Helmholtz free energy due to temperature-dependent lattice vibrations, density-functional perturbation theory [8,9,26] is used to evaluate second-order derivatives of U_{SL} with respect to atomic displacements as is necessary to compute the dynamical matrix and the normal mode frequencies $\omega^{\nu}(\mathbf{q})$ as a function of wave vector \mathbf{q} . The dependence of $\omega^{\nu}(\mathbf{q})$ on wave vector \mathbf{q} will be presented in terms of phonon band diagrams. The phonon density of states $g(\omega)$ is given by

$$g(\omega) = \frac{V}{(2\pi)^3} \int d^3q \sum_{\nu=1}^{3N} \delta(\omega - \omega^{\nu}(\mathbf{q})), \quad (1)$$

where V denotes the volume of the simulation cell containing N atoms and the mode index ν runs from 1 to the total number of the normal modes $3N$. It is also possible to evaluate the

projected density of phonon modes function for a specified atomic type a using the expression

$$g^a(\omega) \equiv \frac{V}{(2\pi)^3} \int d^3q \sum_a^{3N} (\delta(\omega - \omega_a^{\nu}(\mathbf{q})) W_a^{\nu}(\mathbf{q})). \quad (2)$$

Here $W_a^{\nu}(\mathbf{q})$, defined in Eq. (11) of Ref. [17], represents the amplitude weight factor of mode ν for atomic type a . By construction, the sum of $g^a(\omega)$ over all atomic types gives the total phonon density of states $g(\omega)$.

From the total phonon density of states, the Helmholtz free energy $F(T)$ in the harmonic approximation for system with fixed volume V and temperature T can be computed according to

$$F(T) = U_{\text{SL}} + F_{\text{vib}}(T), \quad (3)$$

where $F_{\text{vib}}(T)$ is the vibrational contribution to the Helmholtz free energy, or the phonon free energy which takes the following form [25]:

$$F_{\text{vib}}(T) = k_B T \int_0^{\infty} d\omega \ln \left[2 \sinh \left(\frac{\hbar\omega}{2k_B T} \right) \right] g(\omega). \quad (4)$$

Here k_B is the Boltzmann constant.

Results for the static lattice optimizations, the phonon analyses, and the Helmholtz free-energy analysis for the Li_3BO_3 and Li_3BN_2 structures are given below, focusing first on the monoclinic phases of both materials, known to have measurable ionic conductivity, and then on some of the other phases of Li_3BN_2 that have been identified.

A. Structural analysis of Li_3BO_3

The literature on Li_3BO_3 reports a single crystal phase initially reported by Stewner in 1971 [27] characterized by the monoclinic structure $P2_1/c$ (space group No. 14) [28] with four formula units per conventional unit cell. In preparation for further experimental studies, Li_3BO_3 was prepared at Argonne National Labs by mixing a 3:1 stoichiometric ratio of LiOH monohydrate (Sigma Aldrich) with Boric acid (Sigma Aldrich), respectively. The material was loaded into an alumina crucible, calcined/annealed at 450 °C for 4 h, and finally ground with a mortar and pestle. The powdered samples was then pressed into a pellet (diameter: 0.5") at 15 MPa, loaded into an alumina crucible, and annealed/sintered at 600 °C for 8 hours. The x-ray diffraction pattern of the resulting powder agreed to high precision with the analysis of Stewner [27].

As shown in Fig. 1, the crystal structure of Li_3BO_3 is constructed from isolated BO_3 units formed into planes with triangular symmetry with the Li ions arranged in the voids of the framework. All contained sites have multiplicity and Wyckoff label 4e. In each unit cell, the Li ions occupy three distinct symmetry positions Li(1), Li(2), and Li(3) as indicated in the structural diagram of Fig. 1 by three different shades of blue. The atomic arrangement makes intuitive sense that the large voids within the structure could facilitate Li ion mobility. Table I summarizes the calculated lattice parameters and fractional coordinates compared with the experimental measurements [27]. The comparison presents a good agreement between computational and experimental results, finding

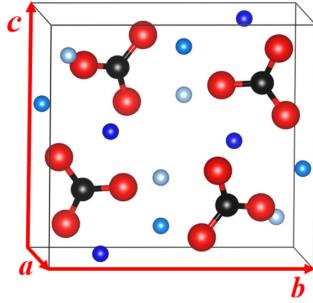


FIG. 1. Ball and stick visualization of Li_3BO_3 in the monoclinic $P2_1/c$ (No. 14) structure with Li, B, and O represented by blue, black, and red balls, respectively. Three shades of blue are used to indicate the three inequivalent Li sites in this structure.

differences in the lattice parameters of less than 0.05 \AA , for example.

To analyze the vibrational modes of Li_3BO_3 , it is efficient to use the primitive unit cell and to use the ABINIT code for evaluating the density-functional perturbation theory, the dynamical matrix, and finding the normal modes. For the primitive cell of Li_3BO_3 , there are 28 atoms per unit cell and 84 vibrational modes which can be decomposed into irreducible representations according to group theory analysis [28]: $21 A_g + 21 A_u + 21 B_g + 21 B_u$, comprising three zero-frequency acoustic modes $A_u + 2 B_u$, infrared active optic modes $20 A_u + 19 B_u$, and Raman active optic modes $21 A_g + 21 B_g$. The phonon band structure along with the corresponding projected density of states for Li_3BO_3 are presented in Fig. 2. The low-frequency region less than 650 cm^{-1} involves significant motions of the Li ions while the high phonon modes above 650 cm^{-1} are attributed to primarily BO_3 motions with the maximum frequency up to 1379 cm^{-1} . The observed flat modes at around 910 cm^{-1} are characteristic of the internal stretching motion of BO_3 units with almost stationary B ions. All real frequencies throughout the vibra-

TABLE I. Lattice parameters of Li_3BO_3 in the $P2_1/c$ (No. 14) structure. The column labeled Wyck lists the conventional cell multiplicity and Wyckoff labels, comparing the present paper (cal) with the experimental analysis of Stewner [27] (exp).

	a (Å)	b (Å)	c (Å)	α (deg)	β (deg)	γ (deg)
Li_3BO_3 (cal)	3.24	9.16	8.28	90.00	100.98	90.00
Li_3BO_3 (exp)	3.27	9.18	8.32	90.00	101.05	90.00
Fractional coordinates (x, y, z)						
Atom	Wyck	Li_3BO_3 (cal)		Li_3BO_3 (exp)		
Li(1)	4 e	(0.493, 0.233, 0.018)		(0.493, 0.233, 0.018)		
Li(2)	4 e	(0.276, 0.477, 0.113)		(0.271, 0.477, 0.113)		
Li(3)	4 e	(-0.091, 0.423, 0.368)		(-0.093, 0.429, 0.367)		
B	4 e	(0.198, 0.186, 0.255)		(0.198, 0.186, 0.254)		
O(1)	4 e	(0.028, 0.137, 0.099)		(0.026, 0.139, 0.100)		
O(2)	4 e	(0.227, 0.093, 0.389)		(0.225, 0.094, 0.386)		
O(3)	4 e	(0.366, 0.327, 0.279)		(0.361, 0.325, 0.278)		

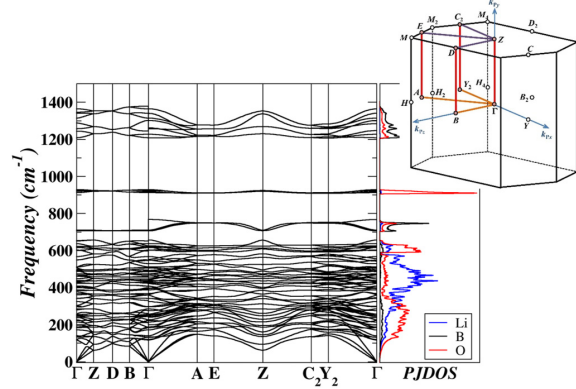


FIG. 2. Phonon dispersion curves and the corresponding projected density states for Li_3BO_3 in the $P2_1/c$ (No. 14) structure. The Brillouin zone diagram for this structure was reproduced from Hinuma *et al.* in Ref. [29] with permission from the publisher.

ational range suggest that crystalline Li_3BO_3 is dynamically stable.

B. Structural analysis of Li_3BN_2

The literature reports at least three crystalline phases for Li_3BN_2 . Yamane *et al.* [30] carefully analyzed the low temperature α and higher temperature β forms, finding the transition temperature to be approximately 1135 K and the melting temperature of the β form to be approximately 1189 K. The high temperature β form could be quenched to room temperature. The α form was initially characterized with the space group $P4_22_12$ (space group No. 94) [28], which was later found to be equivalent to the higher symmetry $P4_2/mnm$ structure [31] (space group No. 136) [28]. The β form was characterized with the monoclinic $P2_1/c$ (space group No. 14) [28]. A distinct tetragonal (γ) phase of Li_3BN_2 was found by Pinkerton and Herbst [32] with the symmetry $I4_1/amd$ (space group No. 141) [28], obtained by removing hydrogen from fine powders containing LiNH_2 and LiBH_4 . Since the γ phase is synthesized at relative low temperature $T \approx 2500 \text{ }^\circ\text{C}$, it is not clear how it fits into the overall phase diagram of Li_3BN_2 . Each of

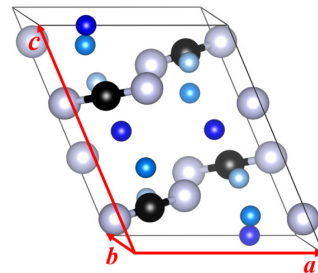


FIG. 3. Ball and stick visualization of a conventional unit cell of $\beta\text{-Li}_3\text{BN}_2$ having $P2_1/c$ (space group No. 14). Li, B, and N ions are represented by three shades of blue, black, and gray balls, respectively.

TABLE II. Summary of lattice parameters for Li_3BN_2 in the $P2_1/c$ (β form, No. 14), comparing computational (cal) results with experimental measurements (exp).

	a (Å)	b (Å)	c (Å)	α (deg)	β (deg)	γ (deg)
$P2_1/c$ (cal)	5.11	7.00	6.71	90.00	113.08	90.00
$P2_1/c$ (exp [30])	5.15	7.08	6.79	90.00	112.96	90.00
Fractional coordinates (x, y, z)						
Atom	Wyck	$P2_1/c$ (cal)		$P2_1/c$ (exp [30])		
Li(1)	4 e	(0.249, 0.481, 0.498)		(0.250, 0.485, 0.498)		
Li(2)	4 e	(0.250, 0.012, 0.375)		(0.252, 0.012, 0.375)		
Li(3)	4 e	(0.741, 0.208, 0.314)		(0.744, 0.207, 0.314)		
B	4 e	(0.215, 0.320, 0.176)		(0.215, 0.320, 0.176)		
N(1)	4 e	(0.437, 0.439, 0.219)		(0.434, 0.437, 0.219)		
N(2)	4 e	(0.991, 0.203, 0.135)		(0.994, 0.205, 0.135)		
Ang(N(1)-B-N(2)) (deg)		180.00		180.00		
d(N-B) (Å)		1.342		1.339		

the three characterized phases of Li_3BN_2 is composed of Li ions arranged among linear or nearly linear $(\text{BN}_2)^{3-}$ units.

1. Structural analysis of β - Li_3BN_2

While β - Li_3BN_2 has the same space group as Li_3BO_3 , its structure looks quite distinct. Figure 3 shows the ball and stick drawing of the ideal β - Li_3BN_2 crystal, which has four formula units in the conventional monoclinic unit cell.

Here we see that the structure is characterized by linear N–B–N units aligned approximately in **ab** planes and spaced along the **c** axis. The Li ions are located in the empty cavities between $(\text{BN}_2)^{3-}$ units, with three inequivalent types [Li(1), Li(2), and Li(3)] all having the multiplicity and Wyckoff label 4*e*. From the viewpoint shown in Fig. 3, it is seen that type Li(3) ions are approximately in the same planes as the $(\text{BN}_2)^{3-}$ units, while the Li(1) and Li(2) ions are arranged in different planes along the **c** axis.

The results of the optimized static lattice calculation are reported in Table II. Here we see the comparison with experiments is reasonable with a discrepancy of approximately 0.08 Å or less in the lattice lengths and less than 0.004 in fractional coordinates.

The phonon dispersion curves of β - Li_3BN_2 are presented in Fig. 4. It is interesting to note that the frequencies of several top modes, due to the vibration motions of B–O units, higher by about 400 cm^{-1} than those of Li_3BN_2 in Fig. 2. The diagram also shows nearly flat dispersion curves at around 1100 cm^{-1} , reflecting the typical feature of the internal B–O stretch. Furthermore, all frequencies are found to be positive, indicating that Li_3BN_2 in the β phase is dynamically stable. From these results, we can then estimate the vibrational Helmholtz free energy which will be discussed below.

2. Structural analysis of γ - Li_3BN_2

Figure 5 shows the ball and stick drawing of the ideal γ - Li_3BN_2 crystal which has eight formula units in the conventional tetragonal $I4_1/amd$ unit cell. Here we see that the structure consists of linear N–B–N units aligned along the **a** or **b** axes with Li ions arranged between occupying 16*g* and 4*e* sites in the Wyckoff multiplicity and site label convention.

In this structure, it is found that the B–N–B angle is slightly bent in the $I4_1/amd$ structure.

The results of the optimized static lattice calculation are reported in Table III. Here we find a relatively large discrepancy of approximately 0.15 Å in the calculated and measured length of the *c* lattice parameter while the $a = b$ lattice parameters differ only by 0.04 Å.

The phonon bands calculated from the optimized primitive unit cell of γ - Li_3BN_2 are presented in Fig. 6, with a remarkably similar dispersion profile as seen in Fig. 4 for the β form. Again in this case, we see that all frequencies are found to be positive, indicating that the system is dynamically stable. From these results, we can then estimate the vibrational Helmholtz free energy which will be discussed below.

3. Structural analysis of α - Li_3BN_2 based on literature analysis

Figure 7 shows the ball and stick drawings of α - Li_3BN_2 in the reported $P4_2/mnm$ (No. 136) [31] structure, which has two formula units in the conventional tetragonal unit cell. As illustrated in the figure, the structure is characterized by linear N–B–N units aligned in the **ab** planes with alternating

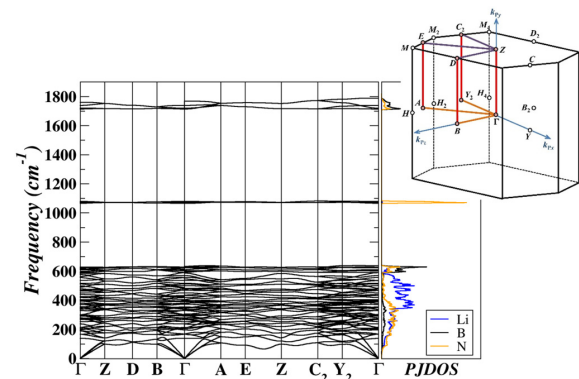


FIG. 4. Phonon dispersion curves and the corresponding projected density states for Li_3BN_2 in the $P2_1/c$ (β form) structure. The Brillouin zone diagram for this structure was reproduced from Hinuma *et al.* in Ref. [29] with permission from the publisher.

TABLE III. Summary of lattice parameters for Li_3BN_2 in the $I4_1/amd$ (γ form, No. 141), comparing computational results with experimental measurements.

	a (Å)	b (Å)	c (Å)	α (deg)	β (deg)	γ (deg)
$I4_1/amd$ (cal)	6.56	6.56	10.20	90.00	90.00	90.00
$I4_1/amd$ (exp [32])	6.60	6.60	10.35	90.00	90.00	90.00
Fractional coordinates (x, y, z)						
Atom	Wyck	$I4_1/amd$ (cal)		$I4_1/amd$ (exp [32])		
Li(1)	$8e$	(0.000, 0.000, 0.126)		(0.000, 0.000, 0.120)		
Li(2)	$16g$	(0.275, 0.275, 0.000)		(0.271, 0.271, 0.000)		
B	$8e$	(0.000, 0.000, 0.354)		(0.000, 0.000, 0.353)		
N	$16h$	(0.000, 0.205, 0.349)		(0.000, 0.209, 0.345)		
Ang(N-B-N) (deg)		175.61		172.86		
d(N-B) (Å)		1.347		1.382		

directions along the c axis and by two crystallographically distinct Li sites as indicated with two shades of blue balls. The Li ion at Wyckoff site d and its four symmetry equivalents are located between the layers of $(\text{BN}_2)^{3-}$ units while the Li ion at the b site and its two equivalents are located within the $(\text{BN}_2)^{3-}$ layers. The B atoms are in a bcc arrangement, each is linearly bonded to two N's with straight bond angles. In addition, the orientation of N–B–N bonds in the corners are parallel to each other and are orthogonal to those in the center of the lattice.

The results of the optimized static lattice calculation are reported in Table IV. Here we see the comparison with experiments finds an underestimate of the $a = b$ lattice parameter of 0.01 Å and of the c lattice parameter of 0.11 Å.

The phonon dispersion curves are presented in Fig. 8. Here we see that the phonon mode of the $P4_2/mnm$ structure has imaginary frequencies around M point along $M \rightarrow X$, $M \rightarrow \Gamma$, and $M \rightarrow A$ involving doubly degenerate modes, implying instability of that structure. To check this result, we recalculated the analysis substituting the local density approximation (LDA) [33] for the PBEsol [6] exchange-correlation form. In our experience, the LDA exchange-correlation functional generally models lattice vibrations in closer agreement with the experiment. However, in this case, the same imaginary

modes were found, implying the structure is dynamically unstable and that further analysis is needed to identify the correct structural form of α - Li_3BN_2 .

4. Proposed corrected structure of α - Li_3BN_2 based on dynamic stability in the harmonic phonon approximation

The analysis of imaginary frequency solutions of the dynamical equations involved with phonon modes has been extensively discussed in the literature [10,34–37]. In the simplest case, the eigenvectors of the imaginary modes indicate lattice distortions associated with lower symmetry phase transitions.

In the present case of the reported $P4_2/mnm$ structure of α - Li_3BN_2 , the results of Fig. 8 suggest that eigenvectors of the two degenerate imaginary modes at the M (0.5, 0.5, 0.0) point in the Brillouin zone should be examined. As illustrated in Fig. 9, which indicates with colored arrows the dominating amplitudes of these two modes, the instability is mainly attributed to the vibrations of b -type Li(2) ions along the c axis, perpendicular to the direction of the wave vector \mathbf{q} at the M point.

Since these modes are associated with the M (0.5, 0.5, 0.0) point of the Brillouin zone of the $P4_2/mnm$ structure, this suggests that the corresponding lattice distortion can best

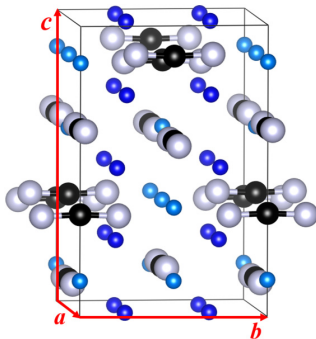


FIG. 5. Ball and stick visualization of a conventional unit cell of γ - Li_3BN_2 having the $I4_1/amd$ space group No. 141). Li, B, and N ions are represented by two shades of blue, black, and gray balls, respectively.

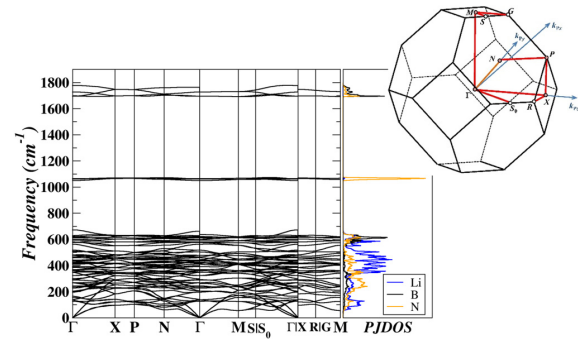


FIG. 6. Phonon dispersion curves and the corresponding projected density states for γ - Li_3BN_2 in the $I4_1/amd$ structure. The Brillouin zone diagram for this structure was reproduced from Hinuma *et al.* in Ref. [29] with permission from the publisher.

TABLE IV. Summary of lattice parameters for Li_3BN_2 in the $P4_2/mnm$ (α form, No. 136), comparing computational results (cal) with experimental measurements (exp).

	a (Å)	b (Å)	c (Å)	α (deg)	β (deg)	γ (deg)
$P4_2/mnm$ (cal)	4.63	4.63	5.15	90.00	90.00	90.00
$P4_2/mnm$ (exp [31])	4.64	4.64	5.26	90.00	90.00	90.00
Fractional coordinates (x, y, z)						
Atom	Wyck	$P4_2/mnm$ (cal)		$P4_2/mnm$ (exp [31])		
Li(1)	4d	(0.000, 0.500, 0.250)		(0.000, 0.500, 0.250)		
Li(2)	2b	(0.000, 0.000, 0.500)		(0.000, 0.000, 0.500)		
B	2a	(0.000, 0.000, 0.000)		(0.000, 0.000, 0.000)		
N	4f	(0.206, 0.206, 0.000)		(0.204, 0.204, 0.000)		
Ang(N-B-N) (deg)		180.00		180.00		
d(N-B) (Å)		1.346		1.339		

be described in a supercell structure having lattice vectors ($\mathbf{a}_s, \mathbf{b}_s, \mathbf{c}_s$) along the M directions and related to the conventional $P4_2/mnm$ cell constants (a_c, b_c, c_c) according to

$$\mathbf{a}_s = a_c \hat{x} + b_c \hat{y}, \quad \mathbf{b}_s = a_c \hat{x} - b_c \hat{y}, \quad \mathbf{c}_s = c_c \hat{z}. \quad (5)$$

Starting with the ($\mathbf{a}_s, \mathbf{b}_s, \mathbf{c}_s$) supercell of this structure, we calculated the static lattice parameters using several initial displacements of the b -type Li ions along the \hat{z} direction and the dominating displacements of the eigenvectors of the imaginary modes shown in Fig. 9. The optimized structure is characterized with the space group symmetry of orthorhombic $Pmnm$ (space group No. 59), a lower energy structure compared to the $P4_2/mnm$ structure based on which this structure for α - Li_3BN_2 was derived. Fig. 10 compares the perfect supercell of the $P4_2/mnm$ structure with the optimized $Pmnm$ structure while Table V lists the detailed comparison of the structural parameters. It is apparent that the visualization of the $Pmnm$ structure is similar to that of the $P4_2/mnm$ structure, except for some small differences in the arrangements of Li ions. The Li sites with Wyckoff labels $4d$ in the supercell of the $P4_2/mnm$ structure have a one-to-one correspondence with those at $8g$ sites in the $Pmnm$ structure with very slight deviations. At the same time, the Li sites with Wyckoff labels $2b$ for the $P4_2/mnm$ structure map to the sites with Wyckoff labels $2a$ and $2b$ in the $Pmnm$ structure, respectively, with small distortion mainly in the c direction. Additionally, the

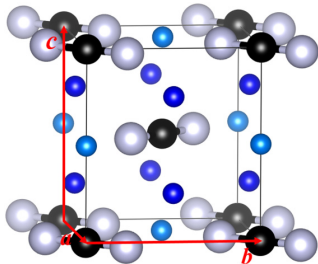


FIG. 7. Ball and stick visualization of a conventional unit cell of α - Li_3BN_2 having the $P4_2/mnm$ (space group No. 136). Li, B, and N ions are represented by two shades of blue, black, and grey balls, respectively.

N–B–N bonds of the modified structure experience slight deformation, although the bond lengths remain unchanged, the bond angles are not straight anymore, especially for those in close proximity to the Li ions at the $2a$ sites. From Table V, we see that the distortions relative to the literature structure are very small, so it is understandable that the higher symmetry structure has been reported in previous literature.

To examine the stability of this low-symmetry orthorhombic phase, phonon analysis in the harmonic phonon approximation was performed. Phonon dispersion curves along the main symmetry directions and the projected phonon density of states for $Pmnm$ structure are displayed in Fig. 11. In Table VI, we give the one-to-one mapping relation between the high-symmetry \mathbf{q} points in the tetragonal $P4_2/mnm$ structure and those in the orthorhombic $Pmnm$ structure. It is notable that the M point which associates with the unstable phonon modes of the $P4_2/mnm$ structure is mapped onto the Γ point, the center of the Brillouin zone, in the $Pmnm$ structure. Unlike the acoustic phonon instabilities exhibited at the M point of the $P4_2/mnm$ structure, from Fig. 11 we see that the $Pmnm$ structure is dynamically stable along various high-symmetry lines throughout the Brillouin zone.

According to group theory (Ref. [28]), the zone-center phonon modes of the α phase in the $Pmnm$ structure are classified into acoustic modes $B_{1u} + B_{2u} + B_{3u}$ and optic modes including infrared active modes $10B_{1u} + 9B_{3u} + 9B_{3u}$ and Raman active modes $11A_g + 5B_{1g} + 10B_{2g} + 10B_{3g}$. The irreducible representation of zone-center phonon modes of the β phase is decomposed of acoustic modes $A_u + 2B_u$, infrared active optic modes $17A_u + 16B_u$, and Raman active optic modes $18A_g + 18B_g$. For the case of γ - Li_3BN_2 , the symmetry-adapted phonon modes for Γ point decompose as acoustic modes $A_{2u} + E_u$, infrared active optic modes $5A_{2u} + 9E_u$, and Raman active optic modes $5A_{1g} + 6B_{1g} + 2B_{2g} + 10E_g$. Given this demonstration of the dynamical stability, we propose that the correct structure of α - Li_3BN_2 must be characterized by the $Pmnm$ structure.

C. Comparison of the Helmholtz free energies in the harmonic approximation

From the harmonic phonon results for the stable structures presented in Sec. III, the vibrational contributions to the

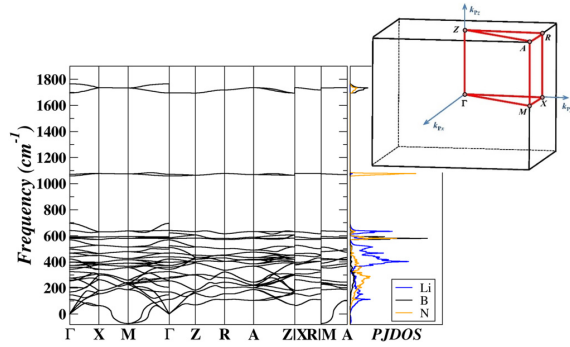


FIG. 8. Phonon dispersion curves and the corresponding projected density states for Li_3BN_2 in the $P4_2/mmm$ (α form) structure. The Brillouin zone diagram for this structure was reproduced from Hinuma *et al.* in Ref. [29] with permission from the publisher.

Helmholtz free energy as a function of temperature can be calculated as shown in Fig. 12. This figure shows that, while (understandably) $F_{\text{vib}}(T)$ for Li_3BO_3 is different from $F_{\text{vib}}(T)$ for Li_3BN_2 , the curves for all three stable phases of Li_3BN_2 are nearly identical. According to our simulation results, it is interesting to see that the three known structures of Li_3BN_2 , despite their different symmetries and arrangements of component ions, have very similar static lattice U_{SL} energies with a difference in the order of 10^{-3} eV per formula unit, which is close to the expected numerical accuracy of the calculations. Similarly, the phonon densities of states shown in Figs. 4, 6, and 11, while not identical, are also very similar, covering the same range of normal mode frequencies up to about 1800 cm^{-1} . As we can see from these figures, the vibrational amplitudes of the Li ions contribute to mode frequencies less than 600 cm^{-1} , while the vibrations of $(\text{BN}_2)^{3-}$ ions spread over the whole frequency range. In particular, the pure internal stretching vibrations of $(\text{BN}_2)^{3-}$ units results in flat dispersion curves with frequencies of about 1100 cm^{-1} in each case. This N-stretching mode is likely to be related to the Raman active spectral feature reported by Somer for α - Li_3BN_2 at

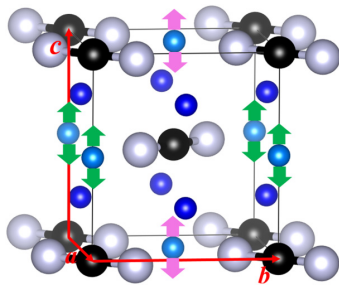


FIG. 9. Ball and stick diagram of the $P4_2/mmm$ structure of Li_3BN_2 , similar to Fig. 7. The up and down arrows indicate the dominating amplitudes of the motions associated with the two eigenvectors of the imaginary phonon modes at the M point of the Brillouin zone involving the Li(2) atoms at b sites. The green and purple arrow colors are used to indicate separate site amplitudes for the group of atoms.

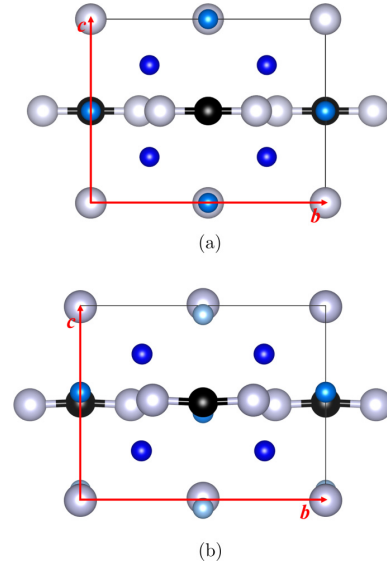


FIG. 10. Ball and stick diagrams projected onto the bc plane for (a) the supercell of the tetragonal $P4_2/mmm$ structure as defined by Eq. (5) and (b) the optimized orthorhombic $Pmmn$ structure. The ball conventions are the same as for Fig. 7 except that the three crystallographically distinct Li sites of the $Pmmn$ structure are indicated with three shades of blue balls.

1057 cm^{-1} [38]. As a result of these similar phonon distributions, the vibrational contribution to the Helmholtz free energy [Eq. (4)] is nearly identical for the three phases. These results are shown in Fig. 12, which plots $F_{\text{vib}}(T)$ for Li_3BO_3 and the α , β , and γ phases of Li_3BN_2 . While the phonon free-energy profile for Li_3BO_3 is distinct from that of Li_3BN_2 , the three phases of Li_3BN_2 are remarkably similar. This leads to the conclusion that to explain the experimental observation that the α phase is the low temperature phase, a higher level of theory should be considered.

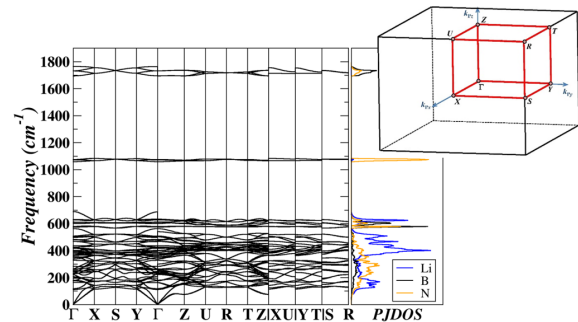


FIG. 11. Phonon dispersion curves along high symmetry directions of the Brillouin zone and the corresponding projected density states for Li_3BN_2 in the $Pmmn$ structure. The Brillouin zone diagram for this structure was reproduced from Hinuma *et al.* in Ref. [29] with permission from the publisher.

TABLE V. Summary of lattice parameters for the $Pm\bar{m}n$ structure compared to the results on the $P4_2/m\bar{m}m$ structure in the supercell setting defined in Eq. (5).

	a (Å)	b (Å)	c (Å)	α (deg)	β (deg)	γ (deg)
$Pm\bar{m}n$ (cal)	6.539	6.543	5.179	90.00	90.00	90.00
Super $P4_2/m\bar{m}m$ (cal)	6.559	6.559	5.146	90.00	90.00	90.00

$Pm\bar{m}n$			Super $P4_2/m\bar{m}m$		
Atom	Wyck	(x, y, z)	Atom	Wyck	(x, y, z)
Li(1)	8g	(0.239, 0.751, 0.250)	Li(1)	4d	(0.250, 0.750, 0.250)
Li(2)	2a	(0.000, 0.000, 0.553)	Li(2)	2b	(0.000, 0.000, 0.500)
Li(3)	2b	(0.500, 0.000, 0.046)	Li(2)	2b	(0.500, 0.000, 0.000)
B(1)	2a	(0.000, 0.000, 0.004)	B(1)	2a	(0.000, 0.000, 0.000)
B(2)	2b	(0.500, 0.000, 0.499)	B(1)	2a	(0.500, 0.000, 5.000)
N(1)	4f	(0.206, 0.000, -0.006)	N(1)	4f	(0.205, 0.000, 0.000)
N(2)	4e	(0.500, 0.795, 0.488)	N(1)	4f	(0.500, 0.795, 0.500)

IV. CORRECTED STRUCTURAL ANALYSIS FOR α - Li_3BN_2 USING QUASIHARMONIC PHONON ANALYSIS

Having seen some shortcomings of the harmonic phonon analysis discussed in Sec. III, we explored the possibility of a more accurate treatment using the quasiharmonic approximation [10,39,40]. In the harmonic approximation, it is assumed that the optimized static lattice internal energy U_{SL} well approximates the optimal lattice parameters of the system and the vibrational Helmholtz free energy $F_{\text{vib}}(T)$ based on second derivatives of U_{SL} with respect to atomic coordinates, evaluated at those lattice parameters, well approximates the phonon contributions to the free energy. However, this approach does not account for temperature-dependent changes in the lattice parameters which may be important for these systems. While this more accurate treatment might be of interest for all the materials of this paper, we focus our attention on α - Li_3BN_2 in the proposed $Pm\bar{m}n$ structure. For this orthorhombic structure, the lattice angles are all 90° so the temperature dependence is considered for the three lattice lengths a , b , and c . The quasiharmonic generalization of Eq. (3) is given by [40]

$$F^{\text{QH}}(T, a, b, c) = U_{\text{SL}}(a, b, c) + F_{\text{vib}}(T, a, b, c), \quad (6)$$

where the a, b, c arguments here are evaluated on a three-dimensional grid of values. For each a, b, c grid point, the static lattice internal energy $U_{\text{SL}}(a, b, c)$ is calculated by self-consistent density-functional optimization of the internal atomic coordinates and its second derivatives with respect to atomic coordinates are evaluated to evaluate the lattice parameter-dependent phonon density of states $g(\omega, a, b, c)$

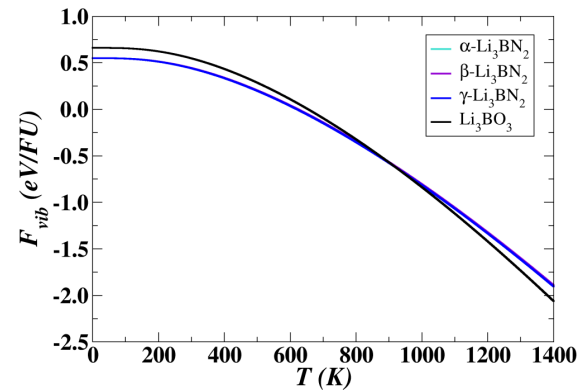
TABLE VI. The mapping of the high-symmetry \mathbf{q} points in the $P4_2/m\bar{m}m$ structure onto the corresponding points in the $Pm\bar{m}n$ structure.

	$P4_2/m\bar{m}m$	$Pm\bar{m}n$
A \rightarrow Z	(0.50, 0.50, 0.50)	(0.00, 0.00, 0.50)
$\Gamma \rightarrow \Gamma$	(0.00, 0.00, 0.00)	(0.00, 0.00, 0.00)
M $\rightarrow \Gamma$	(0.50, 0.50, 0.00)	(0.00, 0.00, 0.00)
R \rightarrow R	(0.00, 0.50, 0.50)	(0.50, 0.50, 0.50)
X \rightarrow S	(0.00, 0.50, 0.00)	(0.50, 0.50, 0.00)
Z \rightarrow Z	(0.00, 0.00, 0.50)	(0.00, 0.00, 0.50)

according to Eq. (1). Note that for this process to work, it is necessary for the phonon frequencies to be real, for each set of lattice parameters a, b, c as was found to be the case for this $Pm\bar{m}n$ system. We also assume that for the electronically insulating systems considered here, the static lattice energy $U_{\text{SL}}(a, b, c)$ is temperature independent. From the phonon densities of states, the vibrational contributions to the Helmholtz free energy $F_{\text{vib}}(T, a, b, c)$ can also be determined at each temperature T according to Eq. (4).

In practice, the calculations start with the construction of a three-dimensional $3 \times 3 \times 4$ regular grid of the lattice constants defined in a range of values near the equilibrium values calculated in the harmonic phonon approximation. These are $a_{\text{H}} = 6.5393$ Å, $b_{\text{H}} = 6.5433$ Å, and $c_{\text{H}} = 5.1794$ Å. Consequently, the three-dimensional grid range was chosen to be $6.4599 \leq a \leq 6.6187$, $6.4639 \leq b \leq 6.6227$ and $5.1000 \leq c \leq 5.3381$ in Å units.

For each temperature T , Eq. (6) is directly evaluated at the $3 \times 3 \times 4$ grid points and by using cubic spline interpolation [41], it is now possible to estimate the lattice parameter-dependent Helmholtz free energy $F^{\text{QH}}(T, a, b, c)$ as a continuous function of lattice parameters within the original range of evaluated grid points. The physical Helmholtz

FIG. 12. Plots of $F_{\text{vib}}(T)$ [Eq. (4)] for Li_3BO_3 and Li_3BN_2 in the α (as corrected in the $Pm\bar{m}n$ structure), β , and γ phases. The curves for the three phases of Li_3BN_2 are superposed in the figure.

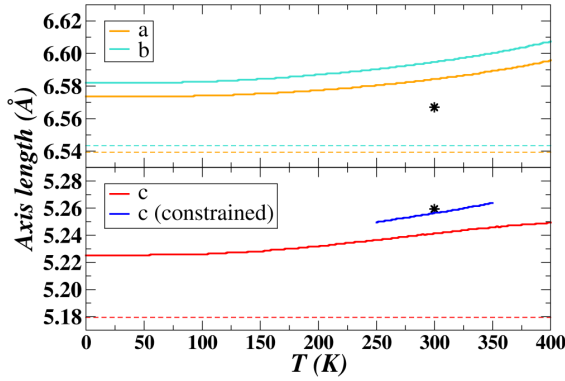


FIG. 13. Lattice parameters a , b , and c in units of \AA for $\alpha\text{-Li}_3\text{BN}_2$ in the $Pm\bar{m}n$ structure. Full lines represent the temperature-dependent results of the quasiharmonic approximation. The constrained quasiharmonic results are indicated with the full blue line for a range of temperatures near 300 K. Dashed lines represent the temperature-independent results of the harmonic approximation. Experimental results presumed to be measured at room temperature as reported in Ref. [30] and transformed to the $Pm\bar{m}n$ structure are indicated with *.

free energy [$F_{\min}^{\text{QH}}(T)$] at temperature T is expected to be the minimum value according to

$$F_{\min}^{\text{QH}}(T) = \min_{(a,b,c)} F^{\text{QH}}(T, a, b, c). \quad (7)$$

The lattice parameters that optimize the right-hand side of Eq. (7) determine the temperature-dependent lattice constants $a(T)$, $b(T)$, and $c(T)$. These are shown in Fig. 13 in comparison with the harmonic phonon values indicated with dashed lines. The quasiharmonic analysis indicates that all three lattice constants generally increase as the temperature increases. The accumulated results are summarized in Table VII. Also included in this table are results which we call constrained quasiharmonic results in which, for temperatures near $T = 300$ K, the a and b lattice parameters are fixed at the experimental values and $F^{\text{QH}}(T, a, b, c)$ is optimized with respect over c .

Examining the quasiharmonic results a little more closely, we noticed that $F^{\text{QH}}(T, a, b, c)$ has an extremely shallow minimum as a function of the lattice parameters, particularly at $T = 300$ K. Figure 14 illustrates contour diagrams of $F^{\text{QH}}(T, a, b, c_{\min})$ and $F^{\text{QH}}(T, a, b_{\min}, c)$ evaluated at $T = 300$ K. Interestingly, these plots show that the depth of the shallow minimum of Helmholtz free energy, which includes

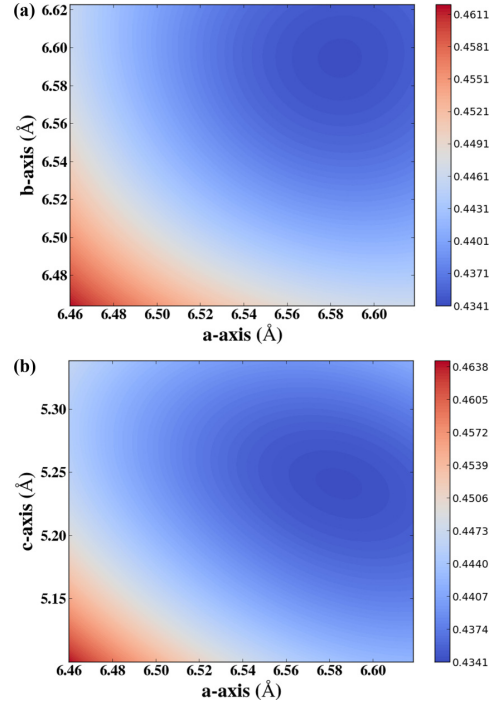


FIG. 14. Contour plots of (a) $F^{\text{QH}}(T = 300 \text{ K}, a, b, c_{\min})$ and (b) $F^{\text{QH}}(T = 300 \text{ K}, a, b_{\min}, c)$ of $\alpha\text{-Li}_3\text{BN}_2$ in the $Pm\bar{m}n$ structure. Values of the Helmholtz free energy in units of eV/FU are represented in terms of the color chart shown beside each contour.

the range of the experimental lattice constants, is well within the range of expected errors of the calculation due to physical and numerical approximation of ± 0.001 eV/FU. The numerical values $\Delta F^{\text{QH}}(T = 300 \text{ K}, a, b, c)$ referenced to $F_{\min}^{\text{QH}}(T = 300 \text{ K})$ are listed in the last column of Table VII.

X-ray diffraction patterns from the numerical simulations are shown in Fig. 15, together with the experimental data for the $P4_2/m\bar{m}n$ structure [31] in the bottom panel. In practice, the experimental curve was generated from the published structural parameters using the same MERCURY software [23] as used to visualize the calculated results. The calculated pattern of the $P4_2/m\bar{m}n$ structure in the top panel was visually nearly identical to those of the $Pm\bar{m}n$ structure, but slightly incongruent with the experimental observations in the positions of the main peaks. The plots for the $Pm\bar{m}n$ structure using the data obtained from the global and constrained minima of quasiharmonic approximation at $T = 300$ K, however,

TABLE VII. Summary of calculated and experimental lattice parameters (in \AA) for $\alpha\text{-Li}_3\text{BN}_3$ in the $Pm\bar{m}n$ structure at room temperature (300 K). Last column lists the corresponding value of $F^{\text{QH}}(a, b, c)$ referenced to the optimized value in eV/FU.

	a	b	c	$\Delta F^{\text{QH}}(a, b, c)$
Exp. (Ref. [30])	6.5669	6.5669	5.2593	0.0007
Harmonic phonon approximation	6.5393	6.5433	5.1794	0.0008
QH approximation (unconstrained)	6.5844	6.5947	5.2416	0.0000
QH approximation (constrained)	6.5669	6.5669	5.2566	0.0007

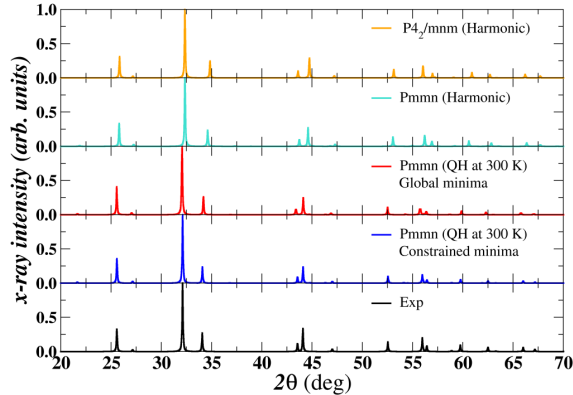


FIG. 15. X-ray diffraction patterns of Li_3BN_2 in the $P4_2/mmm$ and the $Pmnn$ structures approximated in the harmonic phonon approximation (top two panels), in the $Pmnn$ structure approximated in the quasiharmonic approximation at $T = 300$ K (red and blue curves), and experiment of Ref. [30]. The MERCURY software [23] at an x-ray wavelength of $\lambda = 1.54056 \text{ \AA}$ was used to generate all the x-ray patterns.

agree very well with the experimental pattern. The results, once again, demonstrate the rationality of the $Pmnn$ structure as a representation for the distorted structure of the $P4_2/mmm$ structure. Furthermore, it shows that the quasiharmonic correction improves the agreement between theory and experiment.

Figure 16 summarizes the Helmholtz free energy as a function of temperature for Li_3BN_2 in the α , β , and γ structures within the harmonic phonon approximation (top plots) together with quasiharmonic approximation results for α - Li_3BN_2 . Even in this smaller range, it is apparent that within the harmonic phonon approximation, the Helmholtz free energy of the $Pmnn$ structure is indistinguishable from those of the $P2_1/c$ and $I4_1/amd$ structures throughout the explored temperature range. However, the quasiharmonic plot for the $Pmnn$ structure is below the other three, suggesting a

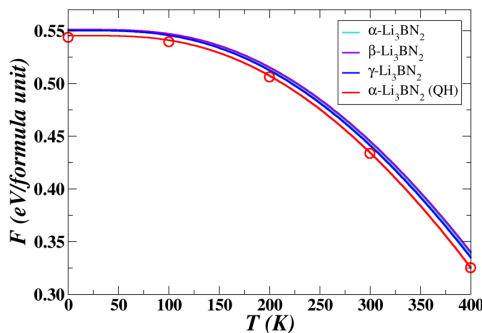


FIG. 16. Plot of Helmholtz free energy in eV/formula unit as a function of T in Kelvin for Li_3BN_2 . The results for the $Pmnn$ α (turquoise), β (purple), and the γ (blue) phases are obtained from harmonic approximations, and the quasiharmonic analysis of $F_{\min}(T)$ for the $Pmnn$ α phase are displayed in red curve and circles.

relatively stable structure with lower Helmholtz free energy. It is worth mentioning that the red curve representing $F_{\min}^{\text{QH}}(T)$ is defined by Eq. (7). However, the results shown as red circles for various temperature T are obtained by directly calculating $U_{\text{SL}}(a(T), b(T), c(T)) + F_{\text{vib}}(T, a(T), b(T), c(T))$ using the lattice parameters $(a(T), b(T), c(T))$ that gives $F_{\min}^{\text{QH}}(T)$ obtained from the interpolation analysis. The good agreement between the data represented by the curve and the points verifies the accuracy of the interpolation used in these quasiharmonic calculations. Interestingly, because the quasiharmonic optimizes the sum of static lattice energy $U_{\text{SL}}(a, b, c)$ and the vibrational free energy $F_{\text{vib}}^{\text{QH}}(T, a, b, c)$, while the harmonic approximation only optimizes $U_{\text{SL}}(a, b, c)$ and calculates $F_{\text{vib}}(T)$ at those optimized lattice parameters, the estimated free energies may differ at all temperatures, as seen in Fig. 16. To properly model the phase stability of Li_3BN_2 , it would be necessary to perform a more extensive quasiharmonic treatment of the α phase (considering a wider range of lattice parameters) and also consider similar treatments of the β and γ phases. While such compute intensive simulations are certainly manageable, they were considered beyond the scope of the present paper.

V. ANALYSIS OF POSSIBLE CHEMICAL DECOMPOSITION REACTION FOR MONOCLINIC FORMS OF Li_3BO_3 and β - Li_3BN_2

Since the monoclinic forms of Li_3BO_3 and Li_3BN_2 are of great practical interest as electrolyte or coating materials, we focus attention on those phases. To evaluate the chemical stabilities of Li_3BO_3 and β - Li_3BN_2 , we estimated the decomposition energy relative to a range of likely products. The stability of a target material or its possible interaction with a second material is estimated from the difference in Helmholtz free energies ΔF of predicted reactions between the reactants \mathbf{R} and the products \mathbf{P} . Specifically, the reaction energy is given by

$$\Delta F = \sum_i F_i^{\text{P}} - \sum_j F_j^{\text{R}}. \quad (8)$$

The energy of each material in the reaction is a sum of the static energies of the optimized structures and the phonon contributions according to the harmonic phonon approximation [Eq. (3)]. We used this approach to study both decomposition of the materials themselves, and also their reactivity with Li meta.

The results for decomposition are summarized in Table VIII. For each predicted decomposition reaction, the energy difference ΔF , calculated according to Eq. (8), includes contributions from both the static lattice energy and the phonon free energy of each material. Since the temperature-dependent electronic excitation of metallic Li is trivial, the contribution was not counted. It is worth mentioning for both materials, the energy from vibrational contribution is quite small compared to the static lattice part, indicating that the static lattice energy plays a dominant role in determining the stabilities. The positive ΔF of these proposed pathways suggests endothermic reactions, meaning the left-side reactants need to absorb energy to achieve the decomposition. While this is not an exhaustive study, it does provide some

TABLE VIII. Computed energy differences for reactions indicated by the first column. All energies are given in eV units and the phonon vibrational energy F_{vib} is evaluated at $T = 300$ K.

Crystal	Reaction: $R \rightarrow P$	ΔU_{SL}	ΔF_{vib}	ΔF
Li_3BO_3	$\text{Li}_3\text{BO}_3 \rightarrow \text{LiBO}_2^{\text{a}} + \text{Li}_2\text{O}^{\text{b}}$	0.55	0.06	0.61
	$\text{Li}_3\text{BO}_3 \rightarrow \frac{3}{2}\text{Li}_2\text{O} + \frac{1}{2}\text{B}_2\text{O}_3^{\text{c}}$	1.40	0.07	1.47
	$\text{Li}_3\text{BO}_3 \rightarrow \frac{1}{3}\text{LiB}_3\text{O}_5^{\text{d}} + \frac{4}{3}\text{Li}_2\text{O}$	1.12	0.04	1.16
$\beta\text{-Li}_3\text{BN}_2$	$\beta\text{-Li}_3\text{BN}_2 \rightarrow \text{Li}_3\text{N}^{\text{e}} + \text{BN}^{\text{f}}$	0.85	0.09	0.94
	$\beta\text{-Li}_3\text{BN}_2 \rightarrow \frac{7}{3}\text{Li}^{\text{g}} + \text{B}^{\text{h}} + \frac{2}{3}\text{LiN}_3^{\text{i}}$	4.69	-0.07	4.62

^aTetragonal ($\gamma\text{-LiBO}_2$) with Space Group $I - 42d$ (No. 122); from Ref. [42].

^bCubic with Space Group $Fm\bar{3}m$ (No. 225); from Ref. [43].

^cOrthorhombic with Space Group $Cmc2_1$ (No. 36); from Ref. [44].

^dOrthorhombic with Space Group $Pna2_1$ (No. 33); from Ref. [45].

^eHexagonal with Space Group $P6/mmm$ (No. 191); from Ref. [46].

^fCubic with Space Group $Fm\bar{3}m$ (No. 225).

^gCubic with Space Group $Im\bar{3}m$ (No. 229).

^hRhombohedral with Space Group $R\bar{3}m$ (No. 166); from Ref. [47].

ⁱMonoclinic with Space Group $C2/m$ (No. 12); from Ref. [48].

confidence for stating that the Li_3BO_3 and $\beta\text{-Li}_3\text{BN}_2$ are chemically stable at room temperature.

In anticipation of the use of Li_3BO_3 and $\beta\text{-Li}_3\text{BN}_2$ as coating materials or electrolytes in batteries with metallic Li anodes, we also examined some possible reactions between the electrolyte materials and metallic Li as the results summarized in Table IX. The positive reaction energy ΔF , calculated using Eq. (8) for each predicted reaction, indicates that the interactions with metallic Li are stable at equilibrium at 300 K.

VI. MODELS OF IDEALIZED INTERFACES OF MONOCLINIC FORMS OF Li_3BO_3 AND $\beta\text{-Li}_3\text{BN}_2$ WITH LAYERS OF LI ANODE MATERIAL

A. Interface configurations and energetics

To model the possible use of Li_3BO_3 and $\beta\text{-Li}_3\text{BN}_2$ for battery applications with pure Li metal anodes, we performed some simulations of model interfaces, using an approach similar to that of Lepley and Holzwarth [49] and references cited therein.

Modeling interfaces between the electrolyte and electrode starts with identifying the plausible cleavage plane for constructing a surface. For a supercell in a slab geometry including vacuum, it is convenient to evaluate the extra energy needed for surface formation according to

$$\gamma_s = \frac{E_{\text{slab}} - nE_{\text{bulk}}}{2A_s} \quad (9)$$

TABLE IX. Some predicted reactions for interfaces $\text{Li}_3\text{BO}_3/\text{Li}$ and $\text{Li}_3\text{BN}_2/\text{Li}$. The Li metal is assumed to have the optimized bcc [space group $Im\bar{3}m$ (No. 229)] structure.

Crystal	Reaction: $R \rightarrow P$	ΔU_{SL}	ΔF_{vib}	ΔF
Li_3BO_3	$\text{Li}_3\text{BO}_3 + \frac{3}{4}\text{Li} \rightarrow \frac{3}{4}\text{LiBO}_2 + \frac{1}{4}\text{B} + \frac{3}{2}\text{Li}_2\text{O}$	0.19	0.07	0.26
	$\text{Li}_3\text{BO}_3 + \text{Li} \rightarrow 2\text{Li}_2\text{O} + \frac{1}{3}\text{B} + \frac{1}{3}\text{B}_2\text{O}_3$	0.64	0.08	0.72
$\beta\text{-Li}_3\text{BN}_2$	$\beta\text{-Li}_3\text{BN}_2 + 3\text{Li} \rightarrow 2\text{Li}_3\text{N} + \text{B}$	1.91	0.06	1.97
	$\beta\text{-Li}_3\text{BN}_2 + \frac{3}{2}\text{Li} \rightarrow \frac{3}{2}\text{Li}_3\text{N} + \frac{1}{2}\text{B} + \frac{1}{2}\text{BN}$	1.38	0.07	1.45

TABLE X. Surface energies for several likely surface cleavage planes of Li_3BO_3 (LBO) and $\beta\text{-Li}_3\text{BN}_2$ (LBN) electrolytes [γ_s in units of ($\text{eV}/\text{\AA}^2$)].

Plane	$\gamma_s(\text{LBO})$	$\gamma_s(\text{LBN})$
[100]	0.048	0.243
[010]	0.057	0.076
[001]	0.051	0.042

Here E_{slab} denotes the total energy of the slab configuration containing n formula units of the bulk electrolyte exposed in a vacuum region. E_{bulk} denotes the total energy per formula unit of the bulk electrolyte. $2A_s$ accounts for two surface plane areas in the periodic simulation cell. Generally, E_{slab} achieves convergence when the length of vacuum norm to the surface is comparable to the lattice constant of the bulk material in the same direction.

The interface properties between two materials can be quantitatively measured using the interface energy. For an interface slab made up from the electrolyte material a and the electrode material b , the interface energy γ_{ab} is defined by the equation [49]

$$\gamma_{ab}(\Omega, n_b) = \frac{E(\Omega, A_i, n_a, n_b) - n_a E_a - n_b E_b}{2A_i} \quad (10)$$

where A_i represents the interface contact area, n_a and n_b denote the number of formula units of materials a and b , whose bulk energies per formula unit are E_a and E_b , respectively. $E(\Omega, A, n_a, n_b)$ is the total electronic energy of the optimized interface configuration Ω . The calculations of $\gamma_{ab}(\Omega)$ with respect to the number of metallic Li ions, in turn, result in a linear equation of the form

$$\gamma_{ab}(\Omega, n_b) = \gamma_{ab}^{\text{lim}}(\Omega) - \sigma_i n_b \quad (11)$$

Here the slope of the best-fitting line σ_i denotes the interface strain factor which characterizes the strain energy associated with holding the electrolyte and electrode materials together. The intercept value of $\gamma_{ab}^{\text{lim}}(\Omega)$ can be used to reference the energy of a coherent interface formed by two perfect compatibility lattice planes with zero strain.

For understanding the interface properties, we simulated the idealized interfaces between the electrolytes in contact with pure lithium metal, $\text{Li}_3\text{BO}_3/\text{Li}$ and $\beta\text{-Li}_3\text{BN}_2/\text{Li}$, using a periodic arrangement of electrolytes and metallic slabs.

Using Eq. (9), the surface energies for several selected cleavage planes of the Li_3BO_3 and $\beta\text{-Li}_3\text{BN}_2$ were calculated as the results listed in Table X. For Li_3BO_3 , the [100] and [001] vacuum cleavages were found to have relatively lower

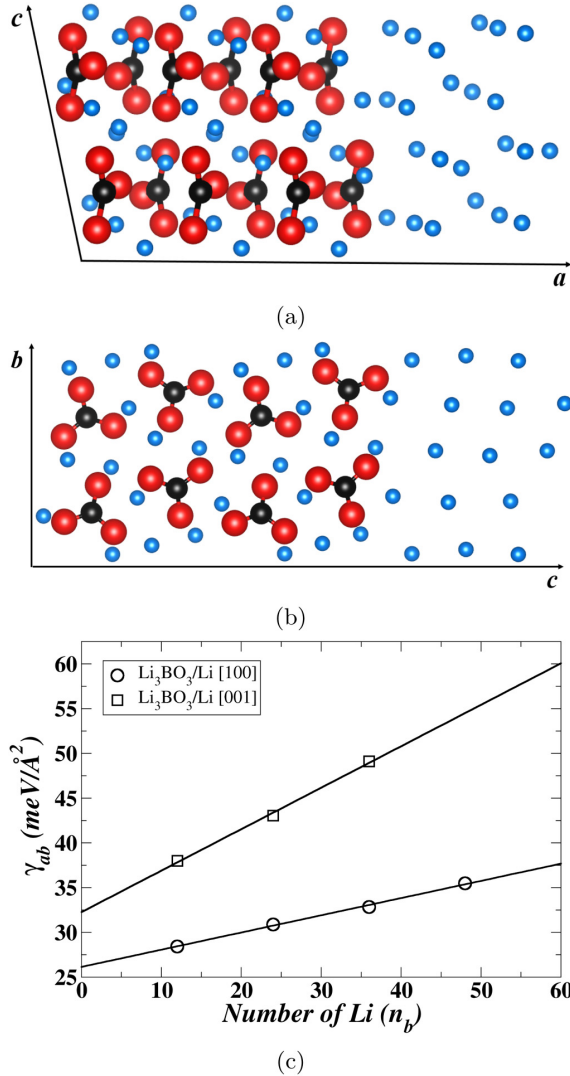


FIG. 17. Ball and stick diagrams of optimized interface structures between (a) $3 \times 1 \times 1$ supercell of Li_3BO_3 and Li slab in [100] direction, viewed in a projection onto the ac plane, and (b) $2 \times 1 \times 2$ supercell of Li_3BO_3 and Li slab in [001] direction viewed in a projection onto the bc plane. Both configurations contain 24 Li ions in the electrode. The Li, B, and O sites are represented with blue, black, and red balls, respectively. (c) Plot of interface energy γ_{ab} as a function of the number of Li ions in Li metal.

surface energy while, for $\beta\text{-Li}_3\text{BN}_2$, it shows that the energetically most favorable surface is the [001] cleavage with surface energy of $0.042 \text{ eV}/\text{\AA}^2$.

As illustrated in Fig. 17, two possible ideal models of the interface between the electrolyte Li_3BO_3 and the Li anode material are investigated. The corresponding example configurations are constructed from the optimized structure of multiple pure metallic Li layers placed on the [100] and [001] surfaces of a Li_3BO_3 slab. In both cases, the Li

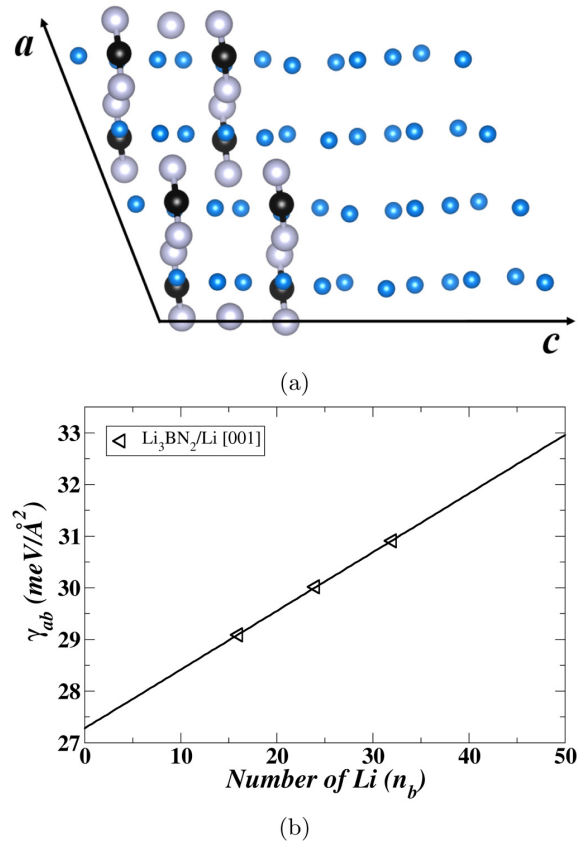


FIG. 18. (a) Ball and stick diagrams of optimized interface structures between $2 \times 1 \times 1$ supercell of $\beta\text{-Li}_3\text{BN}_2$ and 24 metallic Li ions in [001] direction, viewed in a projection of the ac plane. The Li, B, and N sites are represented with blue, black, and gray balls, respectively. (b) Plot of interface energy γ_{ab} as a function of the number of Li ions in Li metal.

atoms in the metal, retaining a comparable density of fcc Li, are relaxed to a pattern dissimilar to any phase of bulk Li.

Figure 18(a) shows one ideal $\beta\text{-Li}_3\text{BN}_2/\text{Li}$ interface configuration in the [001] direction. The metallic Li ions, initially in fcc crystalline layout, relaxed to a pattern resembling that of Li ions in the bulk $\beta\text{-Li}_3\text{BN}_2$, presenting remarkable continuity across the interface plane. In addition, the clear-cut distinction between $\beta\text{-Li}_3\text{BN}_2$ and Li metal indicates the stability of the possible interface structure.

The interface energies are analyzed based on the model with a fixed number of atoms in the electrolyte and varying numbers of Li atoms contained in metallic slabs. In practice, only the lattice constant in the direction perpendicular to the interface of the trial structures is allowed to change. By carrying out such constrained calculations, the optimized lattice constants and the minimum energy of the simulation slab are determined. Figures 17(c) and 18(b) display the optimized total energy of the supercell as a function of the number of metallic Li atoms for Li_3BO_3 and $\beta\text{-Li}_3\text{BN}_2$, respectively, with the results listed in Table XI. In the case of Li_3BO_3 , the

TABLE XI. Summary of the calculated values of γ_{ab}^{lim} in units of $\text{meV}/\text{\AA}^2$ and the strain energies σ_i in units of $\text{meV}/\text{\AA}^2/\text{Li}$ for interface configurations indicated by the first column.

Configuration	γ_{ab}^{lim}	σ_i	Visualization
LBO[100]/Li	26.13	19.00	Fig. 17(a)
LBO[001]/Li	32.26	46.33	Fig. 17(b)
LBN[001]/Li	27.28	0.11	Fig. 18(a)

extrapolated interface energy of the electrolyte γ_{ab}^{lim} for the interface normal to [100] is $26.13 \text{ meV}/\text{\AA}^2$, and the strain factor σ_i of the metallic Li in particular configuration, obtained from the slope of the linear fitting line, is $19.00 \text{ meV}/\text{\AA}^2/\text{Li}$ while for the interface normal to [001], the extrapolated interface energy is $\gamma_{ab}^{\text{lim}} = 32.26 \text{ meV}/\text{\AA}^2$ and the strain factor σ_i is up to $46.33 \text{ meV}/\text{\AA}^2/\text{Li}$. It seems that the interface configuration along the a axis is more viable. In the case of $\beta\text{-Li}_3\text{BN}_2$, the interface energy $\gamma_{ab}^{\text{lim}} = 27.28 \text{ meV}/\text{\AA}^2$ at the [001] orientation is comparable to those of Li_3BO_3 , however, the lattice strain factor at the interface is as low as $0.11 \text{ meV}/\text{\AA}^2/\text{Li}$, suggesting it is relatively easy to bring the two material systems into alignment.

B. Electronic density of states analysis

To gain insight into the electronic structures of the plausible $\text{Li}_3\text{BO}_3/\text{Li}$ and $\beta\text{-Li}_3\text{BO}_3/\text{Li}$ interfaces, it is helpful to analyze the partial densities of states $N^a(E)$ which we evaluated according to Eq. (2) in Ref. [50]. $N^a(E)$ evaluates the weighted electronic density of states using a weight factor defined by the charge within the augmentation sphere surrounding the specified atomic type and averaged for all spheres of that type. In this paper, the augmentation radii are $r_c^{\text{Li}} = 1.6$, $r_c^{\text{B}} = 1.4$, $r_c^{\text{O}} = 1.2$, and $r_c^{\text{N}} = 1.2$ in units of Bohr. The results are shown in Figs. 19(a) and 19(b), each with separate $N^a(E)$ contributions for the three forms of Li, the interface, and the interior of electrolyte regions.

The Fermi level, due to the placement of the metallic Li layers, is found to be below the unoccupied conduction bands of the electrolytes with values of 3.64 eV and 2.71 eV for $\text{Li}_3\text{BO}_3/\text{Li}$ and $\beta\text{-Li}_3\text{BN}_2/\text{Li}$, respectively. It is observed that for each material, the interface and bulk electrolyte have quite similar partial density of states profiles, suggesting the states are relatively consistent during the transition from the bulk electrolyte to the interface geometry in contact with Li metal.

VII. SUMMARY AND CONCLUSIONS

In summary, we have studied the structural and interface properties for the crystal structures of Li_3BO_3 and Li_3BN_2 using first-principles simulation techniques. Li_3BO_3 and Li_3BN_2 were comparatively investigated in this paper for the reason that they have some structural similarities and also in preparation for their expected future development for battery technology. While Li_3BO_3 crystallizes in the monoclinic $P2_1/c$ structures, Li_3BN_2 has three reported structures $P4_2/mnm$ (α form), $P21/c$ (β form), and $I4_1/amd$ (γ form), respectively, in the experiment. Generally, our structural optimizations are in good agreement with the experimental

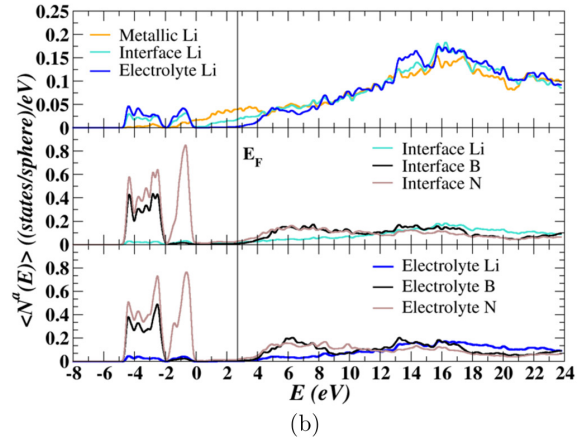
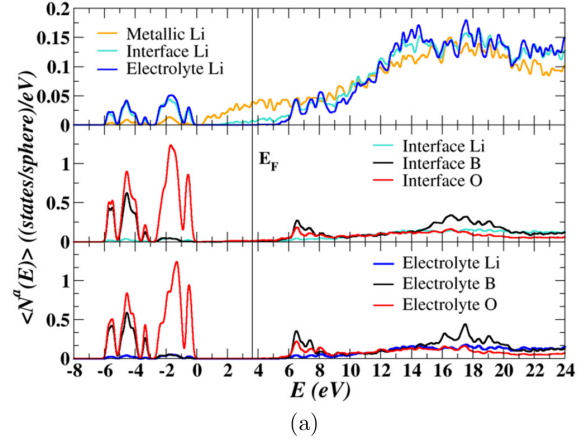


FIG. 19. Plots of partial densities of states, in units of states (approximate charge) within the augmentation sphere per eV, for (a) Li_3BO_3 corresponding to configuration shown in Figs. 17(a) and (b) $\beta\text{-Li}_3\text{BN}_2$ corresponding to configuration shown in Fig. 18(a). The zero of energy for each subplot was adjusted to the top of the filled valence band.

measurement. However, the phonon analysis shows that the reported α phase of Li_3BN_2 in the tetragonal symmetry is dynamically unstable due to the imaginary phonon modes at M point. The correct α phase is found to have the $Pmnm$ orthorhombic structure containing twice formula units as many as the tetragonal unit cell. The excellent agreement between the x-ray diffraction results of the quasiharmonic approximation on the orthorhombic structure and the experimental pattern provide further evidence of the $Pmnm$ structure of $\alpha\text{-Li}_3\text{BN}_2$.

Results find the calculated structures of Li_3BO_3 and $\beta\text{-Li}_3\text{BN}_2$ to be stable with respect to the possible decomposition reactions summarized in Table VIII. Since the three crystalline forms of Li_3BN_2 are equivalently favorable in terms of harmonic Helmholtz free energy, it is expected that the stability results on $\beta\text{-Li}_3\text{BN}_2$ are also tenable for the γ and α phases of Li_3BN_2 . In addition, we have evaluated the

phase stability of the possible interface geometries between the metallic Li anode and the relatively high ionic conducting electrolytes: Li_3BO_3 and $\beta\text{-Li}_3\text{BN}_2$. On one hand, the quantitative results suggest that both $\text{Li}_3\text{BO}_3/\text{Li}$ and $\beta\text{-Li}_3\text{BN}_2/\text{Li}$ interfaces are thermodynamically stable considering the endothermic reactions as listed in Table IX. On the other hand, the direct modeling of the supercell in the presence of metallic Li ions allows us to visualize the physical and chemical stabilities of the interfaces in Figs. 17 and 18(a). For $\text{Li}_3\text{BO}_3/\text{Li}$, the interface configuration along [100] is more probable than that along [001] because of the smaller γ_{ab}^{lim} associated with the effects of lattice strain. For $\beta\text{-Li}_3\text{BN}_2/\text{Li}$, the trivial γ_{ab}^{lim} of the (001) plane indicates a more likely realized interface for this system.

The simulated results for the $\text{Li}_3\text{BO}_3/\text{Li}$ and $\beta\text{-Li}_3\text{BN}_2/\text{Li}$ interfaces found in Sec. VI and the estimated chemical stability of Li_3BO_3 and $\beta\text{-Li}_3\text{BN}_2$ with Li metal summarized in Table IX encourage the development of these electrolytes as interfaces with Li anodes. The results are somewhat reminiscent of earlier studies on LiPON related materials [49,51] which provided insight into the demonstrated viability [52] of

this pioneering solid electrolyte for developing all solid-state batteries. In fact, several simulations [49,51,53] suggest that LiPON is chemically reactive with Li metal, tending to form Li_2O , Li_3P , and LiPN_2 . A recent *in situ* electron microscopic study of a LiPON/Li interface showed [54] that an effective passivating layer tends to form in this system, providing the observed stability with Li anodes. The results of Table IX showing that Li_3BO_3 and $\beta\text{-Li}_3\text{BN}_2$ are unreactive with Li suggest that these boron materials may form stable interfaces with Li anodes without the need for a passivating layer.

ACKNOWLEDGMENTS

This work was supported by NSF Grant No. DMR-1940324. Computations were performed on the Wake Forest University DEAC cluster, a centrally managed resource with support provided in part by the university. Z.D.H. was supported by Laboratory Directed Research and Development (LDRD) funding from Argonne National Laboratory, provided by the Director, Office of Science, of the US Department of Energy under Contract No. DE-AC02-06CH11357.

-
- [1] Y. Li, Z. D. Hood, and N. A. W. Holzwarth, *Phys. Rev. Materials* **5**, 085402 (2021).
- [2] P. Hohenberg and W. Kohn, *Phys. Rev.* **136**, B864 (1964).
- [3] W. Kohn and L. J. Sham, *Phys. Rev.* **140**, A1133 (1965).
- [4] P. E. Blöchl, *Phys. Rev. B* **50**, 17953 (1994).
- [5] N. A. W. Holzwarth, A. R. Tackett, and G. E. Matthews, *Comput. Phys. Commun.* **135**, 329 (2001), <http://pwpaw.wfu.edu>.
- [6] J. P. Perdew, A. Ruzsinszky, G. I. Csonka, O. A. Vydrov, G. E. Scuseria, L. A. Constantin, X. Zhou, and K. Burke, *Phys. Rev. Lett.* **100**, 136406 (2008).
- [7] P. Giannozzi, S. de Gironcoli, P. Pavone, and S. Baroni, *Phys. Rev. B* **43**, 7231 (1991).
- [8] X. Gonze, *Phys. Rev. B* **55**, 10337 (1997).
- [9] X. Gonze and C. Lee, *Phys. Rev. B* **55**, 10355 (1997).
- [10] S. Baroni, S. De Gironcoli, A. Dal Corso, and P. Giannozzi, *Rev. Mod. Phys.* **73**, 515 (2001).
- [11] P. Giannozzi and S. Baroni, in *Handbook of Materials Modeling*, edited by S. Yip (Springer, The Netherlands, 2005), pp. 195–214.
- [12] X. Gonze, F. Jollet, F. A. Araujo, D. Adams, B. Amadon, T. Applencourt, C. Audouze, J.-M. Beuken, J. Bieder, A. Bokhanchuk, E. Bousquet, F. Bruneval, D. Caliste, M. Côté, F. Dahm, F. D. Pieve, M. Delaveau, M. D. Gennaro, B. Dorado, C. Espejo *et al.*, *Comput. Phys. Commun.* **205**, 106 (2016), <https://www.abinit.org>.
- [13] X. Gonze, B. Amadon, G. Antonius, F. Arnardi, L. Baguet, J.-M. Beuken, J. Bieder, F. Bottin, J. Bouchet, E. Bousquet *et al.*, *Comput. Phys. Commun.* **248**, 107042 (2020), <https://www.abinit.org/>.
- [14] P. Giannozzi, O. Andreussi, T. Brumme, O. Bunau, M. Buongiorno Nardelli, M. Calandra, R. Car, C. Cavazzoni, D. Ceresoli, M. Cococcioni *et al.*, *J. Phys.: Condens. Matter* **29**, 465901 (2017).
- [15] P. Giannozzi, O. Baseggio, P. Bonfà, D. Brunato, R. Car, I. Carnimeo, C. Cavazzoni, S. de Gironcoli, P. Delugas, F. Ferrari Ruffino, A. Ferretti, N. Marzari, I. Timrov, A. Urru, and S. Baroni, *J. Chem. Phys.* **152**, 154105 (2020), <http://quantumespresso.org>.
- [16] H. J. Monkhorst and J. D. Pack, *Phys. Rev. B* **13**, 5188 (1976).
- [17] Y. Li, Z. D. Hood, and N. A. W. Holzwarth, *Phys. Rev. Mater.* **4**, 045406 (2020).
- [18] MATLAB, 2021, *version 9.10.0.1602886 (R2021a)* (The MathWorks Inc., Natick, MA, 2010).
- [19] <https://www.python.org>.
- [20] K. Momma and F. Izumi, *Appl. Crystallogr.* **44**, 1272 (2011), code available from <http://jip-minerals.org/vesta/en/>.
- [21] A. Kokalj, *Comput. Mater. Sci.* **28**, 155 (2003), code available at <http://www.xcrysden.org>.
- [22] H. T. Stokes and D. M. Hatch, *J. Appl. Crystallogr.* **38**, 237 (2008), <http://iso.byu.edu/iso/isotropy.php>.
- [23] C. F. Macrae, I. Sovago, S. J. Cottrell, P. T. A. Galek, P. McCabe, E. Pidcock, M. Platings, G. P. Shields, J. S. Stevens, M. Towler, and P. A. Wood, *J. Appl. Crystallogr.* **53**, 226 (2020).
- [24] M. Born and K. Huang, *Dynamical Theory of Crystal Lattices* (Oxford University Press, Oxford, England, 1954).
- [25] A. A. Maradudin, E. W. Montroll, G. H. Weiss, and I. P. Ipatova, *Theory of Lattice Dynamics in the Harmonic Approximation*, 2nd ed., Solid State Physics: Supplement, Vol. 3 (Academic Press, Cambridge, MA, 1971).
- [26] X. Gonze, *Phys. Rev. A* **52**, 1086 (1995).
- [27] V. F. Stewner, *Acta Crystallogr. Sect. B* **27**, 904 (1971).
- [28] M. I. Aroyo, J. M. Perez-Mato, D. Orobengoa, E. Tasci, G. De La Flor, and A. Kirov, *Bulgarian Chem. Commun.* **43**, 183 (2011), <http://www.cryst.ehu.es/>.
- [29] Y. Hinuma, G. Pizzi, Y. Kumagai, F. Oba, and I. Tanaka, *Comput. Mater. Sci.* **128**, 140 (2017).

- [30] H. Yamane, S. Kikkawa, and M. Koizumi, *J. Solid State Chem.* **71**, 1 (1987).
- [31] K. Cenzual, L. M. Gelato, M. Penzo, and E. Parthé, *Acta Crystallogr. Sect. B* **47**, 433 (1991).
- [32] F. E. Pinkerton and J. F. Herbst, *J. Appl. Phys.* **99**, 113523 (2006).
- [33] J. P. Perdew and Y. Wang, *Phys. Rev. B* **45**, 13244 (1992).
- [34] L. L. Boyer and J. R. Hardy, *Phys. Rev. B* **24**, 2577 (1981).
- [35] A. I. M. Rae, *J. Phys. C* **15**, 1883 (1982).
- [36] J. D. Althoff, P. B. Allen, R. M. Wentzcovitch, and J. A. Moriarty, *Phys. Rev. B* **48**, 13253 (1993).
- [37] M. Buongiorno Nardelli, S. Baroni, and P. Giannozzi, *Phys. Rev. B* **51**, 8060 (1995).
- [38] M. Somer, *Z. Naturforsch.* **46b**, 1664 (1991).
- [39] S. Baroni, P. Giannozzi, and E. Isaev, *Rev. Mineral. Geochem.* **71**, 39 (2010).
- [40] J. Howard, Z. D. Hood, and N. A. W. Holzwarth, *Phys. Rev. Mater.* **1**, 075406 (2017).
- [41] C. de Boor, *A Practical Guide to Splines* (Springer, New York, NY, 2001).
- [42] M. Marezio and J. P. Remeika, *J. Chem. Phys.* **44**, 3348 (1966).
- [43] T. W. D. Farley, W. Hayes, S. Hull, M. T. Hutchings, and M. Vrtis, *J. Phys.: Condens. Matter* **3**, 4761 (1991).
- [44] C. T. Prewitt and R. D. Shannon, *Acta Crystallogr. Sect. B* **24**, 869 (1968).
- [45] H. König and R. Hoppe, *Z. Anorg. Allg. Chem.* **439**, 71 (1978).
- [46] A. Huq, J. W. Richardson, E. R. Maxey, D. Chandra, and W.-M. Chien, *J. Alloys Compd.* **436**, 256 (2007).
- [47] B. Morosin, A. W. Mullendore, D. Emin, and G. A. Slack, *AIP Conf. Proc.* **140**, 70 (1986).
- [48] G. E. Pringle and D. E. Noakes, *Acta Crystallogr. Sect. B* **24**, 262 (1968).
- [49] N. D. Lepley and N. A. W. Holzwarth, *Phys. Rev. B* **92**, 214201 (2015).
- [50] L. E. Rush, Z. D. Hood, and N. A. W. Holzwarth, *Phys. Rev. Mater.* **1**, 075405 (2017).
- [51] N. D. Lepley, N. A. W. Holzwarth, and Y. A. Du, *Phys. Rev. B* **88**, 104103 (2013).
- [52] J. Li, C. Ma, M. Chi, C. Liang, and N. J. Dudney, *Adv. Energy Mater.* **5**, 1401408 (2015).
- [53] Y. Zhu, X. He, and Y. Mo, *ACS Appl. Mater. Interfaces* **7**, 23685 (2015).
- [54] Z. D. Hood, X. Chen, R. L. Sacci, X. Liu, G. M. Veith, Y. Mo, J. Niu, N. J. Dudney, and M. Chi, *Nano Lett.* **21**, 151 (2021).

Appendix E

First principles simulations of Li
boracites $\text{Li}_4\text{B}_7\text{O}_{12}\text{Cl}$ and
 $\text{Li}_5\text{B}_7\text{O}_{12.5}\text{Cl}$

First principles simulations of Li boracites $\text{Li}_4\text{B}_7\text{O}_{12}\text{Cl}$ and $\text{Li}_5\text{B}_7\text{O}_{12.5}\text{Cl}$

Yan Li¹ and N. A. W. Holzwarth¹

¹*Department of Physics, Wake Forest University, Winston-Salem, NC 27109, USA*

(Dated: November 27, 2021)

Lithium boracite crystals have been identified as promising ion conductors for possible use in all-solid-state batteries. With the help of first principles modeling techniques, we are able to show that these materials have structures with natural interstitial sites which play important roles in Li ion migration processes. The arrangements of these natural interstitial sites follow from group theory analyses of the computed and experimentally analyzed structures. Specifically, the low temperature α phase of $\text{Li}_4\text{B}_7\text{O}_{12}\text{Cl}$ is computed to have the face centered rhombohedral $R3c$ structure which is closely related to an ideal face centered cubic $F43c$ structure with 24 natural interstitial sites per conventional unit cell. Li ion diffusion in this material is found to proceed largely by a concerted motion involving these interstitial sites and two neighboring host lattice sites, consistent with the large measured ionic conductivity of this material. Adding one additional Li_2O cluster per formula unit to $\text{Li}_4\text{B}_7\text{O}_{12}\text{Cl}$ forms $\text{Li}_5\text{B}_7\text{O}_{12.5}\text{Cl}$ which crystallizes in the face centered cubic $F23$ structure, a subgroup of the $F43c$ structure. While these $F23$ crystals have 16 natural interstitial sites per conventional unit cell, their distribution is such that they do not participate in Li ion diffusion mechanisms, as is consistent with the negligible ionic conductivity measured for this material. Phonon spectral analysis of $\text{Li}_4\text{B}_7\text{O}_{12}\text{Cl}$ in its $R3c$ structure and $\text{Li}_5\text{B}_7\text{O}_{12.5}\text{Cl}$ in its $F32$ structure show that both crystals are dynamically stable. Chemical stability of these materials is indicated by convex hull analysis of $\text{Li}_4\text{B}_7\text{O}_{12}\text{Cl}$ and $\text{Li}_5\text{B}_7\text{O}_{12.5}\text{Cl}$ with respect to their building blocks of LiCl , Li_2O , and B_2O_3 .

I. INTRODUCTION

Recent literature has identified lithium boracites as promising ion conducting electrolytes for possible use in all-solid-state batteries. These materials are related to the naturally occurring magnesium borate mineral, $\text{Mg}_3\text{B}_7\text{O}_{13}\text{Cl}$, which is characterized by a rigid framework of B-O bonds composed of triangular BO_3 and tetrahedral BO_4 units, together with a regular void structure. The magnesium borate mineral has been found in several crystalline forms including a face centered cubic structure ($F43c$; space group [1] #219) determined in 1973 from a single crystal specimen by Sueno and co-workers [2].

Lithium boracite was developed and characterized in the 1970's by a number of authors including Levasseur and co-workers [3–6] and Jeitschko and co-workers [7, 8]. This work established that $\text{Li}_4\text{B}_7\text{O}_{12}\text{Cl}$ has the same borate framework and void structure of the boracite minerals and showed that the Li ions are associated with the void channels of the structure which serve to facilitate their mobility. More recent work [9–12] has developed efficient synthesis methods. For example, using the so-called low-temperature ionothermal synthesis method, Tan and co-workers [12] were able to improve the degree of purity of samples of $\text{Li}_4\text{B}_7\text{O}_{12}\text{Cl}$, resulting in the enhancement of the Li ion mobilities with measured room-temperature ionic conductivity up to 3×10^{-4} S/cm. Their work also found that $\text{Li}_4\text{B}_7\text{O}_{12}\text{Cl}$ presents a wide voltage stability window and, more generally, exhibits promising performance with Li metal electrodes. Other recent work has studied improved ionic conductivity due to alloying on the halogen site [8, 13] and on the boron site [14, 15]. On the other hand, the addition of Li_2O to

$\text{Li}_4\text{B}_7\text{O}_{12}\text{Cl}$ with the end composition of $\text{Li}_5\text{B}_7\text{O}_{12.5}\text{Cl}$ was studied by several authors [6, 16, 17] who showed that the additional Li_2O systematically reduces the ionic conductivity by several orders of magnitude. Extrapolating the measured ionic conductivity data [6] to room temperature estimates the room temperature conductivity of $\text{Li}_5\text{B}_7\text{O}_{12.5}\text{Cl}$ to be smaller than 10^{-10} S/cm.

In order to improve the promising electrolyte properties of lithium boracites, it is useful to examine the detailed crystal structures and to study mechanisms of ionic conductivity. With the help of first principles modeling techniques, we are able to show that lithium boracites are beautiful examples of structures with natural interstitial sites which play important roles in Li ion migration processes. In this case, the natural interstitial structure follows from group theory analysis of the ideal ground state structure and related structures.

This paper focuses on a detailed comparison of the lithium boracites $\text{Li}_4\text{B}_7\text{O}_{12}\text{Cl}$ and $\text{Li}_5\text{B}_7\text{O}_{12.5}\text{Cl}$. The general calculation methods are briefly described in Sec. II. Section III presents the results of the optimized structures of the idealized crystals, including identifying the optimized structure of α - $\text{Li}_4\text{B}_7\text{O}_{12}\text{Cl}$ and showing how it is related to the ideal cubic $F43c$ structure and a plausible model for β - $\text{Li}_4\text{B}_7\text{O}_{12}\text{Cl}$. The optimization of the $\text{Li}_5\text{B}_7\text{O}_{12.5}\text{Cl}$ structure, and comparison with the α - $\text{Li}_4\text{B}_7\text{O}_{12}\text{Cl}$ structure helps explain the decrease in ionic conductivity, following the work of Vlasse and co-workers [16]. The phonon analysis of the ground state structures of $\text{Li}_4\text{B}_7\text{O}_{12}\text{Cl}$ and $\text{Li}_5\text{B}_7\text{O}_{12.5}\text{Cl}$ show that both structures are dynamically stable as discussed in Sec. IV. In Sec. V, we examined the relative stability of the two materials with respect to their possible decompositions. Section VI examines the Li ion migration mechanisms

for the supercells of bulk materials using both trajectory analysis and molecular dynamics simulations. The molecular dynamics results approximately follow experimental conductivity measurements. The results of this study are discussed and summarized in Sec. VII.

II. COMPUTATIONAL METHODS

The computational methods were based on density functional theory (DFT) [18, 19] and density functional perturbation theory (DFPT) [20–24], using the projector augmented wave (PAW) [25] formalism. The modified generalized gradient formulation known as PBEsol [26] was used to treat the exchange and correlation effects. The PAW basis and projector functions for Li, B, O, and Cl were generated by the ATOMPAW code [27]. Simulations for the primitive and conventional models of the studied crystals were carried out using ABINIT [28, 29] and QUANTUM ESPRESSO packages [30, 31]. To be specific, the lattice optimization and phonon calculations based on primitive unit cells were performed using ABINIT package with plane-wave expansions of the wavefunctions including $|\mathbf{k} + \mathbf{G}|^2 \leq 70 \text{ Bohr}^{-2}$ and with a \mathbf{k} -point sampling of $4 \times 4 \times 4$ to approximate the Brillouin zone integrals. The phonon modes were evaluated with $|\mathbf{k} + \mathbf{G}|^2 \leq 50 \text{ Bohr}^{-2}$ on a regular $4 \times 4 \times 4$ grid of \mathbf{q} -vectors in the irreducible Brillouin zone of each crystal. Investigations of Li ions migration were evaluated by using the QUANTUM ESPRESSO package, using eight-formula unit conventional cells for both $\text{Li}_4\text{B}_7\text{O}_{12}\text{Cl}$ and $\text{Li}_5\text{B}_7\text{O}_{12.5}\text{Cl}$. For these large systems, the Brillouin zone integrals could be well approximated by sampling the single $\mathbf{k} = 0$ point. To achieve well-converged wave functions, the plane-wave expansions were chosen to be $|\mathbf{k} + \mathbf{G}|^2 \leq 64 \text{ Bohr}^{-2}$. Structural visualizations were constructed using the XCrySDEN [32] and VESTA [33] software packages. The program FINDSYM [34] was used in analyzing symmetry properties of the optimized crystal structures.

III. CRYSTAL STRUCTURES

A. $\text{Li}_4\text{B}_7\text{O}_{12}\text{Cl}$

In 1977, Jeitschko and co-workers [8] carried out single crystal analyses of the crystalline phases of $\text{Li}_4\text{B}_7\text{O}_{12}\text{Cl}$, finding three distinct phases, designated as α , β , and γ . The high temperature γ phase, stable at temperature $T > 348 \text{ K}$, is fully characterized with the face centered cubic space group [1] $F43c$ (No. 219) with temperature dependent partial occupancies of Li sites. The β phase is stable within the temperature range $348 > T > 310 \text{ K}$ while the α phase is stable at temperatures below 310 K . From the discontinuities of the ionic conductivity plots at the transition temperatures, one expects that latent heat is associated with each of these transitions, consistent

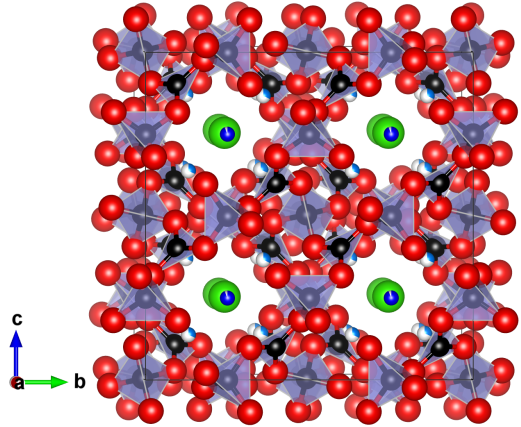


FIG. 1: Ball and stick diagram of conventional cell of $\text{Li}_4\text{B}_7\text{O}_{12}\text{Cl}$ in the $F43c$ structure as analyzed from single crystal samples at room temperature [8]. Ball colors of blue, black, red, and green indicate Li, B, O, and Cl ions, respectively. The polyhedral constructions illustrate the BO_4 tetrahedra and BO_3 planar structures. The shading of two distinct Li sites indicates their fractional occupancy.

with the first order transition designation. Jeitschko and co-workers [8] provided some information on the structures of the β and α phases, but the detailed analysis was not possible at the time. It was suggested that the α structure has a rhombohedrally distorted lattice with space group $R3$ (No. 146) with lattice constant $a = 12.141 \text{ \AA}$ and rhombohedral angle $\alpha = 90.083 \text{ deg}$. The β structure was suggested to have the cubic space group symmetry of $P43n$ (No. 218) with lattice constant $a = 12.161 \text{ \AA}$. Additionally, Jeitschko and co-workers [8] were able to perform a constrained analysis of the X-ray patterns of the α and β phases by assuming the face centered cubic structure $F43c$. This scheme finds differing Li ion occupancies on the sites, as labeled by their conventional cell multiplicity and Wyckoff letter, $24c$ and $32e$. While these correlations provide guidance to the structural analysis, they do not tell the full story of the low temperature structures. A visualization of the $F43c$ structure based on the analysis of Ref. 8 is shown in Fig. 1. This visualization presents the geometry of the B_7O_{12} framework in terms of connected BO_4 tetrahedra and BO_3 planar triangles. It is interesting to note that while all of the O ion sites are geometrically equivalent corresponding to the multiplicity and Wyckoff letter $96h$, there are two types of B ion sites. The tetrahedral B ion sites correspond to the label $24d$ while the triangular B ion sites correspond to $32e$. These triangular B ion sites are geometrically and symmetrically related to fractionally occupied Li ion sites having the same $32e$ label.

Using computation, we are in a position to examine the likely ground state structure, the α structure, which has not yet been analyzed from the experiment data. Start-

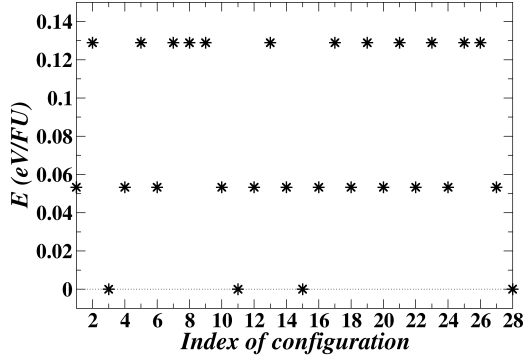


FIG. 2: The relative static lattice energy per formula unit for the 28 optimized configurations of $\text{Li}_4\text{B}_7\text{O}_{12}\text{Cl}$ in the primitive lattice setting.

ing from the available data [8] of the ideal $F\bar{4}3c$ model and assuming $1/4^{\text{th}}$ occupancy of the $32e$ sites, we systematically computed the total energies of the 28 unique configurations of the primitive cell. Figure 2 shows the relative static lattice energy per formula unit for each optimized atomic arrangement with an index ranging from #1 to #28. The results indicate that all the relaxed configurations are energetically divided into three distinct groups. While both the two high energy groups are found to have the space group $P1$, the four lowest energy configurations #3, #11, #15, and #28 are identified as having rhombohedral lattice with space group $R3c$ (No. 161). Those four symmetrically equivalent structures are ordered with fully occupied Li sites. From these results, it seems likely that the ideal ground state form of $\alpha\text{-Li}_4\text{B}_7\text{O}_{12}\text{Cl}$ is characterized by the $R3c$ space group in a face centered structure. This result is similar but not identical to the single crystal analysis of Jeitschko and co-workers [8]. Specifically, the $R3c$ structure differs from the $R3$ structure suggested by the experimental work [8] by having three additional symmetry operations.

Rhombohedral structures appear to be the least commonly realized structures in nature. Interestingly, for a face centered structure with the $R3c$ space group, the $R3c$ space group symmetry applies to both the primitive and conventional cell structures. Generally, a rhombohedral crystal has three lattice vectors of equal length and equal angles between each pair of lattice vectors. For the conventional unit cell setting we denote the lattice vector length a_c and the angle between lattice vectors as θ_c . The cubic structure is a special case with $\theta_c = 90$ deg. More generally, a convenient representation of the conventional lattice vectors of a rhombohedral structure similar to that used in the QUANTUM ESPRESSO code [30, 31] is given by

$$\begin{aligned} \mathbf{a}_c &= a_c (\hat{\mathbf{x}}(\lambda_c + 2\mu_c) + \hat{\mathbf{y}}(\lambda_c - \mu_c) + \hat{\mathbf{z}}(\lambda_c - \mu_c)) \\ \mathbf{b}_c &= a_c (\hat{\mathbf{x}}(\lambda_c - \mu_c) + \hat{\mathbf{y}}(\lambda_c + 2\mu_c) + \hat{\mathbf{z}}(\lambda_c - \mu_c)) \\ \mathbf{c}_c &= a_c (\hat{\mathbf{x}}(\lambda_c - \mu_c) + \hat{\mathbf{y}}(\lambda_c - \mu_c) + \hat{\mathbf{z}}(\lambda_c + 2\mu_c)) \end{aligned} \quad (1)$$

Here

$$\lambda_c \equiv \frac{\sqrt{1 + 2 \cos \theta_c}}{3} \quad \text{and} \quad \mu_c \equiv \frac{\sqrt{1 - \cos \theta_c}}{3}. \quad (2)$$

The primitive cell for our face centered rhombohedral lattice is given by

$$\begin{aligned} \mathbf{a}_p &= \frac{1}{2}(\mathbf{a}_c + \mathbf{b}_c) \\ &= a_p (\hat{\mathbf{x}}(\lambda_p + \mu_p) + \hat{\mathbf{y}}(\lambda_p + \mu_p) + \hat{\mathbf{z}}(\lambda_p - 2\mu_p)) \\ \mathbf{b}_p &= \frac{1}{2}(\mathbf{b}_c + \mathbf{c}_c) \\ &= a_p (\hat{\mathbf{x}}(\lambda_p - 2\mu_p) + \hat{\mathbf{y}}(\lambda_p + \mu_p) + \hat{\mathbf{z}}(\lambda_p + \mu_p)) \\ \mathbf{c}_p &= \frac{1}{2}(\mathbf{a}_c + \mathbf{c}_c) \\ &= a_p (\hat{\mathbf{x}}(\lambda_p + \mu_p) + \hat{\mathbf{y}}(\lambda_p - 2\mu_p) + \hat{\mathbf{z}}(\lambda_p + \mu_p)) \end{aligned} \quad (3)$$

Here

$$\lambda_p \equiv \frac{\sqrt{1 + 2 \cos \theta_p}}{3} \quad \text{and} \quad \mu_p \equiv \frac{\sqrt{1 - \cos \theta_p}}{3}, \quad (4)$$

and the primitive cell length is

$$a_p = \frac{a_c}{\sqrt{3 - 2 \cos(\theta_p)}}. \quad (5)$$

The relationship of the primitive angle and the conventional angle is given by

$$\cos(\theta_p) = \frac{1 + 3 \cos(\theta_c)}{2(1 + \cos(\theta_c))} \quad \text{or} \quad \cos(\theta_c) = \frac{2 \cos(\theta_p) - 1}{3 - 2 \cos(\theta_p)}, \quad (6)$$

where the special case of face centered cubic corresponds to $\theta_p = 60$ deg. Note that the volume of primitive cell, V_p is

$$V_p = a_p^3 (1 - \cos(\theta_p)) \sqrt{1 + 2 \cos(\theta_p)}, \quad (7)$$

which is $1/4^{\text{th}}$ the volume of the conventional cell, as expected.

The atomic positions \mathbf{R}^a within the unit cell can be expressed in terms of the fractional coordinates of the conventional cell (x_c, y_c, z_c) or the fractional coordinates of the primitive cell (x_p, y_p, z_p) , with the relationship between the two

$$\begin{aligned} x_p &= x_c + y_c - z_c \\ y_p &= -x_c + y_c + z_c \\ z_p &= x_c - y_c + z_c \end{aligned} \quad (8)$$

The primitive $R3c$ structure of $\alpha\text{-Li}_4\text{B}_7\text{O}_{12}\text{Cl}$ contains 2 formula units per primitive cell or 48 atoms while the conventional cell contains 8 formula units or 192 atoms. In order to assess how this computed structure compares with experiment, we show in Fig. 3 the X-ray pattern deduced from the optimized structure compared with the X-ray pattern constructed from the analysis of Jeitschko and co-workers [8] for measurements at a temperature of 298 K, analyzed in terms of the $F\bar{4}3c$ space group.

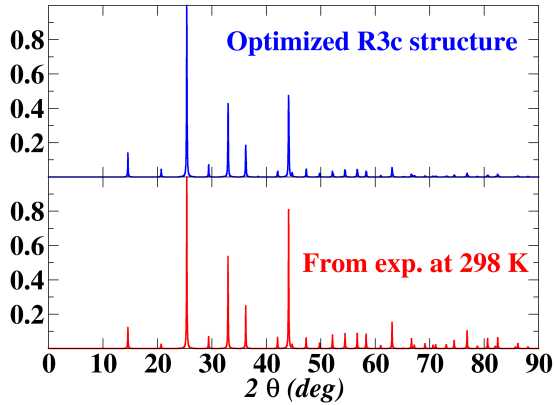


FIG. 3: X-ray patterns determined from structural analysis of $\text{Li}_4\text{B}_7\text{O}_{12}\text{Cl}$ for wavelengths $\lambda = 1.54056$ Å as calculated using Mercury software [35] from the computed idealized $R3c$ structure (top) and the analysis of single crystal data at 298 K based on the $F\bar{4}3c$ space group reported by Jeitschko and co-workers [8].

TABLE I: Static lattice results in the conventional cell setting for $\text{Li}_4\text{B}_7\text{O}_{12}\text{Cl}$, comparing the fully optimized structure (“Full”) with the optimized structure with cubic constraint (“Cubic”) and various experimental results reported in Ref. 8. The computed results also list ΔE (eV/FU), the estimate of the static lattice energy difference between the “Full” and “Cubic” optimizations.

	a_c (Å)	θ_c (deg)	ΔE (eV/FU)
Full	12.13	90.1	0.000
Cubic	12.14	90.0	0.002
Exp ($R3$)	12.141	90.083	
Exp ($F\bar{4}3c$ at 298 K)	12.141	90.0	
Exp ($F\bar{4}3c$ at 328 K)	12.161	90.0	
Exp ($F\bar{4}3c$ at 353 K)	12.167	90.0	

The optimized structure of $\alpha\text{-Li}_4\text{B}_7\text{O}_{12}\text{Cl}$ is visualized in the primitive cell and conventional cell settings in Fig. 4, where the B-O framework is indicated with thin bonds so that the Li and Cl positions can be more easily visualized. In addition to the optimized Li ion sites indicated in this diagram, natural Li interstitial sites are also indicated, as explained in more detail below.

A summary of computed static lattice parameters of $\alpha\text{-Li}_4\text{B}_7\text{O}_{12}\text{Cl}$ are given in Table I based on the conventional unit cell. In this case, we see that while the optimized structure of $\alpha\text{-Li}_4\text{B}_7\text{O}_{12}\text{Cl}$ is definitely rhombohedral, the rhombohedral angle θ_c is very close to the ideal cubic angle of 90 degrees. We can also optimize a con-

strained rhombohedral structure with $\theta_c = 90$ degrees. The result, which is also listed in Table I, is very slightly higher energy than the unconstrained optimization [36].

In order to examine the structure of $\alpha\text{-Li}_4\text{B}_7\text{O}_{12}\text{Cl}$ in more detail, we note that the face centered rhombohedral structure $R3c$ and the face centered cubic structure $F\bar{4}3c$ are very closely related in that the former is a subgroup of the latter. The Wyckoff labels and fractional coordinates of the primitive cells for these two space groups are detailed in Tables V and VI in the Appendix A. From the comparison of these tables, it is possible to map the cubic coordinates and Wyckoff labels of the $F\bar{4}3c$ structure to rhombohedral coordinates and Wyckoff labels of

TABLE II: Representative primitive cell fractional coordinates for $\text{Li}_4\text{B}_7\text{O}_{12}\text{Cl}$, comparing the optimized $R3c$ structure (left) with the experimental analysis of single crystal data measured at 298 K based on the $F\bar{4}3c$ structure from Ref. 8. ^a Here “Label” refers to the primitive cell multiplicity and the Wyckoff label with “Occ.” representing the corresponding number of occupied sites.

$R3c$				$F\bar{4}3c$			
Atom	Label	Occ.	(x_p, y_p, z_p)	Atom	Label	Occ.	(x_p, y_p, z_p)
Li(1)	6b	6	(0.035, 0.036, 0.465)	Li(2)	6c	6	(0.000, 0.000, 0.500)
Li(2)	2a	2	(0.869, 0.869, 0.869)	Li(1)	8e	2	(0.871, 0.871, 0.871)
Li(i) ^b	6b	0	(0.869, 0.869, 0.393)				(0.871, 0.871, 0.388)
B(1)	6b	6	(0.251, 0.261, 0.753)	B(1)	6d	6	(0.250, 0.250, 0.750)
B(2)	2a	6	(0.602, 0.602, 0.603)	B(2)	8e	8	(0.600, 0.600, 0.600)
B(3)	6b	6	(0.109, 0.109, 0.698)				(0.100, 0.100, 0.699)
O(1)	6b	6	(0.438, 0.613, 0.757)	O(1)	24h	24	(0.439, 0.606, 0.757)
O(2)	6b	6	(0.447, 0.766, 0.197)				(0.439, 0.757, 0.198)
O(3)	6b	6	(0.187, 0.772, 0.615)				(0.198, 0.757, 0.606)
O(4)	6b	6	(0.712, 0.942, 0.106)				(0.698, 0.939, 0.106)
Cl	2a	2	(0.250, 0.250, 0.250)	Cl	2b	2	(0.250, 0.250, 0.250)

^a Similar but not identical experimental results were reported by Ref. 17.

^b Interstitial Li coordinate estimated as the coordinate $(x, x, -3x)$ as suggested from Table VI. Corresponding optimized Li interstitial site was found to have coordinates (0.876, 0.880, 0.400).

the $R3c$ structure as given in Table VII. Most interestingly for this case, only the e label of the $F\bar{4}3c$ structure maps to both a and b labels of the $R3c$ structure while all of the other labels of the $F\bar{4}3c$ structure map exclusively to either the a or b labels of the $R3c$ structure.

The optimized structure of $\alpha\text{-Li}_4\text{B}_7\text{O}_{12}\text{Cl}$ corresponds to Li sites analyzed in the $F\bar{4}3c$ structure with Wyckoff label e with the fractional occupancy of 25% which in the $R3c$ structure corresponds to full occupancy of the Wyckoff site labeled a . This implies that the remaining 6 sites, corresponding the Wyckoff label b , should be available as natural vacancies in this structure. Representative fractional coordinates for the computed $R3c$ structure of $\text{Li}_4\text{B}_7\text{O}_{12}\text{Cl}$ are given in Table II together with the corresponding coordinates based on the $F\bar{4}3c$ analysis, using the primitive cell coordinates for both. We see significant agreement between the two structures. In addition to the occupied lattice sites, the analysis finds 6 natural interstitial Li sites which correspond to three-quarters of the $8e$ sites in the $F\bar{4}3c$ setting which map to $6b$ sites in the $R3c$ setting. The typical method of identifying interstitial sites in a crystal is to carry out a systematic search of positions throughout the crystal for low energy sites, which optimize the ideal structure with the addition of one Li ion and a uniform compensation charge. We performed this search for the $\alpha\text{-Li}_4\text{B}_7\text{O}_{12}\text{Cl}$ structure and found the lowest energy interstitial sites to be quite close to the ideal $6b$ sites. In Table II a representative ideal site is listed in the table and the computed interstitial is listed in the table note.

These static lattice optimization studies provide strong evidence that the ground state structure of $\alpha\text{-Li}_4\text{B}_7\text{O}_{12}\text{Cl}$ is face centered $R3c$. The results also suggest that an idealized rhombohedral structure, optimized with the constraint that $\theta_p = 60$ deg and $\theta_c = 90$ deg, may be a good model for the β structure of the boracite. The

notion that $\beta\text{-Li}_4\text{B}_7\text{O}_{12}\text{Cl}$ has the $R3c$ structure with $\theta_p = 60$ deg and $\theta_c = 90$ deg makes it identical with $F\bar{4}3c$ structure with special quarter occupancy of the Li(2) $8e$ sites suggested by Table VII. This would also be consistent with the notion that the higher temperature $\gamma\text{-Li}_4\text{B}_7\text{O}_{12}\text{Cl}$ phase has the $F\bar{4}3c$ structure with fractional occupancy on both the Li(1) $6c$ sites and the Li(2) $8e$ sites as established from the single crystal analyses of Jeitschko and co-workers [8]. While this suggestion for the structure of the intermediate β phase seems reasonable from the group theory and geometric viewpoints, the actual intermediate structure may be more complicated. The suggestion by Jeitschko and co-workers [8] that the β structure has $P\bar{4}3n$ (No. 218) symmetry is, however, hard to imagine since this would require a transition between a face centered rhombohedral lattice and a primitive cubic lattice as the crystal transforms from the α to β phase and a transition between a primitive cubic lattice and a face centered cubic lattice as the crystal transforms from the β to γ phase.

B. $\text{Li}_5\text{B}_7\text{O}_{12.5}\text{Cl}$

There are several literature reports [6, 16, 17] focused on studying the effects of filling the natural interstitial sites in $\text{Li}_4\text{B}_7\text{O}_{12}\text{Cl}$ by forming solid solutions with Li_2O with the composition $\text{Li}_{4+x}\text{B}_7\text{O}_{12+x/2}\text{Cl}$ for $0 \leq x \leq 1$. The most concentrated material has the stoichiometry $\text{Li}_5\text{B}_7\text{O}_{12.5}\text{Cl}$ which was found to crystallize in the ordered face centered cubic space group $F23$ (No. 196) [16] shown in Fig. 5. Interestingly, the space group $F23$ is a subgroup of the space group $F\bar{4}3c$ and the structures of $\text{Li}_5\text{B}_7\text{O}_{12.5}\text{Cl}$ and $\text{Li}_4\text{B}_7\text{O}_{12}\text{Cl}$ are closely related [37]. Table III shows the comparison of representative frac-

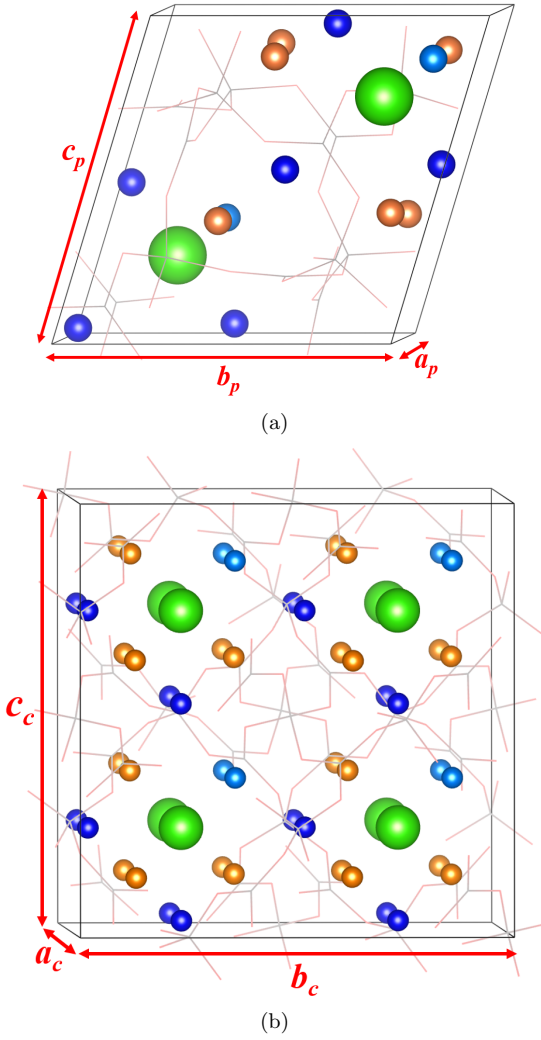


FIG. 4: Ball and stick diagram of $\text{Li}_4\text{B}_7\text{O}_{12}\text{Cl}$ in the (a) primitive and (b) conventional cell settings with the B-O framework represented by thin sticks and Cl indicated by green balls. The host Li ions with labels b and a are represented by dark blue and light blue balls, respectively. The unoccupied Li sites which serve as natural interstitials with Wyckoff label b are represented by brown balls.

tional coordinates of the two structures based on the experimental data of Ref. 16 and Ref. 8 in the conventional cell settings. The table shows quantitative agreement for the fully occupied B, O, and Cl sites of the two structures. Additionally, $\text{Li}_5\text{B}_7\text{O}_{12.5}\text{Cl}$ accommodates 4 extra O ions at $4a$ sites in the $F23$ structure. There is also good correspondence between the two structures in the positions of Li ions in $24g$ sites of the $F23$ structure and

those in the higher symmetry $24c$ sites of the $F43c$ struc-

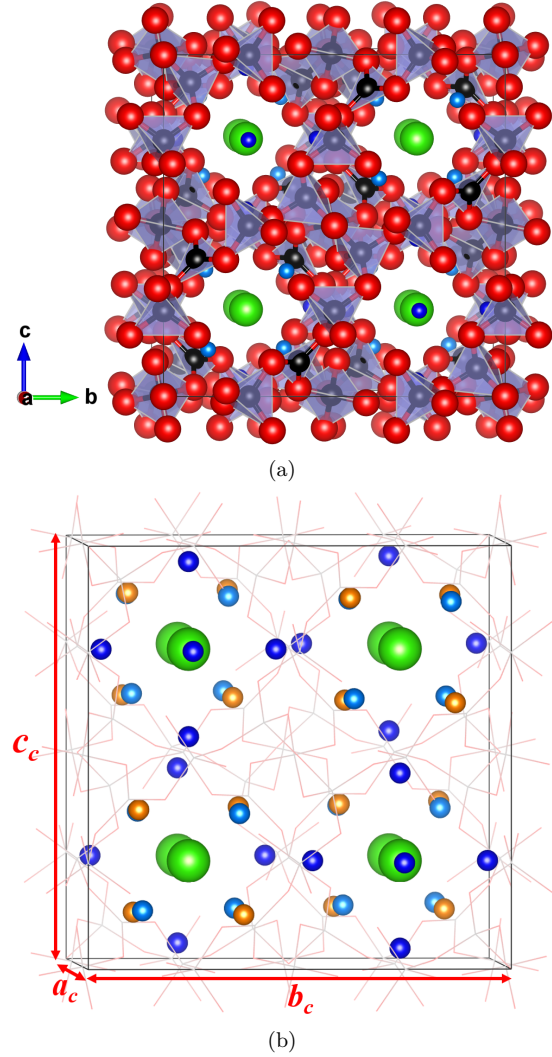


FIG. 5: (a) Ball and stick diagram of conventional cell of $\text{Li}_5\text{B}_7\text{O}_{12.5}\text{Cl}$ in the $F23$ structure. Ball colors of blue, black, red, and green indicate Li, B, O, and Cl ions, respectively. (b) Thin stick representation of B-O framework to fully display the positions of host Li sites (dark blue for $24g$ and light blue for $16e$) and the lowest energy interstitial Li sites (brown for $16e$).

ture. The 8 remaining Li ions in $\text{Li}_4\text{B}_7\text{O}_{12}\text{Cl}$ and the 8 extra Li ions in $\text{Li}_5\text{B}_7\text{O}_{12.5}\text{Cl}$ are accommodated in 16e sites of the $F23$ structure which are closely related to half of the $32e$ sites of the $F43c$ structure. This leaves 16 natural Li ion vacancies at shifted $16e$ sites in the $F23$ structure which are related to 24 natural interstitial sites of the $F43c$ structure associated with the $1/4^{\text{th}}$ occupied $32e$ sites in $\text{Li}_4\text{B}_7\text{O}_{12}\text{Cl}$.

TABLE III: Representative conventional cell fractional coordinates for the 204 ions of $\text{Li}_5\text{B}_7\text{O}_{12.5}\text{Cl}$ in the $F23$ space group from the room temperature experimental analysis of Ref. 16 compared with corresponding conventional cell fractional coordinates for the 192 ions of $\text{Li}_4\text{B}_7\text{O}_{12}\text{Cl}$ in the space group $F\bar{4}3c$ structure from the experimental analysis of Ref. 8 (which are similar but not identical experimental results reported by Ref. 17). Here “Label” refers to the conventional cell multiplicity and the Wyckoff label with “Occ.” represents the corresponding number of occupied sites of the ideal structures at low temperature.

$\text{Li}_5\text{B}_7\text{O}_{12.5}\text{Cl}$ ($F23$)				$\text{Li}_4\text{B}_7\text{O}_{12}\text{Cl}$ ($F\bar{4}3c$)			
Atom	Label	Occ.	(x_c, y_c, z_c)	Atom	Label	Occ.	(x_c, y_c, z_c)
Li(1)	24g	24	(0.250, 0.250, 0.042)	Li(2)	24c	24	(0.250, 0.250, 0.000)
Li(2)	16e	16	(0.865, 0.865, 0.865)	Li(1)	32e	8	(0.871, 0.871, 0.871)
Li(i) ^a	16e	0	(0.365, 0.365, 0.365)				(0.371, 0.371, 0.371)
B(1)	24f	24	(0.000, 0.000, 0.252)	B(1)	24d	24	(0.000, 0.000, 0.250)
B(2)	16e	16	(0.081, 0.081, 0.081)	B(2)	32e	32	(0.100, 0.100, 0.100)
B(3)	16e	16	(0.601, 0.601, 0.601)				(0.600, 0.600, 0.600)
O(1)	48h	48	(0.020, 0.097, 0.181)	O(1)	96h	96	(0.023, 0.098, 0.182)
O(2)	48h	48	(0.023, 0.183, 0.599)				(0.023, 0.182, 0.598)
O(3)	4a	4	(0.000, 0.000, 0.000)	-	-	-	-
Cl(1)	4c	4	(0.250, 0.250, 0.250)	Cl	8b	8	(0.250, 0.250, 0.250)
Cl(2)	4d	4	(0.750, 0.750, 0.750)				(0.750, 0.750, 0.750)

^a Coordinates deduced from corresponding $F\bar{4}3c$ symmetry.

The computational results for the lattice constant and fractional coordinates of the optimized structure of $\text{Li}_5\text{B}_7\text{O}_{12.5}\text{Cl}$ are listed in Table IV. The computed fractional coordinates of the occupied sites agree within ± 0.002 the results of Ref. 16 listed in Table III. In addition to the optimized occupied sites, the optimized coordinate of the lowest energy interstitial Li site is also given.

As seen from the ball and stick drawing of eight formula units of the conventional cell illustrated in Fig. 5a, the rigid three-dimensional B-O framework making up of interconnected BO_3 triangles and BO_4 tetrahedra is similar to that of other boracites. Notably, $\text{Li}_5\text{B}_7\text{O}_{12.5}\text{Cl}$ contains extra O ion of O(3) type fully occupying 4a sites at (0.000, 0.000, 0.000), while the corresponding position is empty in cubic $F\bar{4}3c$ models of $\text{Li}_4\text{B}_7\text{O}_{12}\text{Cl}$. Figure 5b highlights the arrangement of Li ions, including two distinct host and the lowest energy metastable interstitial sites as indicated by two shades of blue and brown balls, respectively. Within the conventional cell, the computed interstitial sites have Wyckoff labels 16e and are located at fractional positions equivalent to (0.374, 0.374, 0.374).

Besides the major differences in the amount and occupation of O ion, the ordering of Li ions is also responsible for the change in symmetry from $R3c$ structure of $\text{Li}_4\text{B}_7\text{O}_{12}\text{Cl}$ to $F23$ structure of $\text{Li}_5\text{B}_7\text{O}_{12.5}\text{Cl}$. On the other hand, it is interesting to analyze the correlations between the Li ions in these two materials. Specifically, the Li sites with Wyckoff labels 24g in the cubic $\text{Li}_5\text{B}_7\text{O}_{12.5}\text{Cl}$ have a one-to-one correspondence with those at $4 \times 6b$ sites in the conventional cell of rhombohedral $\text{Li}_4\text{B}_7\text{O}_{12}\text{Cl}$. The case of the e type sites is less immediately apparent. It is found that the 16e type host sites of $\text{Li}_5\text{B}_7\text{O}_{12.5}\text{Cl}$ together with its lowest-energy

metastable interstitial sites can map to 8 host and 24 vacant sites in the rhombohedral $\text{Li}_4\text{B}_7\text{O}_{12}\text{Cl}$.

IV. LATTICE VIBRATIONS

The calculation of vibrational properties follows the methods discussed in detail in a previous study [39]. The phonon dispersion relations of $\text{Li}_4\text{B}_7\text{O}_{12}\text{Cl}$ and $\text{Li}_5\text{B}_7\text{O}_{12.5}\text{Cl}$, both calculated in the primitive cell setting, together with the corresponding projected atomic density of states are shown in Fig. 6, suggesting very similar profiles for the two crystals. For $\text{Li}_4\text{B}_7\text{O}_{12}\text{Cl}$, which has 48 atoms per primitive cell, the total number of lattice vibrational modes is 144. The highest frequency is computed to be 1435 cm^{-1} . With the atomic motion assigned to symmetry under the $C_{3v}(3m)$ point group, the zone center acoustic and optic normal modes break into the following irreducible components [1].

$$\begin{aligned} \Gamma_{\text{acoustic}}^{R3c} &= A_1 + E \\ \Gamma_{\text{optic}}^{R3c} &= 23A_1 + 24A_2 + 47E \end{aligned} \quad (9)$$

Here the A modes are due to a non-degenerate vibration with the subscripts 1 and 2 indicating symmetric and anti-symmetric with respect to the principal rotation axis, respectively; E denotes the doubly degenerate modes. Further group theoretical analysis finds that among the three types of optical modes, the 23 A_1 and 47 E optical modes simultaneously belong to infrared active and Raman active modes as well. The situation suggests that, without considering the three silent acoustic modes, a vibration associated with the A_1 or E type mode leads to change in both dipole moment and polarizabil-

TABLE IV: Computed optimized structure of $\text{Li}_5\text{B}_7\text{O}_{12.5}\text{Cl}$ in the face centered cubic space group $F23$, compared with the room temperature experimental analysis of Ref. 16. Note that the experimental conventional cell fractional coordinates are also listed in Table VII. Here “Label” refers to the conventional cell multiplicity and the Wyckoff label with “Occ.” represents the corresponding number of occupied sites of the ideal structures at low temperature.

$\text{Li}_5\text{B}_7\text{O}_{12.5}\text{Cl}$	$a = b = c$ (Å)	$\alpha = \beta = \gamma$ (deg)
Cal.	12.106	90.000
Exp.	12.136	90.000

Atom	Label	Occ.	(x_c, y_c, z_c)
Li(1)	24 <i>g</i>	24	(0.250, 0.250, 0.043)
Li(2)	16 <i>e</i>	16	(0.865, 0.865, 0.865)
Li(i) ^a	16 <i>e</i>	0	(0.374, 0.374, 0.374)
B(1)	24 <i>f</i>	24	(0.000, 0.000, 0.251)
B(2)	16 <i>e</i>	16	(0.081, 0.081, 0.081)
B(3)	16 <i>e</i>	16	(0.601, 0.601, 0.601)
O(1)	48 <i>h</i>	48	(0.018, 0.098, 0.180)
O(2)	48 <i>h</i>	48	(0.022, 0.183, 0.600)
O(3)	4 <i>a</i>	4	(0.000, 0.000, 0.000)
Cl(1)	4 <i>c</i>	4	(0.250, 0.250, 0.250)
Cl(2)	4 <i>c</i>	4	(0.750, 0.750, 0.750)

^a Determined by optimizing system with extra Li ion.

ity. While the 24 remaining A_2 modes are normal optical modes with no particular attribution.

For $\text{Li}_5\text{B}_7\text{O}_{12.5}\text{Cl}$, which has 51 atoms per primitive cell, the total number of phonon modes is 153 with the highest frequency computed to be 1404 cm^{-1} . Due to relatively higher symmetry, the dispersion curves of $\text{Li}_5\text{B}_7\text{O}_{12.5}\text{Cl}$ in the $F23$ structure display more degeneracy. Depending on symmetries originating from point group $T(23)$, the zero center phonon modes decompose into irreducible representations [1] as follows

$$\begin{aligned} \Gamma_{\text{acoustic}}^{F23} &= T \\ \Gamma_{\text{optic}}^{F23} &= 11 A + 11^1 E + 11^2 E + 39 T. \end{aligned} \quad (10)$$

Here the notation T represents the triply degenerate modes in a three dimensional crystal system. Further symmetry analysis finds the Raman active modes $\Gamma_{\text{Raman}} \equiv \Gamma_{\text{optic}}$ in Eq. (10), whereas the infrared active modes only include the T type modes.

In both materials, there are no imaginary phonon modes exhibited, indicating that each crystal structure is dynamically stable. Whereas the primary involvement of Li motion occurs in the lower frequency modes in the range of $0 - 600 \text{ cm}^{-1}$, the higher frequency modes are predominately attributed to motions of the B and O ions. In particular, the B(1) type ions located in the center of the planar B-O triangles are found to have relatively larger vibrational amplitudes in the top branches with mode indices 129 - 144 and frequencies ranging from 1285

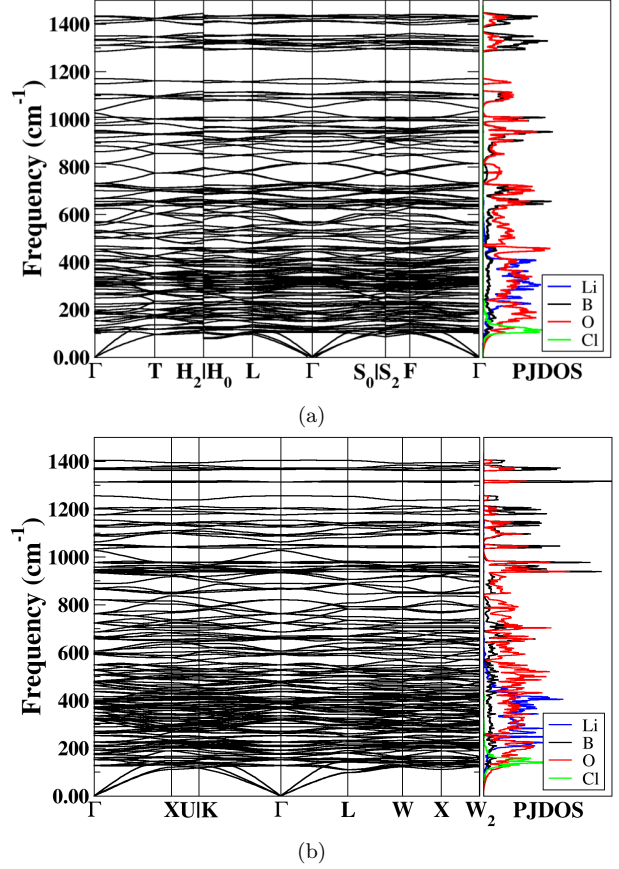


FIG. 6: Calculated phonon spectrum along high-symmetric crystallographic directions and their corresponding projected densities of states for each atom type (PJDOS) for (a) $\text{Li}_4\text{B}_7\text{O}_{12}\text{Cl}$ and (b) $\text{Li}_5\text{B}_7\text{O}_{12.5}\text{Cl}$. The range of the PJDOS plots was fixed at the maximum PJDOS value for $\text{Li}_5\text{B}_7\text{O}_{12.5}\text{Cl}$. The high-symmetry \mathbf{q} lines were selected according to the recommendation from Ref. 38 for each particular space group. For the $R3c$ structure of (a), the labels refer to the equivalent hexagonal structure, while for the $F23$ structure of (b), the labels refer to the standard face centered cubic structure.

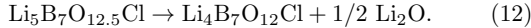
- 1434 cm^{-1} . It is also interesting to note that the vibration modes involving appreciable Cl ion motion have an even lower of frequency less than 240 cm^{-1} , which is perhaps not surprising because of the “immobility” of the massive Cl ions and weak bonding strength of Cl with other ions. The vibrational modes were also analyzed for the constrained rhombohedral lattice with $\theta_p = 60$ degrees (corresponding to the one labeled “Cubic” in Table I), finding indistinguishable phonon dispersion curves from those of the fully optimized rhombohedral structure shown in Fig. 6a.

Having established that both $\text{Li}_4\text{B}_7\text{O}_{12}\text{Cl}$ and $\text{Li}_5\text{B}_7\text{O}_{12.5}\text{Cl}$ are dynamically stable in their ground state structures, it is possible to study their stability more quantitatively by estimating their Helmholtz free energies. For well-ordered and electronically insulating crystalline material, it is reasonable to approximate the Helmholtz free energy as a function of temperature T to be

$$F(T) = U_{\text{SL}} + F_{\text{vib}}(T). \quad (11)$$

Here U_{SL} represents the temperature-independent static lattice energy which is well approximated by the total energy of the DFT calculation of the optimized structure. The phonon free energy $F_{\text{vib}}(T)$ is obtained by integrating the phonon density of states over the whole frequency range, which is essential to quantify the contributions of the lattice vibrations as described (for example) in Eqs. (1-4) of Ref. 40. This can be done for $\text{Li}_4\text{B}_7\text{O}_{12}\text{Cl}$ and $\text{Li}_5\text{B}_7\text{O}_{12.5}\text{Cl}$ from the phonon results illustrated in Fig. 6.

For example, consider the following transformation



We can compare the Helmholtz free energies of both sides of Eq. (12). In addition to contributions from $\text{Li}_4\text{B}_7\text{O}_{12}\text{Cl}$ and $\text{Li}_5\text{B}_7\text{O}_{12.5}\text{Cl}$, the static lattice energy and phonon spectrum of Li_2O in its antiflorite structure [41] was also calculated. The results are shown in Fig. 7, suggesting that $\text{Li}_5\text{B}_7\text{O}_{12.5}\text{Cl}$ is more stable than separate crystals of $\text{Li}_4\text{B}_7\text{O}_{12}\text{Cl}$ and Li_2O throughout the temperature range considered. However, in absence of excess Li_2O , lithium boracite $\text{Li}_4\text{B}_7\text{O}_{12}\text{Cl}$ is expected to be stable. Additionally, the embedded plot of $F_{\text{vib}}(T)$ in Fig. 7 shows that the vibrational energy difference between the two sides of Eq. (12) is trivial across the explored temperature range. For this system, the Helmholtz free energy difference is dominated almost exclusively by the static lattice energy part. For example, at 300 K, the vibrational energy difference is $F_{\text{vib}}(\text{Li}_4\text{B}_7\text{O}_{12}\text{Cl}) + 1/2 F_{\text{vib}}(\text{Li}_2\text{O}) - F_{\text{vib}}(\text{Li}_5\text{B}_7\text{O}_{12.5}\text{Cl}) = 0.02 \text{ eV/FU}$, while the corresponding static lattice energy difference is 1.0 eV/FU .

V. STABILITY ANALYSIS

The phase stability of the crystal structures of $\text{Li}_4\text{B}_7\text{O}_{12}\text{Cl}$ and $\text{Li}_5\text{B}_7\text{O}_{12.5}\text{Cl}$ was also evaluated using the convex hull approach [42], which is based on the idea that the phase stability of a crystal structure can be determined from the energy of its components. Within this framework, the stability of a compound requires it to be on a convex hull construction composed of a set of tie lines that connect all the related lowest energy phases [43]. Also, a compound lying on the convex hull suggests that it has lower energy than the stoichiometric linear combinations of other phases in the system with the same composition.

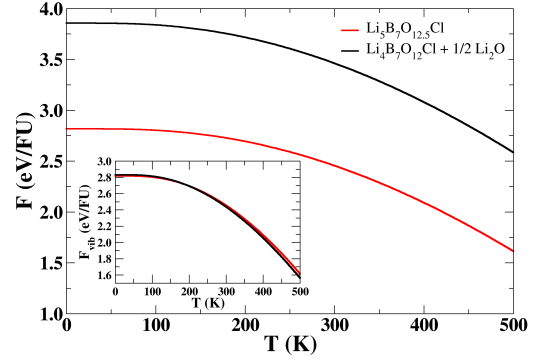


FIG. 7: Plot of Helmholtz free energy and the vibrational free energy (inset) for the left- and right-hand side components of Eq. (12).

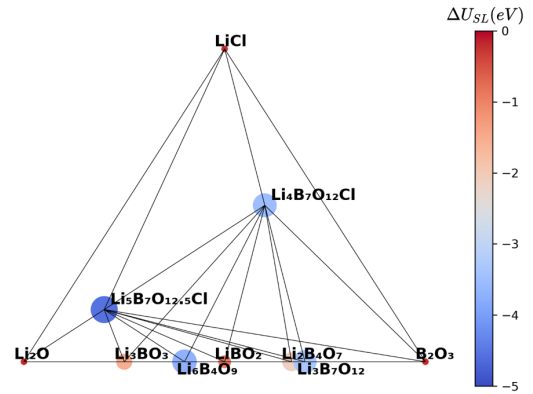


FIG. 8: Convex hull of the Li_2O - B_2O_3 - LiCl system with filled colored circles indicating values of the energy differences ΔU_{SL} as defined in Eq. (13) for each of the stable phases. The color bar indicates the values of ΔU_{SL} in units of eV/formula unit. Additionally, the circle radii are drawn in proportion to the magnitudes of $|\Delta U_{\text{SL}}|$.

In the present study, it is convenient to construct the convex hull analysis using the building blocks of Li_2O , B_2O_3 , and LiCl which span the composition space of $\text{Li}_4\text{B}_7\text{O}_{12}\text{Cl}$, $\text{Li}_5\text{B}_7\text{O}_{12.5}\text{Cl}$, and many of their possible decomposition products. For this analysis, we focus on the DFT static ground state energies. With the effort of computing phonon properties, it is possible to perform a more advanced stability analysis at given temperatures. However, it is evident from Fig. 7 that the pure phonon energy is less likely to change the qualitative picture of the stability properties of the materials. Therefore, the finite-temperature vibrational effects were not taken into account in this analysis. Accordingly for each material,

we calculate the energy difference

$$\Delta U_{\text{SL}} = U_{\text{SL}} - \sum_{i=1}^3 x_i U_{\text{SL}}^i \quad (13)$$

where U_{SL} is the total static energy per formula unit of a specific compound, and U_{SL}^i is the total static energy per formula unit of the reference compounds with indices $i = \text{Li}_2\text{O}, \text{B}_2\text{O}_3, \text{and LiCl}$. The compositional parameters x_i are chosen such that the specific compound and the sum of the reference compounds have the same atomic composition.

Results for the convex hull diagram based on the ternary $\text{Li}_2\text{O}-\text{B}_2\text{O}_3-\text{LiCl}$ composition space is presented in Fig. 8. The energy difference of each stable phase was calculated according to Eq. (13) and is represented by a node on the diagram. For each node, its color and size represents the value and magnitude, respectively, of ΔU_{SL} . The computed values of ΔU_{SL} are enumerated in Table VIII in the Appendix B. Although the results show that $\text{Li}_5\text{B}_7\text{O}_{12.5}\text{Cl}$ is relatively more stable than $\text{Li}_4\text{B}_7\text{O}_{12}\text{Cl}$ in terms of decomposing into the three reference compounds $\text{Li}_2\text{O}, \text{B}_2\text{O}_3, \text{and LiCl}$, $\text{Li}_4\text{B}_7\text{O}_{12}\text{Cl}$ is unlikely to react without excess Li_2O . In other words, by controlling the weight fraction of precursor constituents, the results are consistent with the experimental findings that it is possible to synthesize crystals of $\text{Li}_4\text{B}_7\text{O}_{12}\text{Cl}$.

VI. MECHANISMS FOR LI ION MIGRATION

In Sec. III we established that the structures of both $\text{Li}_4\text{B}_7\text{O}_{12}\text{Cl}$ and $\text{Li}_5\text{B}_7\text{O}_{12.5}\text{Cl}$ have a significant number of natural interstitial sites available to Li ions. Within the conventional cell setting, for $\text{Li}_4\text{B}_7\text{O}_{12}\text{Cl}$ with 192 ions, there are 24 of these natural interstitial sites. Correspondingly for $\text{Li}_5\text{B}_7\text{O}_{12.5}\text{Cl}$ with 204 ions, there are 16 of these natural interstitial sites. Using both the nudged elastic band (NEB) approach [44–46] and molecular dynamics simulations, we can examine how these may or may not participate in Li ion diffusion.

A. The nudged elastic band simulations

Using the NEB method, we estimated the migration energies E_m of Li ion diffusion for several most likely paths in $\text{Li}_4\text{B}_7\text{O}_{12}\text{Cl}$ and $\text{Li}_5\text{B}_7\text{O}_{12.5}\text{Cl}$.

1. $\text{Li}_4\text{B}_7\text{O}_{12}\text{Cl}$

For the case of $\text{Li}_4\text{B}_7\text{O}_{12}\text{Cl}$, it is reasonable to speculate that the metastable b type site (based on the $R3c$ space group) may play an essential role in the course of Li ion transport as they are native interstitials in the simulation cell. Here host a type and metastable b type sites are all derived from the e type sites of the $F43c$ structure.

All calculations were carried out using the 192 ion conventional cell of the $R3c$ structure as visualized in Fig. 9. Figure 9a shows sites considered in this analysis, involving a natural interstitial at a meta-stable b site (labeled mb) and nearest neighbor host Li sites host a (labeled ha) and host b (labeled hb). Using the structural optimization algorithms in the QUANTUM ESPRESSO software we find that the direct migration of $hb \rightarrow mb$ is not stable, while the migration of $ha \rightarrow mb$ is metastable with an energy gain of 0.30 eV. Furthermore, we found that the host b type sites (hb) are the most stable positions for accommodating Li ions. Once such a site is vacant, the Li ion at adjacent host a site (ha) or metastable b site (mb) will immediately hop into this available position.

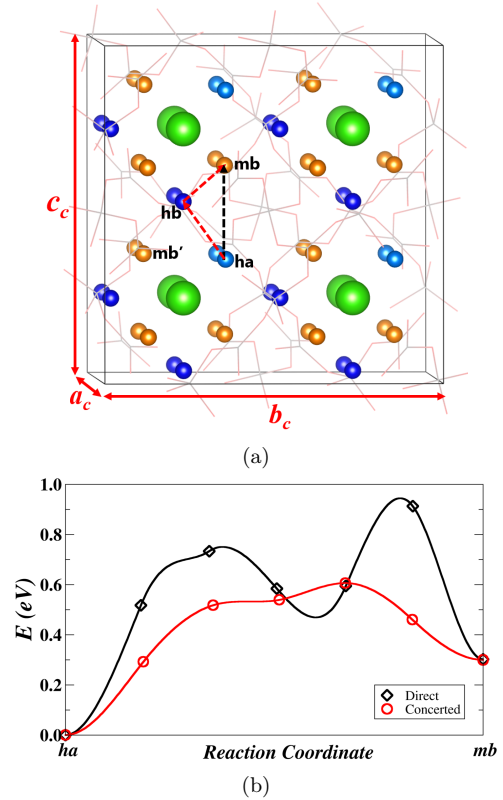


FIG. 9: (a) Ball and stick diagram of Li ion sites of $\text{Li}_4\text{B}_7\text{O}_{12}\text{Cl}$ with the migration path indicated with arrows and by labels (ha : host a site; hb : host b site; mb and mb' : metastable b sites). (b) NEB energy path diagram for the direct (black) and concerted (red) Li ion migration processes.

From these results, there are two possible migration paths. One possibility, called the “direct” hop, is the process $ha \rightarrow mb$. Another possibility, called the “concerted” hop involves the same final configuration but involves a concerted motion of $hb \rightarrow mb$ simultaneously with the motion of $ha \rightarrow hb$. These two paths were an-

alyzed using the NEB method with the corresponding migration energy diagrams shown in Fig. 9b.

By comparison, the concerted hop has migration energy E_a of 0.61 eV, lower by about 0.33 eV than the direct hop. Interestingly, the direct migration is found to be accompanied by a local minimum located near the third NEB image of the energy diagram. Further inspection revealed that, instead of hopping in the direction toward the mb site, the active Li ion originating from site ha , appears to be attracted by the host site hb and attempts to occupy this low-energy position by kicking the currently resting Li ion out to a metastable site labeled with mb' in the diagram, causing the special intermediate configuration with locally minimal energy. Because of the NEB algorithm in which the final state is well-defined, the intermediate configuration involving the mb' site is not realized in the direct hop simulation; the Li ion now at hb continues to move to site mb and the one at mb' also returns back to site hb . While for the concerted migration, the process consists of two simultaneous hopping events consisting of $hb \rightarrow mb$ and $ha \rightarrow hb$ as described before. We find that, within the NEB algorithm, the first hop progresses much faster than the second one. In other words, when the Li ion originating in the hb site jumps into the target position mb , the other host Li ion has just left its original position of site ha .

As discussed above, even in the direct Li ion migration between ha and mb , the participation of the third type site hb was observed. What the direct and the concerted migrations have in common is that the motions of the Li ions at the a type host sites ha will instantly affect the states of the Li ions at hb type sites, as they will be promptly stimulated to hop into an available metastable site in the vicinity. It is, therefore, reasonable to speculate that the concerted migration involving two distinct host sites and a metastable site dominates the Li ion transport in $\text{Li}_4\text{B}_7\text{O}_{12}\text{Cl}$.

2. $\text{Li}_5\text{B}_7\text{O}_{12.5}\text{Cl}$

For the case of $\text{Li}_5\text{B}_7\text{O}_{12.5}\text{Cl}$, the smallest distance between natural interstitial sites is greater than 4.30 Å, so the Li ion migration involving these sites is less likely. Consequently, it is speculated that a vacancy process may play a dominant role in Li ion transport. Each vacancy defect configuration is modeled by directly removing a Li ion from the host site while adding a compensating uniform charge of the opposite sign to the system.

It is found that the most efficient Li ion conduction path within the supercell consists of the relatively short hops between neighboring g type sites with a distance of 3.54 Å and those between adjacent g and e type sites [47] at a distance of 2.92 Å apart. One example of the smallest path unit is indicated by the labels on these three Li sites in Fig. 10a. Multiple energetically equivalent paths with such patterns expand in all directions, connecting to form continuous paths throughout the crystal.

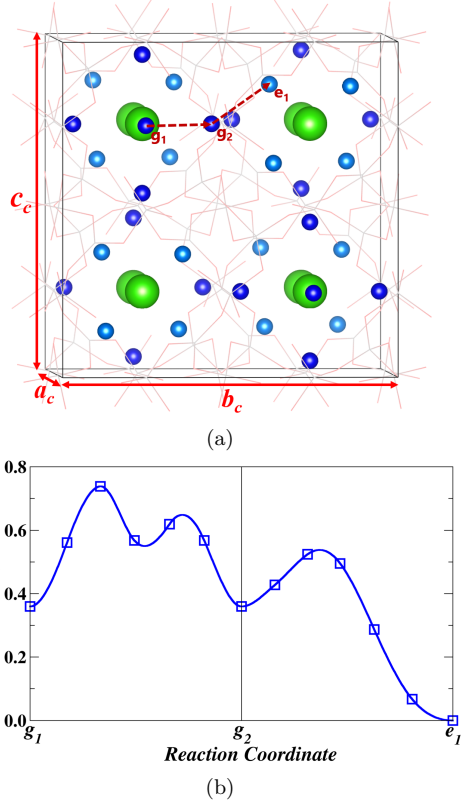


FIG. 10: (a) Ball and stick diagram of $\text{Li}_5\text{B}_7\text{O}_{12.5}\text{Cl}$ with the Li ions migration pathway indicated by labels and arrows. (b) NEB energy path diagram for this vacancy mechanism.

Figure 10b shows the corresponding NEB energy diagram with the zero of the energy was taken as the energy of the Li ion vacancy at a site of e type. It shows the vacancies g_1 and g_2 of the same g type have vacancy defect energy higher by about 0.36 eV than the e type vacancy. The overall migration energy E_m is determined by the maximum energy difference along the path which is $E_m = 0.75$ eV. Taking into account the contribution of the defect formation energy needed to produce a mobile Li ion, the activation energy E_a for Li ion conductivity is estimated to be 1.06 eV according to the relation $E_a = E_m + \frac{1}{2}E_f$. The high activation energy indicates that $\text{Li}_5\text{B}_7\text{O}_{12.5}\text{Cl}$ is expected to have poor Li ion conductivity.

B. Molecular dynamics simulation

The statistical behavior of Li ion diffusion in $\text{Li}_4\text{B}_7\text{O}_{12}\text{Cl}$ and $\text{Li}_5\text{B}_7\text{O}_{12.5}\text{Cl}$ was investigated using ab initio molecular dynamics (MD) simulation, which allows for directly simulating the dynamical diffusion of Li ions

in real-time. These simulations are likely to reveal more details of the ionic transport mechanisms. The simulations were carried out for a microcanonical NVE ensemble with a time integration step of $\Delta t = 2.4$ fs for conventional units cells of $\text{Li}_4\text{B}_7\text{O}_{12}\text{Cl}$ (containing 192 ions) and $\text{Li}_5\text{B}_7\text{O}_{12.5}\text{Cl}$ (containing 204 ions).

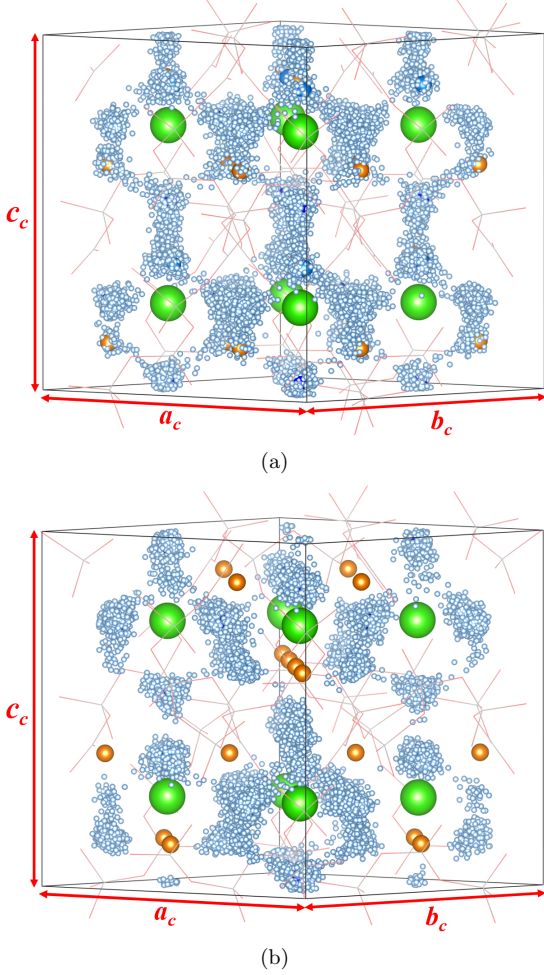


FIG. 11: Diagrams of MD simulations over $t = 50$ ps at intervals of $50\Delta t = 0.12$ ps for (a) $\text{Li}_4\text{B}_7\text{O}_{12}\text{Cl}$ at $\langle T \rangle = 1162$ K and (b) $\text{Li}_5\text{B}_7\text{O}_{12.5}\text{Cl}$ at $\langle T \rangle = 1171$ K. The little blue balls indicate the time-dependent positions of Li ions. The atomic positions of the initial configurations and natural vacancies are also shown, using the same color conventions as in Figs. 4b and 5b, respectively.

Figure 11 illustrates the examples of the migration patterns of Li ions during MD simulations in each material. For the case $\text{Li}_4\text{B}_7\text{O}_{12}\text{Cl}$, it is not surprising to note that the mb type native vacant sites, represented by brown balls in Fig. 11a, are frequently visited by the mobile

Li ions in the course of diffusion. Careful examination of this visualization from different viewpoints finds that there is no direct hopping between the host ha and mb type sites. Instead, the most efficient pathway for conducting Li ions is comprised of path segments between sites $hb \rightarrow mb$ and $ha \rightarrow hb$. For the $\text{Li}_5\text{B}_7\text{O}_{12.5}\text{Cl}$ case, as displayed in Fig. 11b, the fully presented Li ion positions of MD simulations share somewhat similarity with those of $\text{Li}_4\text{B}_7\text{O}_{12}\text{Cl}$ as the ionic conduction mainly occurs in the hollow cavity formed by robust B-O units. Different from the nearly continuous diffusion pathway observed in the $\text{Li}_4\text{B}_7\text{O}_{12}\text{Cl}$ cell, we can see clearly that the Li ions exhibit comparatively low mobility with most of them being trapped near their initial host sites. Besides, it seems that the interstitial defect sites, indicated by brown balls in the diagram, are not evolved in the Li ion diffusion process visualized in this simulation. Only a few Li ion hops take place between the neighboring host sites of g and e type which have a relatively shallow migration barrier energy as computed in the NEB analysis. However, those hopping events are localized and unable to achieve long-range conduction of Li ions. Generally, the MD simulation results on $\text{Li}_4\text{B}_7\text{O}_{12}\text{Cl}$ and $\text{Li}_5\text{B}_7\text{O}_{12.5}\text{Cl}$ are compatible with the NEB analysis in Sec. VIA.

To better analyze the molecular dynamics simulations, it is convenient to define a time-dependent site occupancy factor $f_s(t)$

$$f_s(t) = \frac{1}{N_s^{\text{Li}}} \sum_{i=1}^{N^{\text{Li}}} n_s^i(t), \quad i = 1, 2, \dots, N^{\text{Li}} \quad \text{and} \quad (14)$$

$$\sum_s N_s^{\text{Li}} = N^{\text{Li}}$$

where N^{Li} is the total number of Li ions in the simulation cell, s denotes the reference site type: host a , b , and metastable b for $\text{Li}_4\text{B}_7\text{O}_{12}\text{Cl}$, and host g , e , and metastable e for $\text{Li}_5\text{B}_7\text{O}_{12.5}\text{Cl}$. N_s^{Li} indicates the multiplicity number of site s based on the conventional lattice. (Note that the conventional unit cell of the $R3c$ structure has 4 times as many ions as the primitive cell discussed in Sec. III A.) At each time step t , the label of a Li ion is determined by the closest reference site relative to this ion's instantaneous position. The counter $n_s^i(t) = 1$ if the i -th Li ion has the shortest distance with the reference site s ; otherwise, $n_s^i(t) = 0$. Accordingly, $f_s(t)$ measures the occupation probability of s type site at t .

It is found that the curve of $f_s(t)$ is very noisy; as computed from the MD trajectories, the Li ion labels change rapidly. More conveniently, we can define a time-averaged site occupancy factor by integrating the instantaneous site occupancy over a time duration t

$$\bar{f}_s(t) = \frac{1}{t} \int_0^t f_s(t') dt'. \quad (15)$$

Figure 12a shows the plot of $\bar{f}_s(t)$ for distinct sites of $\text{Li}_4\text{B}_7\text{O}_{12}\text{Cl}$ in the rhombohedral structure, comparing

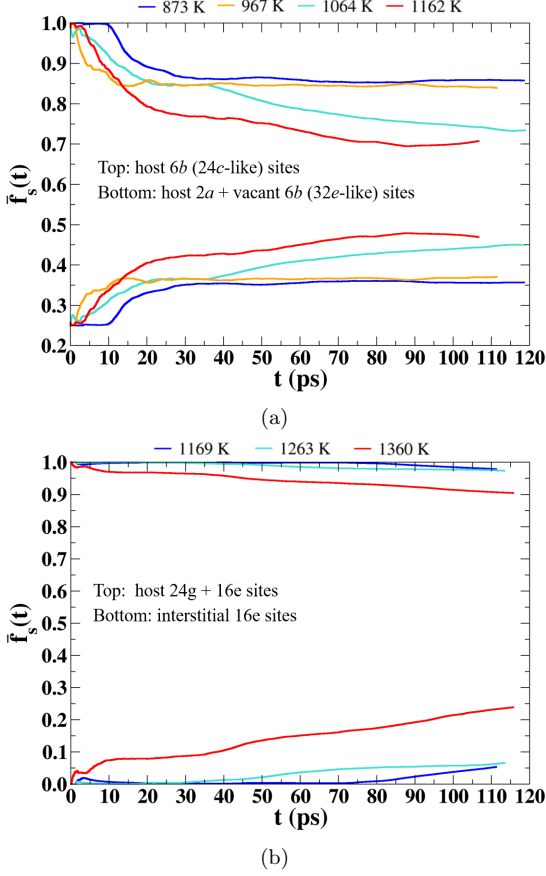


FIG. 12: Plots of $\bar{f}_s(t)$ as defined in Eq. (15) for (a) $\text{Li}_4\text{B}_7\text{O}_{12}\text{Cl}$ and (b) $\text{Li}_5\text{B}_7\text{O}_{12.5}\text{Cl}$. The subscript s of $f_s(t)$ denotes the reference site type as described in the text of each figure, using the Wyckoff labels of the $R3c$ and $F23$ structures as appropriate. The average temperature of each plot is listed in the legend.

results at various temperatures ranging from 900 to 1200 K. Note that $t = 0$ corresponds to the ground state configuration in which the $6b$ sites of the $R3c$ structure, mapped from the $24c$ type sites of the ideal $F43c$ model, are fully occupied, whereas the occupancy of the remaining Li sites, mapped from the $32e$ type of the cubic cell, is 25%. As time progresses, \bar{f}_s varies and tends to an asymptotic value at long times. It is also evident that the fractional occupancy of host $24c$ like sites decreases, and that of the $32e$ like sites increases at higher temperatures. In other words, at low temperatures the Li ions have a preference to reside in the most energetically favorable positions of $6b$ type. This phenomenon is consistent with what the experiment observed upon heating from the room temperature α phase to the high-temperature phases. Since for this particular material, the MD temperatures are necessary to be high enough to

overcome the migration barrier and therefore to achieve conduction of Li ions, the simulated value of site occupancy factor for the experimentally reported phase transition temperatures 310 K for α to β , and 348 K for β to γ are unattainable. Although the exact functional relationship between the temperature and the site fractional occupancy is unknown/undefined, the calculated $\bar{f}_s(t)$ curves appear to be qualitatively consistent with temperature dependent X-ray analysis reported in Ref. 8.

For the case of $\text{Li}_5\text{B}_7\text{O}_{12.5}\text{Cl}$ with the calculated $\bar{f}_s(t)$ displayed in Fig. 12b, we find that the role of the interstitial defects is nontrivial only at simulation temperature above 1300 K. Generally, most hop events occur between the host sites via vacancy diffusion process. While optimizing the electrolyte properties of $\text{Li}_5\text{B}_7\text{O}_{12.5}\text{Cl}$ is beyond the scope of the present work, it is proposed that, in view of the NEB analysis in Sec. VIA, the possible way to enhance the ionic conductivity of $\text{Li}_5\text{B}_7\text{O}_{12.5}\text{Cl}$ is by introducing vacancy defects in the lattice.

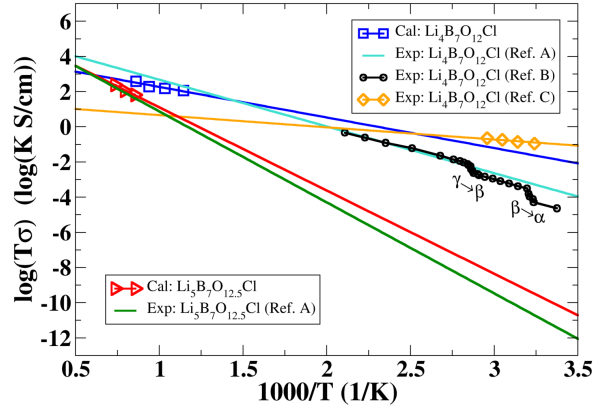


FIG. 13: Plots of simulated ionic conductivities of $\text{Li}_4\text{B}_7\text{O}_{12}\text{Cl}$ and $\text{Li}_5\text{B}_7\text{O}_{12.5}\text{Cl}$, together with the available experimental values obtained by digitizing the published graphs from Refs. 6 (A), 8 (B), and 12 (C).

All straight lines represent least squares fits of the $\log(T\sigma)$ vs. $1000/T$ data.

The ionic conductivity σ , a measure of the ability of a material to conduct ions, is related to the tracer diffusion coefficient D_{tr} according to the Nernst-Einstein relationship

$$\sigma(T) = \rho q^2 \frac{D_{tr}(T)}{k_B T H_r}. \quad (16)$$

Here ρ represents the average number density of mobile Li ions in the simulation cell, k_B denotes the Boltzmann constant, H_r , known as the Haven ratio [48], is commonly used to access the co-operative motion of ions. In this work, we make the simplifying assumption that $H_r = 1$. $D_{tr}(T)$ is directly calculated from Li ion displacements of the MD simulations and follows an Arrhenius behavior

$$D_{tr}(T) = D_0 e^{-E_a^{\text{MD}}/k_B T} \quad (17)$$

Here D_0 is the diffusivity at $T \rightarrow \infty$. E_a^{MD} , the activation energy of Li ion diffusion, is usually deduced from the slope of the $\log(T\sigma)$ versus $1/T$ plot according to Eqs. (16) and (17).

For the $\text{Li}_5\text{B}_7\text{O}_{12.5}\text{Cl}$ material, the calculated results on the perfect crystal are not far off from the experimental measurements on polycrystalline samples [6]. However, the higher activation barrier and the extremely low ionic conductivity at room temperature indicate that this material is an extremely poor ionic conductor. For the $\text{Li}_4\text{B}_7\text{O}_{12}\text{Cl}$ material, the simulations, represented by blue points and straight line, agrees very well with the experimental data reported recently by Tan *et al.* [12], in the room temperature range. At high temperatures, the two early measurements [6, 8] represented in turquoise and black, respectively, show a range of values that are roughly in the same range of the MD simulation results. As is evident by two abrupt conductivity discontinuities at about 310 K and 350 K, the work in Ref. 8 was able to identify the phase transitions between two high-temperature cubic phases, and a low-temperature rhombohedral phase.

VII. SUMMARY AND CONCLUSIONS

Lithium boracites are high symmetry materials with intriguing properties from both theoretical and technological perspectives. In this work, we show how group theory analysis explains many of the properties of both $\text{Li}_4\text{B}_7\text{O}_{12}\text{Cl}$ and $\text{Li}_5\text{B}_7\text{O}_{12.5}\text{Cl}$. Detailed first principles simulations are able to provide a more complete picture of structural, stability, and ionic conductivity properties, consistent with recent experimental evidence [12, 15] that $\text{Li}_4\text{B}_7\text{O}_{12}\text{Cl}$ and related materials are technologically promising as stable electrolytes for all-solid-state batteries with good Li ion conductivity.

These materials are characterized by a boron oxide framework consisting of tetragonal BO_4 and triangular BO_3 components forming a regular void structure containing Li and Cl ions. The reference space group symmetry [1] of these materials is the face centered cubic structure $F\bar{4}3c$ (No. 219) which was identified as the high temperature phase $\gamma\text{-Li}_4\text{B}_7\text{O}_{12}\text{Cl}$ by Jeitschko and co-workers [8]. From those experimental results at lower temperature, which found $32e$ sites to be 25% occupied by Li ions, our first principles optimization studies found the ground state structure to be face centered rhombohedral, having the space group $R3c$ (No. 161), with the rhombohedral angle very close to the cubic angle. Interestingly, the space group $R3c$ is a subgroup of the space group $F\bar{4}3c$ and the relationships between the Wyckoff labels of the two space groups are given in Table VII. Even more interestingly, the group theory analysis shows how the Li ions which occupy 25% of the $32e$ sites at low temperature are associated with 8 sites with Wyckoff label a in the conventional cell of the $R3c$ structure, while the unoccupied 75% are associated with 24 sites with Wyck-

off label b in the conventional cell of the $R3c$ structure. In this case, the energetic splitting of the site symmetry is computed to be very small, close to or within the computational error of the density functional calculations themselves. While group theory analysis predicts the natural interstitial structure of $\text{Li}_4\text{B}_7\text{O}_{12}\text{Cl}$, first principles nudged elastic band and molecular dynamics simulations are needed to study the Li ion conductivity properties of this material. Both of these simulation studies show that the natural interstitial sites are occupied at higher temperatures and that the process involves a concerted motion of Li ions at two neighboring sites. While the molecular dynamics simulations are performed at quite high temperatures in order to generate results with significant statistics, the quantitative results assuming $H_r = 1$, are in reasonable agreement with experimental measurements as shown in Fig. 13. The molecular dynamics results were also analyzed in terms the site occupancies of the host and interstitial Li ion lattice sites according to Eqs. (14) and (15), showing qualitative agreement with experiment.

For analyzing $\text{Li}_5\text{B}_7\text{O}_{12.5}\text{Cl}$, group theory analysis also plays an important role in explaining its properties as a very poor ionic conductor. In this case, only one crystal structure has been reported [16] with the face centered cubic space group $F32$ (No. 196), and this is consistent with the computational results. Interestingly, the $F32$ space group is also a subgroup of the $F\bar{4}3c$ structure and the relationships between the Wyckoff labels of the two space groups is given in Table III. In this case, the $F32$ space group analyzed in the conventional cell has 48 basic elements while the $F\bar{4}3c$ has 96 basic elements. This means that some of the Wyckoff multiplicities and labels of the $F\bar{4}3c$ structure are split into two Wyckoff multiplicities and labels in the $F32$ structure. Additionally, $\text{Li}_5\text{B}_7\text{O}_{12.5}\text{Cl}$ contains 4 extra Li_2O units per conventional cell compared with $\text{Li}_4\text{B}_7\text{O}_{12}\text{Cl}$. Comparing the structural diagrams of $\text{Li}_4\text{B}_7\text{O}_{12}\text{Cl}$ in Fig. 4b and $\text{Li}_5\text{B}_7\text{O}_{12.5}\text{Cl}$ in Fig. 5b, we see evidence of the lower symmetry of the $F32$ structure compared with that of the $F\bar{4}3c$. For $\text{Li}_5\text{B}_7\text{O}_{12.5}\text{Cl}$, we see that there are 16 natural interstitial sites in the conventional unit cell. Unfortunately, close examination finds that the placement and energetics associated with these interstitial sites does not result in Li ion migration. Further study using first principles nudged elastic band and molecular dynamics simulations confirm the conclusion that $\text{Li}_5\text{B}_7\text{O}_{12.5}\text{Cl}$ has very poor Li ion conductivity, a result which is consistent with experiment.

Analysis of the phonon spectra in Sec. IV show that these Li boracites are dynamically stable and analysis of the convex hull based on Li_2O , B_2O_3 , and LiCl building blocks in Sec. V show that they are chemically stable as well.

As an extended study of the Li boracite systems, our preliminary simulations suggest that the Li ion conductivity can be enhanced by ionic substitutions to form analog compounds such as $\text{Li}_4\text{Al}_3\text{B}_4\text{O}_{12}\text{Cl}$, $\text{Li}_4\text{B}_7\text{S}_{12}\text{Cl}$,

and $\text{Li}_4\text{Al}_3\text{B}_4\text{S}_{12}\text{Cl}$. In the near future, we plan to investigate the properties of those related materials in more detail.

Appendix A: Details of the relationship between the $R3c$ and $F43c$ space group

It is most convenient to compare the structures using the primitive cell settings. The Wyckoff positions for the $R3c$ (No. 161) system is given in Table V based on the rhombohedral structure.

The Wyckoff positions for the $F43c$ (No. 219) system is given in Table VI based on the primitive cell of the face centered cubic structure.

Note that since the $R3c$ and $F43c$ space groups do not have a center of inversion, the set of fractional coordinates $\{(x, y, z)\}$ and the set $\{(-x, -y, -z)\}$ describe equivalent but not identical crystals.

From the results of Tables VI and V, it is possible to map the relationships between the Wyckoff labels of the $F43c$ and $R3c$ space groups as listed in Table VII.

TABLE V: Wyckoff labels and fractional coordinates (x, y, z) for Group $R3c$ (No. 161) in its primitive cell setting. In this case (x, y, z) refers to the primitive lattice coordinates (x_p, y_p, z_p) .

Mul.	Lab.	Fractional coordinates
6	b	(x, y, z) (z, x, y) (y, z, x) $(z + \frac{1}{2}, y + \frac{1}{2}, x + \frac{1}{2})$ $(y + \frac{1}{2}, x + \frac{1}{2}, z + \frac{1}{2})$ $(x + \frac{1}{2}, z + \frac{1}{2}, y + \frac{1}{2})$
2	a	(z, z, z) $(z + \frac{1}{2}, z + \frac{1}{2}, z + \frac{1}{2})$

TABLE VI: Wyckoff labels and fractional coordinates for Group $F43c$ (No. 219). In this case, the listed fractional coordinates refers to the primitive lattice (x_p, y_p, z_p) expressed in terms of a general point (x, y, z) of the conventional lattice.

Mul.	Lab.	Fractional coordinates
24	h	$(x + y - z, -x + y + z, x - y + z)$ $(z + x - y, -z + x + y, z - x + y)$ $(y + z - x, -y + z + x, y - z + x)$ $(z + y - x + \frac{1}{2}, -z + y + x + \frac{1}{2}, z - y + x + \frac{1}{2})$ $(y + x - z + \frac{1}{2}, -y + x + z + \frac{1}{2}, y - x + z + \frac{1}{2})$ $(x + z - y + \frac{1}{2}, -x + z + y + \frac{1}{2}, x - z + y + \frac{1}{2})$ $(-x - y - z, x - y + z, -x + y + z)$ $(z - x + y, -z - x - y, z + x - y)$ $(-y + z + x, y + z - x, -y - z - x)$ $(z - y + x + \frac{1}{2}, -z - y - x + \frac{1}{2}, z + y - x + \frac{1}{2})$ $(-y - x - z + \frac{1}{2}, y - x + z + \frac{1}{2}, -y + x + z + \frac{1}{2})$ $(-x + z + y + \frac{1}{2}, x + z - y + \frac{1}{2}, -x - z - y + \frac{1}{2})$ $(-x + y + z, x + y - z, x - y - z)$ $(-z - x - y, z - x + y, -z + x + y)$ $(y - z + x, -y - z - x, y + z - x)$ $(-z + y + x + \frac{1}{2}, z + y - x + \frac{1}{2}, -z - y - x + \frac{1}{2})$ $(y - x + z + \frac{1}{2}, -y - x - z + \frac{1}{2}, y + x - z + \frac{1}{2})$ $(-x - z - y + \frac{1}{2}, x - z + y + \frac{1}{2}, -x + z + y + \frac{1}{2})$ $(x - y + z, -x - y - z, x + y - z)$ $(-z + x + y, z + x - y, -z - x - y)$ $(-y - z - x, y - z + x, -y + z + x)$ $(-z - y - x + \frac{1}{2}, z - y + x + \frac{1}{2}, -z + y + x + \frac{1}{2})$ $(-y + x + z + \frac{1}{2}, y + x - z + \frac{1}{2}, -y - x - z + \frac{1}{2})$ $(x - z + y + \frac{1}{2}, -x - z - y + \frac{1}{2}, x + z - y + \frac{1}{2})$
12	g	$(x, x, -x + \frac{1}{2})$ $(x, -x + \frac{1}{2}, x)$ $(-x + \frac{1}{2}, x, x)$ $(x + \frac{1}{2}, x + \frac{1}{2}, -x)$ $(x + \frac{1}{2}, -x, x + \frac{1}{2})$ $(-x, x + \frac{1}{2}, x + \frac{1}{2})$ $(-x, -x, x + \frac{1}{2})$ $(-x, x + \frac{1}{2}, -x)$ $(x + \frac{1}{2}, -x, -x)$ $(-x + \frac{1}{2}, -x + \frac{1}{2}, x)$ $(-x + \frac{1}{2}, x, -x + \frac{1}{2})$ $(x, -x + \frac{1}{2}, -x + \frac{1}{2})$
12	f	$(x, x, -x)$ $(x, -x, x)$ $(-x, x, x)$ $(x + \frac{1}{2}, x + \frac{1}{2}, -x + \frac{1}{2})$ $(x + \frac{1}{2}, -x + \frac{1}{2}, x + \frac{1}{2})$ $(-x + \frac{1}{2}, x + \frac{1}{2}, x + \frac{1}{2})$ $(-x, -x, x)$ $(-x, x, -x)$ $(x, -x, -x)$ $(-x + \frac{1}{2}, -x + \frac{1}{2}, x + \frac{1}{2})$ $(-x + \frac{1}{2}, x + \frac{1}{2}, -x + \frac{1}{2})$ $(x + \frac{1}{2}, -x + \frac{1}{2}, -x + \frac{1}{2})$
8	e	(x, x, x) $(x + \frac{1}{2}, x + \frac{1}{2}, x + \frac{1}{2})$ $(-3x, x, x)$ $(-3x + \frac{1}{2}, x + \frac{1}{2}, x + \frac{1}{2})$ $(x, -3x, x)$ $(x + \frac{1}{2}, -3x + \frac{1}{2}, x + \frac{1}{2})$ $(x, x, -3x)$ $(x + \frac{1}{2}, x + \frac{1}{2}, -3x + \frac{1}{2})$
6	d	$(\frac{1}{4}, \frac{3}{4}, \frac{1}{4})$ $(\frac{3}{4}, \frac{1}{4}, \frac{3}{4})$ $(\frac{3}{4}, \frac{1}{4}, \frac{1}{4})$ $(\frac{1}{4}, \frac{3}{4}, \frac{3}{4})$ $(\frac{1}{4}, \frac{1}{4}, \frac{3}{4})$ $(\frac{3}{4}, \frac{3}{4}, \frac{1}{4})$ $(\frac{1}{4}, \frac{1}{4}, \frac{1}{4})$ $(\frac{3}{4}, \frac{3}{4}, \frac{3}{4})$
6	c	$(\frac{1}{2}, 0, 0)$ $(0, \frac{1}{2}, 0)$ $(0, 0, \frac{1}{2})$ $(\frac{1}{2}, \frac{1}{2}, 0)$ $(0, \frac{1}{2}, \frac{1}{2})$ $(\frac{1}{2}, 0, \frac{1}{2})$
2	b	$(\frac{1}{4}, \frac{1}{4}, \frac{1}{4})$ $(\frac{3}{4}, \frac{3}{4}, \frac{3}{4})$
2	a	$(0, 0, 0)$ $(\frac{1}{2}, \frac{1}{2}, \frac{1}{2})$

TABLE VII: Mapping between the multiplicities and Wyckoff labels between the $F43c$ and $R3c$ space groups.

$F43c$	$R3c$
24h	$4 \times 6b$
12g	$2 \times 6b$
12f	$2 \times 6b$
8e	$2a + 6b$
6d	$6b$
6c	$6b$
2b	$2a$
2a	$2a$

Appendix B: Details of the convex hull analysis

In this appendix the energy differences from Eq. (13), used to make the convex hull diagram in Fig. 8 are listed in Table VIII.

TABLE VIII: Computed energy differences according to Eq. (13) for reactions indicated by the first column. All energy values in eV units, corresponding to those on the convex hull shown in Fig. 8, are evaluated from the static lattice analysis.

Reaction: $R \rightarrow P$	ΔU_{SL}
$\text{Li}_5\text{B}_7\text{O}_{12.5}\text{Cl} \rightarrow 2 \text{Li}_2\text{O}^{\text{a}} + 7/2 \text{B}_2\text{O}_3^{\text{b}} + \text{LiCl}^{\text{c}}$	-4.56
$\text{Li}_4\text{B}_7\text{O}_{12}\text{Cl} \rightarrow 3/2 \text{Li}_2\text{O} + 7/2 \text{B}_2\text{O}_3 + \text{LiCl}$	-3.53
$\text{LiBO}_2^{\text{d}} \rightarrow 1/2 \text{Li}_2\text{O} + 1/2 \text{B}_2\text{O}_3$	-0.93
$\text{Li}_2\text{B}_4\text{O}_7^{\text{e}} \rightarrow \text{Li}_2\text{O} + 2 \text{B}_2\text{O}_3$	-2.12
$\text{Li}_3\text{BO}_3^{\text{f}} \rightarrow 3/2 \text{Li}_2\text{O} + 1/2 \text{B}_2\text{O}_3$	-1.51
$\text{Li}_3\text{B}_7\text{O}_{12}^{\text{g}} \rightarrow 3/2 \text{Li}_2\text{O} + 7/2 \text{B}_2\text{O}_3$	-3.36
$\text{Li}_6\text{B}_4\text{O}_9^{\text{h}} \rightarrow 3 \text{Li}_2\text{O} + 2 \text{B}_2\text{O}_3$	-3.73

^a Cubic with Space Group $Fm\bar{3}m$ (No. 225); from Ref. 49.

^b Orthorhombic with Space Group $Cmc2_1$ (No. 36); from Ref. 50.

^c Cubic with Space Group $Fm\bar{3}m$ (No. 225).

^d Tetragonal (γ - LiBO_2) with Space Group $I4_2d$ (No. 122); from Ref. 51.

^e Tetragonal with Space Group $I4_1cd$ (No. 110); from Ref. 52.

^f Monoclinic with Space Group $P2_1/c$ (No. 14); from Ref. 53.

^g Triclinic with Space Group $P\bar{1}$ (No. 2); from Ref. 54.

^h Monoclinic with Space Group $P2_1/c$ (No. 14); from Ref. 55.

ACKNOWLEDGMENTS

This work was supported by NSF grant DMR-1940324. Computations were performed on the Wake Forest University DEAC cluster, a centrally managed resource with support provided in part by the University. Helpful discussions with Dr. Zachary Hood (Argonne National Laboratory) and computer assistance from Dr. Sean Anderson (DEAC Cluster administrator, Wake Forest University) are gratefully acknowledged.

-
- [1] M. I. Aroyo, J. M. Perez-Mato, D. Orobengoa, E. Tasci, G. De La Flor, and A. Kirov, *Bulgarian Chemical Communications* **43**, 183 (2011), available on the website <http://www.cryst.ehu.es/>.
- [2] S. Sueno, J. R. Clark, J. J. Papike, and J. A. Konnert, *American Mineralogist* **58**, 691 (1973).
- [3] A. Lévassieur, C. Fouassier, and P. Hagenmuller, *Materials Research Bulletin* **6**, 15 (1971).
- [4] M. A. Lévassieur and D. J. Lloyd, *Journal of Solid State Chemistry* **8**, 318 (1973).
- [5] J.-M. Réau, A. Lévassieur, G. Magniez, and B. Calès, *Materials Research Bulletin* **11**, 1087 (1976).
- [6] B. Calès, A. Lévassieur, C. Fouassier, J. M. Réau, and P. Hagenmuller, *Solid State Communications* **24**, 323 (1977).
- [7] W. Jeitschko and T. A. Bither, *Zeitschrift für Naturforschung B* **27b**, 1423 (1972).
- [8] W. Jeitschko, T. A. Bither, and P. E. Bierstedt, *Acta Crystallographica Section B* **33**, 2767 (1977), detailed crystal parameters associated with this work are available as cif files from various crystallography databases.
- [9] K. Byrappa, K. V. K. Shekar, and R. Rodriguez-Clemente, *Journal of Materials Research* **8**, 2319 (1993).
- [10] T. Nagase, K. Sakane, and H. Wada, *Journal of Sol-Gel Science and Technology* **13**, 223 (1998).
- [11] Y. Ikeda, T. Hiraoka, and S. Ohta, *Solid State Ionics* **175**, 261 (2004).
- [12] D. Tan, F. Wang, T. Pietsch, M. A. Grasser, T. Doert, and M. Ruck, *ACS Applied Energy Materials* **2**, 5140 (2019).
- [13] N. I. Sorokin, *Physics of the Solid State* **57**, 314 (2015).
- [14] K. Kajihara, N. Tezuka, M. Shoji, J. Wakasugi, H. Munakata, and K. Kanamura, *Bulletin of the Chemical Society of Japan* **90**, 1279 (2017).
- [15] M. Saito, H. Arima, M. Shoji, Y. Kizuki, H. Munakata, K. Kanamura, and K. Kajihara, *Journal of The Electrochemical Society* **168**, 040524 (2021).
- [16] M. Vlasse, A. Lévassieur, and P. Hagenmuller, *Solid State Ionics* **2**, 33 (1981).
- [17] N. Tezuka, Y. Okawa, K. Kajihara, and K. Kanamura, *Journal of the Ceramic Society of Japan* **125**, 348 (2017).
- [18] P. Hohenberg and W. Kohn, *Physical Review* **136**, B864 (1964).
- [19] W. Kohn and L. J. Sham, *Physical Review* **140**, A1133 (1965).
- [20] P. Giannozzi, S. De Gironcoli, P. Pavone, and S. Baroni, *Physical Review B* **43**, 7231 (1991).
- [21] X. Gonze, *Phys. Rev. B* **55**, 10337 (1997).
- [22] X. Gonze and C. Lee, *Phys. Rev. B* **55**, 10355 (1997).
- [23] S. Baroni, S. De Gironcoli, A. Dal Corso, and P. Giannozzi, *Reviews of Modern Physics* **73**, 515 (2001).
- [24] P. Giannozzi and S. Baroni, in *Handbook of Materials Modeling*, edited by S. Yip (Springer, 2005) pp. 195–214.

- [25] P. E. Blöchl, Phys. Rev. B **50**, 17953 (1994).
- [26] J. P. Perdew, A. Ruzsinszky, G. I. Csonka, O. A. Vydrov, G. E. Scuseria, L. A. Constantin, X. Zhou, and K. Burke, Phys. Rev. Lett. **100**, 136406 (2008).
- [27] N. A. W. Holzwarth, A. R. Tackett, and G. E. Matthews, Computer Physics Communications **135**, 329 (2001), available from the website <http://pwpaw.wfu.edu>.
- [28] X. Gonze, F. Jollet, F. A. Araujo, D. Adams, B. Amador, T. Applencourt, C. Audouze, J.-M. Beuken, J. Bieder, A. Bokhanchuk, E. Bousquet, F. Bruneval, D. Caliste, M. Côté, F. Dahm, F. D. Pieve, M. Delaveau, M. D. Gennaro, B. Dorado, C. Espejo, G. Geneste, L. Genovese, A. Gerossier, M. Giantomassi, Y. Gillet, D. R. Hamann, L. He, G. Jomard, J. L. Janssen, S. L. Roux, A. Levitt, A. Lherbier, F. Liu, I. Lukačević, A. Martin, C. Martins, M. J. T. Oliveira, S. Poncé, Y. Pouillon, T. Rangel, G.-M. Rignanese, A. H. Romero, B. Rousseau, O. Rubel, A. A. Shukri, M. Stankovski, M. Torrent, M. J. V. Setten, B. V. Troeye, M. J. Verstraete, D. Waroquiers, J. Wiktor, B. Xu, A. Zhou, and J. W. Zwanziger, Computer Physics Communications **205**, 106 (2016), available at the website <https://www.abinit.org>.
- [29] X. Gonze, B. Amador, G. Antonius, F. Arnardi, L. Baguet, J.-M. Beuken, J. Bieder, F. Bottin, J. Bouchet, E. Bousquet, N. Brouwer, F. Bruneval, G. Brunin, T. Cavignac, J.-B. Charraud, W. Chen, M. Côté, S. Cottenier, J. Denier, G. Geneste, P. Ghosez, M. Giantomassi, Y. Gillet, O. Gingras, D. R. Hamann, G. Hautier, X. He, N. Helbig, N. Holzwarth, Y. Jia, F. Jollet, W. Lafargue-Dit-Hauret, K. Lejaeghere, M. A. L. Marques, A. Martin, C. Martins, H. P. C. Miranda, F. Naccarato, K. Persson, G. Petretto, V. Planes, Y. Pouillon, S. Prokhorenko, F. Ricci, G.-M. Rignanese, A. H. Romero, M. M. Schmitt, M. Torrent, M. J. van Setten, B. V. Troeye, M. J. Verstraete, G. Zerah, and J. W. Zwanziger, Comput. Phys. Commun. **248**, 107042 (2020), available from the website <https://www.abinit.org/>.
- [30] P. Giannozzi, O. Andreussi, T. Brumme, O. Bunau, M. Buongiorno Nardelli, M. Calandra, R. Car, C. Cavazzoni, D. Ceresoli, M. Cococcioni, N. Colonna, I. Carnimeo, A. Dal Corso, S. de Gironcoli, P. Delugas, R. A. DiStasio, A. Ferretti, A. Floris, G. Fratesi, G. Fugallo, R. Gebauer, U. Gerstmann, F. Giustino, T. Gorni, J. Jia, M. Kawamura, H.-Y. Ko, A. Kokalj, E. Küçükbenli, M. Lazzeri, M. Marsili, N. Marzari, F. Mauri, N. L. Nguyen, H.-V. Nguyen, A. Otero-de-la-Roza, L. Paulatto, S. Poncé, D. Rocca, R. Sabatini, B. Santra, M. Schlipf, A. P. Seitsonen, A. Smogunov, I. Timrov, T. Thonhauser, P. Umari, N. Vast, X. Wu, and S. Baroni, Journal of Physics: Condensed Matter **29**, 465901 (2017), available from the website <http://www.quantum-espresso.org>.
- [31] P. Giannozzi, O. Basergio, P. Bonfà, D. Brunato, R. Car, I. Carnimeo, C. Cavazzoni, S. de Gironcoli, P. Delugas, F. Ferrari Ruffino, A. Ferretti, N. Marzari, I. Timrov, A. Urru, and S. Baroni, The Journal of Chemical Physics **152**, 154105 (2020), available from the website quantum-espresso.org.
- [32] A. Kokalj, Computational Materials Science **28**, 155 (2003), code available at the website <http://www.xcrysden.org>.
- [33] K. Momma and F. Izumi, Applied Crystallography **44**, 1272 (2011), code available from the website <http://jp-minerals.org/vesta/en/>.
- [34] H. T. Stokes and D. M. Hatch, J. Appl. Cryst. **38**, 237 (2008), available from the webpage <http://iso.byu.edu/iso/isotropy.php>.
- [35] C. F. Macrae, I. Sovago, S. J. Cottrell, P. T. A. Galek, P. McCabe, E. Pidcock, M. Platings, G. P. Shields, J. S. Stevens, M. Towler, and P. A. Wood, Journal of Applied Crystallography **53**, 226 (2020).
- [36] We note that the lattice constants and rhombohedral angle found in our optimization studies is slightly dependent on initial configuration and also the results differ slightly in the QUANTUM ESPRESSO and ABINIT codes. We believe that these differences are due to the shallow nature of the potential energy surface of this system near equilibrium. However, the reported results are expected to be reliable within the expected overall error of calculations of this type of ± 0.001 eV per formula unit.
- [37] For example, in the conventional cell setting of the $F\bar{4}3c$ structure, it is possible to generate a $F\bar{4}3c$ structure by placing identical atoms at $48h$ sites generated with coordinates (x, y, z) and an additional $48h$ sites generated with coordinates $(y + \frac{1}{2}, x + \frac{1}{2}, z + \frac{1}{2})$.
- [38] Y. Hinuma, G. Pizzi, Y. Kumagai, F. Oba, and I. Tanaka, Computational Materials Science **128**, 140 (2017).
- [39] Y. Li, Z. D. Hood, and N. A. W. Holzwarth, Phys. Rev. Materials **4**, 045406 (2020).
- [40] Y. Li, Z. Hood, and N. A. W. Holzwarth, Physical Review Materials **5**, 085403 (2021).
- [41] T. W. D. Farley, W. Hayes, S. Hull, M. T. Hutchings, and M. Vrtis, Journal of Physics: Condensed Matter **3**, 4761 (1991).
- [42] D. D. Lee, J. H. Choy, and J. K. Lee, Journal of Phase Equilibria **13**, 365 (1992).
- [43] S. P. Ong, L. Wang, B. Kang, and G. Ceder, Chemistry of Materials **20**, 1798 (2008).
- [44] H. Jónsson, G. Mills, and K. W. Jacobsen, in *Classical and Quantum Dynamics in Condensed Phase Simulations*, edited by B. J. Berne, G. Ciccotti, and D. F. Coker (World Scientific, Singapore, 1998) pp. 385–404.
- [45] G. Henkelman, B. P. Uberuaga, and H. Jónsson, J. Chem. Phys. **113**, 9901 (2000).
- [46] G. Henkelman and H. Jónsson, J. Chem. Phys. **113**, 9978 (2000).
- [47] Here we are using the Wyckoff labels for the $F23$ space group as described in Table III.
- [48] Y. Haven and B. Verkerk, Physics and chemistry of glasses **6**, 38 (1965).
- [49] T. W. D. Farley, W. Hayes, S. Hull, M. T. Hutchings, and M. Vrtis, Journal of Physics: Condensed Matter **3**, 4761 (1991).
- [50] C. T. Prewitt and R. D. Shannon, Acta Crystallographica Section B **24**, 869 (1968).
- [51] M. Marezio and J. P. Remeika, The Journal of Chemical Physics **44**, 3348 (1966), publisher: American Institute of Physics.
- [52] J. Krogh-Moe, Acta Crystallographica **15**, 190 (1962).
- [53] V. F. Stewner, Acta Crystallographica Section B **27**, 904 (1971).
- [54] A. Jiang, S. Lei, Q. Huang, T. Chen, and D. Ke, Acta Crystallographica Section C **46**, 1999 (1990).
- [55] G. Rousse, B. Baptiste, and G. Lelong, Inorganic Chemistry **53**, 6034 (2014), publisher: American Chemical Society.

Part 3

References

References

- [1] Mani Pujitha Illa, Mudrika Khandelwal, and Chandra Shekhar Sharma. Bacterial cellulose-derived carbon nanofibers as anode for lithium-ion batteries. *Emergent Materials*, 1(3):105–120, December 2018.
- [2] Noriaki Kamaya, Kenji Homma, Yuichiro Yamakawa, Masaaki Hirayama, Ryoji Kanno, Masao Yonemura, Takashi Kamiyama, Yuki Kato, Shigenori Hama, Koji Kawamoto, and Akio Mitsui. A lithium superionic conductor. *Nature Materials*, 10(9):682–686, September 2011.
- [3] Kavish Kaup, Abdeljalil Assoud, Jue Liu, and Linda F. Nazar. Fast li-ion Conductivity in Superadamantanoid Lithium Thioborate Halides. *Angewandte Chemie International Edition*, 60(13):6975–6980, March 2021.
- [4] M. Stanley Whittingham. Electrical energy storage and intercalation chemistry. *Science*, 192(4244):1126–1127, 1976.
- [5] K. Mizushima, P. C. Jones, P. J. Wiseman, and J. B. Goodenough. Li_xCoO_2 ($0 < x \leq 1$): A new cathode material for batteries of high energy density. *Solid State Ionics*, 3-4:171–174, August 1981.
- [6] Akira Yoshino, Kenichi Sanechika, and Takayuki Nakajima. Secondary battery, u.s. patent (us4668595a), May 1987.

- [7] Kazunori Ozawa. Lithium-ion rechargeable batteries with LiCoO₂ and carbon electrodes: the LiCoO₂/C system. *Solid State Ionics*, 69(3):212–221, August 1994.
- [8] Kang Xu. Nonaqueous Liquid Electrolytes for Lithium-Based Rechargeable Batteries. *Chemical Reviews*, 104(10):4303–4418, October 2004.
- [9] Eliana Quartarone and Piercarlo Mustarelli. Electrolytes for solid-state lithium rechargeable batteries: recent advances and perspectives. *Chemical Society Reviews*, 40(5):2525, 2011.
- [10] Cheng Jiang, Huiqiao Li, and Chengliang Wang. Recent progress in solid-state electrolytes for alkali-ion batteries. *Science Bulletin*, 62(21):1473–1490, November 2017.
- [11] Lei Fan, Shuya Wei, Siyuan Li, Qi Li, and Yingying Lu. Recent Progress of the Solid-State Electrolytes for High-Energy Metal-Based Batteries. *Advanced Energy Materials*, 8(11):1702657, 2018.
- [12] Seong Jin An, Jianlin Li, Claus Daniel, Debasish Mohanty, Shrikant Nagpure, and David L. Wood. The state of understanding of the lithium-ion-battery graphite solid electrolyte interphase (SEI) and its relationship to formation cycling. *Carbon*, 105:52–76, August 2016.
- [13] J.-M. Tarascon and M. Armand. Issues and challenges facing rechargeable lithium batteries. *Nature*, 414(6861):359–367, November 2001.
- [14] Kang Xu. Electrolytes and Interphases in Li-Ion Batteries and Beyond. *Chemical Reviews*, 114(23):11503–11618, December 2014.
- [15] Alexander C. Kozen, Chuan-Fu Lin, Alexander J. Pearse, Marshall A. Schroeder, Xiaogang Han, Liangbing Hu, Sang-Bok Lee, Gary W. Rubloff, and

- Malachi Noked. Next-Generation Lithium Metal Anode Engineering *via* Atomic Layer Deposition. *ACS Nano*, 9(6):5884–5892, June 2015.
- [16] Akihiro Kushima, Kang Pyo So, Cong Su, Peng Bai, Nariaki Kuriyama, Takanori Maebashi, Yoshiya Fujiwara, Martin Z. Bazant, and Ju Li. Liquid cell transmission electron microscopy observation of lithium metal growth and dissolution: Root growth, dead lithium and lithium flocs. *Nano Energy*, 32:271–279, February 2017.
- [17] Theodosios Famprikis, Pieremanuele Canepa, James A. Dawson, M. Saiful Islam, and Christian Masquelier. Fundamentals of inorganic solid-state electrolytes for batteries. *Nature Materials*, 18(12):1278–1291, December 2019.
- [18] Abhik Banerjee, Xuefeng Wang, Chengcheng Fang, Erik A. Wu, and Ying Shirley Meng. Interfaces and Interphases in All-Solid-State Batteries with Inorganic Solid Electrolytes. *Chemical Reviews*, 120(14):6878–6933, July 2020.
- [19] Feng Zheng, Masashi Kotobuki, Shufeng Song, Man On Lai, and Li Lu. Review on solid electrolytes for all-solid-state lithium-ion batteries. *Journal of Power Sources*, 389:198–213, June 2018.
- [20] Zeeshan Ahmad, Tian Xie, Chinmay Maheshwari, Jeffrey C. Grossman, and Venkatasubramanian Viswanathan. Machine Learning Enabled Computational Screening of Inorganic Solid Electrolytes for Suppression of Dendrite Formation in Lithium Metal Anodes. *ACS Central Science*, 4(8):996–1006, August 2018.
- [21] Yunxing Zuo, Mingde Qin, Chi Chen, Weike Ye, Xiangguo Li, Jian Luo, and Shyue Ping Ong. Accelerating materials discovery with bayesian optimization and graph deep learning. *Materials Today*, 2021.
- [22] Peng-Jie Lian, Bo-Sheng Zhao, Lian-Qi Zhang, Ning Xu, Meng-Tao Wu, and Xue-Ping Gao. Inorganic sulfide solid electrolytes for all-solid-state lithium

- secondary batteries. *Journal of Materials Chemistry A*, 7(36):20540–20557, 2019.
- [23] Rusong Chen, Qinghao Li, Xiqian Yu, Liquan Chen, and Hong Li. Approaching Practically Accessible Solid-State Batteries: Stability Issues Related to Solid Electrolytes and Interfaces. *Chemical Reviews*, 120(14):6820–6877, July 2020.
- [24] Michel Armand. The history of polymer electrolytes. *Solid State Ionics*, 69(3):309–319, August 1994.
- [25] Krzysztof Jan Siczek. Chapter Seven - Electrolytes. In Krzysztof Jan Siczek, editor, *Next-Generation Batteries with Sulfur Cathodes*, pages 79–115. Academic Press, January 2019.
- [26] Mahmut Dirican, Chaoyi Yan, Pei Zhu, and Xiangwu Zhang. Composite solid electrolytes for all-solid-state lithium batteries. *Materials Science and Engineering*, 136:27–46, April 2019.
- [27] Penghui Yao, Haobin Yu, Zhiyu Ding, Yanchen Liu, Juan Lu, Marino Lavorgna, Junwei Wu, and Xingjun Liu. Review on Polymer-Based Composite Electrolytes for Lithium Batteries. *Frontiers in Chemistry*, 7, 2019.
- [28] J. B. Bates, N. J. Dudney, G. R. Gruzalski, R. A. Zuhr, A. Choudhury, C. F. Luck, and J. D. Robertson. Electrical properties of amorphous lithium electrolyte thin films. *Solid State Ionics*, 53-56:647–654, July 1992.
- [29] J. B. Bates, N. J. Dudney, G. R. Gruzalski, R. A. Zuhr, A. Choudhury, C. F. Luck, and J. D. Robertson. Fabrication and characterization of amorphous lithium electrolyte thin films and rechargeable thin-film batteries. *Journal of Power Sources*, 43(1):103–110, March 1993.

- [30] J. B. Bates, G. R. Gruzalski, N. J. Dudney, C. F. Luck, and Xiaohua Yu. Rechargeable thin-film lithium batteries. *Solid State Ionics*, 70-71:619–628, May 1994.
- [31] W. C West, J. F Whitacre, and J. R Lim. Chemical stability enhancement of lithium conducting solid electrolyte plates using sputtered LiPON thin films. *Journal of Power Sources*, 126(1):134–138, February 2004.
- [32] Yoongu Kim, Gabriel M. Veith, Jagjit Nanda, Raymond R. Unocic, Miaofang Chi, and Nancy J. Dudney. High voltage stability of LiCoO₂ particles with a nano-scale LiPON coating. *Electrochimica Acta*, 56(19):6573–6580, July 2011.
- [33] Keerthi Senevirathne, Cynthia S. Day, Michael D. Gross, Abdessadek Lachgar, and N. A. W. Holzwarth. A new crystalline LiPON electrolyte: Synthesis, properties, and electronic structure. *Solid State Ionics*, 233:95–101, February 2013.
- [34] André Schwöbel, René Hausbrand, and Wolfram Jaegermann. Interface reactions between LiPON and lithium studied by in-situ X-ray photoemission. *Solid State Ionics*, 273:51–54, May 2015.
- [35] V. Thangadurai, Heiko Kaack, and W. Weppner. Novel Fast Lithium Ion Conduction in Garnet-Type Li₅La₃M₂O₁₂ (M = Nb, Ta). *Journal of the American Ceramic Society*, 86(3):437–440, 2003.
- [36] P. G. Bruce and A. R. West. Ionic conductivity of LISICON solid solutions, Li_{2+2x}Zn_{1-x}GeO₄. *Journal of Solid State Chemistry*, 44(3):354–365, October 1982.
- [37] H. Y-P. Hong. Crystal structures and crystal chemistry in the system Na_{1+x}Zr₂Si_xP_{3-x}O₁₂. *Materials Research Bulletin*, 11(2):173–182, February 1976.

- [38] T Takahashi and H Iwahara. Ionic conduction in perovskite-type oxide solid solution and its application to the solid electrolyte fuel cell. *Energy Conversion*, 11(3):105–111, September 1971.
- [39] Zhonghui Gao, Huabin Sun, Lin Fu, Fangliang Ye, Yi Zhang, Wei Luo, and Yunhui Huang. Promises, Challenges, and Recent Progress of Inorganic Solid-State Electrolytes for All-Solid-State Lithium Batteries. *Advanced Materials*, 30(17):1705702, 2018.
- [40] Mogalahalli V. Reddy, Christian M. Julien, Alain Mauger, and Karim Zaghib. Sulfide and Oxide Inorganic Solid Electrolytes for All-Solid-State Li Batteries: A Review. *Nanomaterials*, 10(8):1606, August 2020.
- [41] A. Hayashi, N. Masuzawa, S. Yubuchi, F. Tsuji, C. Hotehama, A. Sakuda, and M. Tatsumisago. A sodium-ion sulfide solid electrolyte with unprecedented conductivity at room temperature. *Nature Communications*, 10(1):5266, December 2019.
- [42] Y. Kato, S. Hori, T. Saito, K. Suzuki, M. Hirayama, A. Mitsui, M. Yonemura, H. Iba, and R. Kanno. High-power all-solid-state batteries using sulfide superionic conductors. *Nature Energy*, 1(4), 2016.
- [43] Erik A. Wu, Swastika Banerjee, Hanmei Tang, Peter M. Richardson, Jean-Marie Doux, Ji Qi, Zhuoying Zhu, Antonin Grenier, Yixuan Li, Enyue Zhao, Grayson Deysher, Elias Sebti, Han Nguyen, Ryan Stephens, Guy Verbist, Karena W. Chapman, Raphaële J. Clément, Abhik Banerjee, Ying Shirley Meng, and Shyue Ping Ong. A stable cathode-solid electrolyte composite for high-voltage, long-cycle-life solid-state sodium-ion batteries. *Nature Communications*, 12(1):1256, December 2021.

- [44] P. Hohenberg and W. Kohn. Inhomogeneous electron gas. *Physical Review*, 136:B864–B871, 1964.
- [45] W. Kohn and L. J. Sham. Self-consistent equations including exchange and correlation effects. *Physical Review*, 140:A1133–A1138, 1965.
- [46] Paolo Giannozzi, Stefano De Gironcoli, Pasquale Pavone, and Stefano Baroni. Ab initio calculation of phonon dispersions in semiconductors. *Physical Review B*, 43(9):7231, 1991.
- [47] Xavier Gonze. First-principles response of solids to atomic displacements and homogeneous electric fields: Implementation of a conjugate-gradient algorithm. *Physical Review B*, 55:10337–10354, 1997.
- [48] Xavier Gonze and Changyol Lee. Dynamical matrices, Born effective charges, dielectric permittivity tensors, and interatomic force constants from density-functional perturbation theory. *Physical Review B*, 55:10355–10368, 1997.
- [49] Stefano Baroni, Stefano De Gironcoli, Andrea Dal Corso, and Paolo Giannozzi. Phonons and related crystal properties from density-functional perturbation theory. *Reviews of Modern Physics*, 73(2):515, 2001.
- [50] Paolo Giannozzi and Stefano Baroni. Density-functional perturbation theory. In S. Yip, editor, *Handbook of Materials Modeling*, pages 195–214. Springer, 2005.
- [51] H. Jónsson, G. Mills, and K. W. Jacobsen. Nudged elastic band method for finding minimum energy paths of transitions. In B. J. Berne, G. Ciccotti, and D. F. Coker, editors, *Classical and Quantum Dynamics in Condensed Phase Simulations*, pages 385–404. World Scientific, Singapore, 1998.

- [52] Graeme Henkelman, Blas P. Uberuaga, and Hannes Jónsson. A climbing image nudged elastic band method for finding saddle points and minimum energy paths. *The Journal of Chemical Physics*, 113:9901–9904, 2000.
- [53] Graeme Henkelman and Hannes Jónsson. Improved tangent estimate in the nudged elastic band method for finding minimum energy paths and saddle points. *The Journal of Chemical Physics*, 113:9978–9985, 2000.
- [54] Xavier Gonze, Bernard Amadon, Gabriel Antonius, Frédéric Arnardi, Lucas Baguet, Jean-Michel Beuken, Jordan Bieder, François Bottin, Johann Bouchet, Eric Bousquet, Nils Brouwer, Fabien Bruneval, Guillaume Brunin, Théo Cavignac, Jean-Baptiste Charraud, Wei Chen, Michel Côté, Stefaan Cottenier, Jules Denier, Grégory Geneste, Philippe Ghosez, Matteo Giantomassi, Yannick Gillet, Olivier Gingras, Donald R. Hamann, Geoffroy Hautier, Xu He, Nicole Helbig, Natalie Holzwarth, Yongchao Jia, François Jollet, William Lafargue-Dit-Hauret, Kurt Lejaeghere, Miguel A. L. Marques, Alexandre Martin, Cyril Martins, Henrique P. C. Miranda, Francesco Naccarato, Kristin Persson, Guido Petretto, Valentin Planes, Yann Pouillon, Sergei Prokhorenko, Fabio Ricci, Gian-Marco Rignanese, Aldo H. Romero, Michael Marcus Schmitt, Marc Torrent, Michiel J. van Setten, Benoit Van Troeye, Matthieu J. Verstraete, Gilles Zérah, and Josef W. Zwanziger. The abinit project: Impact, environment and recent developments. *Comput. Phys. Commun.*, 248:107042, 2020. Available from the website <https://www.abinit.org/>.
- [55] Paolo Giannozzi, Oscar Baseggio, Pietro Bonfà, Davide Brunato, Roberto Car, Ivan Carnimeo, Carlo Cavazzoni, Stefano de Gironcoli, Pietro Delugas, Fabrizio Ferrari Ruffino, Andrea Ferretti, Nicola Marzari, Iurii Timrov, Andrea Urru, and Stefano Baroni. Quantum espresso toward the exascale. *The Jour-*

- nal of Chemical Physics*, 152(15):154105, 2020. Available from the website quantumespresso.org.
- [56] N. A. W. Holzwarth, A. R. Tackett, and G. E. Matthews. A Projector Augmented Wave (PAW) code for electronic structure calculations, Part I: *atompaw* for generating atom-centered functions. *Computer Physics Communications*, 135:329–347, 2001. Available from the website <http://pwpaw.wfu.edu>.
- [57] E. Schrödinger. Quantisierung als Eigenwertproblem. *Annalen der Physik*, 385:437, 1926.
- [58] M. Born and R. Oppenheimer. Zur Quantentheorie der Molekeln. *Annalen der Physik*, 389(20):457–484, 1927.
- [59] M. Born and K. Huang. *Dynamical Theory of Crystal Lattices*. Oxford University Press, 1954.
- [60] H. Hellmann. Zur Rolle der kinetischen Elektronenenergie für die zwischenatomaren Kräfte. *Zeitschrift für Physik*, 85(3):180–190, March 1933.
- [61] R. P. Feynman. Forces in Molecules. *Physical Review*, 56(4):340–343, August 1939.
- [62] E. Merzbacher. *Quantum mechanics*. Wiley, New York, 3rd edition, 1998.
- [63] J. C. Slater. The Theory of Complex Spectra. *Physical Review*, 34(10):1293–1322, November 1929.
- [64] J. Nocedal and Wright S.J. *Numerical optimization*. Springer, 1999.
- [65] V. Fock. Näherungsmethode zur Lösung des quantenmechanischen Mehrkörperproblems. *Zeitschrift für Physik*, 61(1):126–148, January 1930.
- [66] J. D. Jackson. *Classical electrodynamics*. Wiley, New York, 3rd edition, 1998.

- [67] D. R. Hartree. The Wave Mechanics of an Atom with a Non-Coulomb Central Field. Part I. Theory and Methods. *Mathematical Proceedings of the Cambridge Philosophical Society*, 24(1):89–110, January 1928.
- [68] P. Hohenberg and W. Kohn. Inhomogeneous Electron Gas. *Phys. Rev.*, 136(3B):B864–B871, November 1964.
- [69] W. Kohn and L. J. Sham. Self-Consistent Equations Including Exchange and Correlation Effects. *Phys. Rev.*, 140(4A):A1133–A1138, November 1965.
- [70] L. H. Thomas. The calculation of atomic fields. *Mathematical Proceedings of the Cambridge Philosophical Society*, 23(5):542–548, January 1927.
- [71] E. Fermi. Un metodo statistico per la determinazione di alcune proprieta dell’atome. *Rend. Accad. Naz. Lincei*, 6:602, 1927.
- [72] D. M. Ceperley and B. J. Alder. Ground State of the Electron Gas by a Stochastic Method. *Phys. Rev. Lett.*, 45(7):566–569, August 1980.
- [73] J. P. Perdew and Alex Zunger. Self-interaction correction to density-functional approximations for many-electron systems. *Phys. Rev. B*, 23(10):5048–5079, May 1981.
- [74] David C. Langreth and M. J. Mehl. Easily Implementable Nonlocal Exchange-Correlation Energy Functional. *Phys. Rev. Lett.*, 47(6):446–450, August 1981.
- [75] A. D. Becke. Density-functional exchange-energy approximation with correct asymptotic behavior. *Phys. Rev. A*, 38(6):3098–3100, September 1988.
- [76] John P. Perdew, J. A. Chevary, S. H. Vosko, Koblar A. Jackson, Mark R. Pederson, D. J. Singh, and Carlos Fiolhais. Atoms, molecules, solids, and surfaces: Applications of the generalized gradient approximation for exchange and correlation. *Phys. Rev. B*, 46(11):6671–6687, September 1992.

- [77] John P. Perdew, Kieron Burke, and Matthias Ernzerhof. Generalized Gradient Approximation Made Simple. *Phys. Rev. Lett.*, 77(18):3865–3868, October 1996.
- [78] John P. Perdew, Adrienn Ruzsinszky, Gábor I. Csonka, Oleg A. Vydrov, Gustavo E. Scuseria, Lucian A. Constantin, Xiaolan Zhou, and Kieron Burke. Restoring the density-gradient expansion for exchange in solids and surfaces. *Phys. Rev. Lett.*, 100:136406, Apr 2008.
- [79] Guido Petretto, Shyam Dwaraknath, Henrique P.C. Miranda, Donald Winston, Matteo Giantomassi, Michiel J. van Setten, Xavier Gonze, Kristin A. Persson, Geoffroy Hautier, and Gian-Marco Rignanese. High-throughput density-functional perturbation theory phonons for inorganic materials. *Scientific Data*, 5(1):180065, December 2018.
- [80] Susi Lehtola, Conrad Steigemann, Micael J.T. Oliveira, and Miguel A.L. Marques. Recent developments in libxc — a comprehensive library of functionals for density functional theory. *SoftwareX*, 7:1–5, 2018.
- [81] P. E. Blöchl. Projector augmented-wave method. *Phys. Rev. B*, 50(24):17953–17979, December 1994.
- [82] U. von Barth and C. D. Gelatt. Validity of the frozen-core approximation and pseudopotential theory for cohesive energy calculations. *Phys. Rev. B*, 21:2222–2228, Mar 1980.
- [83] G. Kresse, J. Furthmüller, and J. Hafner. Ab initio Force Constant Approach to Phonon Dispersion Relations of Diamond and Graphite. *Europhysics Letters (EPL)*, 32(9):729–734, December 1995.
- [84] K. Parlinski, Z.Q. Li, and Y. Kawazoe. First-principles determination of the soft mode in cubic ZrO₂. *Physical Review Letters*, 78(21):4063–4066, 1997.

- [85] Stefano Baroni, Paolo Giannozzi, and Andrea Testa. Green's-function approach to linear response in solids. *Phys. Rev. Lett.*, 58(18):1861–1864, May 1987.
- [86] Paolo Giannozzi, Stefano de Gironcoli, Pasquale Pavone, and Stefano Baroni. Ab initio calculation of phonon dispersions in semiconductors. *Phys. Rev. B*, 43:7231, 1991.
- [87] Xavier Gonze. First-principles responses of solids to atomic displacements and homogeneous electric fields: Implementation of a conjugate-gradient algorithm. *Phys. Rev. B*, 55(16):10337–10354, April 1997.
- [88] Stefano Baroni, Stefano de Gironcoli, Andrea Dal Corso, and Paolo Giannozzi. Phonons and related crystal properties from density-functional perturbation theory. *Rev. Mod. Phys.*, 73(2):515–562, July 2001.
- [89] A. Messiah. *Quantum Mechanics*. Elsevier, North-Holland, Amsterdam, 1962.
- [90] Born M. and Huang K. *Dynamical Theory of Crystal Lattices*. Oxford, 1954.
- [91] Xingfeng He, Yizhou Zhu, and Yifei Mo. Origin of fast ion diffusion in superionic conductors. *Nature Communications*, 8(1):15893, August 2017.
- [92] Aris Marcolongo and Nicola Marzari. Ionic correlations and failure of Nernst-Einstein relation in solid-state electrolytes. *Physical Review Materials*, 1(2):025402, July 2017.
- [93] Svetlana S. Petrova and Alexander D. Solov'ev. The Origin of the Method of Steepest Descent. *Historia Mathematica*, 24(4):361–375, November 1997.
- [94] C. G. Broyden. A class of methods for solving nonlinear simultaneous equations. *Mathematics of Computation*, 19(92):577–577, January 1965.

- [95] G. Henkelman, B. P. Uberuaga, and H. Jonsson. A climbing image nudged elastic band method for finding saddle points and minimum energy paths. *The Journal of Chem. Phys.*, 113:9901, 2000.
- [96] John S. Tse. Ab initio molecular dynamics with density functional theory. *Annual Review of Physical Chemistry*, 53:249–290, 2002.
- [97] R. Iftimie, P. Minary, and M. E. Tuckerman. Ab initio molecular dynamics: Concepts, recent developments, and future trends. *Proceedings of the National Academy of Sciences*, 102(19):6654–6659, May 2005.
- [98] Dominik Marx and Jürg Hutter. *Ab Initio Molecular Dynamics: Basic Theory and Advanced Methods*. Cambridge University Press, Cambridge, 2009.
- [99] Loup Verlet. Computer “Experiments” on Classical Fluids. I. Thermodynamical Properties of Lennard-Jones Molecules. *Physical Review*, 159(1):98–103, July 1967.
- [100] William C. Swope, Hans C. Andersen, Peter H. Berens, and Kent R. Wilson. A computer simulation method for the calculation of equilibrium constants for the formation of physical clusters of molecules: Application to small water clusters. *The Journal of Chemical Physics*, 76(1):637, 1982.
- [101] Johannes Grotendorst, Stefan Blügel, and John von Neumann-Institut für Computing, editors. *Computational nanoscience*. Number 31 in NIC series. NIC-Secretariat, Research Centre Jülich, Jülich, 2006.
- [102] D. J. Evans and B. L. Holian. The Nose–Hoover thermostat. *The Journal of Chemical Physics*, 83(8):4069, 1985.
- [103] Shuichi Nosé. Constant Temperature Molecular Dynamics Methods. *Progress of Theoretical Physics Supplement*, 103:1–46, 1991.

- [104] Zachary David Hood. *Lithium and sodium solid electrolytes for next-generation batteries: Bridging mechanistic understanding and their performance*. PhD thesis, Georgia Institute of Technology, 2018.
- [105] Kun Huang. Lattice Vibrations and Optical Waes in Ionic Crystals. *Nature*, 167:779–780, 1951.
- [106] W. Jeitschko, T. A. Bither, and P. E. Bierstedt. Crystal structure and ionic conductivity of Li boracites. *Acta Crystallographica Section B*, 33(9):2767–2775, 1977.
- [107] Deming Tan, Faxing Wang, Tobias Pietsch, Matthias A. Grasser, Thomas Dohert, and Michael Ruck. Low-Temperature Ionothermal Synthesis of Li-Ion Conductive $\text{Li}_{47}\text{O}_{12}\text{Cl}$ Solid-State Electrolyte. *ACS Applied Energy Materials*, 2(7):5140–5145, 2019.
- [108] Marcus Vlasse, Alain Levasseur, and Paul Hagemuller. Crystal structure of $\text{Li}_5\text{B}_7\text{O}_{12.5}\text{Cl}$ at 296 and 425 K. *Solid State Ionics*, 2(1):33–37, 1981.
- [109] Koichi Momma and Fujio Izumi. Vesta 3 for three-dimensional visualization of crystal, volumetric, an morphology data. *Applied Crystallography*, 44:1272–1276, 2011. Code available from the website <http://jp-minerals.org/vesta/en/>.
- [110] <https://www.python.org>.
- [111] ©1994-2021 The MathWorks, Inc.
- [112] H. T. Stokes and D. M. Hatch. Findsym: Program for identifying the space group symmetry of a crystal. *J. Appl. Cryst.*, 38:237–238, 2008. Available from the webpage <http://iso.byu.edu/iso/isotropy.php>.

- [113] Xingfeng He, Yizhou Zhu, and Yifei Mo. Origin of fast ion diffusion in superionic conductors. *Nature Communications*, 8:15893, June 2017.

Part 4

Curriculum Vitae

YAN LI

Department of Physics, Wake Forest University, Winston-Salem, NC 27109-7507

Tel: (336) 541-0821; Email: liy217@wfu.edu

EDUCATION

Doctor of Philosophy (Ph.D.)

2017 – 2021, Department of Physics, Wake Forest University

Advisor: Professor Natalie Holzwarth

Research Focus: Computer Simulations of Electrolyte Materials

Master of Science (M.S.)

2010 – 2013, Department of Physics, China University of Mining and Technology

Advisor: Professor Gang Tang

Research Focus: Scaling Behavior of the Explosive Percolation Model on Erdős-Rényi Network and Scale-Free Network

Bachelor of Science (B.S.)

2006 – 2010, Department of Physics, China University of Mining and Technology

Major: Optical Information Science and Technology

HONORS AND AWARDS

2021 – Outstanding Graduate Research Award, Department of Physics, Wake Forest University

2013 – Outstanding Master's Thesis Award, China University of Mining and Technology

2013 – Outstanding Master's Graduate Award, China University of Mining and Technology

2012 – China National Scholarship

2010 – Outstanding Graduate Award, China University of Mining and Technology

PUBLICATIONS: <http://users.wfu.edu/natalie/recentpubs.html>

- Y. Li and N. A. W. Holzwarth, First principles simulations to understand the structural and electrolyte properties of idealized $\text{Li}_{7.5}\text{B}_{10}\text{S}_{18}\text{X}_{1.5}$ ($\text{X} = \text{Cl}, \text{Br}, \text{I}$), in preparation.
- Y. Li, D. Lynch (co-first), and N. A. W. Holzwarth, Computational investigation of the structural and electrolyte properties of the boracite materials related to $\text{Li}_4\text{B}_7\text{O}_{12}\text{Cl}$, in preparation.
- Y. Li and N. A. W. Holzwarth, First principles simulations of Li boracites $\text{Li}_4\text{B}_7\text{O}_{12}\text{Cl}$ and $\text{Li}_5\text{B}_7\text{O}_{12.5}\text{Cl}$, submitted.
- Y. Li, Z. D. Hood, and N. A. W. Holzwarth, Computational study of Li_3BO_3 and Li_3BN_2 I: Electrolyte properties of pure and doped crystals, *Physical Review Materials* **5**, 085402 (2021). DOI: <https://doi.org/10.1103/PhysRevMaterials.5.085402>
- Y. Li, Z. D. Hood, and N. A. W. Holzwarth, Computational study of Li_3BO_3 and Li_3BN_2 II: Stability analysis of pure phases and of model interfaces with Li anodes, *Physical Review Materials* **5**, 085403 (2021). DOI: <https://doi.org/10.1103/PhysRevMaterials.5.085403>
- Y. Li, Z. D. Hood, and N. A. W. Holzwarth, Computational (Re)investigation of the Structural and Electrolyte Properties of $\text{Li}_4\text{P}_2\text{S}_6$, $\text{Na}_4\text{P}_2\text{S}_6$, and $\text{Li}_2\text{Na}_2\text{P}_2\text{S}_6$, *Physical Review Materials* **4**, 045406 (2020). DOI: <https://doi.org/10.1103/PhysRevMaterials.4.045406>

- Y. Li, W. C. Kerr, and N. A. W. Holzwarth, Continuity of phonon dispersion curves in layered ionic materials, *Journal of Physics: Condensed Matter* **32**, 055402 (2020). DOI: <https://doi.org/10.1088/1361-648X/ab4cc1>
- L.J. Song, G. Tang, Y. Zhang, K. Han, Z.P. Xun, H. Xia, D.P. Hao, and Y. Li, Surface structures of equilibrium restricted curvature model on two fractal substrates, *Chinese Physics B* **23**, 010503 (2014).
- Y. Li, G. Tang, L.J. Song, Z.P. Xun, X. Hui, and D.P. Hao, Numerical simulations of the phase transition property of the explosive percolation model on Erdős Rényi random network, *Acta Physica Sinica* **62**, 046401 (2013).
- Z.P. Xun, Y. Li, H. Xia, D.P. Hao, and G. Tang, Dynamic scaling behaviors of the discrete growth models on fractal substrates, *Journal of Statistical Mechanics* P10014 (2012).
- Z.P. Xun, G. Tang, H. Xia, D.P. Hao, and Y. Li, Asymptotic dynamic scaling behavior of the (1+1)-dimensional Wolf-Villain model, *Physical Review E* **8**, 041126 (2012).

PRESENTATIONS: <http://users.wfu.edu/natalie/presentations.html>

- Oral presentation at the 240th ECS Meeting – “Computational investigation of Li boracite $\text{Li}_4\text{B}_7\text{O}_{12}\text{Cl}$ and related materials as solid electrolytes”
- Oral presentation at the 240th ECS Meeting (Presented by Prof. Holzwarth) – “First principles simulations to understand the structural and electrolyte properties of idealized $\text{Li}_{7.5}\text{B}_{10}\text{S}_{18}\text{X}_{1.5}$ (X = Cl, Br, I)”
- Oral presentation at the March 2021 APS Virtual Meeting – “ Li_3BO_3 and Li_3BN_2 : Computational study of structural and electrolyte properties of pure and doped crystals”
- Annotated slides that would have been presented at the cancelled March 2020 APS Meeting – “Prediction and analysis of a sodium ion electrolyte: $\text{Li}_2\text{Na}_2\text{P}_2\text{S}_6$ ”
- Oral presentation at the 236th Meeting of the Electrochemical Society in Atlanta, GA Oct. 13-17, 2019 – “Computational (Re)investigation of the Structural and Electrolyte Properties of $\text{Li}_4\text{P}_2\text{S}_6$, $\text{Na}_4\text{P}_2\text{S}_6$, and $\text{Li}_2\text{Na}_2\text{P}_2\text{S}_6$ ”
- Poster presentation at the 2019 Workshop on Recent Developments in Electronic Structure at the University of Illinois in Champaign-Urbana, Illinois May 20-22, 2019 – “Computational Reinvestigation of the Structural and Electrolyte Properties of $\text{Li}_4\text{P}_2\text{S}_6$ and $\text{Na}_4\text{P}_2\text{S}_6$ ”
- Oral presentation at the March 2019 APS Meeting, March 4-8, 2019 in Boston, MA – “Computational and experimental investigation of $\text{Na}_4\text{P}_2\text{S}_6$ as a promising solid electrolyte material for sodium metal batteries”

RESEARCH EXPERTISE

- First principles software packages: ABINIT, Quantum ESPRESSO
- DFT-based simulations on crystalline electrolyte materials: Structural optimization, vibrational analysis, NEB calculation, Ab initio molecular dynamics simulations, interface modeling
- Programming skills: Python, MATLAB